Mechanics of Abrasive Wear of Elastomeric Materials

by

Hang Qi

Submitted to the Department of Mechanical Engineering
in partial fulfillment of the requirements for the degree of

Doctor of Science

at the

MASSACHUSETTS INSTITUTE OF TECHNOLOGY

September 2003

Author .....
Department of Mechanical Engineering
August 15, 2003

Certified by .....
Mary C. Boyce
Professor of Mechanical Engineering
Thesis Supervisor

Accepted by .....
Ain A. Sonin
Chairman, Department Committee on Graduate Students

Mechanics of Abrasive Wear of Elastomeric Materials

by

Hang Qi

Submitted to the Department of Mechanical Engineering
on August 15, 2003, in partial fulfillment of
the requirements for the degree of
Doctor of Science

Abstract

Elastomeric materials are widely used as tire and sealing materials due to their ability to undergo large deformations and conform to the mating surface. However, their applications often result in repeated contact with abrasive particles, which act to abrasively wear the elastomers. Elastomeric materials are observed to exhibit a characteristic form of abrasive pattern on the surface after cyclic scratching. The dimension of this pattern is closely related to the wear rate, whereas the formation of this pattern is controlled by abrasive particle sizes, material mechanical properties, loading conditions, thermal conditions, and chemical degradation of materials. Much research has been conducted in the past. However, direct observations of the wear process are rare. The mechanics underlying the abrasive wear of elastomeric materials is unclear.

In order to provide fundamental understanding of the abrasive wear of elastomeric materials due to abrasive particle indentation and scratching, this research studied the wear of elastomeric materials subjected to scratching by knife geometries that simulate abrasive particles and contact conditions. Efforts were focused on establishing direct observations and analysis of the deformation mechanics. An in situ micro scratching test capability operating within a scanning electron microscope (SEM) was developed and used together with image processing to reveal the local deformation fields. Surface profile analyses using both SEM and ZYGO (a non-contact interferometer) were also conducted to observe the surface change during cyclic scratching.

The large strain nonlinear stress-strain behavior of thermoplastic polyurethanes (TPUs) exhibits strong hysteresis, rate dependence and cyclic softening. In this work, a constitutive model capturing the major features of the stress-strain behavior of TPUs was developed. The model decomposed material behavior into an equilibrium component and a rate dependent deviation from equilibrium. The cyclic softening behavior was attributed to be due to the softening of the equilibrium path as a result of the evolution of the effective volume fraction of the soft domain during deformation, upon which the occluded soft material was released to carry load due to the relative motions among hard domains.

Extensive finite element (FE) based simulations of indentation and scratching tests using the proposed constitutive model were conducted. The FE model was verified by comparing the variation of normal and tangential forces and the distributions of displacement and strain fields with those experimentally obtained. The FE simulations

revealed that the transition from the stick phase to the slip phase during scratching was accompanied by a large increase in molecular stretch and maximum principal stress (tensile stress), thus creating conditions for damage initiation. The FE model was then used to investigate the effects of contact conditions, cyclic scratching, friction, scratching speed, and material properties on the variation of molecular stretch and maximum principal stress. The effects of fiber fillers were also investigated by considering three representative fiber orientations: Horizontal, vertical, and lateral orientations. It was found that, for the fiber geometries and abrasive particle geometries studied, fibers do not enhance material wear resistance.

Thesis Supervisor: Mary C. Boyce
Title: Professor of Mechanical Engineering

Acknowledgements

First, I would like to thank my advisor, Prof. Mary C. Boyce, for her support and guidance during the process of my thesis research. Her excellence in academic standard and dedication toward research and teaching will always be a source of inspiration and encouragement to me. I would also like to thank Prof. Nam P. Suh, Prof. Robert E. Cohen, and Prof. Douglas P. Hart for their serving in my thesis committee and for their numerous insightful suggestions.

I am thankful to Caterpillar Inc. for their generous financial support to my thesis work and provide materials.

I would also like thank to my colleagues in the Mechanics and Material group: Franco Capaldi, Adam Mulliken, Ethan Parsons, Mats Danielsson, Jin Yi, Steve Xia, Nuo Sheng, Cheng Su, Yujie Wei, Yin Yuan, Theodora Tzianetopoulou, Rajdeep Sharma, Antonio Pantano, and others. Thank you very much for the friendship and the good time that I had enjoyed with you.

I am grateful to Una Sheenhan, Raymond Hardin, and Leslie Regan, who created an environment where I could concentrate only on my research. Thank you very much for taking care of administrative details.

I also would like to Don Galler of Material Science Department for his help and sharing his experiences on using SEM and designing test apparatus.

I feel indebted to my wife, Zhen Yang, and my parents, Xiangchun Qi and Yan Cheng, my sister, Yun Qi, for their constant support, patience, and love. Thank you all for everything.

Contents

Chapter 1

Introduction

Elastomers are widely used in industry due to their ability to undergo elastically large deformations and to conform to a surface that they are in contact with, making elastomers a material of choice in sealing and tire applications. Although the elastomer-surface interaction is a drive in material selection, it is also a fundamental and major cause of eventual failure where abrasive wear constitutes a major source of failure of elastomeric materials. For instance, abrasive wear is one of the major concerns in mechanical face seal design[1-1][1-2]; Additionally, it is estimated that each year the tire wear debris generated in the U.S. is about 5×10^8 kg[1-3]. In this chapter, we discuss the challenges in the research on the abrasive wear of elastomeric material and the goals for this thesis research. In the first section, the engineering background of elastomer abrasive wear research is introduced. The current research is motivated by the design of wear resistant thermoplastic polyurethane elastomers (TPUs). TPUs have been found to exhibit the characteristic wear feature of more conventional elastomeric (rubbery) materials. Therefore, a general description of the features of abrasive wear of elastomeric materials is also presented. In the second section, a review on previous research on abrasive wear of elastomeric materials is presented. The challenges in this research are also discussed. In the third section, the goal and the research plan for this thesis research are discussed.

1.1 Motivations

1.1.1 Face Seals in Track-type Tractors

Mechanical face seals are used in the pin joint assemblies of track-type tractors, or "bulldozers". The wheel of a tractor translates power to the ground by turning a track (Figure 1-1), which provides the tractor with an enormous amount of traction. The track is comprised of numerous links, each connected by a pin-joint assembly shown in Figure 1-2(a)(b). The sprockets of the tractor's wheel contact the cylindrical bushing which turns freely about the pin. End caps are bolted onto both ends of the pin. Prior to assembly,

seals are pressed into the end caps in order to seal in and maintain lubricant between the pin and bushing and prevent contaminants from entering the joint. The seals and the flat ends of the bushing are in contact and in oscillation motion relative to one another during operation. This type of seal, which contacts its bearing surface along a plane, is classified as a face seal.

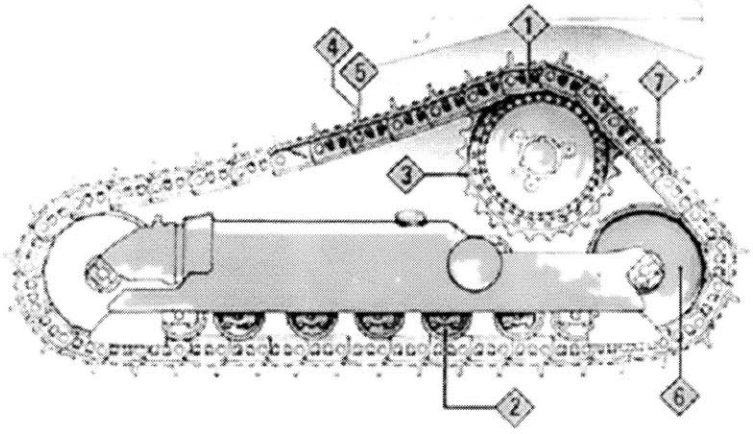

Figure 1-1: A track consists of numerous of links

A typical face seal in this pin-joint assembly is shown in Figure 1-3[1-4][1-6][1-5]. The seal consists of supporting components and a seal lip. The seal lip is the part of the seal that contacts the bushing surface and provides the actual sealing mechanism. It is usually made of thermoplastic polyurethane, which is a type of elastomeric material and is recognized as one of the best wear resistant elastomeric materials.

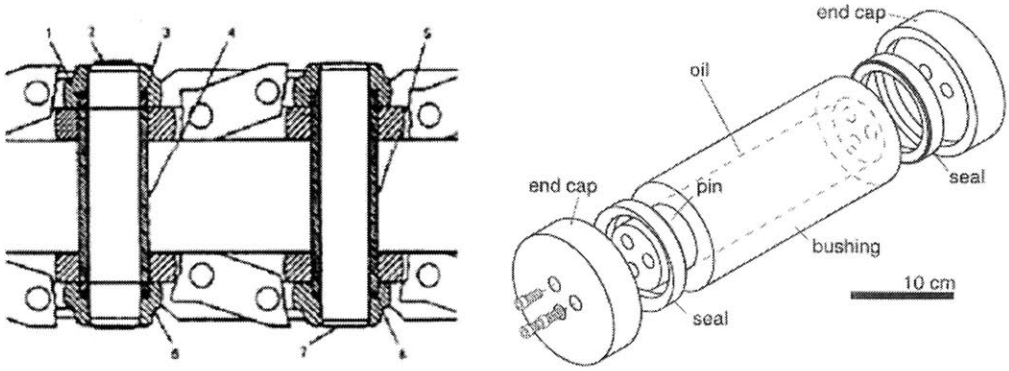

(a) (b)

Figure 1-2: (a) Links are connected by pin joint assembly; (b) a pin joint assembly consists of pin, bushing, end cap and seal

The primary function of the pin-joint assemblies is to transfer load from the driving wheel to the track effectively. If the pin-joint assemblies fail to work, a service must be called in and the tractor must be idled until the service has been completed. Such a service is very costly to both manufacturer and customers. Therefore, it is important to elongate the life of the pin-joint assemblies. In the past, the bushings were worn faster than the seals. The seals thus could be replaced at the same time when a service for the bushings was called in. More recently, new designs have prolonged the life of the bushings, making the seal life a determining factor for the maintenance period. Therefore there is a clear need to improve the design of the track face seals.

1.1.2 Failure of Face Seals due to Abrasive Wear

In a pin joint assembly, the seal lip is pressed onto the bushing surface, forming a contact band of about 1mm by applying proper contact pressure. The outer side of the seal lip interacts with the outside environment, typically full of slurry and soil; whereas the inner side of the seal lip faces the pin-joint assembly, interacting with lubrication oils. During the operation of the track, the seal lip oscillates against the bushing surface. Ayala[1-4][1-5] and Parsons[1-6] built an in-situ seal wear test apparatus in order to mimic the in-service loading conditions and wear the seal surface while simultaneously observing the migration of particles under the seal lip and their evolution/interaction with the seal lip. They found that abrasive particles accommodated their motions to the contact surface by both rotation and slipping, and abraded the seal material surface repeatedly, resulting in eventual failure due to abrasive wear.

Figure 1-3 shows the surface of a failed face seal. The surface shows a pattern of alternating peaks-valleys, typically observed in abrasive wear of elastomeric materials and known as abrasive patterns. Figure 1-3(a) shows the pattern observed by scanning electron microscopy (SEM). Figure 1-3(b) and (c) show the surface of the same sample obtained by ZYGO interferometry, a three-dimensional surface profiler. The periodic form of the ridges over the surface is clearly depicted in Figure1-3(c), which shows the profile along the line AB in Figure 1-3(b). Figure 1-3(c) reveals the average valley-valley distance for this particular sealant material is about 30μm with the maximum peak-to-valley height of about 5μm and average peak-to-valley height of about 2μm.

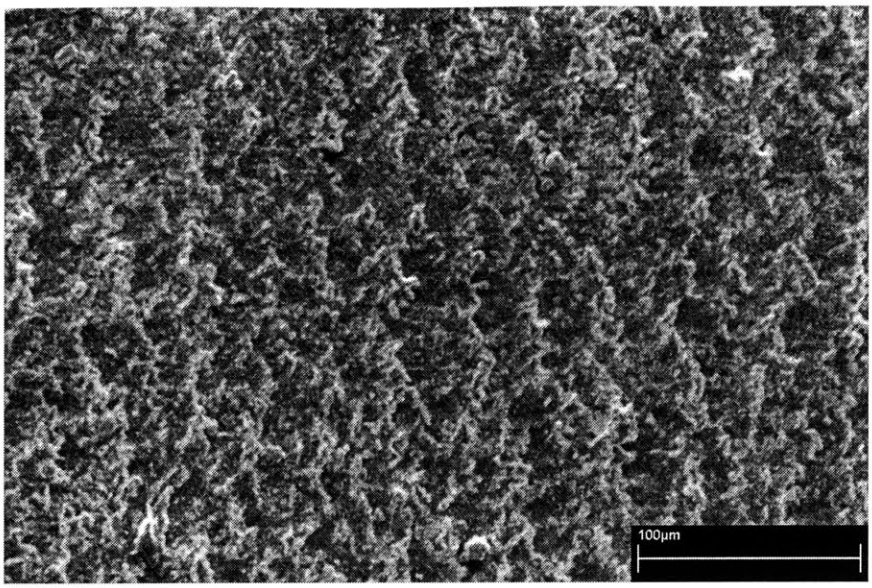

Figure 1-3(a)

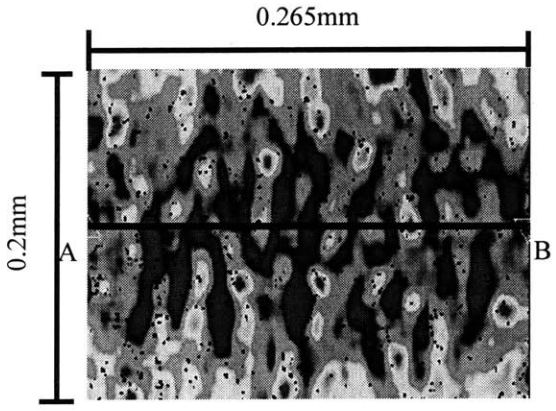

Figure 1-3(b)

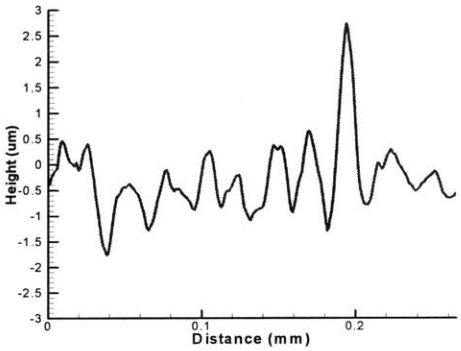

Figure 1-3(c)

Figure1-3 (a) Abrasive pattern seen on worn surface of face seal (a) by SEM; (b) ZYGO; (c) Abrasive pattern profile along line AB in (b), by ZYGO.

1.2 Abrasive Wear of Elastomeric Materials

1.2.1 General Descriptions

When elastomers are operating under aggressive and repetitive surface contact conditions, such as seals and tires, abrasive wear constitutes a primary mode of failure. A dominant feature of abrasive wear of elastomeric materials is the formation of abrasive patterns on the elastomer contact surface after a certain number of cycles, as shown in Figure 1-3.

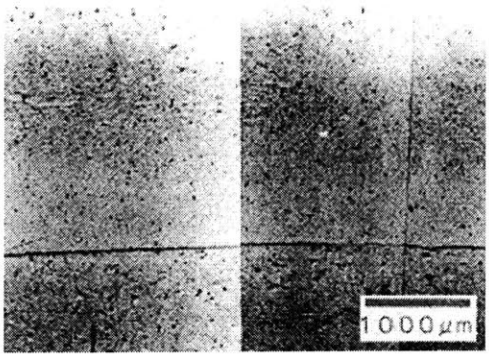

Figure 1-4(a)

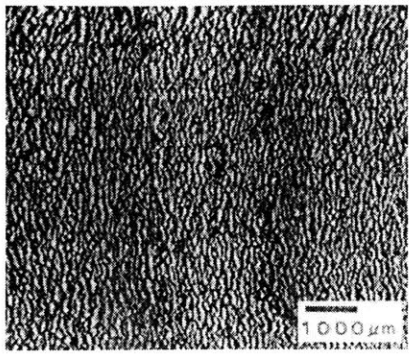

Figure 1-4(b)

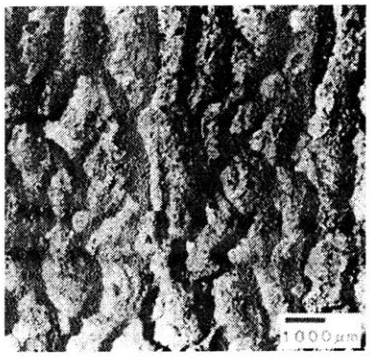

Figure 1-4(c)

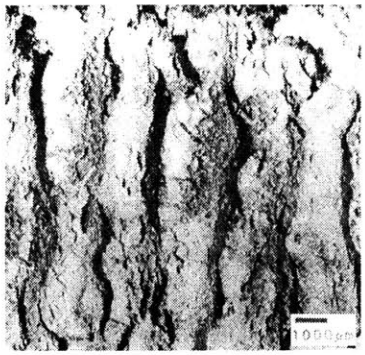

Figure 1-4(d)

Figure 1-4: Formation of abrasive patterns observed on natural rubbers[1-8]. (a) Surface damages observed after a few abrade; (b) and (c) Surface damage grow and form periodic peak-valley patterns. The distance between neighboring ridges increases with increasing number of abrading; (d) Abrasive patterns reach a stable state. The distance between neighboring ridges does not increase but the wear rate is very high.

Schallamach[1-7] is generally recognized to be the first person to systematically study the abrasive wear of elastomers. In his tests on rubbers, he found that when rubber was abraded without change of direction, sets of parallel ridges were often shown on the surface of the samples at an angle normal to the direction of motion[1-7]. These patterns are called 'abrasion patterns', or 'Schallamach patterns'. It was found that these patterns grew gradually to a final periodical form rather than formed suddenly. Figure 1-4 shows the development of abrasive patterns on natural rubber subjected to cyclic abrading by razor blade as observed by Fukahori and Yamazaki[1-8]. After the first few rubbing cycles, numerous small damages with space ranging usually from 10 μm to 50 μm can be observed on the contacting surface (Figure 1-4(a)). As the number of rubbing cycles increases, the micro crack or ridge spacing increases. When a critical space, which is

typically ranging from a few tens of microns to a few millimeters, has been reached, the space stabilizes but the each individual ridge is still moving as a result of continuous generation of new damages and loss of material[1-8]. When the critical space is reached, the wear rate also arrives at a stable and high value.

1.2.2 Mechanism for Abrasive Wear of Elastomeric Materials

Elastomers have found wide applications in seals and tires, due to their ability to undergo very large elastic deformations. However, in comparison with the study on wear of metals and other polymeric materials, the understanding of wear of elastomers is relatively unexplored, partly because of the shorter research history on elastomers, and partly because of less understanding and the complication of the mechanical properties of elastomers.

Schallamach[1-7] found that when rubber was abraded on road surface without change of direction, the contact surface of rubber could be depicted with saw teeth (tears) profiles (Figure 1-5). When being abraded, the saw teeth were bent forward, thus exposing their underside to the abrasive and protecting the forward part of the surface from abrasion, and finally resulting in the formation alternative ridge-valley patterns. The development of the pattern was a relatively slow process. It was found that the pattern maintained its general configuration for short times but moved as a whole across the surface in the direction of abrasion. The so called saw teeth in Schallamach's description were actually known as cracks or micro-cracks. This suggests that the progression of abrasive patterns can be modeled as the propagation of a crack, then one can use fracture and fatigue mechanics to model abrasive wears[1-9][1-10][1-11].

In some carefully controlled tests[1-8][1-12], it was found that the movement of abraders over samples consisted of a stick-slip phase. Fukahori and Yamazaki[1-8][1-11][1-13] observed micro-vibrations during slip. They further proposed that the stick phase was the driving force to propagate cracks whereas the micro-vibration with natural frequency of rubbers was the driving force for the initiation of cracks.

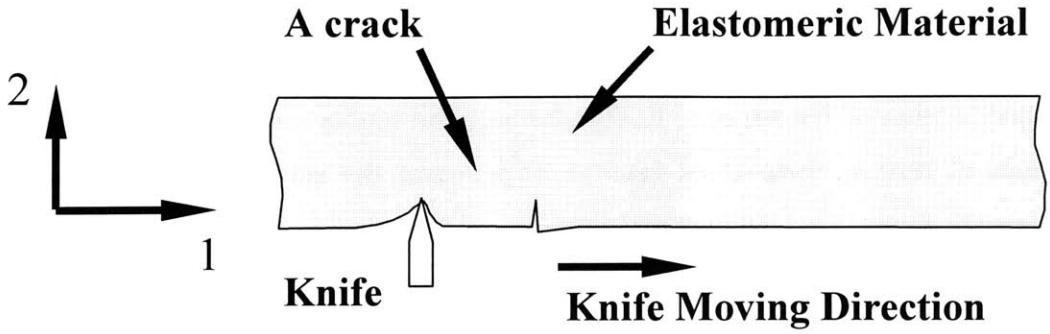

Figure 1-5(a)

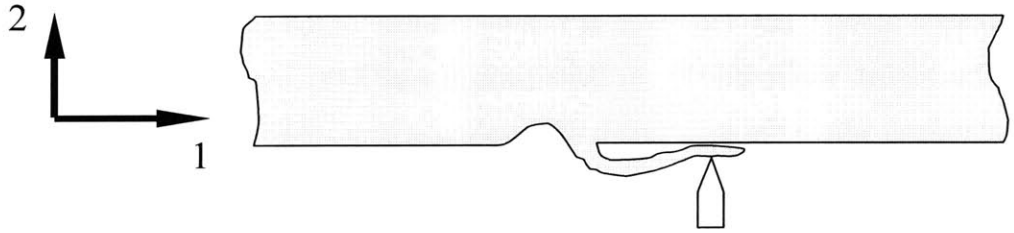

Figure 1-5(b)

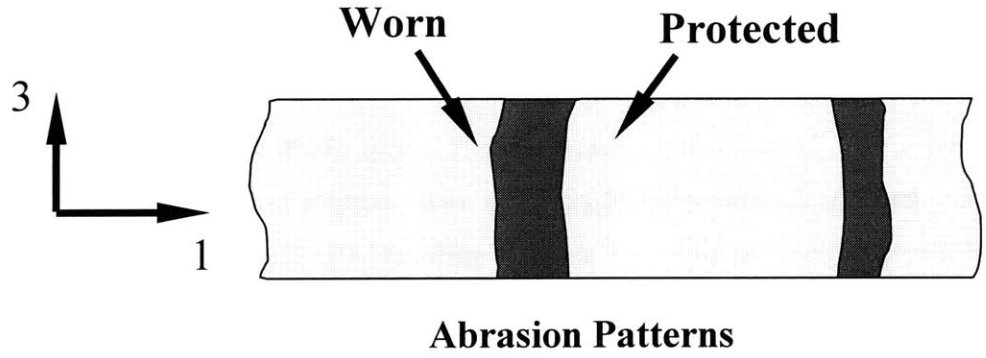

Figure 1-5(c)

Figure 1-5: Formation of abrasive patterns: (a) A knife is scratching over the surface. Note there is a pre-existed crack in front of the knife; (b) As knife moves over the surface, the crack were bent forward, thus exposing their underside to the abrasive and protecting the forward part of the surface from abrasion; (c) An alternative worn-protected surface pattern formed over the abraded surface.

When using blunt glass abraders with large radii (R=2mm) of curvature in friction tests on rubbers, Schallamach[1-14] and Barquins[1-15][1-16] found small regular folds of rubber moving like wrinkles on a carpet and crossing the area of contact at velocities significantly greater than the imposed velocity. This phenomenon is commonly referred as detachment wave or "Schallamach wave" and was attributed to be due to the formation

of vertical junction on the edge of the contact zone because of adhesive forces (molecular attraction forces)[1-14][1-15][1-16], resulting in unstable rubber contact surface during tangential motion of the abrader. Except for soft and highly elastic elastomers, such as pure natural rubber, these folds became ridges over the surface. If the surface was continuously abraded by the abrader, extreme stretching of these ridges would result in damage over the surface[1-16]. However, it is unclear whether Schallamach wave and the resultant extreme stretch can be related to abrasive pattern. The adhesive force between the contact surfaces plays an important role in the mechanism of initiation of Schallamach wave[1-16]. However, it will be reduced in the presence of a tensile stress along the rubber surface[1-17]. In Schallamach and Barquins, the abraders used were blunt abraders, where the penetration of the abrader into rubber was small, resulting in a relatively small tensile stress along the surface surrounding the contact region and preserving the adhesive force. The asperities present in abrasive wear, however, are generally much sharper than the blunt abraders, and create large tensile stress along the surface due to the large ratio between penetration depth and the tip radius of the asperities as the asperities penetrate into the surface. This tensile stress effectively reduces the adhesive force. Nevertheless, abrasive tests using sharp abrader also show abrasive patterns. Indeed, Thomas studied abrasive wear using a razor blade as the abrader and found abrasive patterns over the abraded surface[1-9]. Therefore, it is unclear whether Schallamach wave will present in abrasive wear and how it can be related to abrasive wear.

Gent and Pulford[1-18] found that the abrasive wear process actually took place at two levels. A basic wear process led to the detachment of small rubber particles, $1 \sim 5 \mu m$ in dimension. This process resulted in the formation of the initial cracks or damages. The tips of the cracks were periodically torn away, probably as a result of mechanical fatigue[1-9][1-19]. The later created larger particle debris up to several hundred microns. This bimodal size distribution of abraded particles had been observed indirectly for tires worn under normal service conditions by collecting wear debris near highway[1-3]. The small particles were key to the initiation of the wear process. Gent[1-20] further conjectured that the small particles were formed in each surface scratching process as a result of the explosion of small cavities of dimension $0.1 \sim 1 \mu m$ in the

material due to the inflation pressure or triaxial tension created during frictional sliding. The possible ways to generate the inflation pressure were: (1) Air, forced into solution in rubber by the pressure exerted by a sliding surface; (2) Thermal decomposition of the rubber generating high enough pressures; (3) The dilating action of frictional forces. Currently, there is no direct evidence showing whether these conjectures are correct and which one dominates. After the formation of the initial cracks, the wear process resembles crack growth under cyclic tearing stress and could be modeled using the energy approach[1-19][1-9].

It is well known that the wear resistance of materials is closely related to the hardness of the elastomer (note that elastomer "hardness" is a measure of elastic behavior). Pitman[1-21], Hill et al [1-22] Lancaster[1-23] suggested that the wear rate vs hardness curve could be divided into three regions (Figure 1-6). In region A (hardness value ranging from 60A to 75A), the wear rate decreased with increasing hardness and the mechanism of wear in this region was mainly tearing since the materials were easy to deform due to relatively low elastic modulus. In region B (hardness value ranging from 75A to 95A), the wear rate was approximately independent of the hardness and the mechanism of wear changed from tearing to fatigue. In region C (hardness value ranging from 95A to 65D), the wear rate increased with increasing hardness and the mechanism of wear changed from fatigue to cutting. Generally, abrasion patterns could be observed in regions A and B, but not in region C [1-22][1-24]. A recent study by the author showed that durometer hardness was only an indicator of the elastic property of elastomeric materials[1-25]. Materials having different limiting extensibilities could possess the same durometer hardness value. This shows that hardness cannot be used alone as an indicator for the wear performance of elastomeric materials.

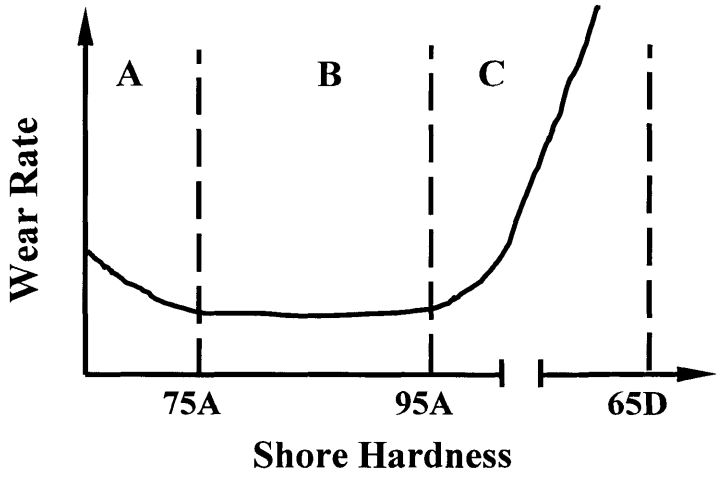

Figure 1-6: Schematics of the relationship between wear rate and hardness for elastomers[1-22].

In most engineering applications, elastomers are filled with fibers or particles to increase their stiffness and strength. Wada and Uchiyama[1-26] found that the addition of polyamide fibers (3mm in length and 28μm in diameter) into carbon black filled chloroprene rubber resulted in improved wear resistance while the largest improvement was achieved when fibers were oriented normal to the contact surface and the least improvement in lateral direction. Fukahori and Yamazaki[1-13] found the addition of carbon black could improve the wear resistance. However, they also found that the rate of crack growth at small cyclic strain amplitudes was not decreased by carbon black, rather an increase in filler content increases the crack growth rate. Therefore, other mechanism might play a role in the mechanism of improving wear resistance. For wear due to abrasive particles, Lancaster [1-23][1-30] suggested that the addition of fillers reduced the elongation to break. It followed that the resistance of reinforced composites to abrasive cutting wear was unlikely to be much better than that of the parent polymers. Yang et al[1-32] in the study of glass sphere filled rubbers found that when the filler size was greater than the asperity spacing, the fillers provided load support and the abrasion of the filler itself became a governing factor in wear. When the filler became comparable in size to the asperity spacing, filler pull-out was a potential wear mechanism and would trigger accelerated wear due to the combination of filler loss and the weakened worn surfaces. When the filler was significantly smaller than the asperity spacing, the worn topography resembled those of the homogeneous materials and the effect of cavitation

and debonding at the filler-matrix interfaces became important.

In the study of abrasive wear of elastomers in seal applications, Ayala et al.[1-33] found that during cyclic motion of a seal operating in a mud box, the wear process consisted of two distinct stages: a break-in period and an aggressive wear period. The break-in period corresponded to the period of operation before the dirt front formed at the seal edge and began to advance, whereas the aggressive wear period corresponded to a constant wear rate and the seal surface was aggressively worn. In a series of seal abrasion experiments with filled and unfilled elastomers, Parsons[1-6] found that the tests with filled elastomers showed much longer break-in period than unfilled elastomers whereas both filled and unfilled elastomers had about the same aggressive wear rate. With the help of numerical simulations, Parsons further conjectured that the reason for the extended break-in period of filled elastomers was because the presence of fibers near the surface created increasing resistance to prevent abrasive particles (dirt) from entering the contact band and aggregating into critical size clusters.

Loading and geometrical factors, such as speed, temperature, normal stress, counter surface, and particle size influence wear usually by affecting the mechanical behavior of the elastomer or the contact conditions. For elastomers, the sliding speed is significant due to dissipative effects of friction and strain-rate effects on mechanical behavior[1-34]. The abrasive wear resistance of unfilled rubber tended to increase with increasing speed mainly because the tensile strength increased with the speed[1-7]. However, by rubbing unfilled rubber against fine abrasive paper(CC1500, $R_a = 2.1\mu m$, $R_z = 13.0\mu m$), Wada and Uchiyama [1-26] found that the wear rate dependence on the sliding speed was very small, even though they observed the spacing of the abrasion pattern became wider with decreasing sliding speeds.

Much less information is available about lubricated polymer wear[1-34]. Lubrication is usually achieved by the addition of some lubricants between the two contacting surfaces; then the wear rate is decreased either by the formation of a thin film which actually isolates the two contacting bodies, or by reducing the tangential frictional force, or by the penetration of the lubricant into the surface layer and the change of the mechanical properties of the material[1-35][1-36][1-37][1-38]. However, both the formation of a thin film and the penetration of the lubricant have close relation with

speed. As the speed increases, there is an increasing tendency to load support from hydrodynamic or elastohydrodynamic lubrication via geometric wedge formation. Polymers are particular susceptible to this effect because of their relatively low moduli[1-39][1-40]. On the other hand, an increase in speed makes the beneficial lubricant difficult to enter the surface layer, then the lubricant effect will decrease[1-34]. From this point of view, high speed will increase wear rate.

When the sliding speed increases to a certain value, the deforming elastomer cannot dissipate all the heat generated by the friction, and the temperature at the contacting surface will increase. The considerable temperature rise is approximately proportional to the square root of the velocity. This dependence has been predicted theoretically by Jaeger[1-41] for very high velocity, but appears to be valid for a wider range than Jaeger's theory[1-7]. Generally, in is known that increasing temperature will soften the material, which in turn increases the wear rate. However, this is not always true. For instance, Hill et al[1-22] showed that for samples with Shore hardness 55D, the un-rested test samples had lower wear rate than rested samples did. Since in un-rested test, the temperature at the contact surface increased sufficiently, this resulted in softening of the elastomer materials. From Figure 1-6, Shore hardness 55D is located in region C, where the wear rate decreases as the hardness decreases. On the other hand, a rapidly increasing temperature is usually an indication that wear is progressing rapidly since it indicates that the interaction has increased significantly, most possibly due to worn surface and/or loss of lubricant.

1.2.3 Challenges

Although much research has been conducted in the past and the overall picture of the development of abrasive patterns has been outlined, several critical questions concerning the mechanism of the abrasive wear of elastomers remain unanswered. For instance, how and in what form is damage initiated during the relative motions of the two contact surfaces? How do the mechanical properties of elastomeric materials relate to the wear performance? How do factors, such as contact conditions, speed, and fillers influence the wear? To answer these questions, the mechanics of abrasive wear must be fundamentally addressed. However, several hurdles discourage the endeavor.

First, direct observation of the wear process is difficult to achieve due to technique challenges in viewing the contact surface during the wear process. In the study of abrasive wear, conventional research methods adapt the routine of testing followed by inspection. During this process, however, detailed information about deformation cannot be achieved.

Second, theoretical modeling of the abrasive wear of elastomeric materials is difficult due to lack of accurate constitutive model of the stress-strain behaviors of elastomers. A salient feature of the stress-strain behavior of elastomers is their low moduli and their capability to recover from large deformation, which is particularly easy to be achieved due to the low moduli of elastomers. Therefore, traditional contact mechanics, such as linear elasticity solution based Hertz theory, are not suitable anymore. Finite element simulations are deterred by the geometric and material nonlinearities occurring during abrasive wear and the lack of a proper model for the stress-strain behavior of the material.

Due to the above reasons, the mechanics of abrasive wear of elastomeric materials is unclear, and the mechanically controlling factors in the mechanism of the problem are uncertain.

In this research, we will try to establish in-situ experimental observation and numerical analyses of the deformation and mechanics of abrasive wear of elastomeric materials, with concentrations on the mechanics regarding the initiation of first cracks/damages on elastomeric materials and the influence of the mechanical properties of elastomeric materials and the contact conditions on their wear performances.

1.2.4 Typical Length Scales in Abrasive Wear of Elastomeric Materials

While tire and seals operate at the macro-scale, the abrasive wear of elastomeric materials generally occurs at a micron scale. It is therefore important to review the typical length scales in the abrasive wear of elastomeric materials in order to identify the proper length scale where experimental and theoretical study should be conducted. Table 1-1 lists the typical length scales.

For seal applications, Parsons[1-6] found that only abrasive particles less than 100 μm could enter the contact surface between sealant material and bushing whereas abrasive particles less than 1μm were too small to cause damage to the material surface.

By deliberately adding particles of different sizes, Parsons noticed that most damage was caused by abrasive particles about a few microns to a few tens of microns. Therefore, the abrasive particle size in the current study is 1μm~100μm. The initial damage in rubber is observed to be about a few microns[1-8][1-18]. For seals, since the abrasive particles are 1μm~100μm, it is reasonable to believe the initial damages are about the same length scales. Three-dimensional surface profile inspection of the seal surface shows that the surface roughness is less than 1μm. At a stable state, the ridge spacing of abrasive patterns is found to be about a few tens of microns to a few millimeters. The dimensions of material structures of rubbers and polyurethanes[1] are about a few nanometers to a few hundred of nano meters. Glass fibers and carbon black are two commonly used fillers for elastomeric materials. Although single carbon black particles are nano-scale materials (diameter typically of about 40 nanometer), they tend to agglomerate into micro scale particles. The glass fibers in the material of the current study have average diameter of 16μm and length to diameter ratio of 8[1-6].

Table 1-1: Typical length scales in abrasive wear of elastomeric materials

Abrasive particles	1μm~100μm
Initial damage	1μm~10μm
Roughness of molded surface	~1μm
Ridge spaces at stable state	10μm~1mm
Material micro structure	10nm~100nm
Fillers	1μm~100μm

From Table 1-1, the initial damage occurs at a length scale similar to the size of abrasive particles but much larger than the microstructure of the homoplolymer. It is therefore possible to treat the homopolymer as a continuum media. The dimensions of fillers are comparable with initial damages and abrasive particles. As suggested by Yang

[1] Some segmented thermoplastic polyurethanes show large supermolecular structures in the form of spheulites of dimensions of about 10-50μm[1-42]. In such case, the spheulites in the material can be treated as inhomogeneities or inclusions in the material.

et al[1-32], for the fillers at the comparable scale to asperities, the interaction between fillers and abrasive particles affect the initiation of damages.

In summary, the current study addresses the problem at the scale of a few microns to a few tens of microns, where the elastomer can be treated as continuum media and the interaction between abrasive particles and fillers should be addressed.

1.3 Research Plan

1.3.1 Three-dimensional to Two-dimensional Simplification

Abrasive wear occurs when an abrasive particle is confined between two contact surfaces. Figure 1-7 shows a two-dimensional schematic of the contact configuration.

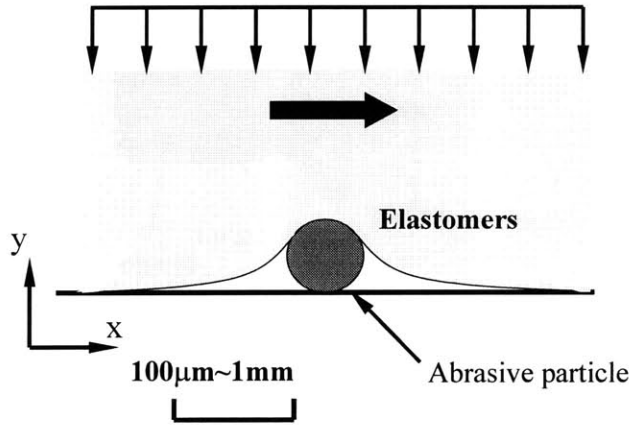

Figure 1-7: Two-dimensional illustration of the typical configuration of abrasive wear.

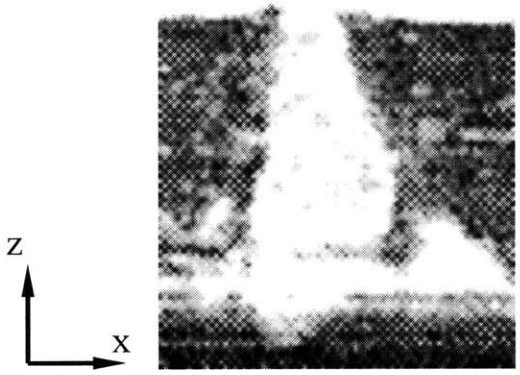

Figure 1-8: A tear-shape abrasive particle is observed between the two contact surfaces.

In figure 1-7, the abrasive particle is idealized as a sphere. In reality, abrasive particles could be any arbitrary shape. It is observed[1-5] that the shape of an abrasive

particle in face seal application resembles a tear (Figure 1-8). Clearly such a three-dimensional configuration results in a very complicated multiaxial deformation. The confined configuration makes it extremely difficult to establish direct observation of the deformation at a micron-scale during the wear process. Moreover, the three-dimensional configuration dramatically increases the cost of numerical simulation addressing nonlinearities arising from large deformation, contact, and material stress-strain behavior, making it unreasonable to implement numerical simulations.

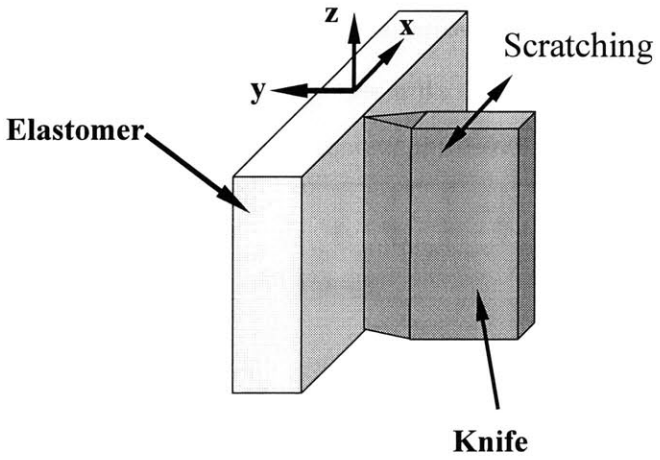

Figure 1-9(a)

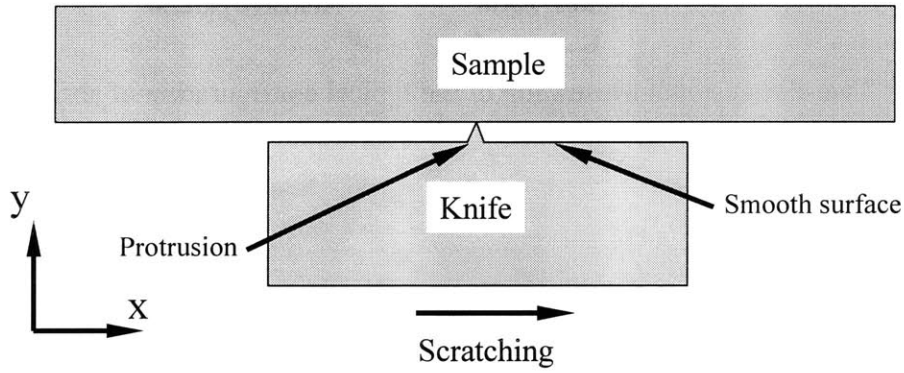

Figure 1-9(b)

Figure 1-9: Abrasive wear is simplified as a process where the surface of an elastomer is scratching by (a) a wedge type knife; and (b) a bulk type knife.

A two-dimensional simplification of the confined configuration is proposed in the current study. Figure 1-9 shows the schematics of the proposed model. Here, abrasive wear is simplified as a process where a knife indents and scratches the surface of an

elastomer. The wedge-type knife (Figure 1-9(a)) simulates the interaction between a single abrasive particle and the elastomer, which is the dominant interaction in abrasive wear, whereas the bulk-type knife(Figure 1-9(b)) studies the effect of an overall surface compression on simultaneous knife indentation and scratching. It is noted that the wedge-type scratching test has been used in literature to emulate more complex abrasive loading and exhibit abrasive patterns[1-9][1-8][1-11][1-13].

The two-dimensional simplification of the abrasive wear process releases partially the confined configuration in Figure 1-7. The advantage of such a simplification is that direct observations of the abrasive wear process can be established and the cost for numerical simulations is reduced significantly. Since the dominant mechanics of abrasive wear of elastomeric materials is associated with processes where an abrasive particle abrades/scratches the surface of elastomers, such a simplification from a highly confined three-dimensional configuration to a partially confined two-dimensional configuration retains the major features of the mechanics.

1.3.2 Research Plan and Thesis Outline

Abrasive wear of elastomers are complicated by the couplings among mechanics, temperatures, and chemical reactions. A comprehensive study where all of these factors are addressed would be extremely complicated. As discussed above, in some circumstances, at elevated temperature mechanical properties of materials will change but the fundamental mechanism of abrasive wear due to cyclic scratching remains the same. Therefore, in this research, in order to provide initial fundamental understanding of abrasive wear due to the dominating effect of abrasive particle indentation and scratching, we will study the mechanics of abrasive wear without considering temperature.

This research provides fundamental understanding of the abrasive wear of elastomeric materials due to abrasive particle indentation and scratching, and studies the wear of elastomeric materials subjected to scratching by knife geometries that simulate abrasive particles and contact conditions. Efforts will be focused on establishing direct observations and analysis of the deformation mechanics. To achieve this goal, both experimental and theoretical studies will be conducted. Figure 1-10 shows the flow chart

of the research plan. The thesis is arranged as the following:

In the second chapter, direct observations of deformations of the indentation/ scratching process using a micro in-situ indentation/scratching system will be established. Micrographs will be collected at different stages of the deformation to provide visualized deformation and will be further used together with an image processing technique to reveal the displacement and strain fields during indentation and scratching.

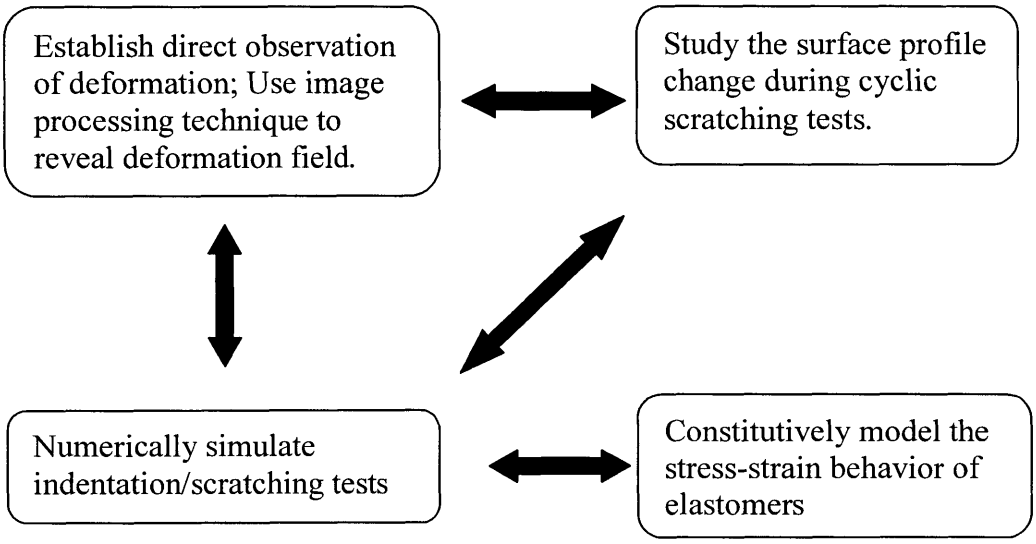

Figure 1-10: Flow chart of research plan.

In the third chapter, topography evolution during cyclic scratching tests will be investigated using both SEM and Zygo (a three-dimensional interferometric surface profiler). Surface change will be monitored after each cycle of scratching tests in order to provide surface evolution during cyclic scratching tests.

The material used in this study is a thermoplastic polyurethane, which exhibits strong hysteresis, rate dependence, and cyclic softening. In order to properly model the indentation/scratching process, it is important to capture the history dependent nonlinear behavior of the material. In the fourth chapter, a constitutive model accounting for the hysteresis and rate dependence will be presented.

In the fifth chapter, numerical simulations of indentation/scratching tests will be conducted. Results obtained from simulations under the same test conditions in the real

tests will be compared with the displacement and strain fields obtained from image processing of the micrographs in Chapter 2, and will be employed to investigate the topography evolution observed in Chapter 3. Numerical simulations will be further conducted to study the effect of contact conditions, material properties, scratching speed, and filler effects on the abrasive wear of elastomers. This study will provide insight into factors which influence initiation of wear and will also provide insight into correlations between the viscoelastic behavior of elastomers and their "traction" capability.

In the last chapter, we will give conclusions and discuss future research directions.

The Durometer hardness test, which measures indentation resistance of materials, is one of the most commonly used measurements to qualitatively assess and compare the mechanical behavior of elastomeric and elastomeric-like materials. The hardness value is commonly related to the elastic behavior of the material using linear elasticity theory and was used by many researchers in the study of abrasive wear resistance. Since both Durometer indentation tests and abrasive wear involve significant amount of large deformation of the material, it is unclear how the stress-strain behavior of the material at large deformation will affect the durometer hardness. In Appendix A, nonlinear finite element simulations of hardness tests, which act to provide a mapping of measured Durometer Shore A and D values to the stress-strain behavior of elastomers, are presented. This work is published in Rubber Chemistry and Technology[1-25].

When indentation tests are conducted at a scale much larger than the length scale of the structures of tested materials, such as durometer hardness indentation and micro indentation on elastomers where the indentation depths are 10μm-1mm and are greater than the structural length scale of the material, it is possible to treat the material as a homogenous media. However, when indentation tests are conducted at a nanometer scale, the interaction between material structure and indentor becomes dominant. In Appendix B, nanoindentation tests on a special type of materials-vertically aligned carbon nanotube (VACNT) forests-are presented. Unlike indentation tests on bulk material, nanoindentations on VACNT forest are a process where the indentor consecutively bends individual nanotubes during the penetration of the indentor into the forest. The indentation resistance is thus the result of the consecutive interaction between the indentor and individual nanotubes. The model of this process shows that indentation

resistance is a function of mechanical properties, geometry, and areal density of constituent nanotubes. The average mechanical properties of nanotubes can hereby be reduced from nanoindentation resistance. A paper[1-43] based on this work is submitted and accepted by Journal of Mechanics and Physics of Solids and will be published soon.

References

[1-1] Muller, H.K., Nau, B.S., Fliud Sealing Technology, Marcel Dekker Inc., 1998.

[1-2] Weiss, H., Seal Failure in Fliud Power Applications, in 14th International Conference on Fliud Sealing, Edited by B. Halligan, 1994.

[1-3] Cadle, S.H., Williams, R.L., Gas and particle emissions from automobile tires in laboratory and field studies, Rubber Chem. Tech., vol.52, pp126~158.

[1-4] Ayala, H.M., The effects of soil abrasives on rotary seal effectiveness. Master's thesis, Massachusetts Institute of Technology, 1995.

[1-5] Ayala, H.M., Soil ingestion by elastomeric seals. Ph.D. thesis, Massachusetts Institute of Technology, 1999.

[1-6] Parsons, E.M., Micromechanics of deformation and abrasive wear of fiber-filled elastomers, Master's thesis, Massachusetts Institute of Technology, 1999.

[1-7] Schallamach, S., Friction and abrasion of rubber, Wear, 1, 1957/58.

[1-8] Fukahori Y., and Yamazaki H., Mechanism of rubber abrasion. Part I: Abrasion pattern formation in natural rubber vulcanizate, Wear, 171, 1994, pp195-202.

[1-9] Thomas A.G., Factor influencing the strength of rubbers, J. Polymer Sci.: Symposium No.48, pp145-157, 1974.

[1-10] Muhr, A.H., Pond, T.J., Thomas, A.G., Abrasion of rubber and the effect of lubricant, J. Chem. Phys. PCB , 84, 1987, pp331-334.

[1-11] Fukahori Y., and Yamzaki H., Mechanism of rubber abrasion. Part 3: How is friction linked to fractue in rubber abrasion, Wear, 188, 1995, pp19-26.

[1-12] Yang A.C., Wu T.W., Wear and friction in glassy polymers: Microscratch on blends of polystyrene and poly (2,6-dimethyl-1,4-phenylene oxide), J. of Polymer Sci., Part B: Polymer Phys.; V35, n9, 1997, pp1295-1309

[1-13] Fukahori Y., and Yamzaki H., Mechanism of rubber abrasion. Part 2: General rule in abrasion pattern formation in rubber-like materials, Wear, 178, 1994, pp109-116.

[1-14] Schallamach A., How does rubber slide? Wear, 17, 1971, pp301-312.

[1-15] Barquins M., On a new mechanism of rubber friction, Wear, 97, 1984, pp111-114.

[1-16] Barquins M., Friction and wear of rubber-like materials, Wear, 160, 1993, pp1-11.

[1-17] Barquins, M., Courtel, R., Maugis, D., Friction on stretched rubber, Wear, 38, 1976, pp385-389.

[1-18] Gent, A.N., Pulford, C.T.R., Mechanisms of Rubber Abrasion, J. Appl. Polym. Sci., vol 28, 943~960, 1983.

[1-19] Champ, D.H., Southern, E., and Thomas, A.G., Am. Chem. Soc., Coatings Plast. Div. Prepr., 34, 237, 1974.

[1-20] Gent, A.N., A hypothetical mechanism for rubber abrasion, Rubber Chem. Tech., vol.62, 750~756.

[1-21] Pitman J.S., Proceedings of 3rd Int. Conf. On internal and external protection of pipes, printed by published by BHRA Fluid Engineering, Cranfield, England, 1979, pp129.

[1-22] Hill D.J.T., Killeen M.I., O'Donnell J.H., Pomery P.J., John D.St., Whittaker A.K., Laboratory wear testing of polyurethane elastomers, Wear 208, 1997, pp155-160.

[1-23] Lancaster, J.K., Abrasive wear of polymers, Wear, 14, 1969, pp223-239.

[1-24] Schallamach, A.S., Abrasion and tyre wear, in L. Bateman (ed.), The Chemistry and Physics of Rubber Like Substance, MacLaren, London, 1963, pp357.

[1-25] Qi, J. H., Joyce, K., Boyce, M.C., Durometer hardness and the stress-strain behavior of elastomeric materials, Rubber Chem. Tech., 76, 2003, pp419-435.

[1-26] Wada, N., Uchiyama Y., Friction and wear of short-fiber reinforced rubber composites under various sliding speeds and loads, Wear, 162-164, 1993, pp930-938.

[1-27] Mullins L., J. Rubber Research, 16, 1947, pp275; J. Phys. & Colloid Chem., 54, 1950, pp239.

[1-28] Mullins L., Tobin N.R., Proc. 3rd Rubber Tech. Conf., London, 1954, pp397.

[1-29] Schallamach A., Trans. Inst. Rubber Ind., 28, 1952, pp256.

[1-30] Lancaster, J.K, Friction and wear, in *Polymer Science*, A Material Science handbook, (ed. Jenkins, A.D.), North Holland, Amsterdam, pp.959-1046, 1972.

[1-31] Bijwe J., Logani, C.M, Tewari U.S., Influence of fillers and fiber reinforcement on abrasive wear resistance of some polymeric composites, Wear, 138, 1990, pp77-92

[1-32] Yang, A., Ayala, J., Bell, A., and Scott, J., Effects of filler particles on abrasive wear of elastomer based composites, Wear, v.146, 1991, pp349-366.

[1-33] Ayala, H.M., Yeh, O.C., Hart, D.P., Boyce, M.C., Seal design for reduced wear in abrasive slurries, Wear, 220, 1998, pp9-21.

[1-34] Dickens, P.M., Sullivan, J.L., and Lancaster, J.K., Speed Effects on the Dry and Lubricated Wear of Polymers Wear, 112, 1986, pp273-289.

[1-35] Lancaster, J.K., The lubricated wear of polymers, Proc. 11th Leeds-Lyon Symp. On Mixed Lubrication and Lubricated Wear, Butterworths, London, 1985.

[1-36] Rubenstein, C., Lubrication of polymers, J. Appl. Phys., 32, 1961, pp1445.

[1-37] Evans, D.C., Polymer-fluid interactions in relation to wear, Proc. 3rd Leeds-Lyon Symp. On Wear of Non-metallic Materials, Mechanical Engineering Publications, London, 1978, pp47.

[1-38] Briscoe, B.J., Stolarski, T.A., Davies, G.J., Boundary lubrication of polymers in model fluids, Tribol. Int., 17, 1984, pp129.

[1-39] Cudworth, C.J., Higginson, G.R., Friction of lubricated soft surface layers, Wear, 37, 1976, pp299.

[1-40] Archard, J.F., Kirk, M.T., Influence of elastic modulus on the lubrication of pont contacts, Proc. Lubrication and Wear. Conv., 1963, Institution of Mechanical Engineering, London, 1963, pp181.

[1-41] Jaeger J.C., J. Proc. Roy. Soc., N.S.W., 76, 1942, pp203.

[1-42] Petrovic, Z.S., Ferguson, J., Polyurethane elastomers, Prog. Polym. Sci., 16, 1991, pp695-836.

[1-43] Qi, H.J., Teo, K.B.K., Lau, K.K.S., Boyce, M.C., Milne, W.I., Robertson, J., Gleason, K.K., Determination of Mechanical Properties of Carbon Nanotubes and Vertically Aligned Carbon Nanotube Forests Using Nanoindentation, accepted by J. Mech. Phys. Solids, 2003.

Chapter 2

In-situ Micro Indentation and Scratching Testing within SEM

One of the challenges in the study of abrasive wear of elastomeric materials is the lack of data on the local deformations occurring during the abrading process due to both the micro-scale deformation and the localized region of material where the abrasive wear process takes place. The simplification of the abrasive wear process from a general three-dimensional (3D) configuration to a two-dimensional (2D) scratching process by a wedge-type knife makes it possible to directly observe the process in an in-situ manner whilst the salient features concerning the basic mechanics are retained. In this chapter, an in situ micro indentation/scratching test system operating within a scanning electron microscope (SEM) developed by the author is introduced first. Tests using this system on unfilled thermoplastic polyurethane were conducted and micrographs taken during the tests are presented in the second section. Image processing of the displacement field, using software VIC 2D together with a software computing the corresponding strain fields using appropriate large deformation continuum mechanics, is conducted to post-process the micrographs from in-situ micro-indentation/scratching tests and to reveal the deformation and strain fields in the abrading process. Finally, summary of experimental observations are presented.

2.1 In-situ Micro Indentation/Scratching Test System

2.1.1 Test Process

The new test setup establishes direct observations of material deformation during the indentation/scratching process. Figure 2-1 schematically illustrates the test process and the surface in-situ observed during deformation as well as the surface observed post deformation.

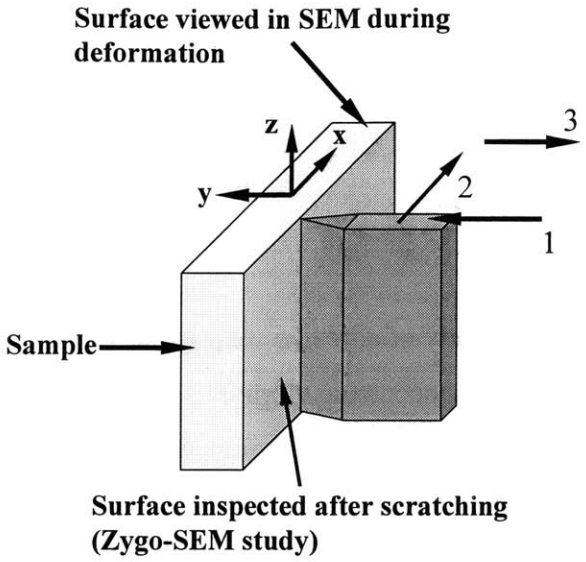

Figure 2-1 (a)

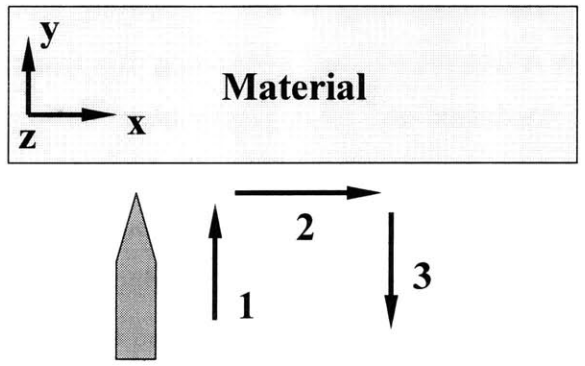

Figure 2-1 (b)

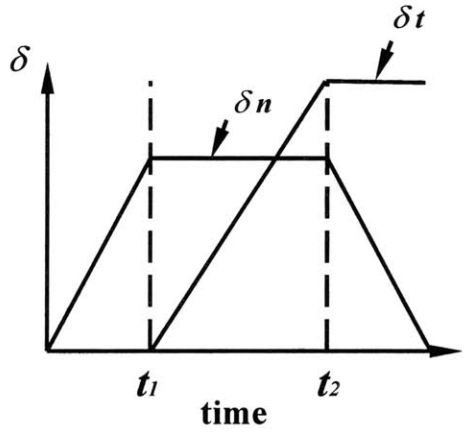

Figure 2-1 (c)

Figure 2-1 Test process: (a) 3D view of test process; (b) Top view of test process; (c) Normal (δn) and tangential (δt) displacement history.

Figure 2-1(a) shows the sample and the relative position of the knife and the observation locations. Figure 2-1(b) and (c) show the test process schematically. The knife, whose sharp edge is parallel to the sample surface, is first driven toward the surface following the loading curve denoted by δ_n in Figure 2-1(c) until a maximum specified indentation depth δ_n is reached. It is then moved tangentially to scratch the surface following the loading curve denoted by δ_t in Figure 2-1(c), whilst the indentation depth is held constant. Finally, a negative motion in the normal direction is applied to

withdraw the knife.

In this chapter, observation is conducted viewing along the z-axis during the test so that the in situ deformation is obtained. In the next chapter, both Zygo interferometry and SEM will be employed to inspect the abraded surface (the surface with normal in the y direction in Figure 2-1(a)), which had been in contact with the knife during the scratching test.

2.1.2 Test System

Conventional experimental studies on abrasive wear use the procedure of surface abrading followed by inspection. In this procedure, however, the in-situ deformation during scratching is unavailable. Establishing direct observation of the deformation during the abrading process becomes an even greater challenge in the study of abrasive wear of sealing materials, where the size of abrasive particle is typically $10 \sim 100 \mu m$.

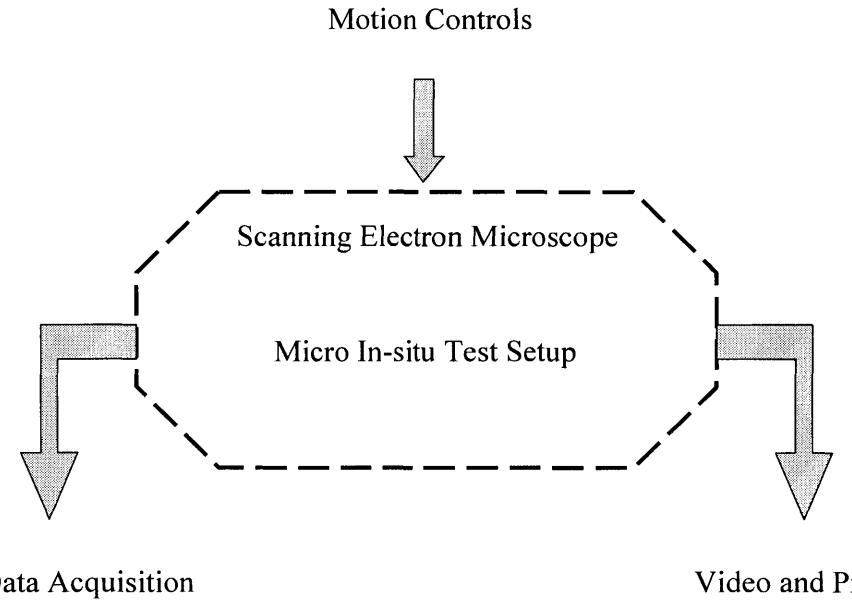

Figure 2-2: In-situ micro-indentation/scratching test system.

In order to obtain detailed in-situ deformation information, an in-situ micro-indentation/scratching test system was developed by the author. Figure 2-2 shows a schematic of the system. The core part of the system is the new in-situ micro indentation/scratching test apparatus, located within an SEM (Scanning Electron

Microscope) chamber. The motion controls of the test apparatus, including indentation and scratching, are fed into the apparatus from outside of the SEM. Force data are acquired by load cells in the test apparatus, and recorded by a computer. Image and video can be obtained through the computer connected with the SEM.

2.1.3 In-situ Micro Indentation/Scratching Test Apparatus

The in-situ micro-indentation/scratching test apparatus was designed using Pro/Engineering software and was realized in a local machine shop. A 3D schematic of the apparatus generated by Pro/engineering is shown in Figure 2-2(a). Figure 2-3(b) shows a photograph of the apparatus sitting on the platform fixed on the door of the SEM and Figure 2-3(c) shows a photograph of the knife. The SEM used in this research is the LEO 438VP from LEO Electron Microscopy Ltd located in Professor Gibson's laboratory in the Material Science Department at MIT. During operation, the SEM door is closed, and the sample is located beneath the SEM beam. The apparatus occupies a space of about 16mm in length, 15mm in width and 10mm in height and fits within the SEM chamber. Figure 2-4 shows the schematics of the front and top view of the apparatus. The setup consists of a lower stage and an upper stage, necessitated due to the limited available space within the SEM chamber, available equipments, and interfaces with external control through ports. The lower stage has two stands, which can move in opposite directions driven by two stepper motors. The sample is fixed on a sample holder mounted on one of the stands. The knife is fixed on the upper stage mounted on another stand in the lower stage, and moves in the direction normal to the motion of the lower stand. Therefore, the upper and lower stages generate two perpendicular motions: The lower stage provides scratching/tangential motion of a range of about 20mm and the minimum displacement larger than 40nm; The upper stage provides indentation/normal motion of a range of about 6mm and the minimum displacement larger than 50nm. Load cells are embedded in the lower and the upper stages to measure the axial forces along the directions of each motion: The one in the lower stage measures the tangential force; The one in the upper stage measures the normal force. The load cells used are Omega LC 101 S-type load cell with load capacity of +/-12kg. The knife and the sample are arranged to be located directly beneath the SEM beam for observation. Motors and load cells are

wired through special ports out of the SEM chamber to enable simultaneous collection of video images of the indentation/scratching tests and the normal/tangential force-displacement data. Data acquisition is realized using Labview of National Instrument.

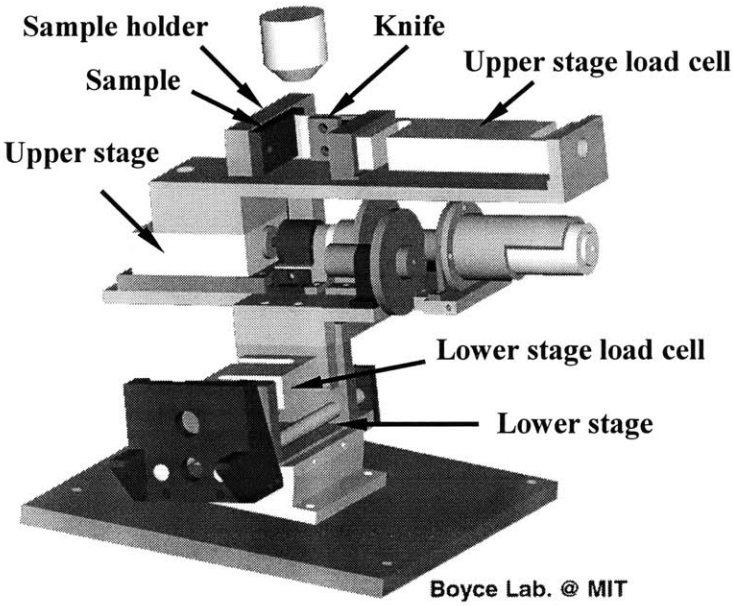

Figure 2-3(a)

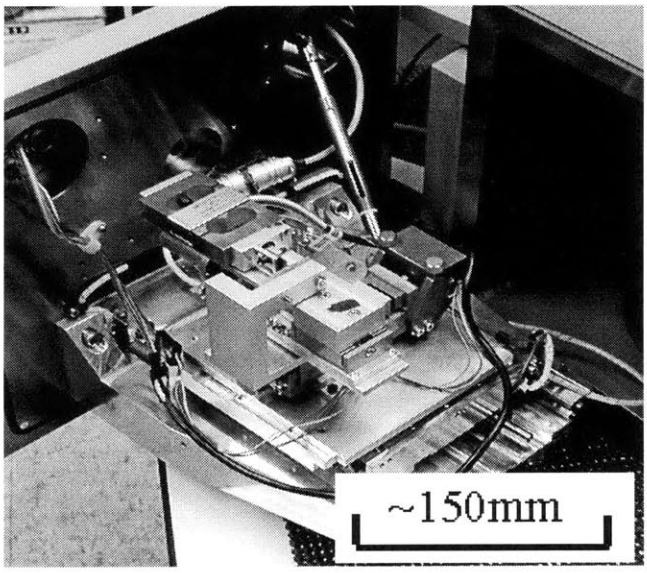

Figure 2-3(b)

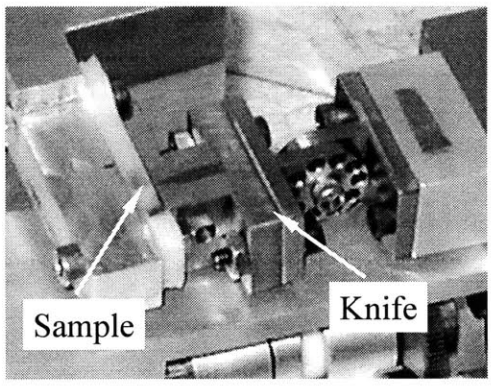

Figure 2-3(c)

Figure 2-3: In-situ micro indentation/scratching test apparatus, (a) schematics from Pro/Engineering; (b) photograph taken besides an SEM; (c) the knife and the sample.

To automatically control the motions, additional instrumentation to measure the

motion of the knife should be used to create a closed-loop control system, which requires extra expense to refine the current test apparatus and is also limited by the available space and available ports leading out of the SEM chamber. In the test, indentation depth is controlled by in-situ measuring the indentation depth using the SEM operating software.

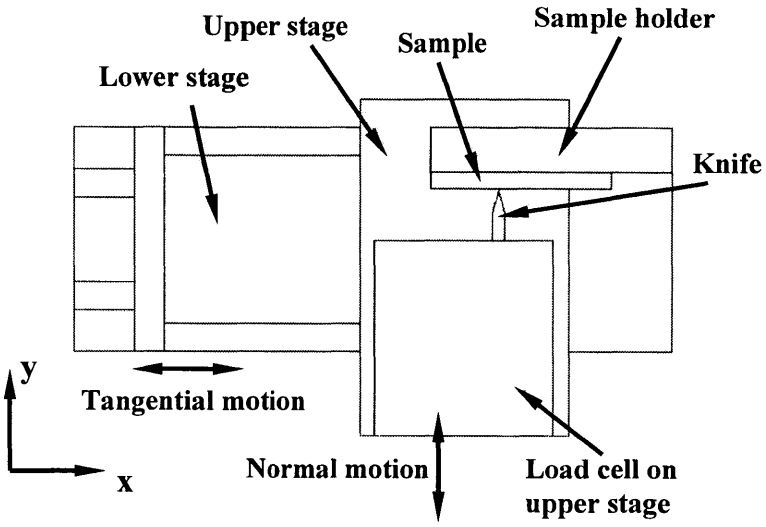

Figure 2-4 (a)

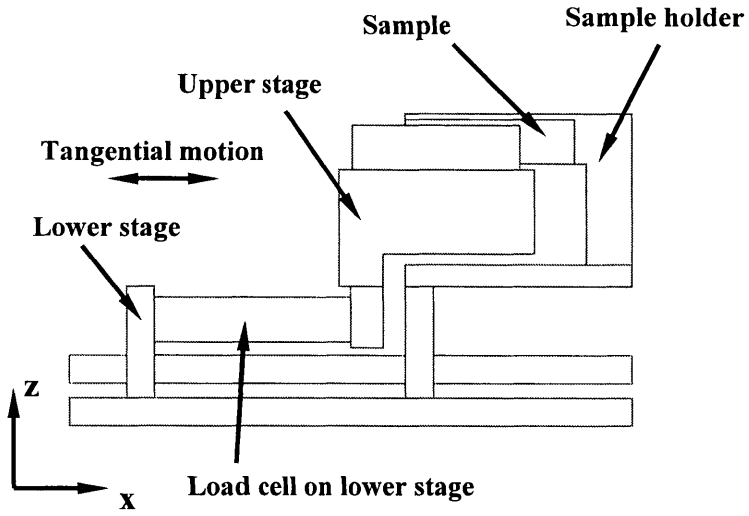

Figure 2-4 (b)

Figure 2-4: Schematic of the mechanism of the new setup, (a) Front View; (b) Top View

2.1.4 Samples

Samples were prepared from 3mm thick thermoplastic polyurethane (TPU) sheets, which were cut into rectangular shapes. Figure 2-5 shows the schematic of the shape and

dimensions of the sample. A cutting die was produced to facilitate preparation of the sample. During the test, the knife cuts into the sample generating a contact zone along the z direction, and scratches along the x direction.

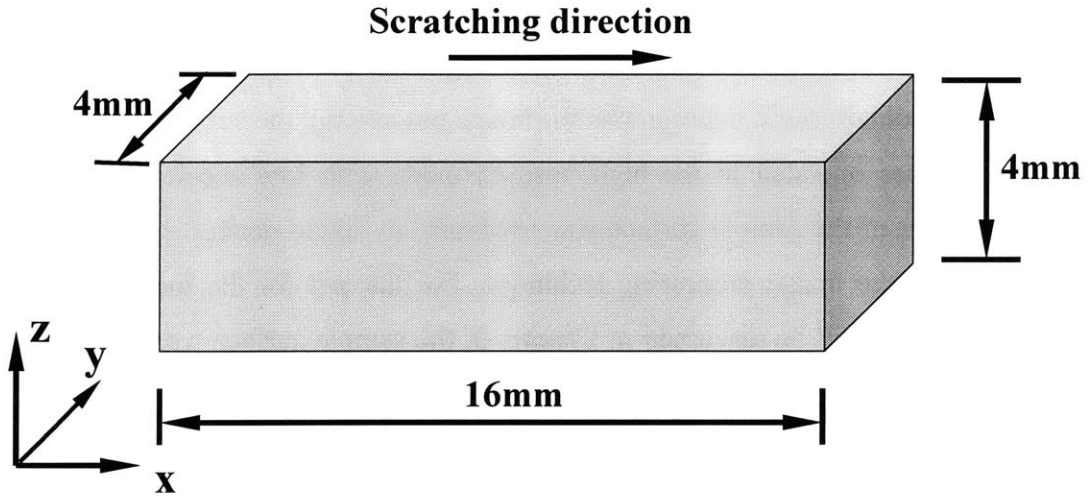

Figure 2-5: Schematics of the shape and dimensions of the sample.

TPUs are electrically and thermally non-conductive polymeric materials. The common issues for obtaining high quality SEM micrographs of the surface of non-conductive materials are electronic charging and heating up of materials. The electronic charge could cause loss of image contrast, creating very bright (edge effect) or dark areas, and image shift, whilst heating up the material could change the properties of the materials and electronic beam could cause crosslinking in the polymer. To avoid these problems, it is common to coat the imaged surface by a thin layer of gold or other metallic thin film of typical thickness of 20~60nm to improve the conduction of electrons and heat[2-1]. When use of a metallic thin film coating is unsuitable, an alternative is to use the technique commonly known as environmental SEM (ESEM, or variable pressure (VP) mode for LEO). Unlike common SEMs operating in high vacuum environments, the ESEM technique allows a low pressure of some gas (about 10~100Pa) in the SEM chamber. The collisions between electrons and the gas molecules ionize the gas. The cloud of ionized gas surrounding the sample acts as a conductor and allows the charge on the sample surface to dissipate. However, the cost of ESEM is the relatively low resolution. To obtain similar quality images, scanning speed has to be reduced by 2 to 4 fold, resulting in lengthened imaging time. It is also possible to inspect non-conductive

uncoated surfaces without using ESEM. In such a situation, a low accelerating voltage should be used to reduce the charge effect.

In this study, samples were prepared according to the specific test conducted. For the indentation/scratching tests where videos were taken, the surface facing the SEM beam was gold coated in order to maintain a high scanning speed essential to obtain videos. For the tests used to obtain static micrographs for image processing, the surface was uncoated and the SEM was operated in the high vacuum mode with low accelerating voltage. Special treatment of the sample surface was necessary to obtain desired surface features to accommodate the image processing technique. For the test for the inspection of the abraded surface, as will be discussed in Chapter 3, the sample surface was uncoated and the SEM ran in the variable pressure mode (ESEM) with a pressure of about 20Pa.

2.1.5 The Knives

Two types of knives were used in the current study. The first one was a wedge-type knife, made of stainless steel and machined on a wire cut EDM machine. Figure 2-6 presents the knife, showing a round tip with radius of about 3-8μm. Tests using this type of knife study the effect of the interaction between a single abrasive particle and the material.

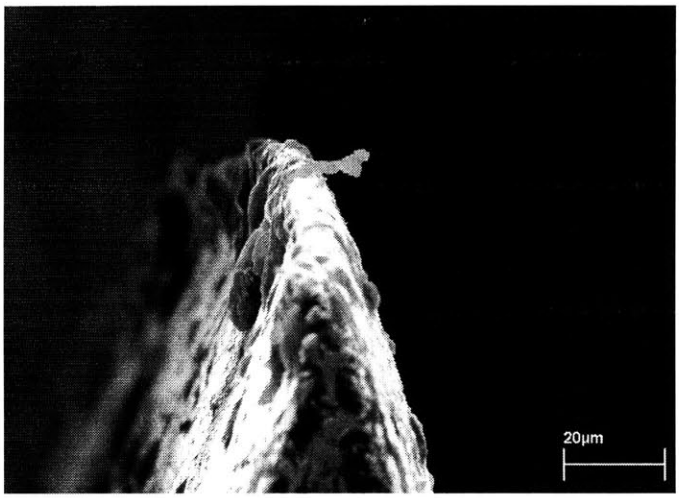

Figure 2-6 Wedge-type knife. The knife is made by stainless.

The second knife will be referred to as a bulk-type knife, presented schematically in Figure 2-7(a) and in the SEM micrograph of Figure 2-7(b). In contrast to the previous wedge-type knife, the latter shows a configuration of a smooth surface with a small sharp protrusion (40~100μm) in the middle of the surface and across the surface. We use this

knife to study the effect of the superposition of an overall compression on the material deformation during indentation/scratching.

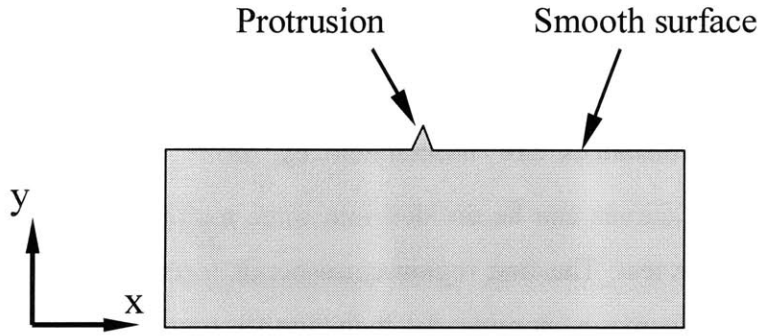

Figure 2-7(a)

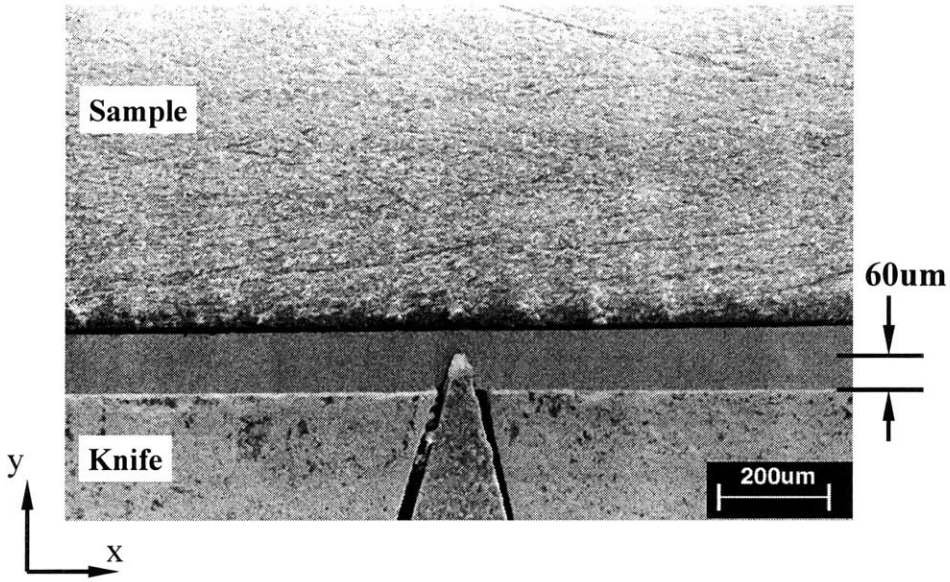

Figure 2-7(b)

Figure 2-7: The bulk-type knife: (a) Schematics of the knife; (b) micrographs of the knife.

2.2 In-situ Micro Indentation/Scratching Tests

In-situ micro indentation/scratching tests with different indentation depths were conducted to obtain the material deformation in these processes. The material tested in this chapter is unfilled thermoplastic polyurethane (TPU), whose mechanical behavior is given in detail in Chapter 4.

2.2.1 Result: δ_n=50μm for Unfilled TPU with Wedge-type Knife

An in-situ micro indentation/scratching test with 50μm indentation depth using a wedge-type knife was first conducted. Figure 2-8(a) shows the normal/tangential force vs time curves of the test whereas Figure 2-8(b) shows the normal/tangential force vs normalized distance curves. The distances are normalized by δ_n^{max} (the specific maximum indentation depth). The curves can be divided into three regions according to different dominant features of the test: The first region corresponds to the indentation, where the normal force initially increases nonlinearly then almost linearly; The second region corresponds to the start of scratching and the tangential force increases almost linearly. During this stage, the test shows the material around the contact surface moving with the knife essentially blocking the knife movement thus giving the increase in the tangential force with tangential displacement, and demonstrating features commonly known as the stick phase. The normal force decreases during this phase since the contact with the backside of the knife is lost. The transition from the second region to the third region corresponds to the curve for the tangential force to gradually bend over toward a constant value. In the third region, a constant tangential force and normal force are observed and the knife slips over the surface (known as slip phase) with essentially a steady state contact configuration between the knife and the TPU. From Figure 2-8(b), the corresponding scratching distance where the constant tangential force and normal force are reached is about 40μm. Finally, the knife is withdrawn. The material partially recovers from the deformed state.

Figure 2-9(a)~(d) show a sequence of the deformations during the test whereas Figure 2-10(a)~(d) show the same images but with outlines (white lines) of the surface profile to clearly illustrate the deformation. Figure 2-9(a) and Figure 2-10(a) show the surface of the material before the indentation. Since the sample used here was uncoated and was observed under the high vacuum mode of the SEM, surface charges can be seen as indicated by the bright zones on the surface. The micrographs were taken with 200X magnification and the scale bars in the micrographs show the dimensions. Note that this surface had been purposely roughened in order to provide the needed image contrast for later image processing.

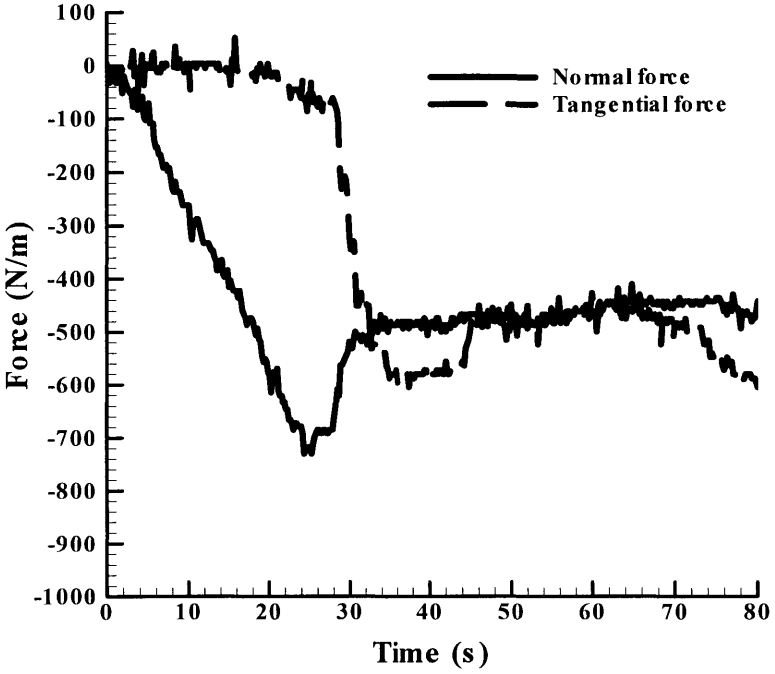

Figure 2-8(a)

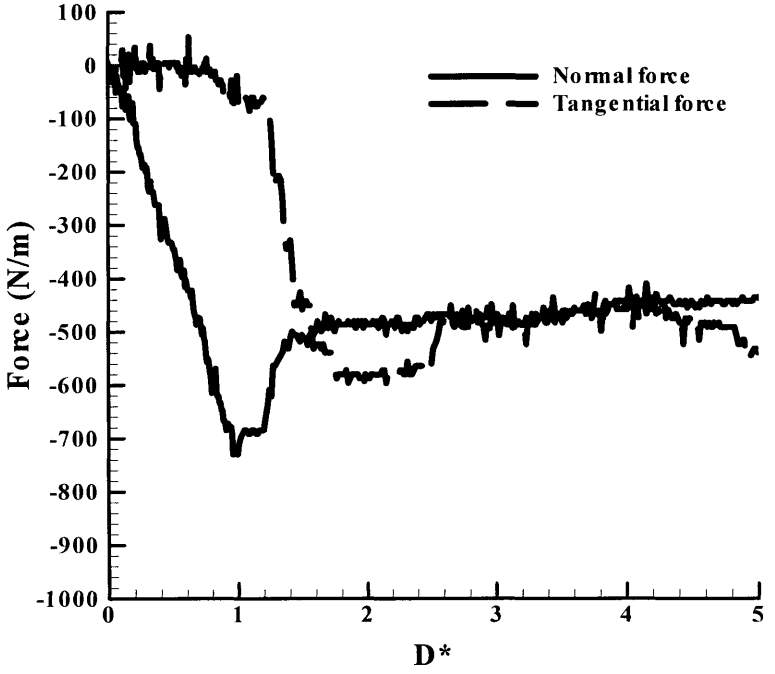

Figure 2-8(b)

Figure 2-8: (a) Normal/tangential force vs time curves, and (b) Normal/tangential force vs normalized distance curves from indentation/scratching test with δ_n=50μm.

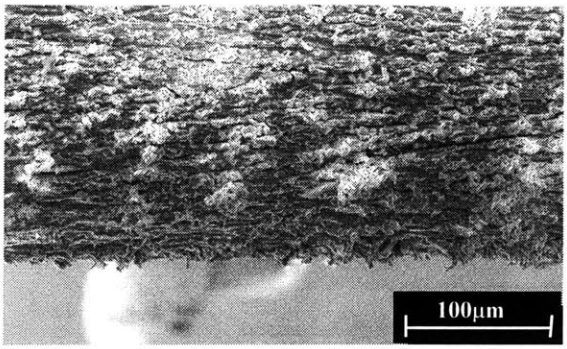

Figure 2-9(a)

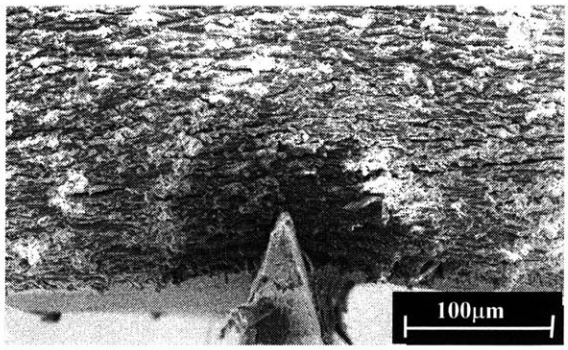

Figure 2-9(b)

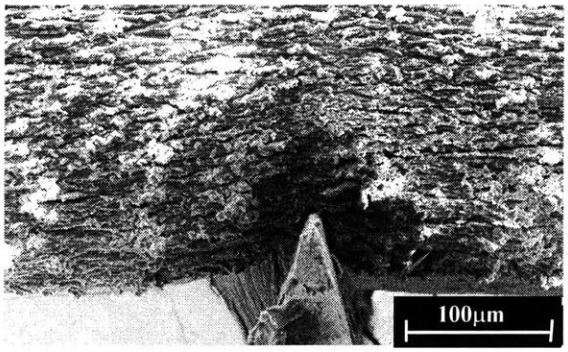

Figure 2-9(c)

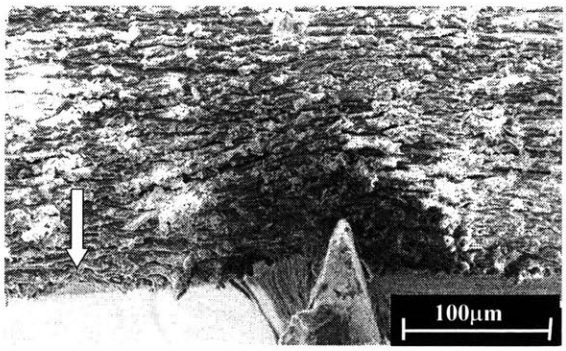

Figure 2-9(d)

Figure 2-9: SEM micrographs of material deformation during indentation/scratching process (the knife moves rightward): (a) before the test; (b) δ_n=50μm, δ_t=0μm (upon indentation); (c) δ_n=50μm, δ_t~40μm (upon scratching); (d) δ_n=50μm, δ_t>100μm (upon scratching).

Figure 2-9(b) and Figure 2-10(b) show the material deformation immediately after indentation. The material shows the conformation around the knife tip (Figure 2-10(b)) due to the large deformation capability of TPUs. The conformation is symmetric and has the contact length of 20~30μm on both sides of the knife. The material also shows features of deforming out of the plane directly beneath the knife as a result of the local Poisson effect due to compression in this region.

Upon scratching (Figure 2-9(c) and Figure 2-10(c)), the material conformation to the knife tip becomes biased: The material on the left side of the knife starts to lose contact with the knife, while the curvature of the surface profile on the right side increases, implying material compression on the right side of the knife. When the micrograph was taken, there was no significant relative movement between the knife and the material. This period is also known as stick phase and corresponds to the increase of the tangential

force and the decrease in the normal force.

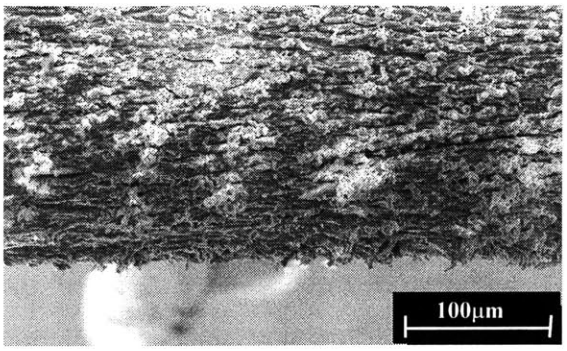

Figure 2-10(a)

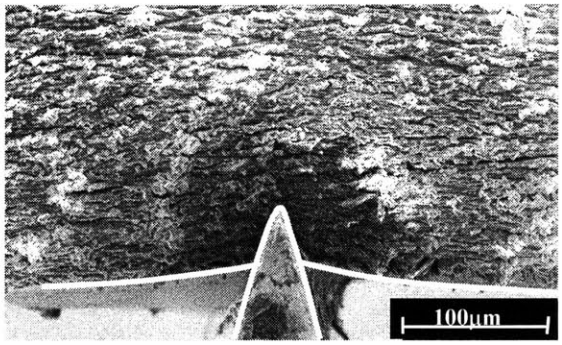

Figure 2-10(b)

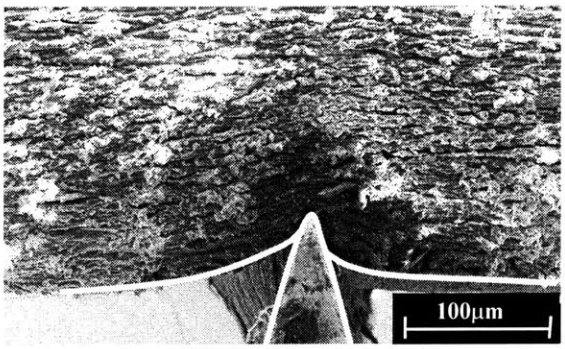

Figure 2-10(c)

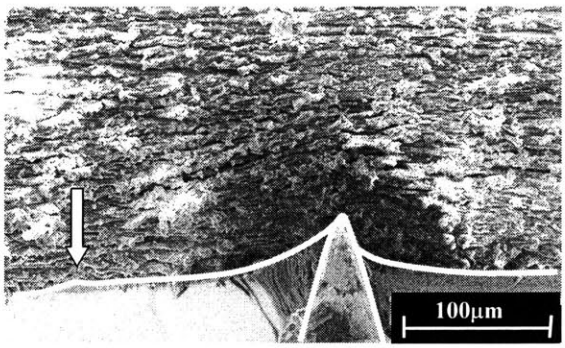

Figure 2-10(d)

Figure 2-10: SEM micrographs of material deformation during indentation/scratching process (the knife moves rightward): (a) before the test; (b) δ_n=50μm, δ_t=0μm (upon indentation); (c) δ_n=50μm, δ_t~40μm (upon scratching); (d) δ_n=50μm, δ_t>100μm (upon scratching). The white lines in the images outline the surface profile.

As the knife further moves to the right (Figure 2-9(d) and Figure 2-10(d)), the conformation is further biased: The material on the left side of the knife almost fully loses contact with the knife, while the material on the right side of the knife is pushed. When the micrograph was taken, the knife is slipping over the contact surface, typically known as slip phase. This period corresponds to a constant tangential force. As the knife moves rightward, the location where the knife indented shows a small amount of residual deformation, indicated by the arrows in Figure 2-9(d) and Figure 2-10(d).

2.2.2 Result: δ_n=80μm for Unfilled TPU with Wedge-type Knife

The in-situ micro indentation/scratching test with indentation depth of 80μm using a wedge-type knife was also conducted. Figure 2-11 shows the normal/tangential force vs time curves. The curves show similar features as the one with δ_n=50μm, i.e. the curves can be divided into three regions according to different dominant features of the test: The indentation corresponding to the increase of the normal force, the stick phase in scratching corresponding to the increase of the tangential force and decrease of the normal force, and the slip phase in the scratching corresponding to a constant tangential force and constant normal force.

Sequential micrographs of deformations during the test are shown in Figure 2-12(a)~(c) whereas Figure 2-13(a)~(c) show the same micrographs but with outlines (white lines) of the surface profile to clearly illustrate the deformation. Figure 2-12(a) and Figure 2-13(a) show the material deformation immediately after indentation. As expected, the material shows similar features as observed in the test with δ_n=50μm but larger conformation to the edge of the knife. The conformation length is 30~40μm on both sides of the knife.

Upon scratching (Figure 2-12(b) and Figure 13(b)), similar to what was observed in the test with δ_n=50μm, the material conformation to the knife tip becomes biased: the material on the left side of the knife starts losing contact with the knife, while the curvature of the surface profile on the right side increases due to the compression force applied by the knife.

As the knife further moves rightward (Figure 2-12(c) and Figure 2-13(c)), the knife starts to slip over the surface. At this stage, the conformation is further biased: the material on the left side of the knife almost fully loses contact with the knife, while the material on the right side is pushed by the knife. It is also noticed that the location where the knife indented shows a small amount of residual deformation, as indicated by the arrows in Figure 2-12(c) and Figure 2-13(c).

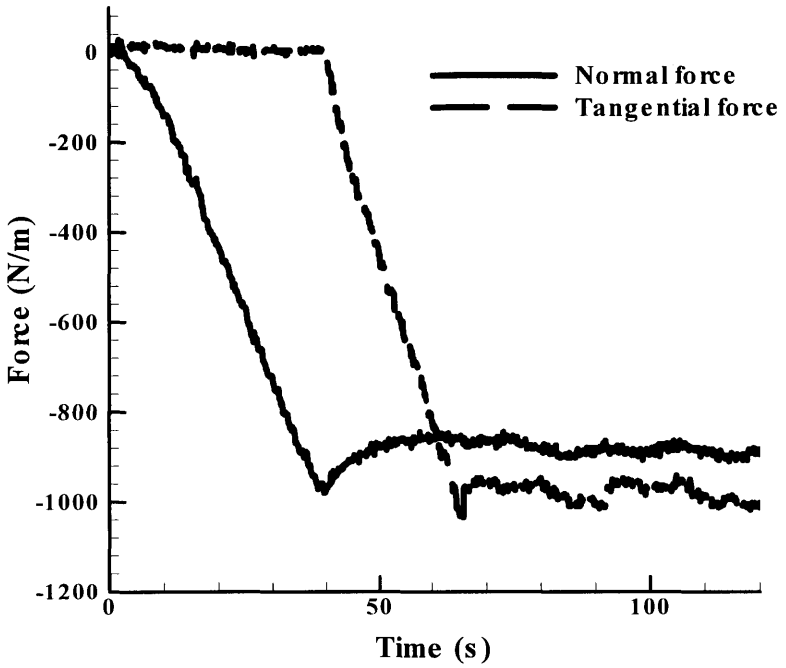

Figure 2-11(a)

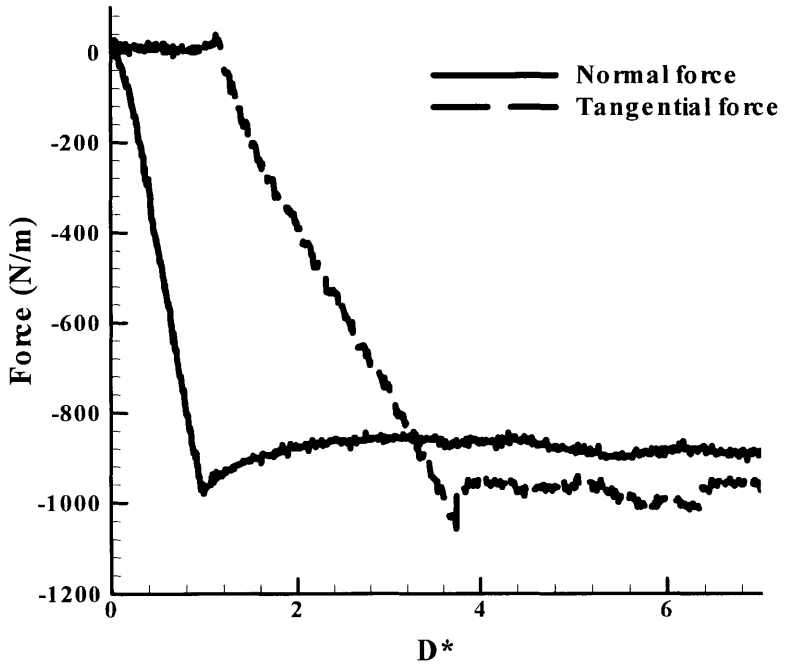

Figure 2-11(b)

Figure 2-11: (a) Normal/tangential force vs time curves, and (b) Normal/tangential force vs normalized distance curves from indentation/scratching test with δ_n=80μm.

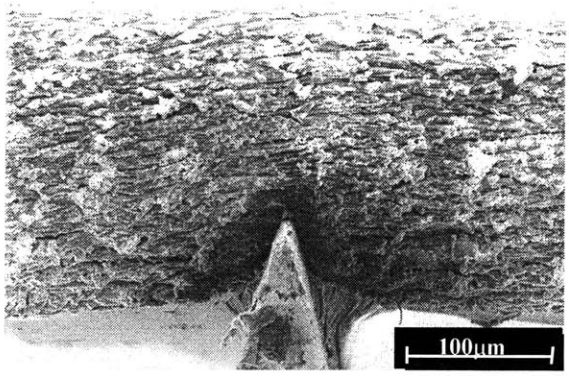

Figure 2-12(a)

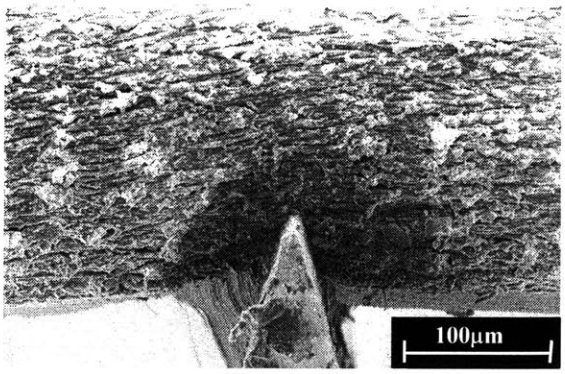

Figure 2-12(b)

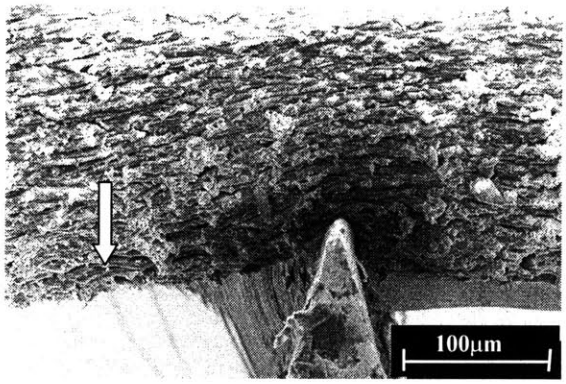

Figure 2-12(c)

Figure 2-12: SEM micrographs of material deformation during indentation/scratching process: (a) δ_n=50μm, δ_t=0μm (upon indentation); (b) δ_n=80μm, δ_t~40μm (upon scratching); (c) δ_n=80μm, δ_t>100μm (upon scratching).

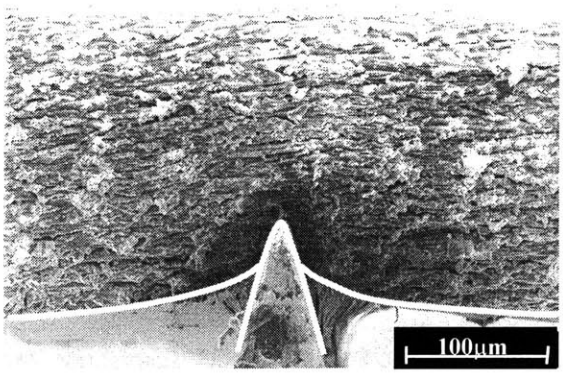

Figure 2-13(a)

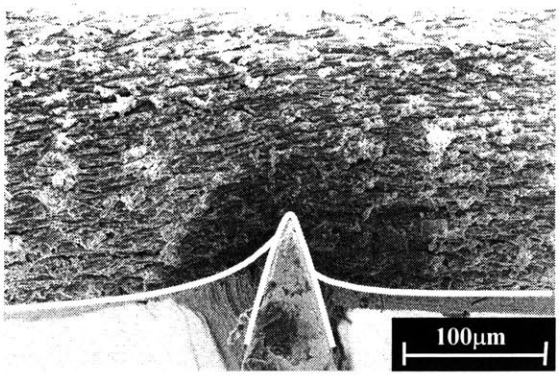

Figure 2-13(b)

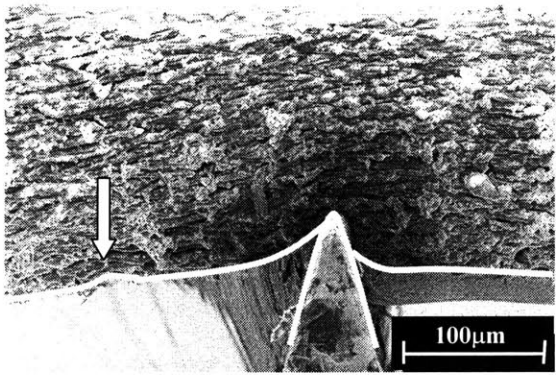

Figure 2-13(c)

Figure 2-13: SEM micrographs of material deformation during indentation/scratching process: (a) δ_n=50μm, δ_t=0μm (upon indentation); (b) δ_n=80μm, δ_t~40μm (upon scratching); (c) δ_n=80μm, δ_t>100μm (upon scratching). The white lines in the micrographs outline the surface profile.

2.2.3 Result: δ_n=80μm for Unfilled TPU with Bulk-type Knife

The in-situ micro indentation/scratching test using a bulk-type knife was also conducted. The knife is shown in Figure 2-7(b). The small protrusion is about 60μm above the bulk surface and has a tip radius of about 15μm. The bulk surface is 10mm in width and 10mm in height. For the bulk-type knife, the penetration of the knife into the material was difficult to measure due to lack of reference for measurement. The force control was therefore used in the tests. Figure 2-14 shows the normal/tangential force vs time curves. A maximum indentation force of 19N was applied to ensure complete contact between the bulk surface and the material. If the bulk surface and material surface could be perfectly parallel, a transition in the slope of the normal force from a lower slope

corresponding to only the protrusion indenting into the material to a greater slope corresponding to both the protrusion and the bulk surface in contact with material surface would have been observed. However, the perfect alignment between the bulk surface and material surface was difficult to achieve in the test. A simple calculation using the geometry of the bulk-knife used in this study shows that a tilt angle of about 0.6 degree between the bulk surface and the material surface would result in the protrusion and one of the end of the bulk surface touching the material surface simultaneously. It was observed in the test that as soon as the protrusion indented into the material, the left end of the bulk surface touched the material surface, and effectively increased the normal reaction force. In figure 2-14, the part of normal force during indentation shows an initial nonlinear increase where the increasing slope corresponds to the increase of contact area. As the bulk surface fully contacts the material surface, the normal force increases almost linearly. Generally, the curves during scratching show similar features as those with wedge-type knife: the stick phase in scratching corresponding to the increase in the tangential force, and the slip phase in the scratching corresponding to a constant tangential force. It is noticed that during the transition from the stick phase to the slip phase, compared to the wedge-type test, the decrease in the normal force is notably relatively small. The small decrease in the normal force during scratching is primarily because the normal force now has major contributions from bulk contact between the smooth surface and the material.

A sequence of deformations during the test is presented in Figure 2-15(a)~(d) whereas Figure 2-16(a)~(c) show the same image but with outlines (white lines) of the surface profile to illustrate the deformation. Figure 2-15(a) and Figure 2-16(a) show the relative positions of the bulk knife and the material before the test. Figure 2-15(b) and Figure 2-16(b) show the material deformation immediately after the indentation. Due to the existence of the protrusion, the material around the protrusion is not in contact with the bulk surface. The material shows conformation to the protrusion with the conformation length of about 20μm on both sides of the protrusion.

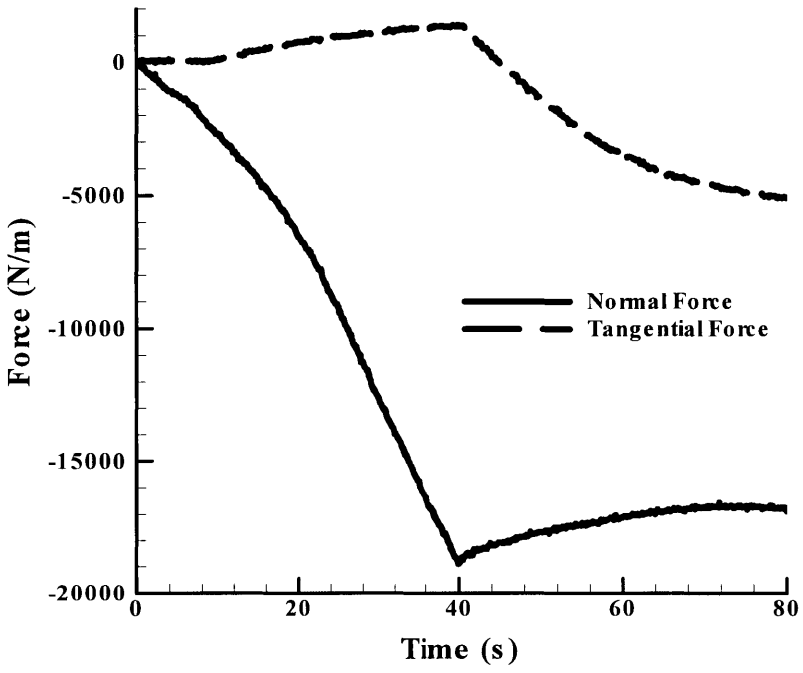

Figure 2-14

Figure 2-14: Normal/tangential force vs time curves from indentation/scratching test using bulk-type knife.

Upon scratching (Figure 2-15(c) and Figure 2-16(c)), the material conformation to the protrusion becomes biased: the material on the left side of the protrusion starts losing contact with the knife, while the curvature of the surface edge on the right side of the knife increases due to compression force applied by the knife.

As the knife further moves rightward (Figure 2-15(d) and Figure 2-16(d)), the knife starts to slip over the surface. However, due to the constraint from the bulk surface, the slip occurs not as obvious as those in the tests using the wedge-type knife. At this stage, the conformation is further biased: the material on the left side of the knife almost fully loses contact with knife, while the material on the right side of the knife is heavily pushed. The edge of the material on the left side of the knife shows an almost straight line with smaller slope, suggesting this part of the material being strongly stretched.

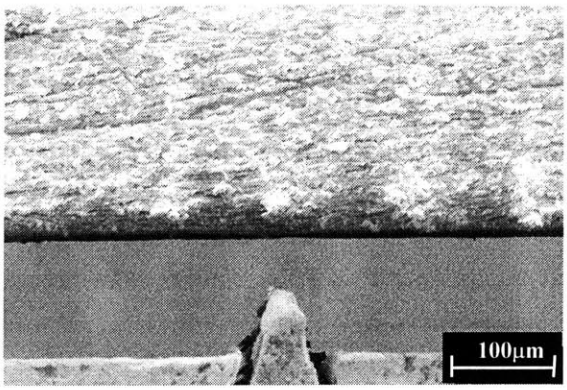

Figure 2-15(a)

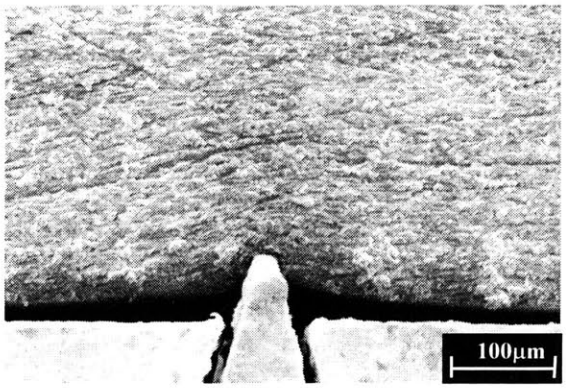

Figure 2-15(b)

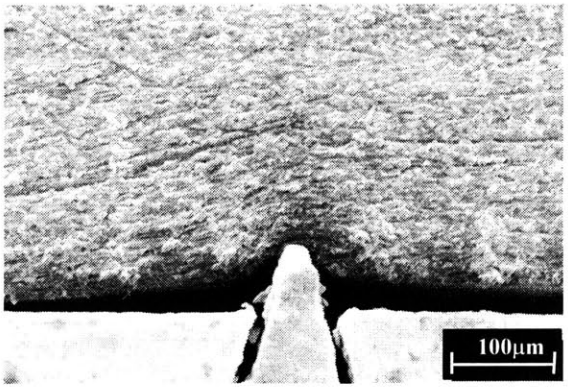

Figure 2-15(c)

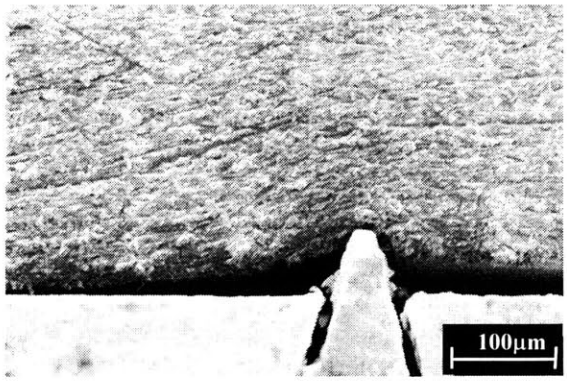

Figure 2-15(d)

Figure 2-13(e)

Figure 2-15: SEM micrographs of material deformation during indentation/scratching process using a bulk-type knife: (a) Before the test; (b) Immediately after indentation; (c) Upon scratching, δ_t~40μm; (d) Upon scratching, δ_t>100μm; (e) After withdrawn the knife.

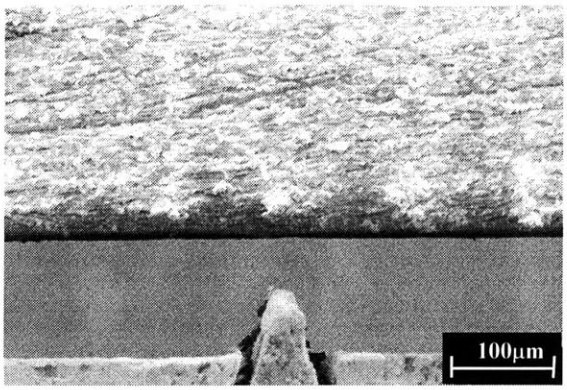

Figure 2-16(a)

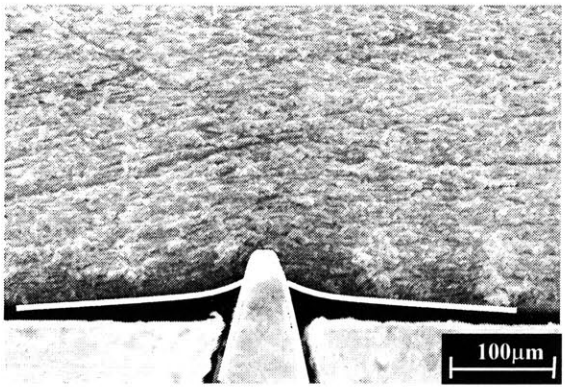

Figure 2-16(b)

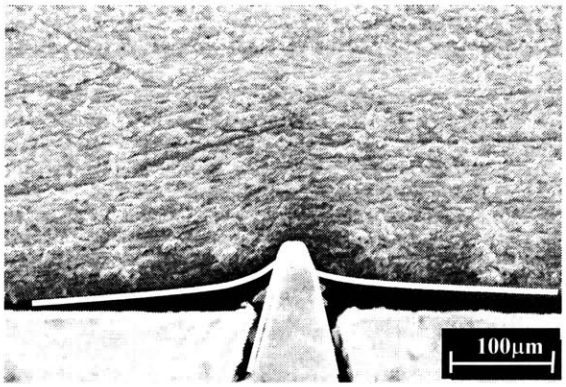

Figure 2-16(c)

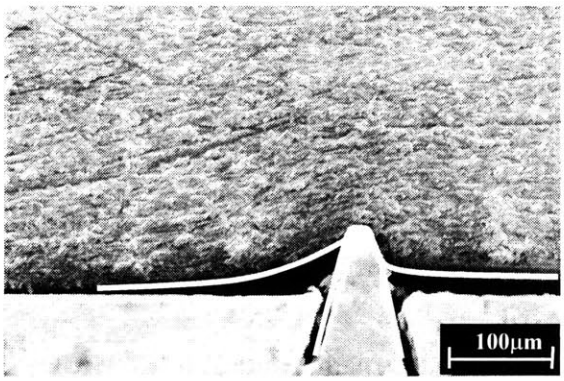

Figure 2-16(d)

Figure 2-16: SEM micrographs of material deformation during indentation/scratching process using a bulk-type knife: (a) Before the test; (b) Immediately after indentation; (c) Upon scratching, δ_t~40μm; (d) Upon scratching, δ_t>100μm; (e) After withdrawn the knife. The white lines in the images outline the surface profile.

2.3 Image Processing

Qualitative information on the local deformation during the indentation/scratching process was obtained from the micrographs in the previous section. To establish quantitative knowledge on the local displacement and strain fields, however, one has to employ image processing techniques to analyze the micrographs. In this section, digital image correlation, an image process technique to quantify displacement and strain using consecutive images taken during deformation, is implemented to reveal quantitative deformation and strain fields.

2.3.1 Introduction to the Software VIC 2D and Sample Preparation

Originated from digital image correlation, VIC 2D is a recent image processing software for experimental displacement analysis of large strain deformation[2-2][2-3]. The so-called digital image correlation technique is a mathematical correlation method to analyze digital image data taken on samples subjected to mechanical deformation. Consecutive images captured during a test will present changes in surface characteristics as the specimen is deformed. The digital image correlation technique determines the displacements of gray value patterns in the digital images by tracking the gray value patterns in small local neighborhoods commonly referred to as subsets. To determine the displacement of the subset center in a second image, a similarity measure is employed. The digital image correlation algorithm finds the subset center displacement by maximizing this similarity measure.

One critical aspect of successful application of the digital image correlation technique is the presence of surface characteristics in the form of patterns or speckles of proper size. These patterns or speckles provide basic information for the algorithm to track. In small strain and regular test conditions, to create such patterns or speckles on the specimen surface is not very difficult: A spray or an ink-pen can fulfill this task. For a test at large strain, however, care must be taken to provide a surface speckle pattern that is robust to large stretches[2-4]. Moreover, for a test running in a high vacuum SEM chamber and under the magnification of about 100~200X, to create sustainable and traceable speckles imposes challenges. Under the magnification of 100X~200X, traceable speckles about the size of 1~2mm in the micrographs should have the physical size of 1-5μm. Spray particles, such as boron nitride, of 1-10m can be easily removed in a high vacuum environment due to the continuous pumping to maintain the high vacuum, resulting in the loss of features shown in previous micrographs. The thin film by gold coating sometimes can create traceable patterns on the size scale of a few microns due to inhomogeneous coating and porosity over the surface. In the current study, however, such coatings will crack due to the large deformation.

An easy way to create the surface feature has been realized. A fine sand paper (600 grain) was employed to abrade the sample surface. After a few rounds of abrasion, the initially shining surface became dull, a symptom of small features over the surface.

Micrographs under the SEM show that the abrasion by fine sand paper created surface features of the size of 1-5μm for TPUs.

2.3.2 Results: δn=50μm for Unfilled TPU with Wedge-type Knife

Micrographs obtained from the indentation/scratching test with δn=50μm were processed first. Images in Figure 2-17 show the results immediately after indentation, i.e. δn=50μm and δt=0μm. Figure 2-17(a), taken at the magnification of 80X, was used together with an image taken before the test to generate the desired contours. For the purpose of comparison, Fig 2-17(b) shows the magnified image, taken at 200X under the same test conditions. It was desired to use the images at a higher magnification to post-process so that more detailed information about the deformation would be revealed. However, two hurdles deterred using higher magnified images. First, at a higher magnification the surface speckles created by fine sand paper appear too large compared with the scope of the observation, resulting in the charge effect becoming pronounced and forming a number of large white-zones, as shown 2-17(b). These white zones are unstable and move during the test, making the micrographs impossible to be applied to the image processing software. The second hurdle is that at a higher magnification there are relatively larger amount of materials flowing in and out of the observation area, making the comparable zone become too small to be valuable for analysis.

Figure 2-17(c) to (g) show the contours for displacements and strains obtained from image processing. The contours are superposed on the micrographs at the same position. Since the image processing software currently cannot generate accurate information on the boundary due to the usage of subsets, the contours only cover the area of about 1.2mm by 0.6mm inside the material. The lower edge of the contour field is about 0.08mm above the lower edge of the material.

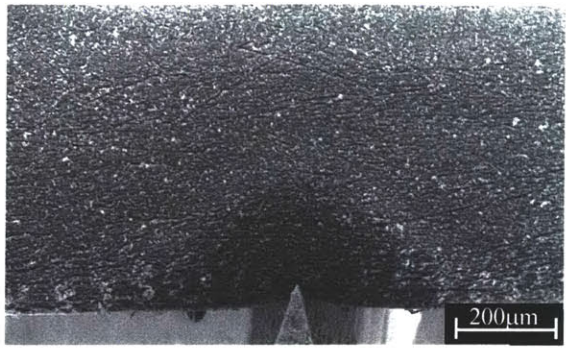

Figure 2-17(a)

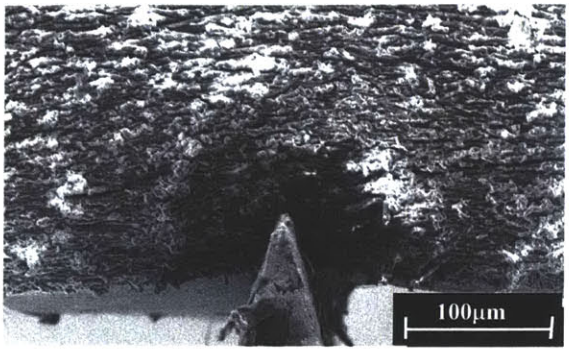

Figure 2-17(b)

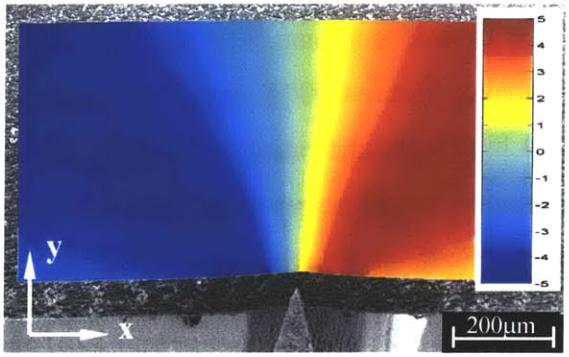

Figure 2-17(c)

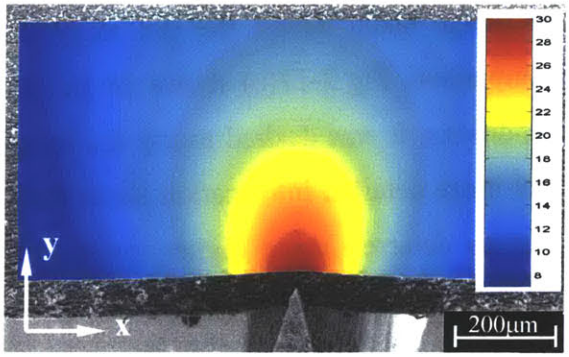

Figure 2-17(d)

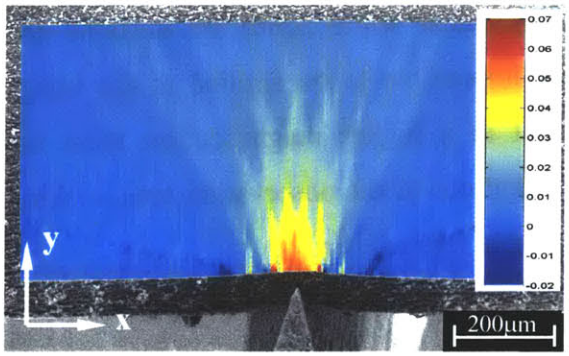

Figure 2-17(e)

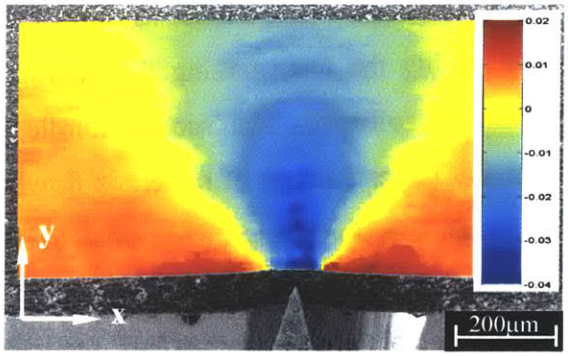

Figure 2-17(f)

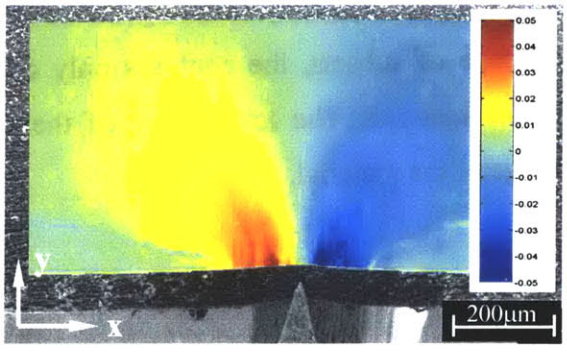

Figure 2-17(g)

Figure 2-17: Results from image processing of SEM micrographs from indentation/ scratching tests with δn=50μm, δt=0μm: (a) unprocessed SEM micrographs; (b) SEM micrograph at larger magnification; contours for (c) u_1; (d) u_2; (e) ε_{11}; (f) ε_{22}; (g) ε_{12}.

Figure 2-17(c) and (d) show the contours of the displacement in the horizontal direction u_1 and the vertical direction u_2, respectively. In figure 2-17(c), the color changes from red, representing the displacement of about 5μm, to blue for the displacement of about -5μm. In Figure 2-17(d), the red color represents the displacement of about 30μm, to the blue for the displacement of about 7μm. The image processing nicely captures the displacement field. As expected, both contours show symmetric features: The u_1 contour shows material being pushed in the horizontal direction with a maximum displacement occurring along 45° lines away from the center line; The u_2 contour shows the decrease of the displacement from the contact point to the far field. It is noticed that u_2 is 50μm at the displacement at contact point and decreases to 30μm at point about 80μm below the contact surface.

The displacement fields were then used to generate true strain contours. Figure 2-17(e), (f) and (g) show the contours of strains ε_{11}, ε_{22}, and ε_{12}, respectively. It should be noted that the contours for strains show some un-smooth changes, most pronounced for ε_{11}, due to the first order derivative to the displacement and numerical discretion over the field. In figure 2-17(e), the red color represents the strain ε_{11} of about 0.07, whilst the blue color for about -0.02. In Figure 2-17(f), the red color represents the strain ε_{22} of about 0.02, to the blue color for the strain ε_{22} of about -0.04. In Figure 2-17(g), the red color represents the strain ε_{12} of about 0.05, to the blue color for about -0.05. Below the contact point, the material is subjected to tensile strain along horizontal direction and compression strain along the vertical direction. The strains decrease along the radial direction.

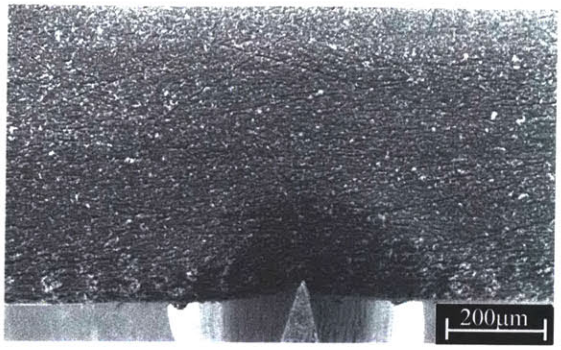

Figure 2-18(a)

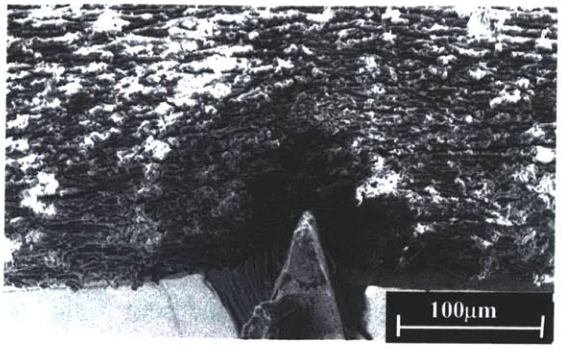

Figure 2-18(b)

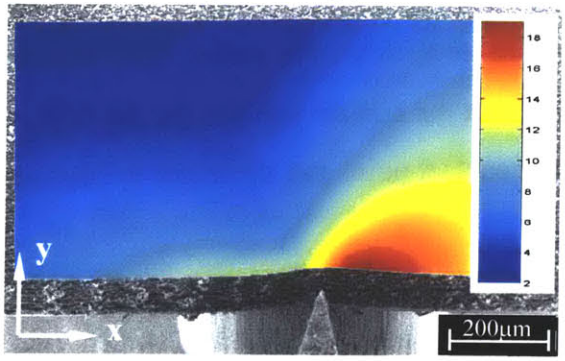

Figure 2-18(c)

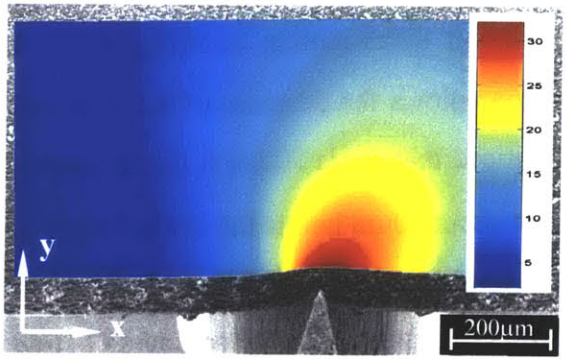

Figure 2-18(d)

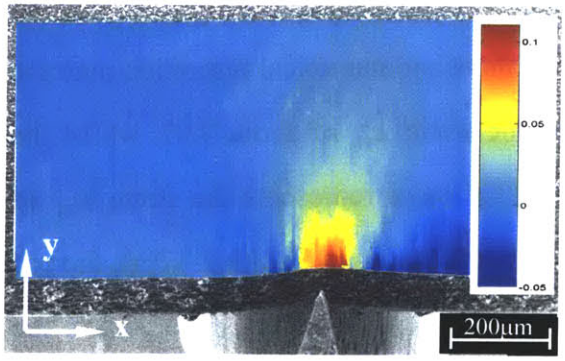

Figure 2-18(e)

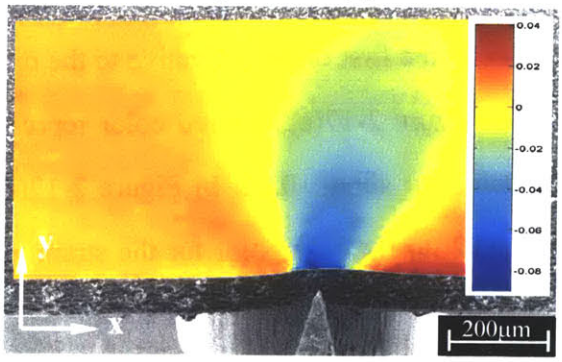

Figure 2-18(f)

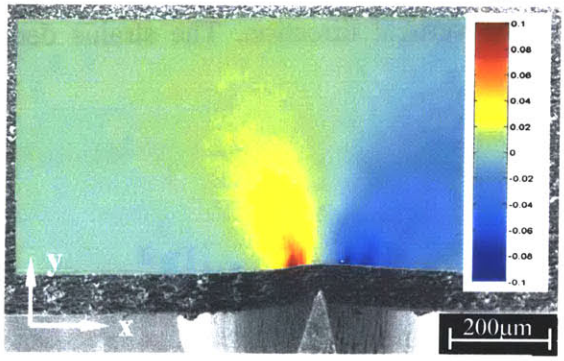

Figure 2-18(g)

Figure 2-18: Results from image processing of SEM micrographs from indentation/ scratching tests with δn=50μm, δt=60μm: (a) unprocessed SEM micrographs; (b) SEM micrograph at larger magnification; contours for (c) u_1; (d) u_2; (e) ε_{11}; (f) ε_{22}; (g) ε_{12}.

Figure 2-18 (a) to (g) show the contours from image processing on micrographs from the indentation/scratching test with δn=50μm, δt=60μm. Figure 2-18(a) shows the micrograph used for image processing while Figure 2-18(b) shows a micrograph taken at a higher magnification but under the same testing conditions. Figure 2-18(c) and (d) show the contours for the displacements u_1 and u_2, respectively. In figure 2-18(c), the scale for the displacement u_1 ranges from 2μm (blue) to 19μm (red), while in Figure 2-18(d), the scale for the displacement u_2 ranges from 2μm (blue) to 32μm (red). The contours very nicely reveal the features of the biased displacements where material is pushed rightward by the knife during scratching. The overall displacement fields are biased. The horizontal displacement shows a beautiful butterfly-like symmetric distribution about the line biased from the vertical line by about 30° to the left. The maximum horizontal displacement occurs in front of the knife along the line of about 30° away from the horizontal direction, whereas the minimum displacement occurs along the line of about 30° away from the vertical direction due to the large drag force from the bulk material in this direction. It is also noticed that the horizontal displacement behind the knife is large. The vertical displacement also shows features of bias: the symmetric line is about 66° away from the horizontal direction.

True strains were calculated based on the obtained displacement fields. Figure 2-18(e), (f), and (g) show the contours of strains ε_{11}, ε_{22}, and ε_{12}, respectively. In figure 2-18(e), the scale for the strain ε_{11} ranges from -0.05 (blue) to 0.11 (red); In Figure 2-18(f), the scale for the strain ε_{22} ranges from -0.09 (blue) to 0.04 (red); In Figure 2-18(g), the scale for the strain ε_{12} ranges from -0.10 (blue) to 0.10 (red). As the knife moves rightward, compression strain in the horizontal direction is developed in front of the knife, providing the resistance to the movement. Compared with the strain contours in Figure 2-17(e), (f), and (g), the magnitudes of the strains increase in both tension, compression, and shear. The strains also tend to concentrate to the contact point as shown in the figures, implying locally more severe deformation is expected during scratching.

2.3.3 Results: δn=80μm for Unfilled TPU with Wedge-type Knife

Micrographs obtained from indentation/scratching test with δn=80μm were processed.

Images in Figure 2-19 show the result immediately after indentation, i.e. δt=0μm. Figure 2-19(a), taken at the magnification of 80X, was used together with an image taken before the test for analysis. For the purpose of comparison, Fig 2-19(b) shows the magnified image, taken at 200X, from a different test but under the same test condition.

Figure 2-19(c) to (g) show the contours for the displacements and strains obtained from image processing. The contours are superposed on the micrographs at the same position. The contour area only covers the part of the analyzed micrographs and is about 1.2mm by 0.5mm. The lower edge of the contour field is about 0.12mm inside the edge of the material.

Figure 2-19(c) and (d) show the contours of the displacements u_1 and u_2, respectively. In Figure 2-19(c) and Figure 2-19(d), the displacement u_1 ranges from -7μm (blue) to 7μm (red), whereas the displacement u_2 ranges from -12μm (blue) to 40μm (red). Compared with the contours for the indentation depth of 50μm, the variations of the maximum and the minimums from those in Figure 2-17(c) and (d) to those from in Figure 2-19(c) and (d) are proportional to the variation in the indentation depth from 50μm to 80μm. The image processing nicely captures the displacement fields: The u_1 contour shows material being pushed horizontally with maximum displacement occurring along about 45° away from the center line; the u_2 contour shows the decrease of the displacement from the contact point to the far field. It is noticed that $u_2 = 80\mu m$ at contact point and decreases to 40μm at point about 120μm inside the material.

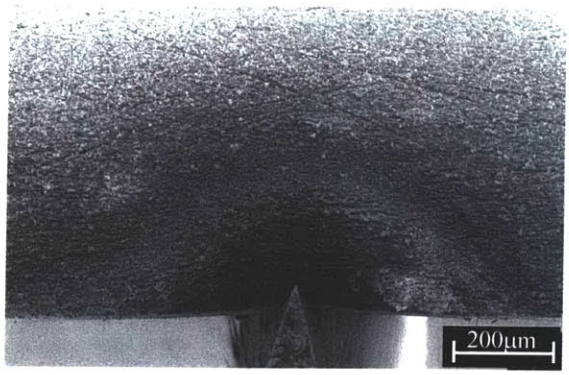

Figure 2-19(a)

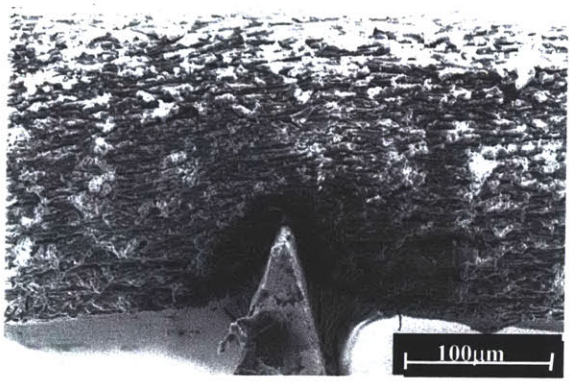

Figure 2-19(b)

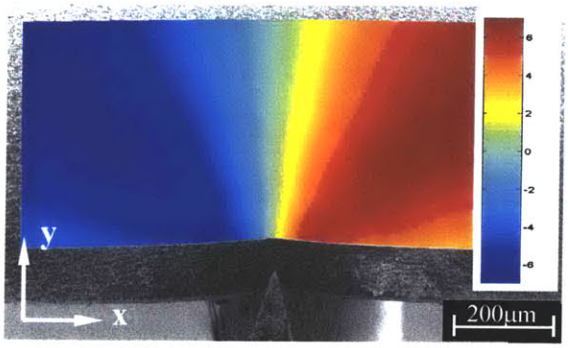

Figure 2-19(c)

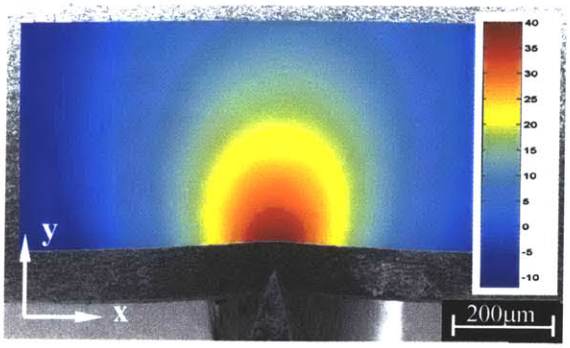

Figure 2-19(d)

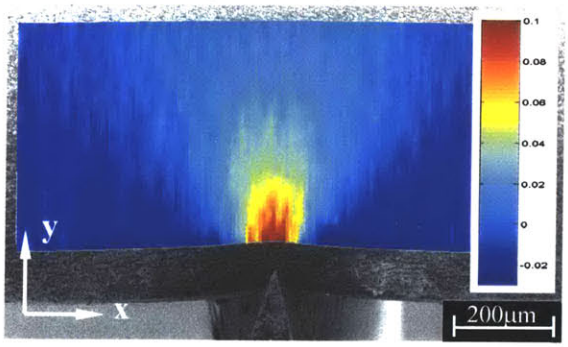

Figure 2-19(e)

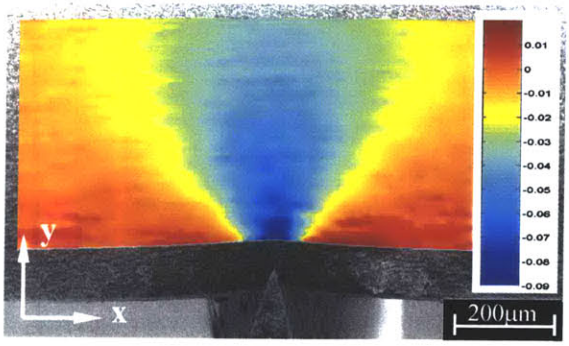

Figure 2-19(f)

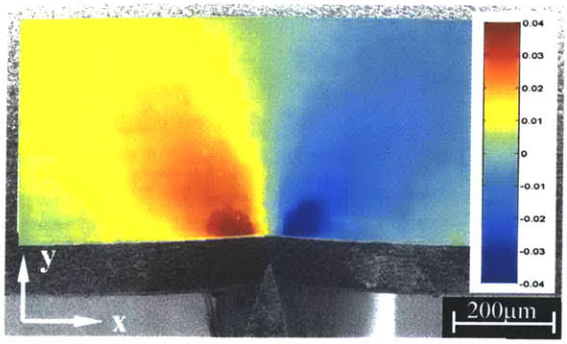

Figure 2-19(g)

Figure 2-19: Results from image processing of SEM micrographs from indentation/ scratching tests with δn=80μm, δt=0μm: (a) unprocessed SEM micrographs; (b) SEM micrograph at larger magnification; contours for (c) u_1; (d) u_2; (e) ε_{11}; (f) ε_{22}; (g) ε_{12}.

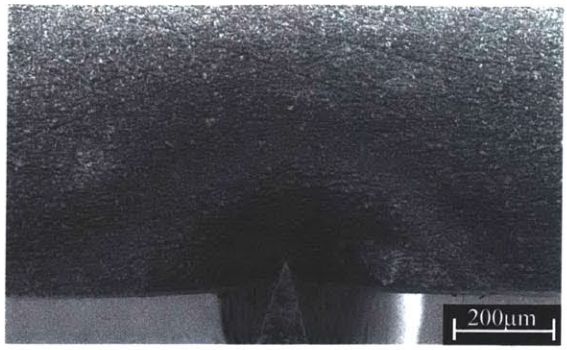

Figure 2-20(a)

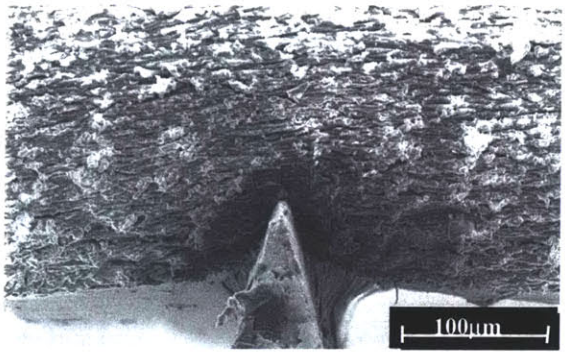

Figure 2-20(b)

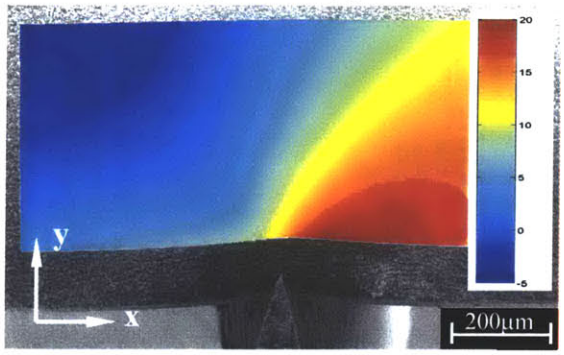

Figure 2-20(c)

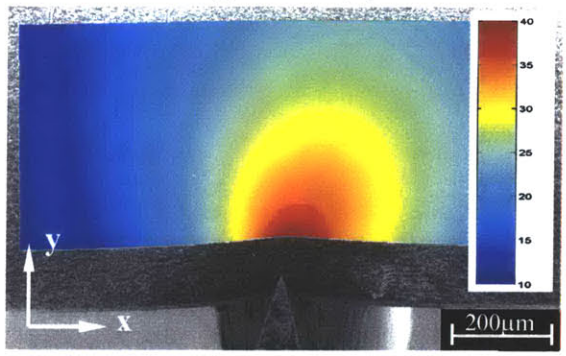

Figure 2-20(d)

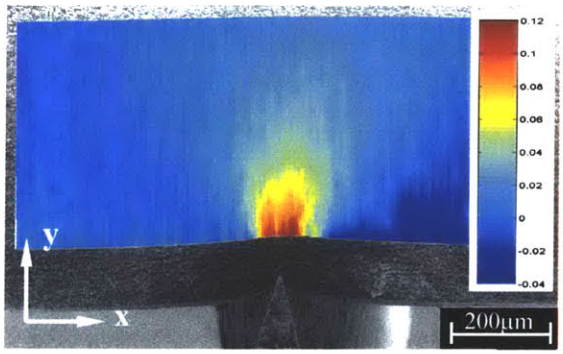

Figure 2-20(e)

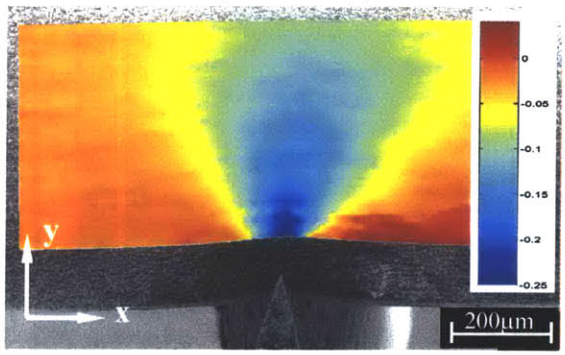

Figure 2-20(f)

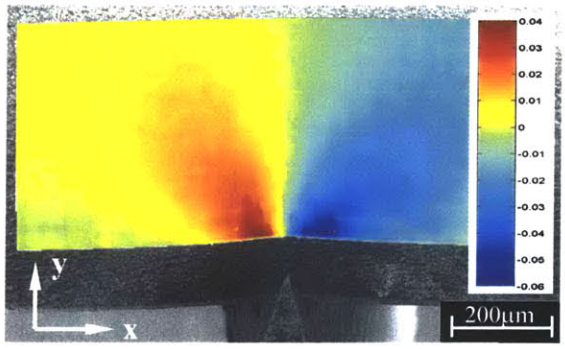

Figure 2-20(g)

Figure 2-20: Results from image processing of SEM micrographs from indentation/ scratching tests with δn=80μm, δt=40μm: (a) unprocessed SEM micrographs; (b) SEM micrograph at larger magnification; contours for (c) u_1; (d) u_2; (e) ε_{11}; (f) ε_{22}; (g) ε_{12}.

The displacement fields were then used to produce true strain contours. Figure 2-19(e), (f) and (g) show the contours of strains ε_{11}, ε_{22}, and ε_{12}, respectively. In Figure 2-19(e), the scale for the strain ε_{11} ranges from -0.03 (blue) to 0.10 (red); in Figure 2-19(f), the scale for the strain ε_{22} ranges from -0.09 (blue) to 0.02 (red); in Figure 2-19(g), the scale for the strain ε_{12} ranges from -0.04 (blue) to 0.04 (red). Similarly as observed in the test with indentation depth of 50μm, below the contact point, the material is subjected to tensile strain along the horizontal direction and compression strain along the vertical direction. The strains decrease along the radial direction.

Figure 2-20 (a) to (g) show the contours from image processing on micrographs from the indentation/scratching test with δn=80μm, δt=40μm. Figure 2-20(a) shows the micrograph used for image processing while Figure 2-20(b) shows a micrograph taken at a higher magnification but under the same testing condition. Figure 2-20(c) and (d) show the contours for the displacement u_1 and u_2. In figure 2-20(c), the scale for the displacement u_1 ranges from -5μm (blue) to 20μm (red), while in Figure 2-20(d), the scale for the displacement u_2 ranges from 10μm (blue) to 40μm (red). The contours very nicely reveal the feature of the biased displacements where material is pushed rightward by the knife during scratching. The distribution of the horizontal displacement shows a symmetric distribution about the line about 45° left to the vertical line. The maximum horizontal displacement occurs in front of the knife along the line of about 31° away from the horizontal direction, whereas the minimum displacement occurs along the line of about 45° away from the vertical direction. The vertical displacement also shows features of bias: the symmetric line is about 20° away from the horizontal direction.

True strains were calculated from the displacement fields. Figure 2-20(e), (f) and (g) show the contours of strains ε_{11}, ε_{22} and ε_{12}, respectively. In figure 2-20(e), the scale for the strain ε_{11} ranges from -0.04 (blue) to 0.12 (red); in Figure 2-20(f), the scale for the strain ε_{22} ranges from -0.25 (blue) to 0.04 (red); in Figure 2-20(g), the scale for the strain ε_{12} ranges from -0.06 (blue) to 0.04 (red). As the knife moves rightward, a certain amount of compressive strain in the horizontal direction is developed in front of the knife, providing the resistance to the movement. Compared with the strain contours in

Figure 2-20(e) and (f), the magnitudes of the strains increase in both tension and compression direction as the knife moves. The strains also tend to concentrate to the contact zone, implying locally more severe deformation is expected during scratching.

2.2.4 Result: δn=80μm for Unfilled TPU with the Bulk-type Knife

Micrographs from the indentation/scratching test using the bulk-type knife were processed. Images in Figure 2-21 show the result immediately after indentation, i.e. δt=0μm. Figure 2-16(a), taken at magnification of 80X, was used together with an image taken before the test for the analysis. For the purpose of comparison, Fig 2-16(b) shows the magnified image, taken at 200X under the same test condition.

Figure 2-21(c) to (f) show the contours for the displacements and strains obtained from image processing. The contours are placed over the original micrographs at the same position and cover an area of about 1.0mm by 0.6mm. The lower edge of the contour field is about 0.12mm below the contact surface.

Figure 2-21(c) and (d) show the contours of the displacements u_1 and u_2, respectively. In figure 2-21(c) and figure 2-21(d), the displacement u_1 ranges from -8μm (blue) to 14μm (red), whereas the displacement u_2 ranges from 20μm (blue) to 45μm (red). The u_1 contour shows asymmetric field. As mentioned before, due to the imperfect alignment between the bulk surface and the material surface, the left end of the knife touched the surface soon after the protrusion indents into the material, causing an overall larger contact force in the right-side of the protrusion and pushing the material leftwards, and resulting in the asymmetry in the u_1 contour. However, the u_1 contour does show the general features of the material being pushed laterally away from the centerline.

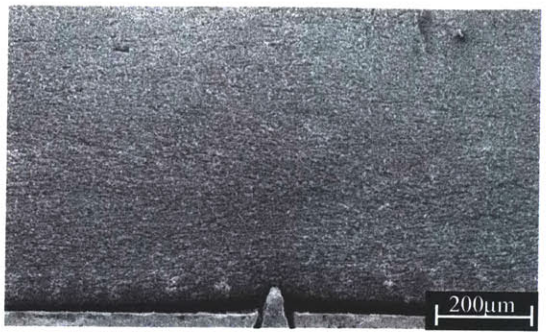

Figure 2-21(a)

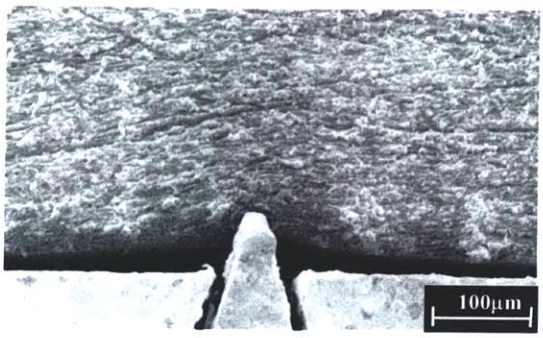

Figure 2-21(b)

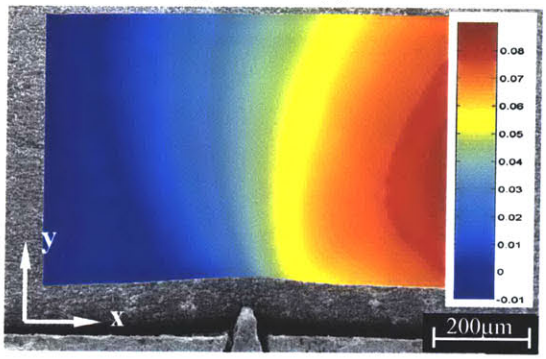

Figure 2-21(c)

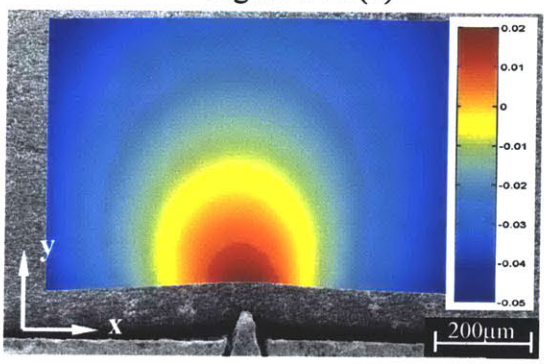

Figure 2-21(d)

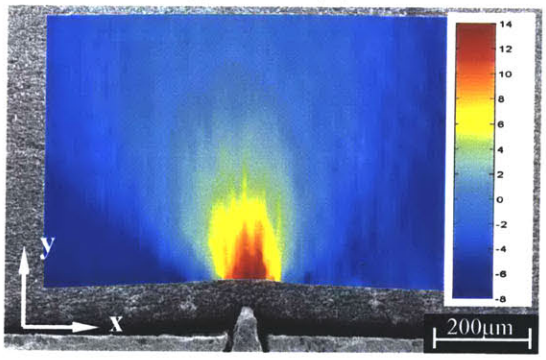

Figure 2-21(e)

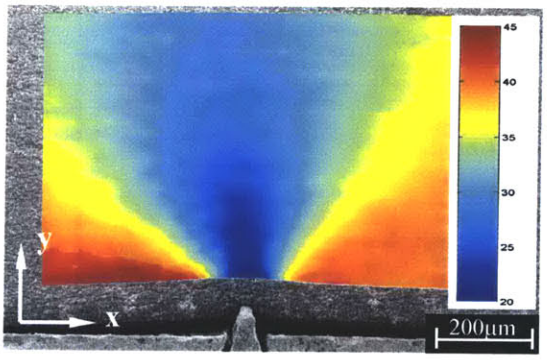

Figure 2-21(f)

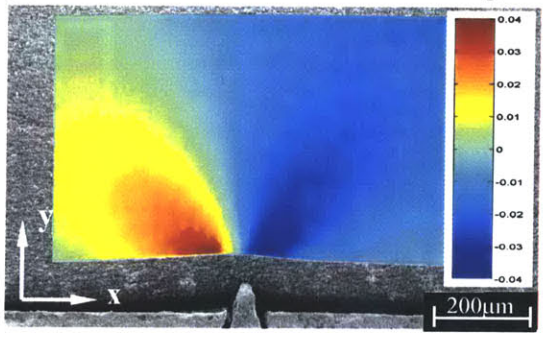

Figure 2-21(g)

Figure 2-21: Results from image processing of SEM micrographs from the indentation/ scratching test immediately after the indentation: (a) unprocessed SEM micrographs; (b) SEM micrograph at a larger magnification; contours for (c) u_1; (d) u_2; (e) ε_{11}; (f) ε_{22}; (g) ε_{12}.

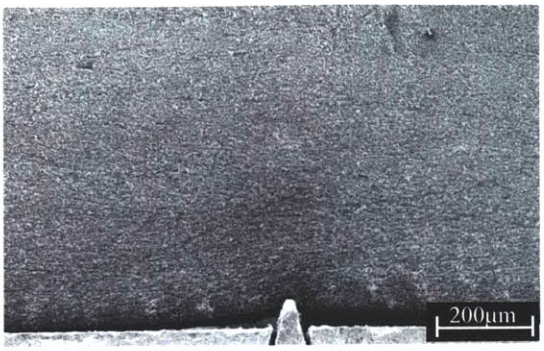

Figure 2-22(a)

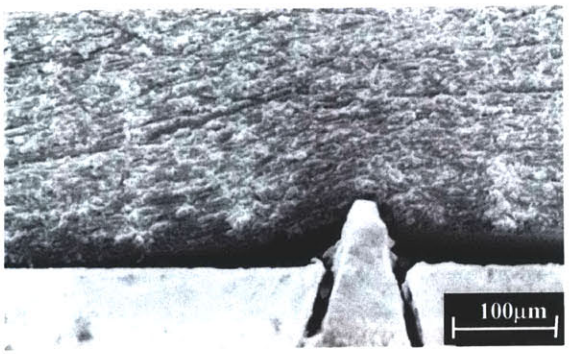

Figure 2-22(b)

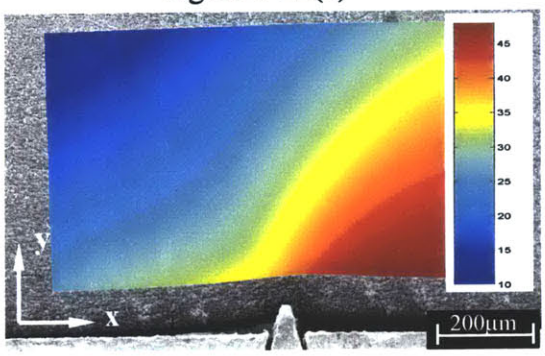

Figure 2-22(c)

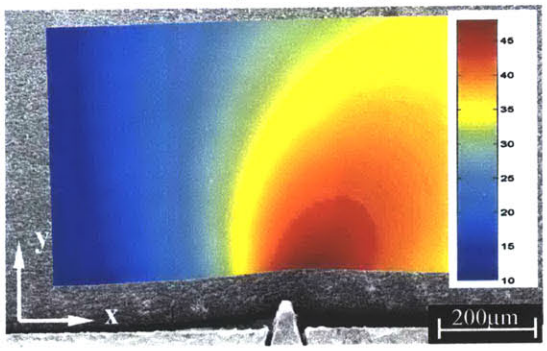

Figure 2-22(d)

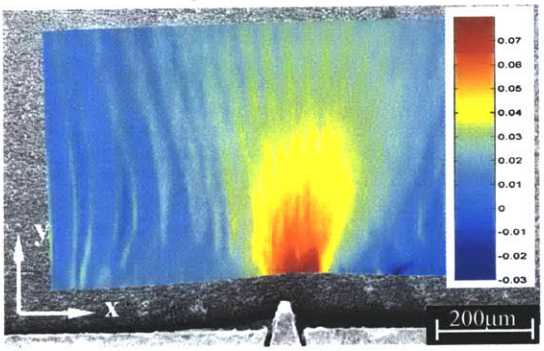

Figure 2-22(e)

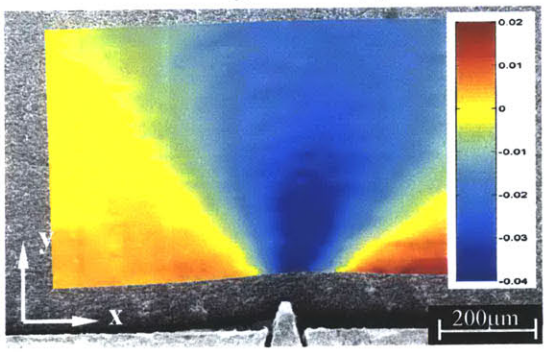

Figure 2-22(f)

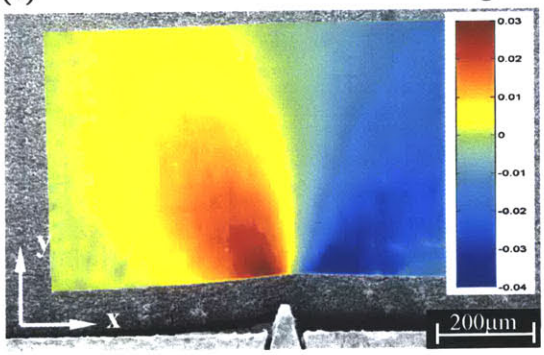

Figure 2-22(g)

Figure 2-22: Results from image processing of SEM micrographs from the indentation/ scratching test upon scratching: (a) unprocessed SEM micrographs; (b) SEM micrograph at a larger magnification; contours for (c) u_1; (d) u_2; (e) ε_{11}; (f) ε_{22}; (g) ε_{12}.

The displacement fields were then used to computer the true strain contours. Figure 2-21(e) and (g) show the contours of strains ε_{11}, ε_{22} and ε_{12}, respectively. In Figure 2-21(e), the scale for the strain ε_{11} ranges from -0.01 (blue) to 0.09 (red); in Figure 2-21(f), the scale for the strain ε_{22} ranges from -0.05 (blue) to 0.02 (red); in Figure 2-21(g), the scale for the strain ε_{12} ranges from -0.04 (blue) to 0.04 (red). It is also noticed that the material surrounding the protrusion is lifted by the protrusion, resulting in the lack of contact of the material surrounding the protrusion, and similar features of the strain contours as those observed from the tests using the wedge-type knife.

Figure 2-22 (a) to (g) show the contours from image processing on micrographs during scratching with δt=100μm. Figure 2-22(a) shows the micrograph used for image processing while Figure 2-22(b) shows a micrograph taken at a higher magnification but under the same testing condition. Figure 2-22(c) and (d) show the contours for the displacement u_1 and u_2. In Figure 2-22(c), the scale for the displacement u_1 ranges from 10μm (blue) to 50μm (red), while in Figure 2-22(d), the scale for the displacement u_2 ranges from 10μm (blue) to 48μm (red). Even though there are factors causing asymmetry in the displacement field upon indentation, the contours during scratching very nicely capture the feature of the biased displacements where material is pushed rightward by the knife as it moves toward right.

True strains were calculated from the displacement fields. Figure 2-22(e), (f) and (g) show the contours of strains ε_{11}, ε_{22}, and ε_{12}, respectively. In Figure 2-22(e), the scale for the strain ε_{11} ranges from -0.03 (blue) to 0.08 (red); in Figure 2-22(f), the scale for the strain ε_{22} ranges from -0.04 (blue) to 0.02 (red); in Figure 2-22(g), the scale for the strain ε_{12} ranges from -0.04 (blue) to 0.03 (red). Compared with the strain contours immediately after indentation (Figure 2-21(e), (f), and (g)), the distributions of the strains during scratching show features of the material being push rightwards, whilst the magnitudes of the strains are generally smaller. This is probably because that the contact between the material and the smooth surface of the knife restrict the relative motion between the protrusion and the material, resulting in less severe deformation than those in the wedge-type knife test where the surface surrounding the knife is essentially free to

move.

2.4 Summary

An in-situ micro indentation/scratching test system was introduced in this chapter. The new system provided micro indentation/scratching test within an SEM and enabled simultaneous collection of video images of the indentation/scratching tests and the normal/tangential force data.

The new system was used to conduct in situ micro indentation/scratching tests within the SEM on thermoplastic polyurethane at different indentation depths to obtain direct observation of deformation as well as normal/tangential forces. Two types of the knives were used in this study. The first one was a wedge-type knife. We used this type knife to study the interaction between an asperity and the sealant material without considering the overall pressure applied by the bushing. The second one was a bulk-type knife, which was designed as a small protrusion (60μm in height) over a large smooth surface. The purpose of using this type of knife was to study the effect of the superposition of an overall compression on the material deformation during indentation/scratching.

For the indentation/scratching test using the wedge-type knife, it was observed that the normal/tangential force vs time curves could be divided into three regions according to different dominant features of the test: The first region corresponded to the indentation, where the normal force increased initially nonlinearly then almost linearly. At this stage, the material symmetrically conformed to the knife; The second region corresponded to the start of scratching. At this stage, the tangential force increased almost linearly and the material around the contact surface moved with the knife, demonstrating features commonly known as stick phase. The material behind the knife gradually loses contact with the knife and the conformation of the material to the knife became biased; At the third region, the curve for tangential force gradually bent over to a constant value, and the knife slipped over the surface (known as slip phase). The material behind the knife lost contact with the knife whereas the material ahead of the knife was pushed by the knife, providing resistance to the knife movement; After the removal of the knife, small amounts of residual deformation were observed at the locations where the knife indented into the material with the indentation depths of 50μm and 80μm.

For the test using the bulk-type knife, during scratching, the transition from stick phase to slip phase was also observed. However, the normal force showed only a small decrease during the transition period primarily because the normal force now had major contributions from bulk contact between the smooth surface and the material. The material deformation around the protrusion showed similar features as those observed in the tests using wedge-type knife.

Image processing, together with a software to compute large strains, was successfully used to obtain displacement and strain fields of the material in the indentation/scratching tests. For the test using the wedge-type knife, symmetric deformation was observed during indentation and biased deformation field was observed during scratching. It was also observed that during scratching, the strains tended to increase and concentrate toward the contact zone, implying more severe deformation during scratching. For the test using the bulk-type knife, it was found that during indentation, due to the material being lifted by the protrusion (or asperity), the deformation of the material around the protrusion/asperity was similar to that from the tests using the wedge-type knife. During scratching, however, due to the constraint applied by the contact between the smooth surface of the knife and the material, the deformation was generally less severe than that using the wedge-type knife. Therefore, the wedge-type knife test created more severe deformation than the bulk-type knife, and might result in accelerated abrasive wear.

References

[2-1] LEO 435VP Operator Manual, LEO Electron Microscopy Ltd.

[2-2] Peters, W.H, Ranson, W.F., Digital imaging techniques in experimental stress analysis, Opt. Eng. 21, 1982, pp 427-431.

[2-3] Sutton, M.A., Cheng, M., Peters, W.H., Chao, Y.J., McNeill, S.R., Application of an optimized digital image correlation method to planar deformation analysis, Image Vision Comput., 4, 1986, pp.143-151.

[2-4] Parsons, E., Boyce, M.C., Parks, D.M., An experimental investigation of the large-strain tensile behavior of neat and rubber-toughened polycarbonate, submitted to Polymer.

Chapter 3

Cyclic Scratching: Effect on Surface Topography

A surface will be damaged after it is subjected to cyclic abrasion. For elastomers, surface damage acts as a precursor to the formation of abrasive patterns. Although the number of scratching cycles for the formation of a characteristic abrasion pattern is generally much longer than that for the formation of initial damage, it is important to study the initiation of damages. The formation of abrasive patterns is a bimodal process where the initiation of new damage and propagation of existing damage occur simultaneously. The former supplies new sources for damage, whilst the latter results in the ultimate loss of material. The formation of initial damage and propagation/progression of this damage during the early stage will eventually influence the form and rate (with respect to number of cycles) of abrasive wear. This chapter studies the topography change during cyclic scratching tests. In the first section, the equipment and methodology used in this study are introduced. The second to fourth section present detailed results from both SEM and Zygo (a three-dimensional noncontact surface profiler) inspections of the surface topography after different numbers of cycles on different materials at different indentation depth, i.e., the second and the third section provide results for unfilled thermoplastic polyurethane (TPU) with indentation depth of 50μm and 80μm, respectively, and the fourth section provides results for glass fiber filled thermoplastic polyurethane with indentation depth of 80μm. The fifth section summarizes the observations.

3.1 Methodology for Topography Study

A surface profiler and a SEM are employed for surface topography study. The surface profiler is the Zygo NewView 5000 from Zygo Corporation. In the following, we

conveniently refer to it as Zygo. The SEM is LEO VP438 from LEO Electron Microscopy Ltd.

3.1.1 Zygo: A 3D Surface Profiler

Zygo is a three-dimensional (3D) non-contact surface profilometer, using scanning white-light interferometry, a traditional technique in which a pattern of bright and dark lines (fringes) resulting from an optical path difference between a reference and a sample beam is used to deduce the surface profile. The mechanism is simple. The incoming light is split inside an interferometer (Figure 3-1), one beam going to an internal reference surface and the other to the sample surface. After reflections, the beams recombine inside the interferometer, undergoing constructive and destructive interference and producing the light and dark fringe pattern. The Zygo instrument uses a precision vertical scanning transducer together with a camera to generate a 3D interferogram of the surface, processed by the computer and transformed by frequency domain analysis resulting in a quantitative 3-D image. The Zygo NewView 5000 offers performance of up to 0.1nm vertical resolution and 0.45μm to 11.8 μm lateral resolution. The interferometric objective used was 20X Mirau, which offered a field of view of 0.35mm by 0.26mm at 1X system magnification and 0.875mm by 0.65mm at 0.4X system magnification. The lateral resolution for 20X Mirau objective is 0.88μm at 1.0X system magnification and 2.2μm at 0.4X [3-2].

Unlike SEM, where only two-dimensional (2D) information about the surface is obtained, Zygo provides a quantitative 3D surface profile of the surface and the white-light avoids the issues of heating and radiation. However, the drawback of Zygo is that it requires the surface to be relatively smooth and surface features with dramatic changes are difficult to identify from surface profile solely. In this chapter, Zygo and SEM are combined to provide desired information: SEM shows the surface visually, and Zygo provides quantitative information about the surface.

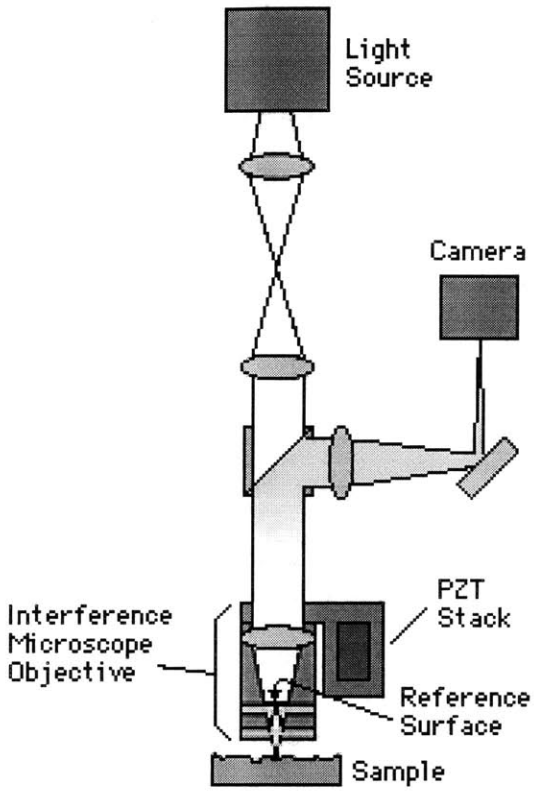

Figure 3-1: Mechanism for Zygo, a 3D surface profiler.

3.1.2 Zygo-SEM study

In this chapter, the topography change during cyclic scratching will be inspected using a systematic method. Figure 3-2 shows the procedure of this method. It should be mentioned that in this chapter it is the abraded surface, i.e. the x-z surface plane (Figure 3-3) being inspected using both Zygo and SEM.

A fresh sample prepared into the rectangular shape (Figure 2-5) is first inspected using both SEM and Zygo. In SEM, several random locations are inspected at magnifications of 100X to 200X. Since the purpose of the SEM study is to provide visual information of damages, which are unknown before the test runs, the SEM micrographs before the test can be regarded as the overall landscape of the surface. For Zygo inspection, an area of about 1mm by 6mm is analyzed to provide an overall 3D surface profile. The locations inspected by SEM are also analyzed by Zygo.

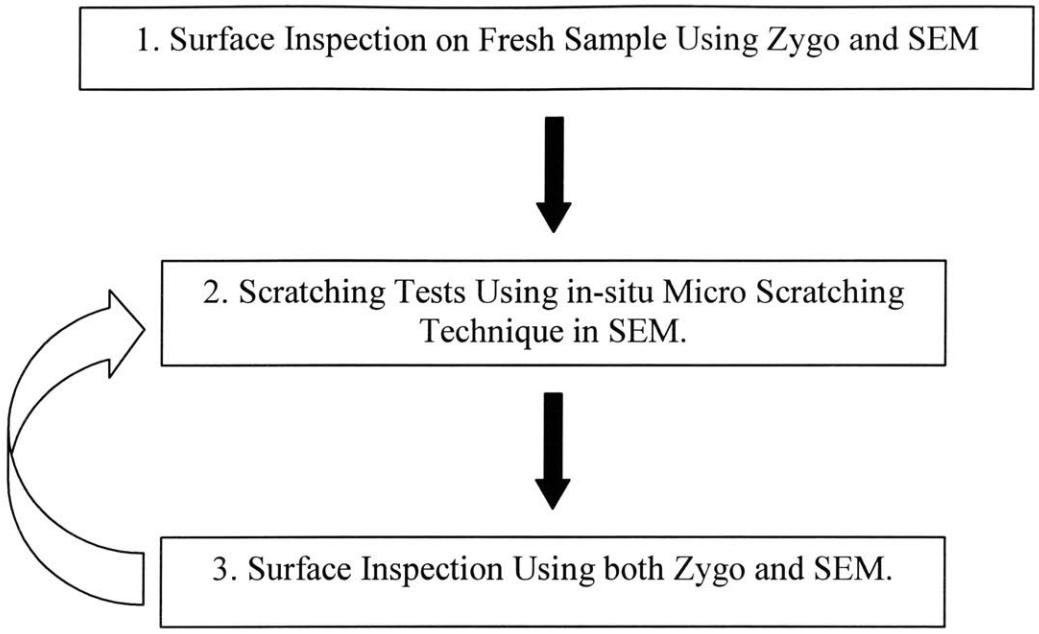

Figure 3-2: Flow chart of the procedure for the Zygo-SEM study.

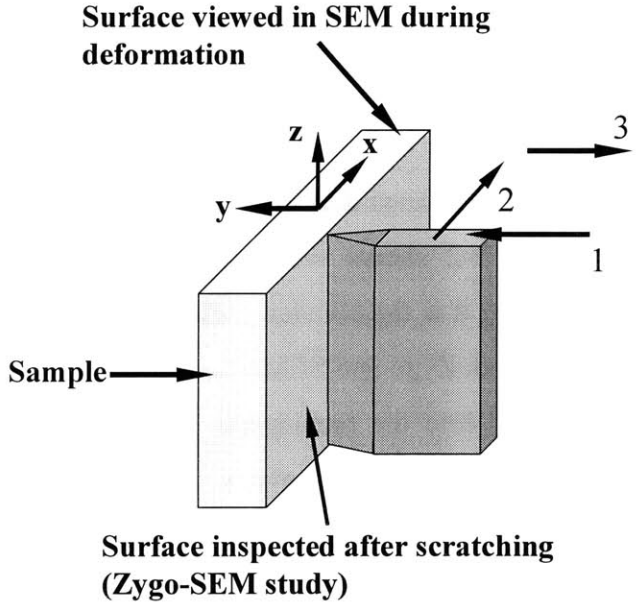

Figure 3-3: Surface inspected in Zygo-SEM study

The sample is then tested following the test process outlined in Figure 2-1 with the indentation depth of δn. The distance of the scratching should cover the area of Zygo and SEM study in step 1.

The sample is inspected by Zygo and SEM after the scratching test. Both SEM and Zygo will be used to inspect the locations inspected previously as well as locations of damage, which will continue to be inspected in the thereafter tests. Step 2 and Step 3 will be repeated.

It is arguable that material properties in the small area where the SEM image is taken might have been changed due to electron radiation and heating. However, it is unclear and difficult to evaluate the degree of such change. In the test, operation scheme for reducing charge and heating should be carefully followed and locations of SEM inspections are limited to a few areas. In the case where surface properties do change, such an area should be taken as locally inhomogeneous region with different material properties, and damage due to scratching might be accelerated.

3.2 Result: Scratching Tests with δ_n=50μm for Unfilled TPU

The images in Figure 3-4 show the overall topography change during cyclic scratching tests with indentation depth of $\delta_n = 50\mu m$. The arrow in Figure 3-4(a) indicates the scratching direction. In Figure 3-4, each image covers an area of about 1.2mm (width) by 4.6mm (length). Since a single Zygo image only covers an area of 0.875mm by 0.65mm (here, 20X Mirau objective is used under the system magnification of 0.4X), each image in the figure consists of 18 small image patches, resulting in certain mismatch on the boundary of these patches. Attention should be paid to the overall topography instead of these mismatches.

3.2.1 Topography of Fresh Sample

The images in Figure 3-4(a) show the topography before the scratching tests. The surface is smooth overall, except for a few marks on the surface due to scratches on the surface of the mold used for TPU production. From Figure 3-4(b), the surface roughness is about 0.6μm overall, except for a few local region showing rougher than most of the areas. For instance, the area indicated by a rectangle shows a locally high region of about 0.20mm by 0.15mm on the surface. The variation of height in this area is gentle and the surface roughness around this area is about 1μm.

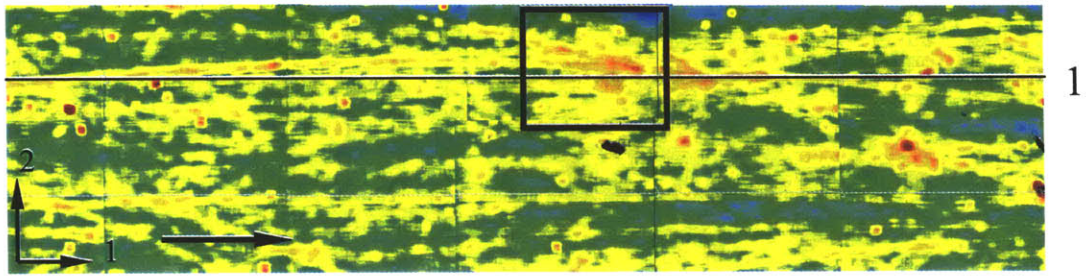

Figure 3-4 (a)

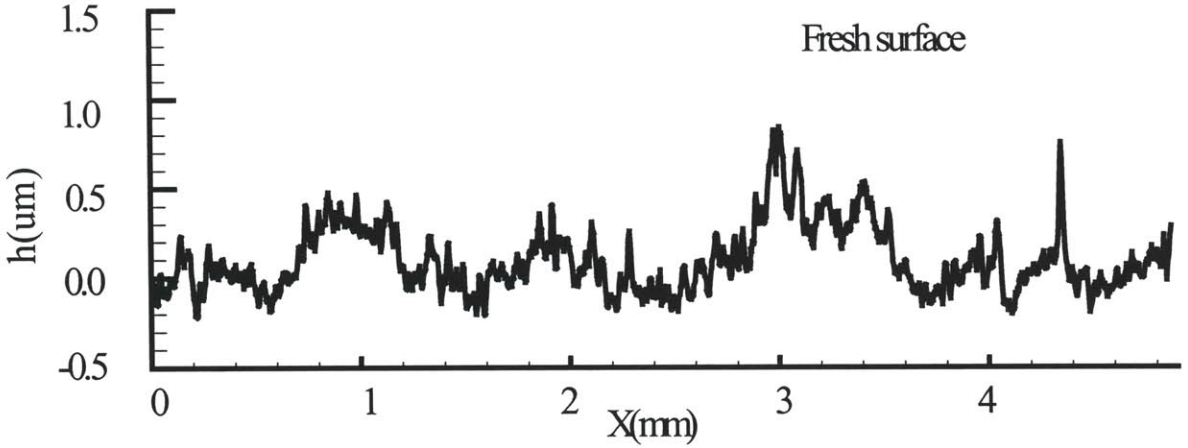

Figure 3-4 (b)

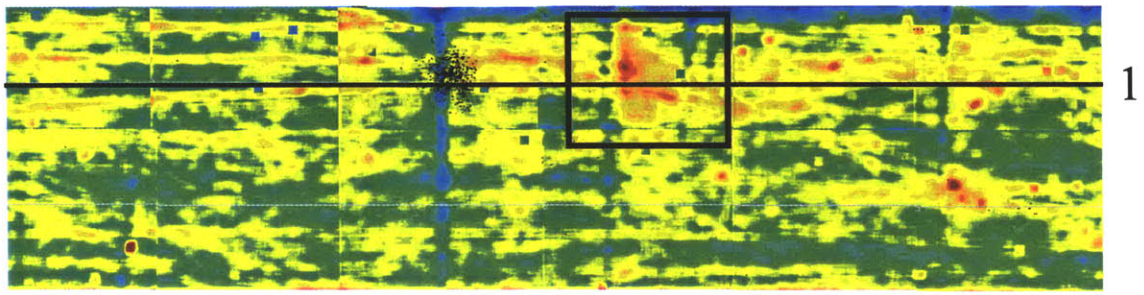

Figure 3-4 (c)

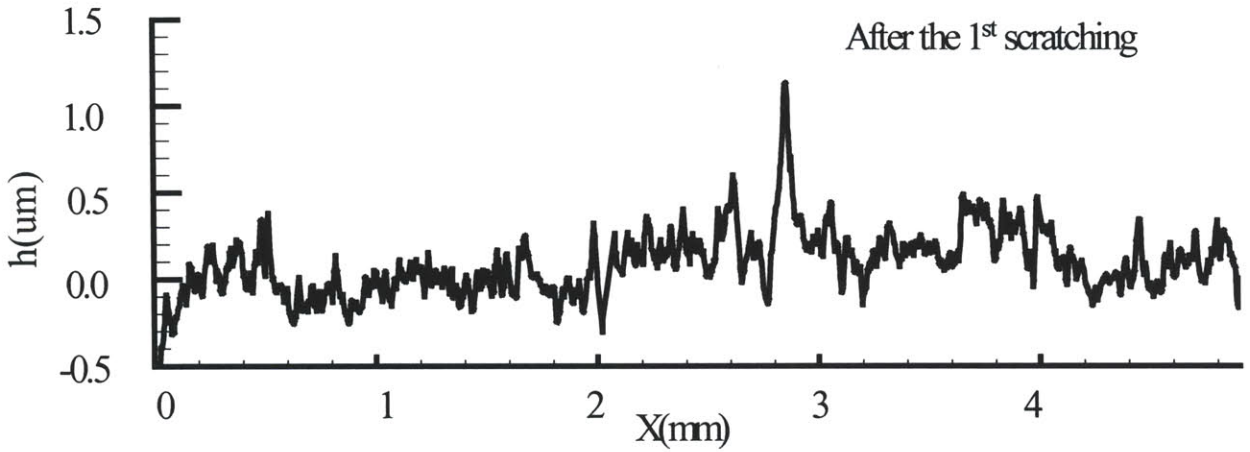

Figure 3-4 (d)

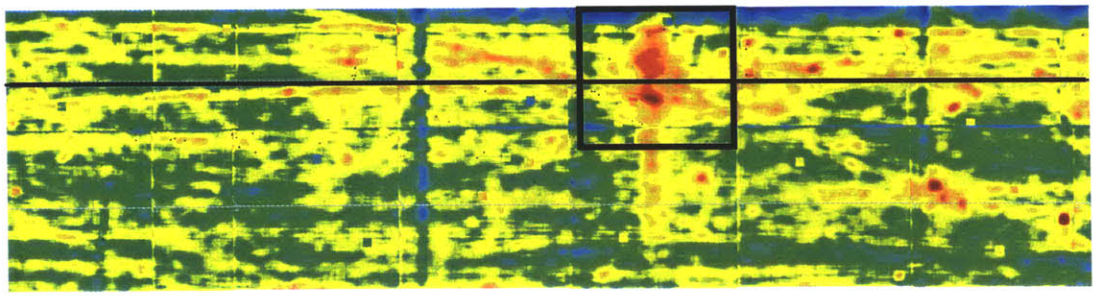

Figure 3-4 (e)

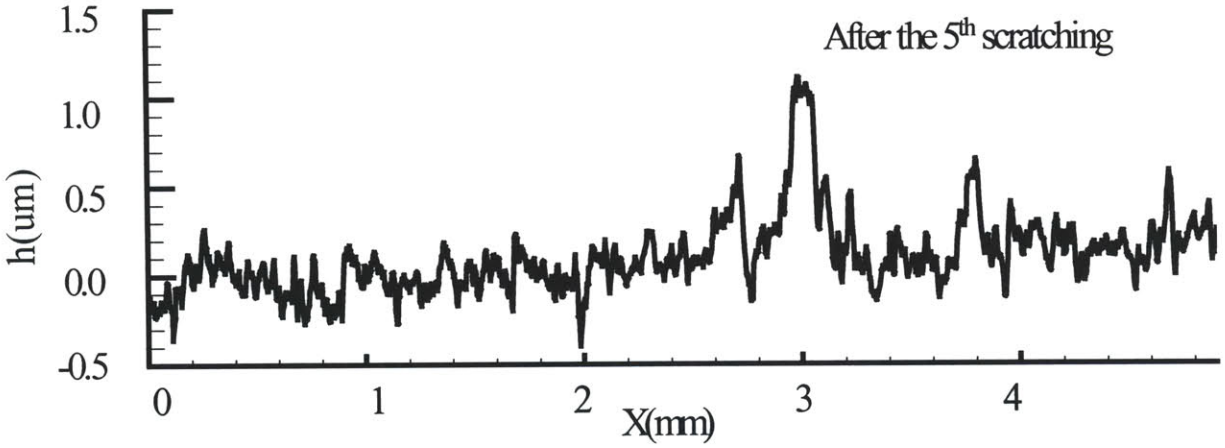

Figure 3-4 (f)

Figure 3-4: Surface profile by Zygo after scratching tests on unfilled TPU with indentation depth of $\delta_n = 50\mu m$; (a) Fresh surface; (b) Surface profile along line 1 in (a); (c) Surface after the 1st scratching; (d) Surface profile along line 1 in (c); (e) Surface after the 5th scratching. (f) Surface profile along line 1 in (e).The dimension of the area is 1.2mm by 4.9mm. The scratching direction is illustrated in (a).

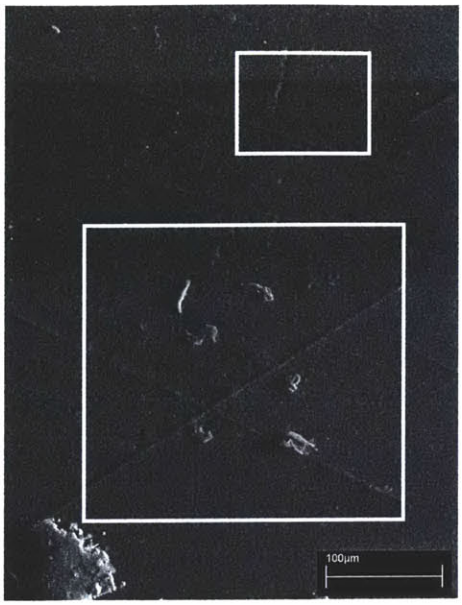

Figure 3-5(a)

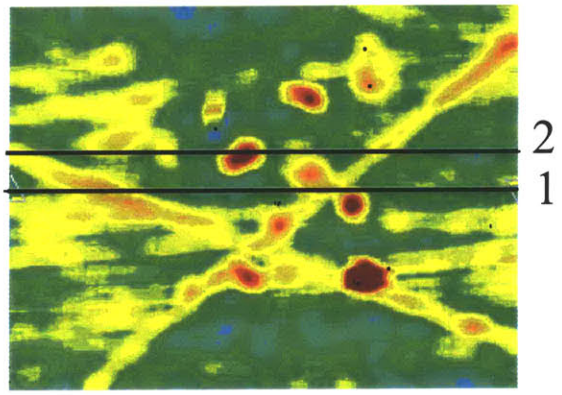

Figure 3-5(b)

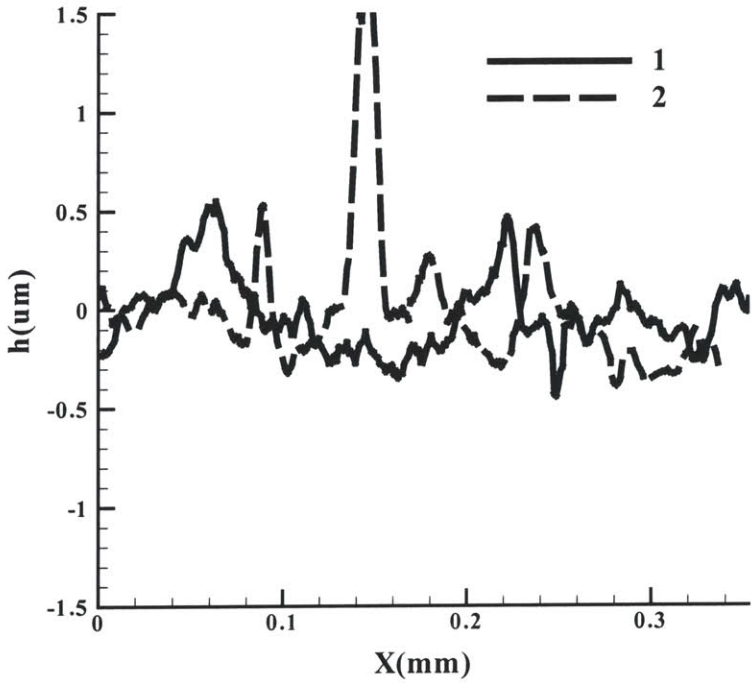

Figure 3-5(c)

Figure 3-5: Surface before the scratching: (a) SEM image; (b) Surface profile obtained by Zygo; (c) Surface roughness along line 1 and line 2 in (b). The area shown by Zygo corresponds to the same area enclosed by the larger rectangle in SEM image.

Figure 3-5(a) shows a close-up micrograph image taken by the SEM, the area enclosed by the larger rectangle was also investigated by Zygo, shown in Figure 3-5(b).

Figure 3-5(c) shows the surface profile along line 1 and line 2 in Figure 3-5(b). The surface roughness is less than 1μm. Before the scratching test, there are some small dirt particles attached to the surface. The line 2 in Figure(b) is deliberately chosen to cross one of the dirt particles, showing the height of the dirt particle is about 1.5μm.The marks left by the mold are also clearly shown on the surface. Zygo image reveals the height of these mold marks is about 0.8μm.

3.2.2 Topography after the 1st Scratch

Figure 3-4(c) shows the surface profile after the 1st scratching. The surface profile does not change significantly overall, even though there are some new features. The previously observed locally high region (enclosed by the rectangle in Figure 3-4(a)) shows a steep peak. The height of the peak is about 1.1μm, the width is about 30μm (measured at h=0.6μm), and the length in the 2-direction increases to 300μm, probably as a result of local permanent deformation due to scratching. It is also noticed that there is an indentation mark left on the surface after the 1st scratching. Since the scratching test was running continuously, a conjecture about the formation of this indentation mark is due to local effect, such as a locally strong blocking effect perhaps due to material inhomogeneity. Since only one such indentation mark is observed in the course of scratching, we attribute it to be due to a random event. However, we note that such random event may be responsible for the initiation and initial stage of damage.

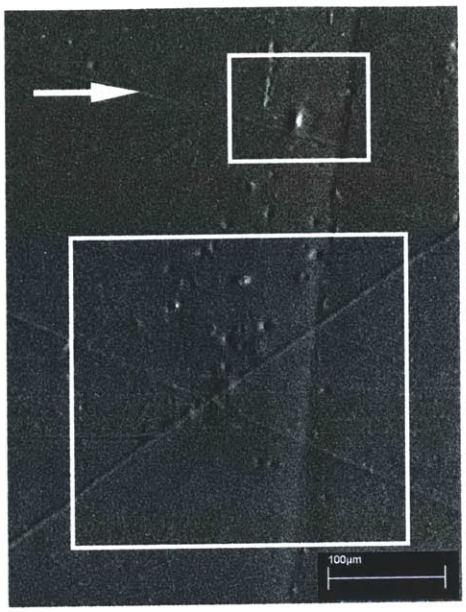

Figure 3-6(a)

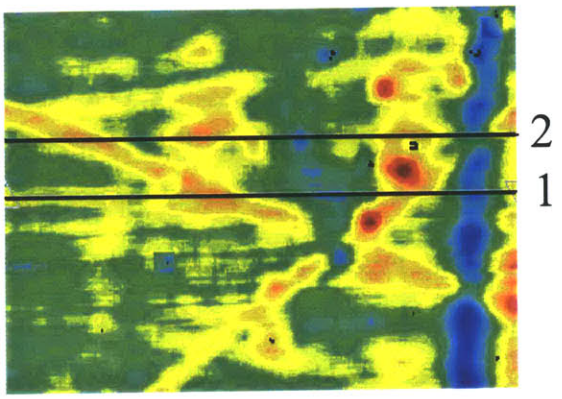

Figure 3-6(b)

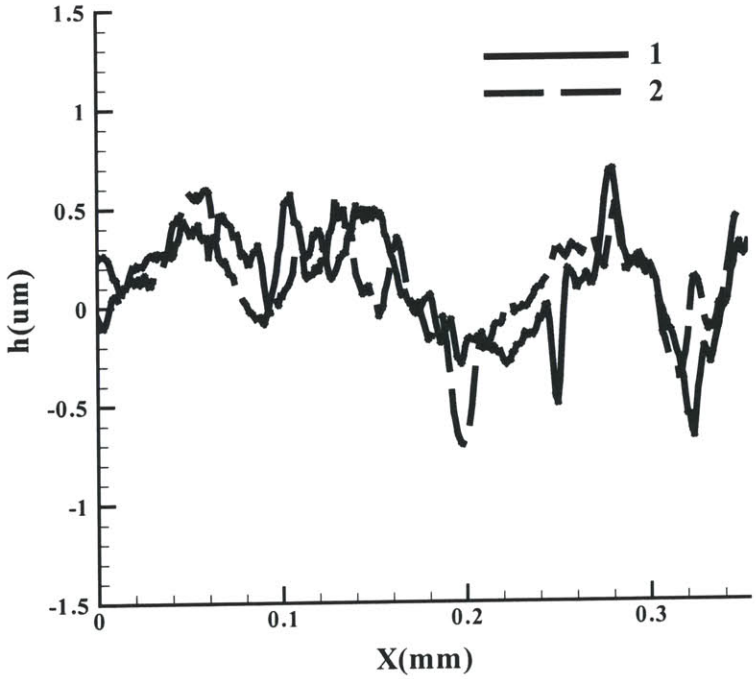

Figure 3-6(c)

Figure 3-6 Surface after the 1st scratching: (a) SEM image; (b) Surface profile obtained by Zygo; (c) Surface roughness along line 1 and line 2 in (b). The area shown by Zygo corresponds to the same area enclosed by the larger rectangle in SEM image. The arrow in (a) indicates the scratching direction.

Figure 3-6 shows the close-up surface by SEM and Zygo. The same surface was inspected before the 1st scratching test (Figure 3-5). The previously shown dirt particles were removed due to sweeping of the knife over the surface. The indentation mark shown in Figure 3-6 was created before the 1st scratching test and served as a reference to locate the area during the cyclic scratching. The SEM image reveals that there is no significant topography change due to its presence. One surface feature after the 1st scratching is that there are a number of small pits present on the previously smooth surface. These pits show the shape resembling the feature of the crater of a volcano and are a few microns in size. The line 2 in Figure 3-6(b) is chosen to cross one of the pits and reveals by Figure 3-6(c) that the depth of the pit is about 0.75μm. It is unclear about the reason for the formation of these pits, but one conjecture is that these pits are due to the loss of small inclusions or material irregularities close to the surface. The dimensions of these pits coincide with the dimension of small damage in the bimodal form of abrasive wear of rubber proposed by Gent and Pulford[3-3] and indirectly observed by Cadle and Williams in road test[3-4]. This may strongly suggest that these pits are the small initial damage. However, it is still premature to make such a conclusion since direct observations of the small damage proposed Gent and Pulford are unavailable. Another interesting feature is the presence of a new small protrusion on the surface, as indicated in the smaller rectangle in Figure 3-6(a), in contrast to the smooth surface before the test shown in Figure 3-5(a). Such small protrusion clearly shows the feature of an inclusion initially underneath the surface emerging to the surface due to the local large deformation during the scratching process. These two features will be further inspected after the 5th scratching tests.

3.2.3 Topography after the 5th Scratch

Figure 3-4(c) shows the overall surface profile after the 5th scratching. Even after the 5th scratching, the surface does not show significant change. The previously observed locally high region (enclosed by the rectangle in Figure 3-4(a) and the peak in Figure 3-4(b)) becomes a plateau of the height of 1.1μm, the width of 60μm and length in the 2-direction of about 450μm, due to the accumulation of local permanent deformation

during scratching. The indent observed after the 1st scratching, however, neither increases in size nor invokes damage to the surface.

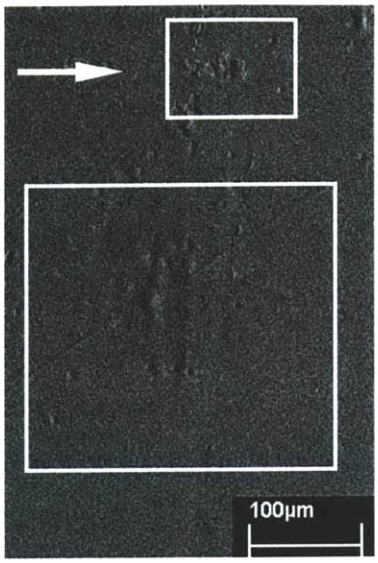

Figure 3-7(a)

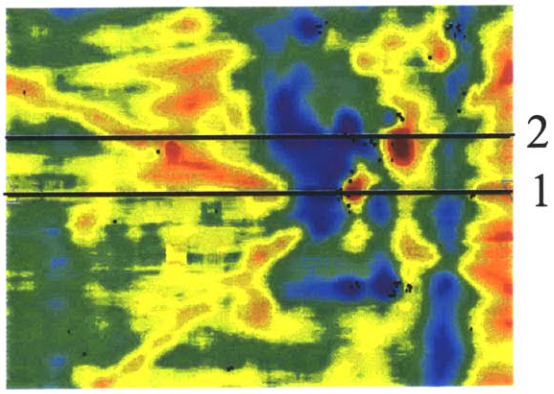

Figure 3-7(b)

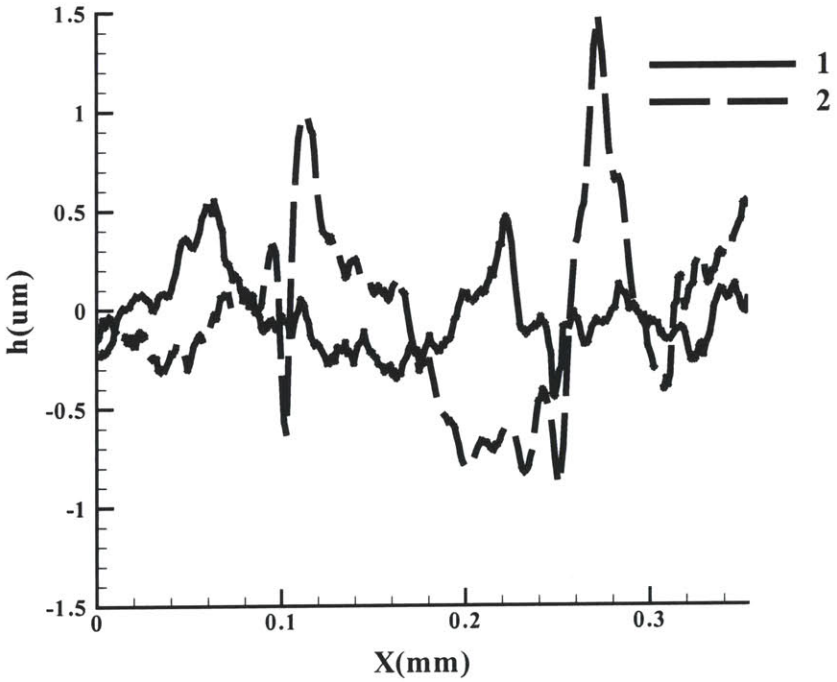

Figure 3-7(c)

Figure 3-7 Surface after the 5th scratching: (a) SEM image; (b) Surface profile obtained by Zygo; (c) Surface roughness along line 1 and line 2 in (b). The area shown by Zygo corresponds to the same area enclosed by the larger rectangle in SEM image. The arrow in (a) indicates the scratching direction.

Figure 3-7 shows the close-up surface by SEM and Zygo. The same surface was inspected before and after the 1st scratching test and is shown in Figure 3-5 and Figure 3-6. In comparison with features in Figure 3-6, several major changes are observed. First, some small pits observed in Figure 3-6 are removed from the surface, and at the same time, some new pits are generated. In Gent and Pulford[3-3], the small damage acted as the precursor to the large damage that results in final loss of materials. Clearly, our observation does not support this conjecture. Second, the small protrusion in the smaller rectangle is removed due to the break of the surface material. The SEM image clearly shows the damage caused by this process. Third, new small damages are observed, for instance, the one on boundary of the smaller rectangle boundary shows material lost. Fourth, permanent deformation in the form of wrinkles is also observed, for example, the one at the center of the larger rectangle. The area of such wrinkle-like permanent deformation is much larger than the damages observed above. Either removal or propagation of this wrinkle-like area will cause more damage on the surface. Therefore, this wrinkle-like permanent region may act a precursor of surface damage. Last, the mold marks are almost totally removed and it seems unlikely there are any damages due to the removal of these mold marks.

3.2.4 Summary of Observations from δ_n=50μm Scratching Tests

Topography changes during the cyclic scratching tests with $\delta_n = 50\mu m$ were inspected. Local high region on the surface may increase in dimensions due to the accumulation of plastic deformation caused by the scratching process. Small inclusions or material irregularities close to the surface may cause small pits over the surface due to the removal of these inclusions. However, the small pits generally are removed in the thereafter scratching and are unlikely to grow into larger damages.

The topography changes observed during the cyclic scratching tests with $\delta_n = 50\mu m$ are generally small in size. Some small features are simply removed during the scratching process. Wrinkle-like permanent deformation, which is susceptible to act as a precursor of surface damage, is observed after the 5th scratching Therefore, for the test with

indentation depth of 50μm, the development of abrasive patterns, if it is possible, will be a very slow process.

3.3 Result: δ_n=80μm for Unfilled TPU

The images in Figure 3-8 show the overall topography change during cyclic scratching tests on unfilled TPU with indentation depth of $\delta_n = 80\mu m$. The arrow in Figure 3-8(a) shows the scratching direction. In Figure 3-8, each image covers an area of about 1.0mm (width) by 4.5mm (length). As discussed in the previous section, there are some sharp color differences in the overall image due to the difference among the image patches used for assembling the overall image. Attention should be given only to the overall topography change instead of these mismatches.

3.3.1 Topography of Fresh Sample

Figure 3-8(a) shows the topography before the scratching tests. Compared with Figure 3-4(a), the overall surface is similar for the two samples: The surface is smooth overall and the surface roughness is about 1μm.

Figure 3-9(a) shows a close-up image taken by the SEM, and Figure 3-9(b) shows the surface inspection by Zygo. The marks left by the mold are clearly shown on the surface. Zygo image reveals the height of these mold marks is less than 1μm.

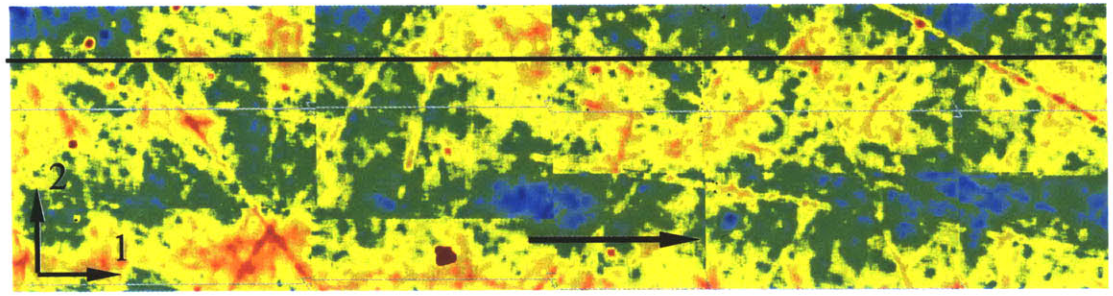

Figure 3-8(a)

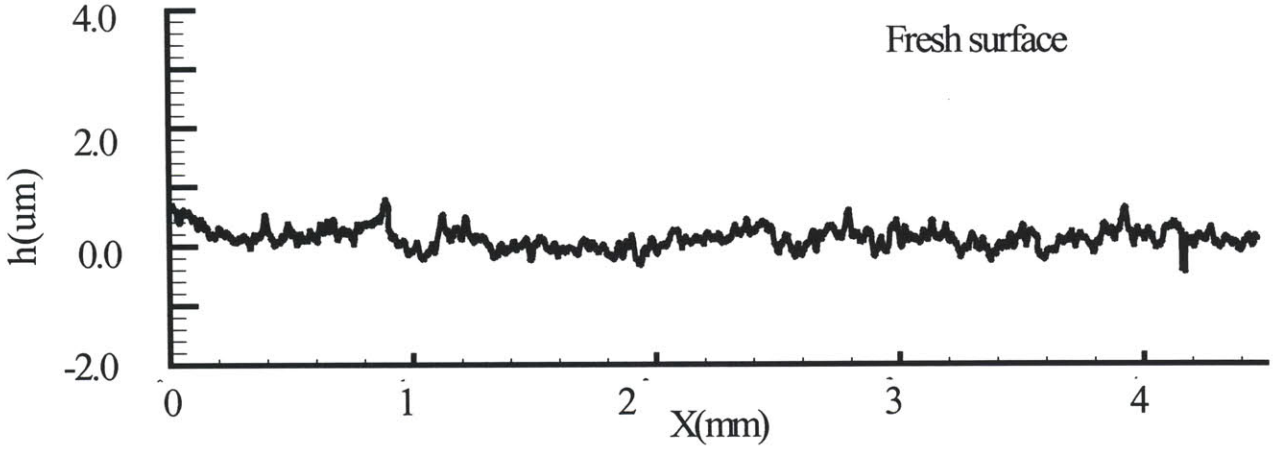

Figure 3-8(b)

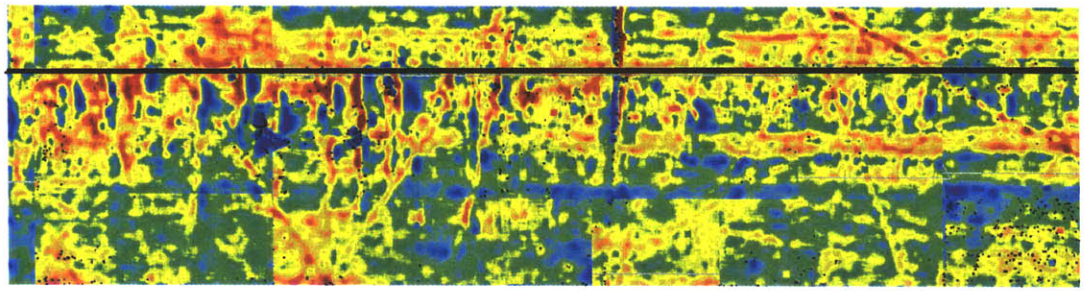

Figure 3-8(c)

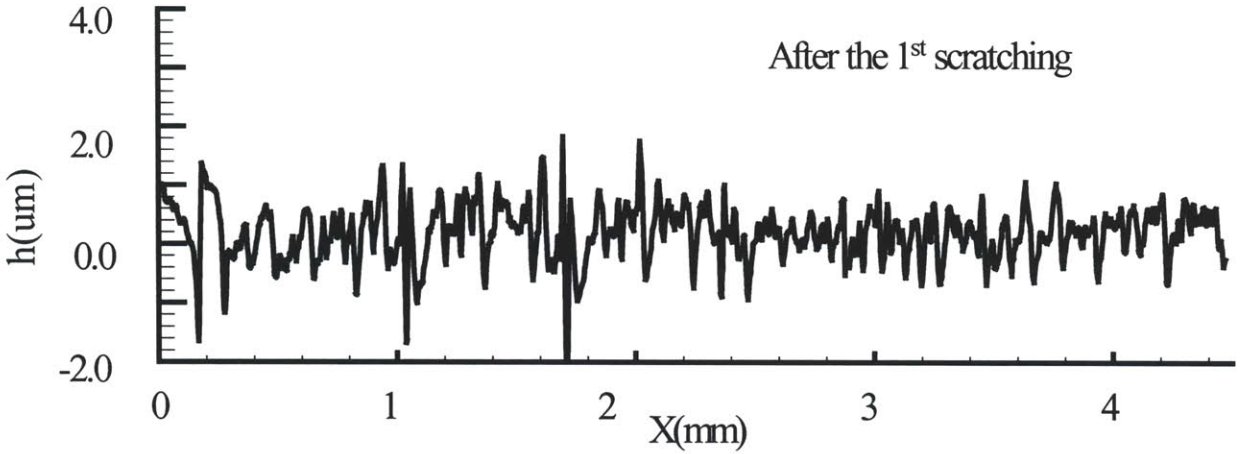

Figure 3-8(d)

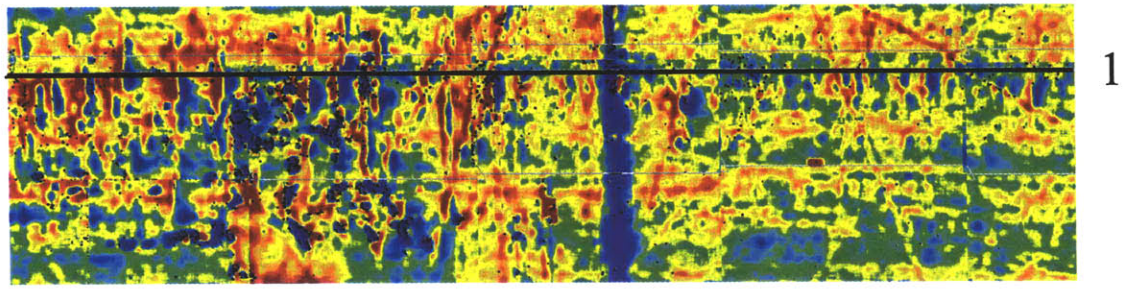

Figure 3-8(e)

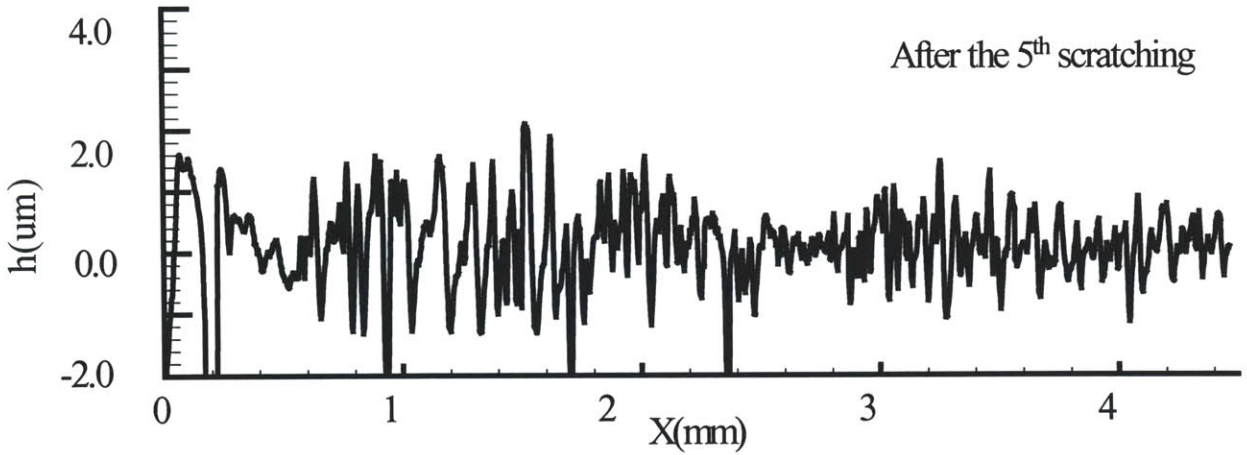

Figure 3-8(f)

Figure 3-8: Surface profile by Zygo after scratching tests on unfilled TPU with indentation depth of $\delta_n = 80\mu m$; (a) Fresh surface; (b) Surface profile along line 1 in (a); (c) Surface after the 1st scratching; (d) Surface profile along line 1 in (c); (e) Surface after the 5th scratching. (f) Surface profile along line 1 in (e). The dimension of the area shown is 1.0mm by 4.5mm.

Figure 3-9(a)

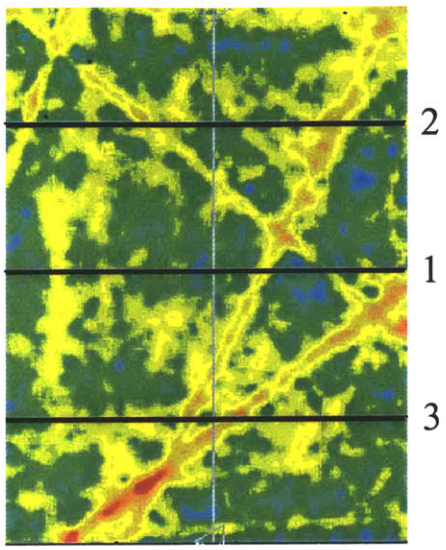

Figure 3-9(b)

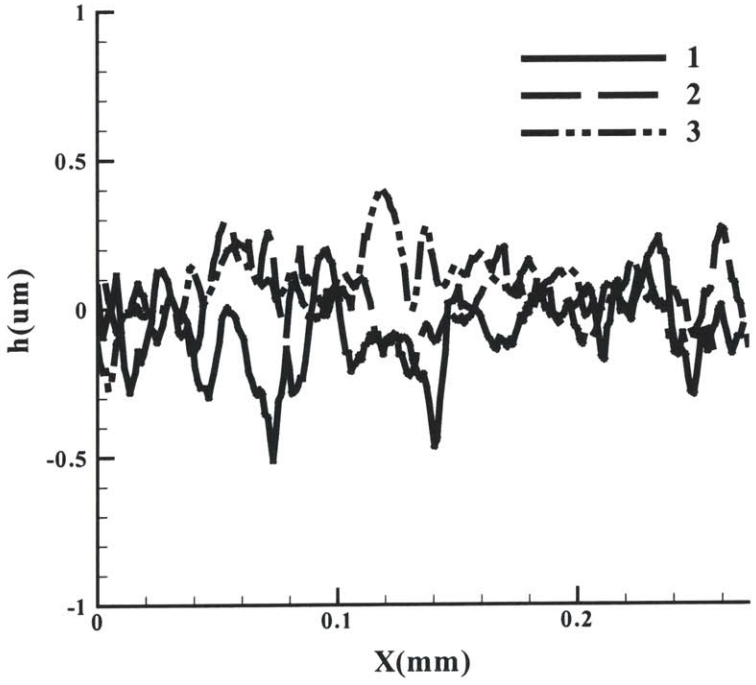

Figure 3-9 Surface before the scratching tests with $\delta_n = 80\mu m$: (a) SEM image; (b) Surface profile obtained by Zygo; (c) Surface roughness along line 1, line 2 and line 3 in (b). SEM and Zygo inspect the same area.

Figure 3-10(a)

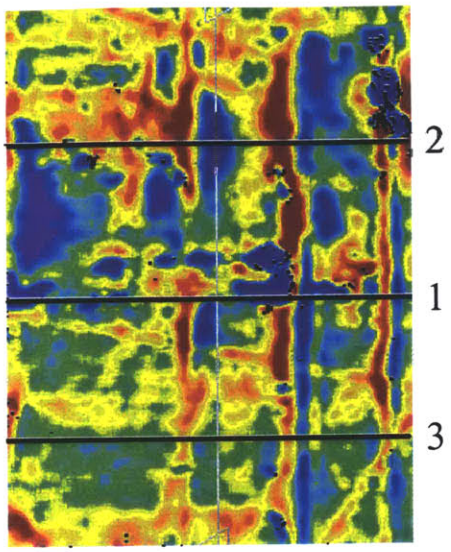

Figure 3-10(b)

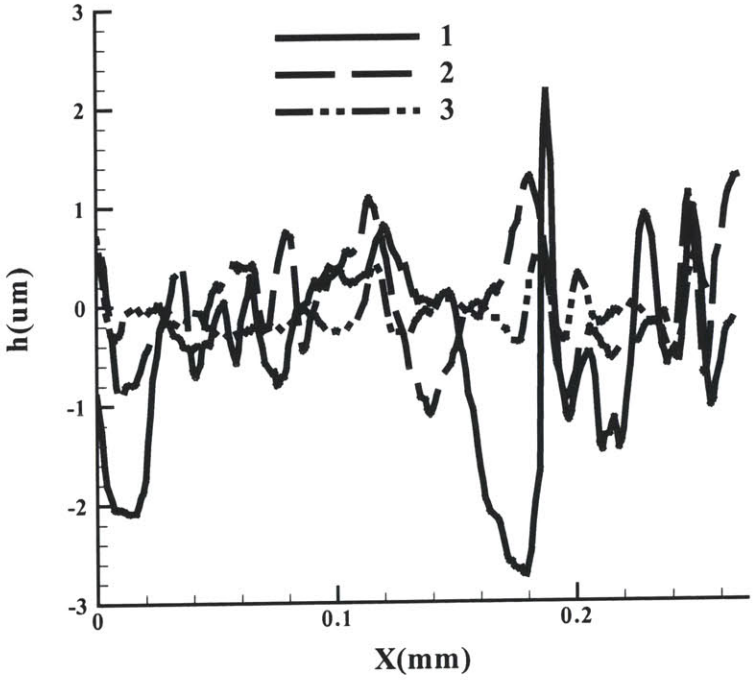

Figure 3-10(c)

Figure 3-10 Surface after the 1st scratching tests with $\delta_n = 80\mu m$: (a) SEM image; (b) Surface profile obtained by Zygo; (c) Surface roughness along line 1, line 2 and line 3 in (b). SEM and Zygo inspect the same area. The arrow in (a) indicates the scratching direction.

3.3.2 Topography after the 1st Scratch

Figure 3-8(c) shows the overall surface profile after the first scratching. With indentation depth of $\delta_n = 80\mu m$, a significant level of surface damage is observed. The damage over the surface shows a pattern of an alternating valley-peak form, with valley-valley distance of 40-170μm and average of about 80μm. From Figure 3-8(d), the surface roughness also increases to about 2μm, with some peaks higher than 1μm and valleys deeper than 1μm. The knife used in this test is the same one used in the tests with $\delta_n = 50\mu m$ and does not show change after the tests. Therefore, the formation of these damages should be mainly due to the increase in indentation depth.

Figure 3-10 shows the surface profile at a higher magnification by SEM and Zygo. The surface inspected by SEM and Zygo here is different from the surface shown in Figure 3-9 because it was difficult to predict where the damage would occur before the test. However, comparison between the surface in Figure 3-9 and Figure 3-10 does provide the contrast about the dramatic topography change resulting from the first scratching test. It is noticed that surface topography changes occur in two forms. One form is plastic deformation, as indicated by the wrinkle-like surface profile changes shown in the SEM micrographs (Figure 3-10(a)). The surface profile along Line 2 (in Figure 3-10(b)), which crosses such wrinkles, shows the distance between these wrinkles is about 70μm, and the peak-valley height is about 2μm. These wrinkles generally have length less than the contact length of the knife with the surface, implying local effects may influence the size of these plastic zones. Another form of topography change is surface damage. The SEM micrograph clearly indicates that such damage is due to local material loss because of tearing and rupture of the material. Line 1 in Figure 3-10(b) crosses one of the damaged area and shows that the depth due to material removal is about 2.8μm and the width is about 40μm. The places of the occurrence of damage are random but most of damages are close to the edge of the wrinkles.

3.3.3 Topography after the 5th Scratch

Figure 3-8(e) shows the surface profile after the fifth scratching. In comparison with Figure 3-8(f), regions of surface damage increase in number. These damaged areas over

the surface also show a clear pattern of alternating valley-peak form with valley-valley distance of 30-170μm and average of about 70μm. The surface roughness increases to about 3-4μm, with significant amount peaks and valleys about 2μm above/below the middle line of the surface.

Figure 3-11(a)

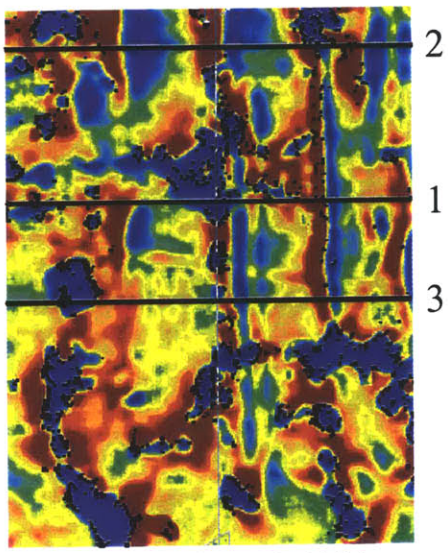

Figure 3-11(b)

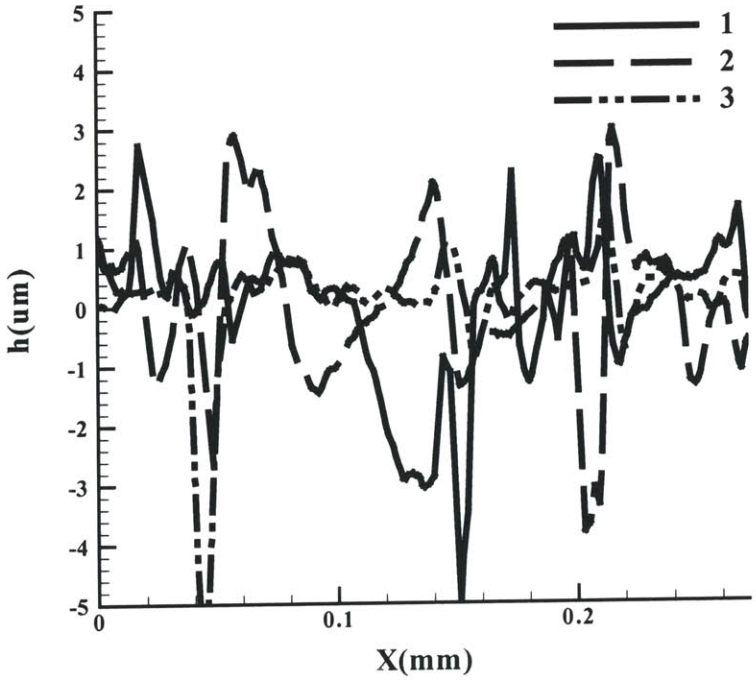

Figure 3-11(c)

Figure 3-11 Surface after the 5th scratching tests with $\delta_n = 80\mu m$: (a) SEM image; (b) Surface profile obtained by Zygo; (c) Surface roughness along line 1, 2 and 3 in (b). SEM and Zygo inspect the same area. The arrow in (a) indicates the scratching direction.

Figure 3-11 shows the surface profile at a higher magnification by SEM and Zygo. The bimodal form of surface topography still exists. The wrinkle-like plastic deformation expanded in width but the distance between these wrinkles remains about 70μm. The height of the previous plastic peak-valley observed in Figure 3-10(b) and crossed by line 2 increases to 4μm. Surface damages occur more frequently and most of the damages occur in the area close to the edges of the plastic deformation zones. It is noticed that the damage formed in the first scratching test increases in width, as shown by the one crossed by line 1 in Figure 3-11(b) being about 3.2μm high and about 60μm wide.

3.3.4 Summary of Observations from δn=80μm Scratching Tests

In contrast to the observations from the tests with $\delta_n = 50\mu m$, where the topography does not change significantly, dramatic topography changes are observed from the tests with $\delta_n = 80\mu m$. The surface topography changes occur in two forms: One is due to local plastic deformations, whereas the other one is due to the rupture of the material. The plastic deformation renders surface peak-valley patterns, whereas the rupture of the material due to extreme stretch causes material loss and occurs randomly over the surface. As the number of scratching cycles increases, the dimensions of both plastic zones and surface damages increase, accompanied by new damages generated after each scratching. Surface damages generally occur around the edge of the plastic zones.

3.4 Result: δn=80μm on 4% Glass Fiber Filled TPU

The images in Figure 3-12 show the overall topography change during cyclic scratching tests with indentation depth of $\delta_n = 80\mu m$ on glass fiber filled TPU. The fibers have average diameters of about 10~16μm and average length to diameter ratio of 8[3-5]. Each image in Figure 3-12 covers an area of about 1.5 mm (width) by 4.5 mm (length). As discussed in the previous section, the sharp color differences in some regions are due to assembling image patches to obtain the overall image. Again, attention should be given only to the overall topography change instead of these mismatches.

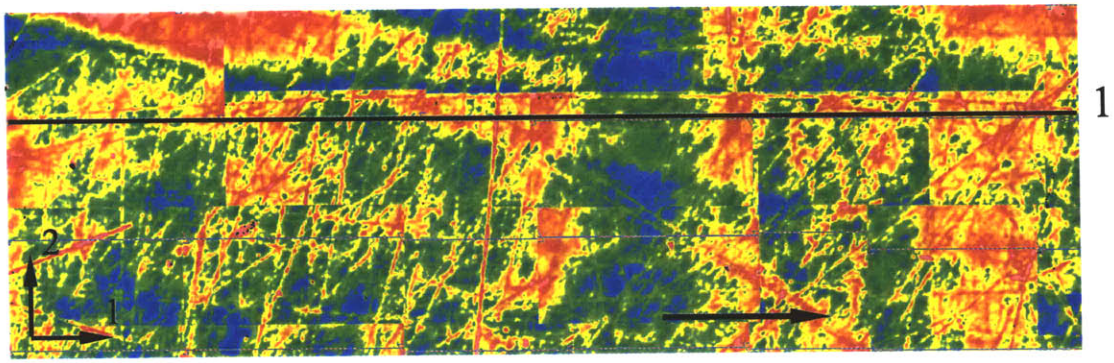

Figure 3-12(a)

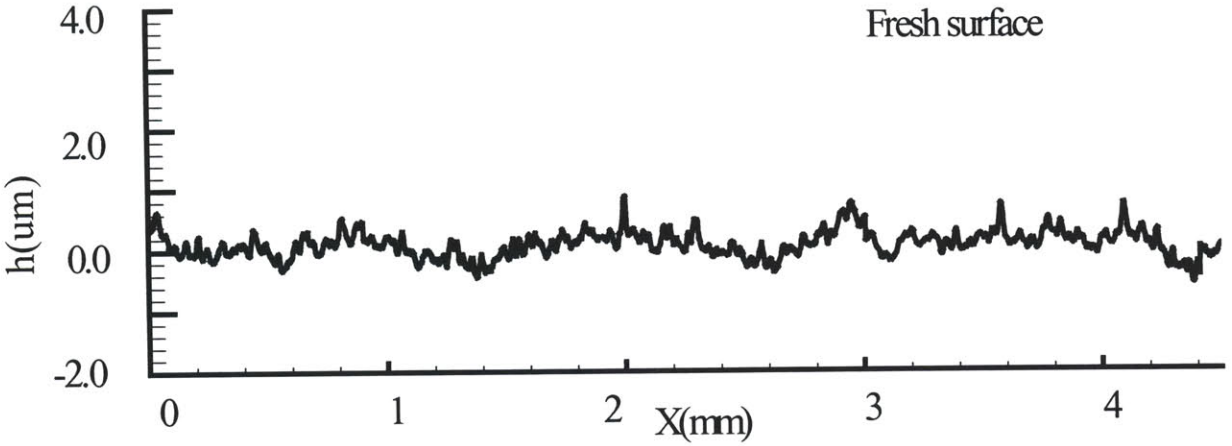

Figure 3-12(b)

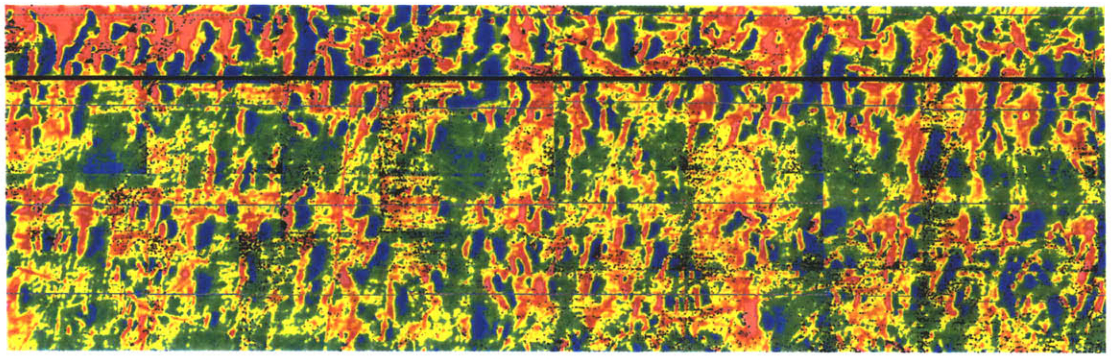

Figure 3-12(c)

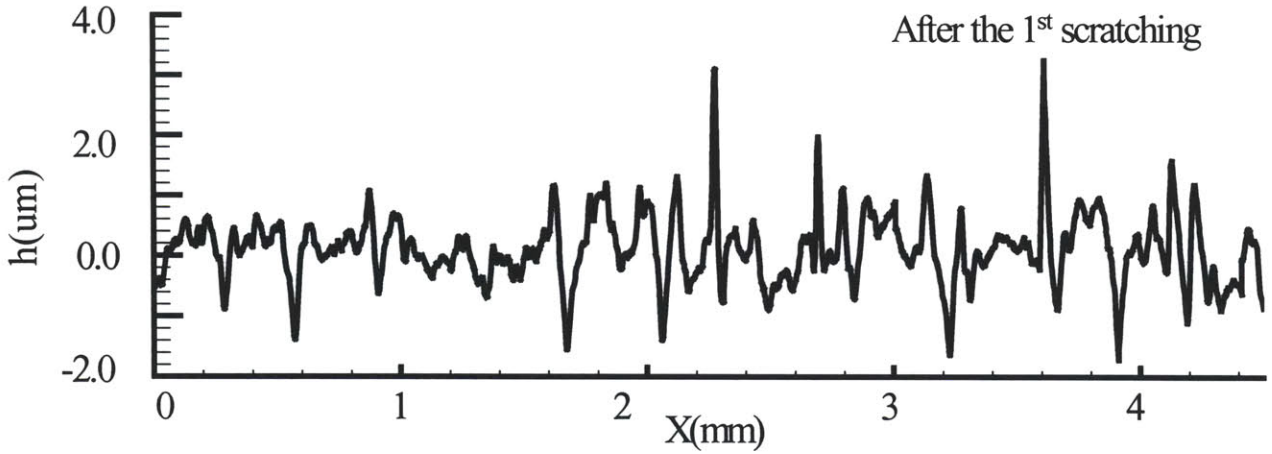

Figure 3-12(d)

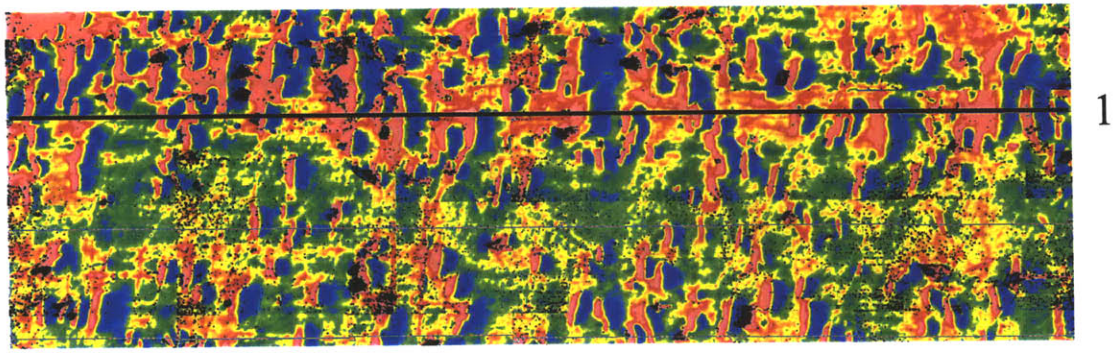

Figure 3-12(e)

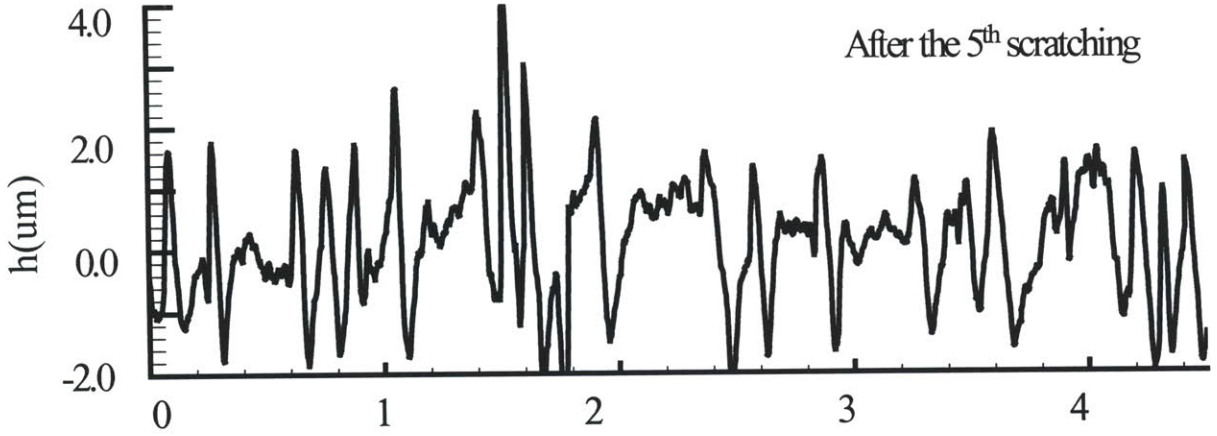

Figure 3-12(f)

Figure 3-12: Surface profile by Zygo after scratching tests for 4% glass fiber filled TPU with indentation depth of $\delta_n = 80\mu m$: (a) Fresh surface; (b) Surface profile along line 1 in (a); (c) Surface after the 1st scratching; (d) Surface profile along line 1 in (c); (e) Surface after the 5th scratching. (f) Surface profile along line 1 in (e). The dimension of the area shown is 1.5mm by 4.5mm.

Figure 3-13(a)

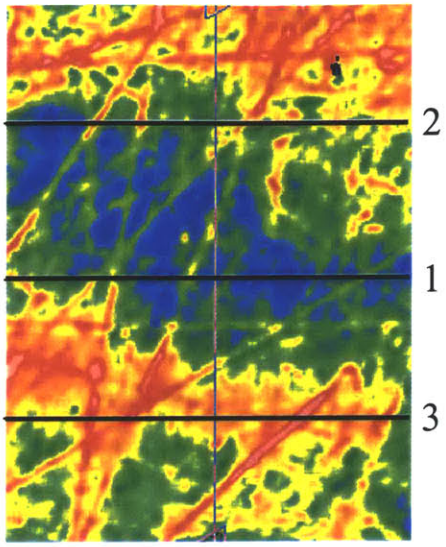

Figure 3-13(b)

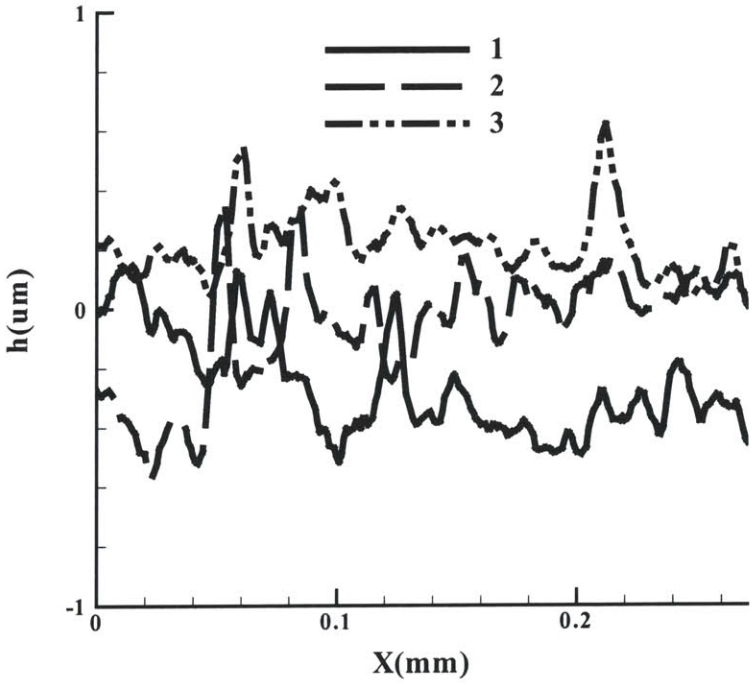

Figure 3-13(c)

Figure 3-13 Surface before the scratching tests with $\delta_n = 80\mu m$: (a) SEM image; (b) Surface profile obtained by Zygo; (c) Surface roughness along line 1, line 2 and line 3 in (b). SEM and Zygo inspect the same area.

3.4.1 Topography of Fresh Sample

Figure 3-12(a) shows the fresh sample surface. The overall surface is smooth. The

surface roughness is below 1μm. The arrow in Figure 3-12(a) shows the scratching direction. Figure 3-13(a) shows a close-up image taken by the SEM, the same area was also investigated by Zygo, shown in Figure 3-13(b). Figure 3-13(c) shows the surface profile along line 1, 2 and 3 in Figure 3-13(b). The marks left by the mold are clearly shown on the surface. Zygo image reveals the height of these mold marks is less than 1μm.

3.4.2 Topography after the 1st Scratch

Figure 3-12(c) shows the surface profile after the first scratching. For the glass fiber filled TPU with indentation depth of $\delta_n = 80\mu m$, a significant amount of surface damages are observed. These damages over the surface show a pattern of the alternating peak-valleys, with valley-valley distance of 60-190μm and average of about 120μm, which is about the same dimension as observed in Figure 3-9(c) for the unfilled TPU. However, the dimensions of single damage are larger than those in Figure 3-9(c). The surface roughness increases to about 2μm. The knife used in this test is the same one used in the tests on unfilled TPU samples and does not show change after the tests. Therefore, such change in the outlook of the damage should be mainly due to the difference of the materials.

Figure 3-14 shows the surface profile at a higher magnification by SEM and Zygo. The surface inspected by SEM and Zygo is the same surface as shown in Figure 3-13. The comparison between them provides the contrast about the dramatic topography change resulted from the first scratching test. It is noticed that surface topography change occurs mainly from plastic deformation, as indicated by the wrinkle-like surface profile changes shown in SEM micrographs (Figure 3-14(a)). The surface profile along Line 1 (in Figure 3-14(b)), which crosses one of such wrinkles, shows the dimension of the wrinkle is about 100μm in width, and the peak-valley height is about 4μm. The length of these wrinkles is less than the contact length of the knife with the material surface, implying local effects may influence the size of these plastic zones. At this stage, surface damage due to material rupture is not as obvious as in unfilled TPU in Figure 3-10. The SEM surface topography also shows a fiber-like inclusion being lifted partially out of the

surface after the first scratching, indicated by the rectangle in Figure 3-14(a). This site will be inspected after the 5th scratching.

Figure 3-14(a)

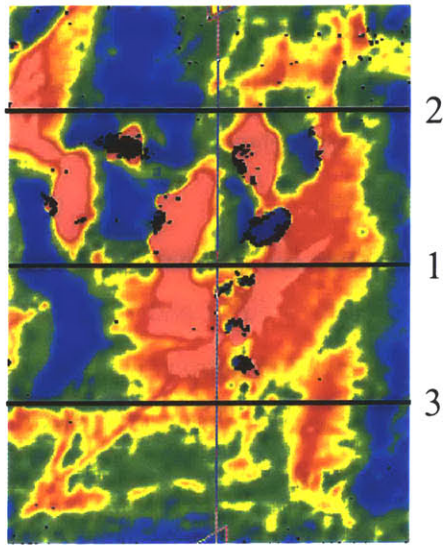

Figure 3-14(b)

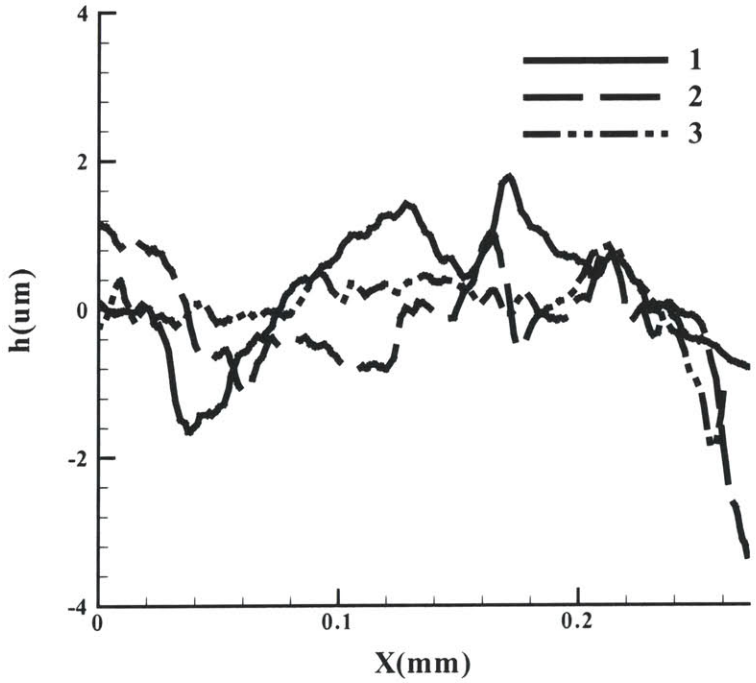

Figure 3-14(c)

Figure 3-14 Surface after the 1st scratching tests with $\delta_n = 80\mu m$: (a) SEM image; (b) Surface profile obtained by Zygo; (c) Surface roughness along line 1, 2 and 3 in (b). SEM and Zygo inspect the same area. The arrow in (a) indicates the scratching direction.

3.4.3 Topography after the 5th Scratch

Figure 3-12(e) shows the overall surface profile after the 5th scratching. These damages over the surface also show a pattern of alternating valley-peak form, with valley-valley distance of 60-190μm and average of about 120μm. The surface roughness increases to about 4-6μm. In comparison with Figure 3-12(c), surface damages increase in both number and dimension.

Figure 3-15 shows the surface profile at a higher magnification by SEM and Zygo. The surface inspected by SEM and Zygo is the same surface shown in Figure 3-14. It is noticed that the surface topography change occurs bimodally, as indicated by the wrinkle-like surface profile changes shown in SEM micrograph and the damages on it (Figure 3-15(a)). The wrinkles shown in Figure 3-14(a) still exist, but they also act to initiate subsequent damages in the form of material rupture. The surface profile along Line 1 (in Figure 3-15(b)) shows the dimension of the wrinkle is about 100μm in width, and the peak-valley height is about 4μm, implying no significant further development of the plastic zone. Surface damage due to material rupture is obvious in Figure 3-15(a). The dimensions of the damages Figure 3-15(a) are about 70μm in width, 100μm in length, and 2-4μm in depth.

It is also noticed that the surface showing features of an inclusion in Figure 3-14(a) after the first scratching changes into a fiber-like geometry in SEM, shown in Figure 3-16(a). Zygo inspection shows such a fiber-like geometry is a hole left by a fiber having been pulled out during the cyclic scratching. Figure 3-16(c) presents the profile of the site, showing the width of the hole is about 20μm and the depth is about 12μm, which are consistent with the dimensions of the fibers in this material. As it can be seen in Figure 3-15(a), the fiber pullout results in the TPU matrix material being stretched along the scratching direction.

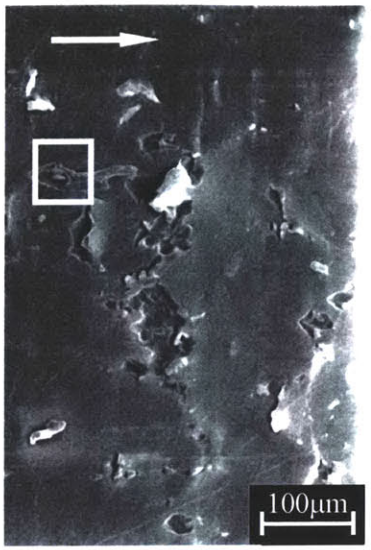

Figure 3-15(a)

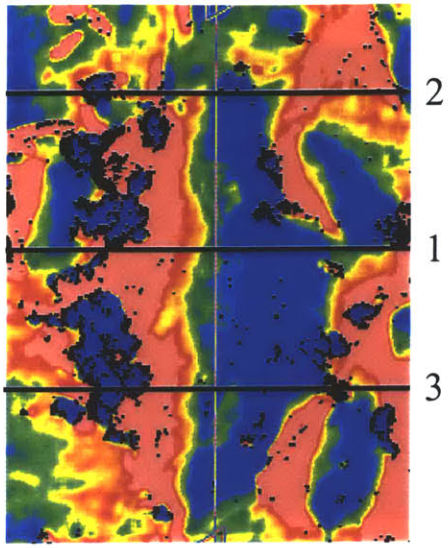

Figure 3-15(b)

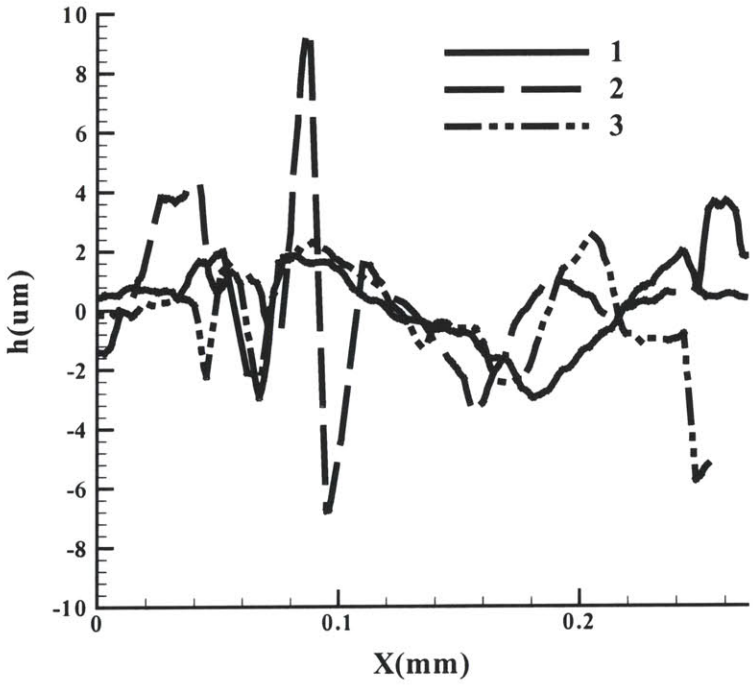

Figure 3-15(c)

Figure 3-15 Surface after the 5th scratching tests with $\delta_n = 80\mu m$: (a) SEM image; (b) Surface profile obtained by Zygo; (c) Surface roughness along line 1, line 2 and line 3 in (b). SEM and Zygo inspect the same area. The arrow in (a) indicates the scratching direction.

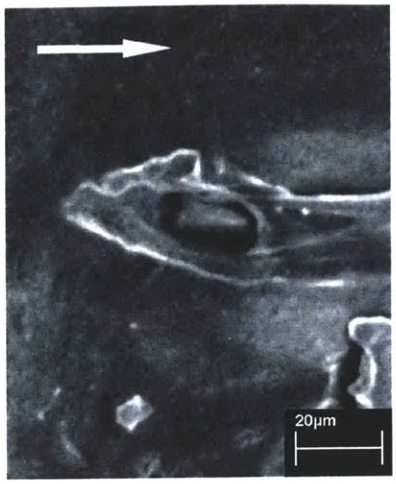

Figure 3-16(a)

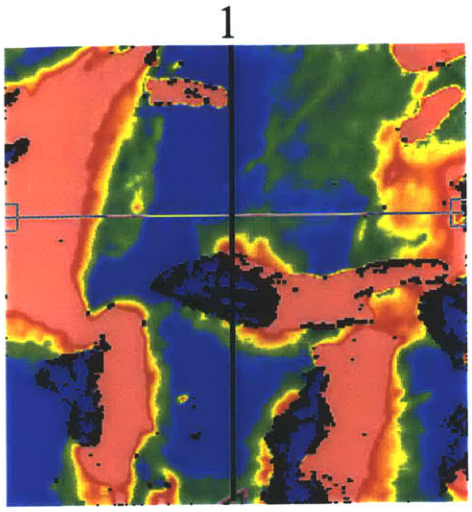

Figure 3-16(b)

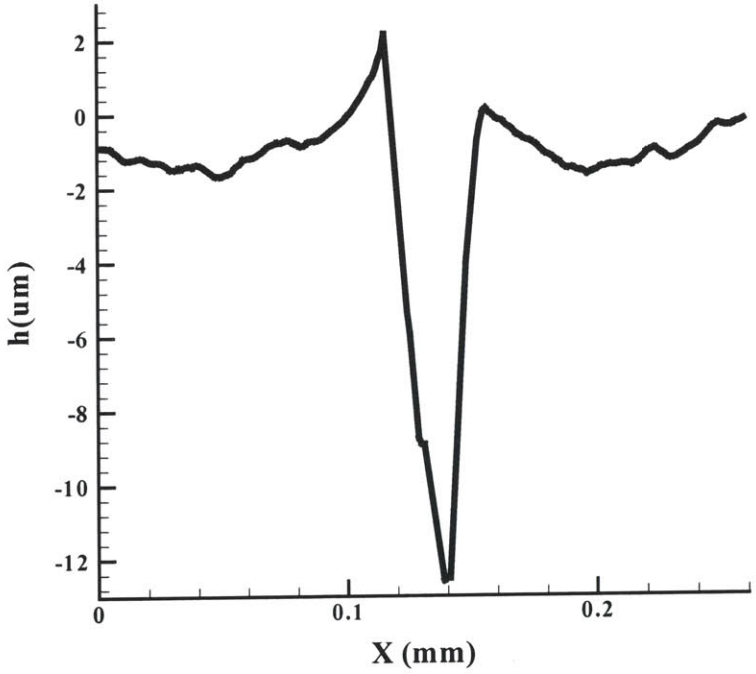

Figure 3-16(c)

Figure 3-16: A fiber was pulled out after the 5th scratching. (a) SEM image shows a fiber-like geometry; (b) Zygo image shows it is a hole left by a fiber being pulled out. (c) Surface profile along line 1 in (b). The arrow in (a) indicates the scratching direction.

3.4.4 Summary of Observations from δn=80μm Scratching Tests

Dramatic topography changes are observed from the tests with $\delta_n = 80\mu m$ on glass fiber filled TPUs. After the first scratching, the plastic deformation in the form of wrinkles

dominates the surface topography. The plastic deformation results in surface damages after the 5th scratching. The plastic deformation renders surface peak-valley patterns and provides the sites for the initiation of damages due to material rupture. Fiber pullouts are also observed after the 5th scratching.

In comparison with unfilled TPU, after the first scratching, the filled TPU shows surface features dominated by wrinkle-like plastic deformation, whereas unfilled TPU shows both wrinkle-like plastic deformation and rupture of the material. After the fifth scratching, both filled and unfilled TPU show both wrinkle-like plastic deformation and rupture of the material, but filled TPU shows larger plastic deformation and smaller rupture zone. The filled TPU seems not to show improved wear resistance over unfilled TPU. This observation is consistent with Parsons' macro-mechanical study[3-5] on filled TPU, where he found that the improved service life of seals using filled TPU was mainly due to prevention of particle ingestion and agglomeration and as soon as wear started, both filled and unfilled TPUs showed about the same wear rate.

3.5 Summary

Topography changes during the cyclic scratching tests with two distinct indentation depths on unfilled and glass fiber filled TPUs were studied using SEM and Zygo in this chapter.

For the test on unfilled TPU with $\delta_n = 50\mu m$, the topography changes were generally small in size. Some small features created during the cyclic scratching, such as small pits over the surface caused by small inclusion close to the surface, were simply removed during the scratching process. Wrinkle-like permanent deformation, which was susceptible to act as a precursor of surface damage, was observed after the 5th scratching. However, the dimension of this wrinkle-like permanent deformation was small. Therefore, for the test with indentation depth of 50μm, the development of abrasive patterns, if it was possible, would be a very slow process.

In contrast to the observations from the tests with $\delta_n = 50\mu m$, dramatic topography changes were observed from the tests with $\delta_n = 80\mu m$ on both unfilled and glass fiber filled TPUs. For unfilled TPUs, the surface topography changes occurred in two forms:

One was due to plastic deformations, whereas the other one was due to the rupture of the material. The plastic deformation rendered surface peak-valley patterns, whereas the rupture of the material due to extreme stretch caused material loss and occurred randomly over the surface but generally around the edge of the plastic zones. As the number of scratching cycles increased, the dimensions of both plastic zones and surface damages increased, accompanied by new damages generated after each scratching.

For glass fiber filled TPUs, dramatic topography changes were also observed from the tests with $\delta_n = 80\mu m$. After the first scratching, the plastic deformation in the form of wrinkles dominated the surface topography. These plastic deformations resulted in surface damages after the 5^{th} scratching. These results implied that the fiber filled TPU would wear at a similar or even faster rate than the unfilled TPU. Therefore, these results were consistent with Parsons macroscopic testing of seals, which indicated the role of the fibers in extending seal life was the prevention of particle ingestion as opposed to actual improvement/delay of material wear rate.

References

[3-1] LEO 435VP Operator Manual, LEO Electron Microscopy Ltd.

[3-2] NewView 5000 Operating Manual, OMP-0423E.

[3-3] Gent, A.N., Pulford, C.T.R., Mechanisms of Rubber Abrasion, J. Appl. Polym. Sci., vol 28, 943~960, 1983.

[3-4] Cadle, S.H., Williams, R.L., Gas and particle emissions from automobile tires in laboratory and field studies, Rubber Chem. Tech., vol.52, pp126~158.

[3-5] Parsons, E.M., Micromechanics of deformation and abrasive wear of fiber-filled elastomers, Master's thesis, Massachusetts Institute of Technology, 1999.

Chapter 4

Stress-Strain Behavior of Thermoplastic Polyurethanes

The large strain nonlinear stress-strain behavior of thermoplastic polyurethanes (TPUs) (also referred to as segmented polyurethane elastomers) exhibits strong hysteresis, rate dependence and cyclic softening. Proper modeling of the multiaxial stress-strain behavior of the material within a large strain continuum mechanics framework is important in the simulation of boundary value problems involving inhomogeneous deformation. In this chapter, a constitutive model capturing the major features of the stress-strain behavior of TPUs is developed. The first section of this chapter introduces TPUs and describes basic morphological features of the material. The second section describes various rate and loading history dependence of the stress-strain behavior of TPUs through a series of uniaxial compression tests. The third section presents a constitutive model for the observed stress-strain behavior of TPUs. In the fourth section, a systematic method to estimate the material parameters for the model is presented. The fifth section presents numerical simulations of the uniaxial compression tests using the new model. Finally, future work on constitutive modeling is discussed.

4.1 Introduction: Thermoplastic Polyurethanes (TPUs)

The first commercial thermoplastic polyurethanes (TPUs) were well established in Germany by Bayer-Fabenfabriken and in the U.S. by B.F. Goodrich in the 1950s[4-1]. The Alliance for the Polyurethane Industry (API) describes TPUs as "bridging the gap between rubber and plastics", since TPUs offer the mechanical performance characteristics of rubber but can be processed as thermoplastics. This special niche of TPUs among other polymers and elastomers imparts TPUs high elasticity, high resilience, and high abrasion resistance, and results in wide applications of TPUs ranging from ski boots and footwear to gaskets, hoses, and seals.

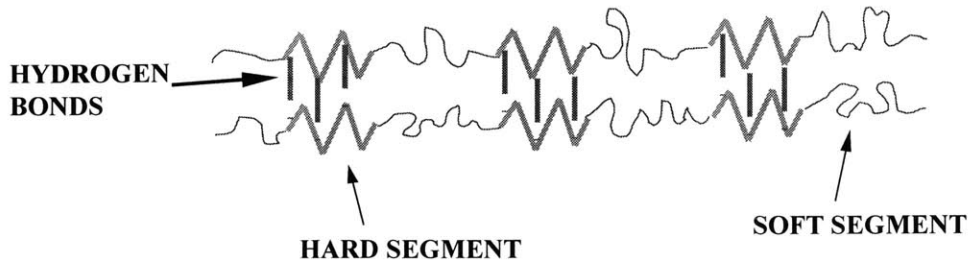

Figure 4-1(c)

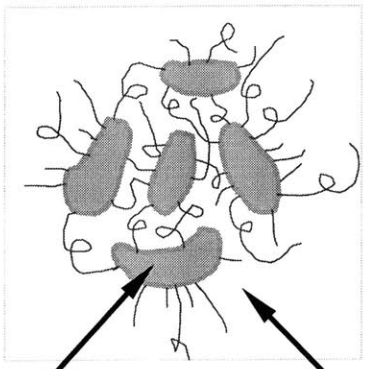

Figure 4-1(b)

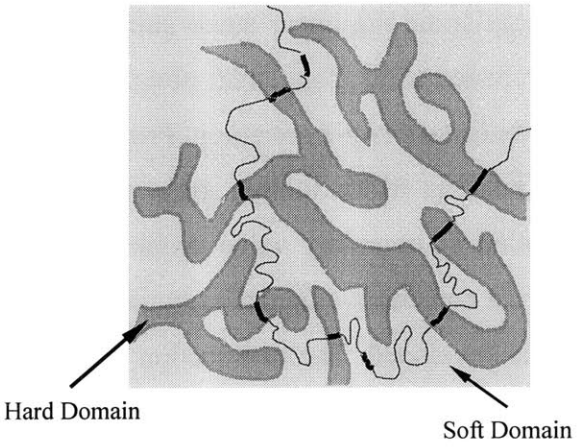

Figure 4-1(c)

Figure 4-1: (a) The alternating -A-B-A-B- structure of TPUs; Hard domains and soft domains of TPUs with (b) a low hard segment content; (c) a high hard segment content[4-2].

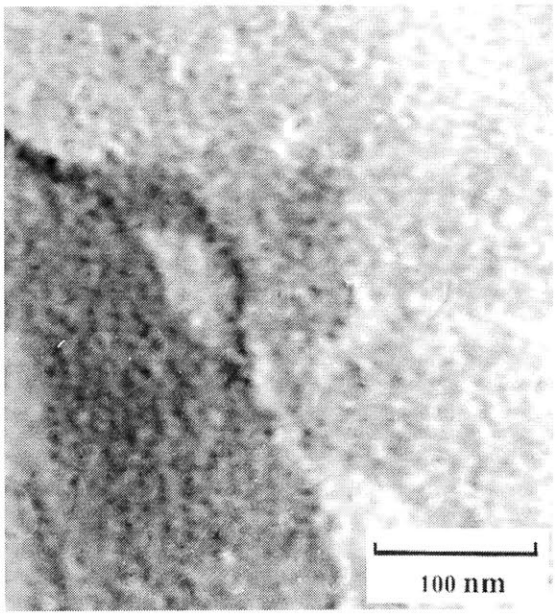

Figure 4-2: Transmission Electron Microscope (TEM) image of TPU (57% soft segment and 43% hard segment). The bright color regions are hard domains and the dark color

regions are soft domains.

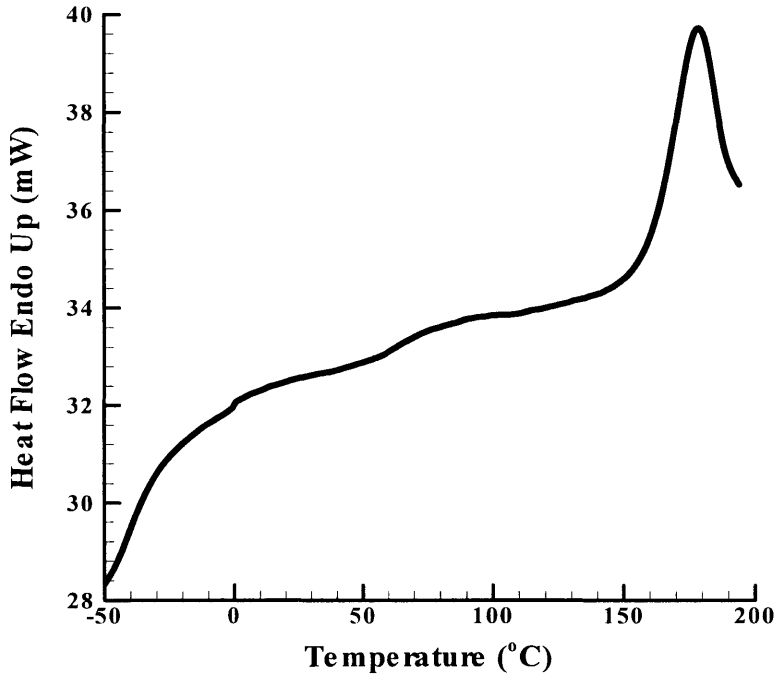

Figure 4-3: DSC test of the TPU used in this study.

Thermoplastic polyurethanes are block copolymers with urethane backbone linkage composed of hard and soft segments, forming an alternating -A-B-A-B- structure (Figure 4-1(a)). The hard segments are polymer blocks from the reaction of a diisocyanate and a short chain diol, whilst the soft segments are either polyesther or polyester oligomeric diol blocks with molecular weights ranging from 400 to 6000, where the molecular weight of 1000~2000 are exclusively used[4-2]. The molecular weight for hard segments is proportional to the molecular weight of soft segments[4-2]. Generally, phase separation occurs in most TPUs due to the intrinsic incompatibility between the hard segments and soft segments: the hard segments, composed of polar materials, can form carbonyl to amino hydrogen bonds and thus tend to cluster or aggregate to ordered hard domains, whereas the soft segments form amorphous domains. Such a phase separation, however, is often incomplete, i.e., some of the hard segments are isolated in the soft domains as illustrated schematically in Figure 4-1(c). In many TPUs, the hard domains are immersed in a rubbery soft segment matrix[4-2][4-3]. Depending on the fraction of hard segments, the morphology of hard domain changes from isolated domains with a lower hard

segment content (Figure4-1(b)) to interconnected domains with a higher hard segment content (Figure4-1(c))[4-2][4-4]. The interconnected domain structure is verified for the TPU sample used in this research by TEM (Transmission Electron Microscope) in Figure 4-2, and DSC (Differential Scanning Calorimeter) test in Figure 4-3. The sample for the TEM was microtomed at -100°C to a thickness of about 50nm, then exposed in osmium tetroxide (OsO_4) vapor for about 4 hours. Since the soft domain has a larger inter-molecular space, the OsO_4 molecules tend to reside in the soft domain, rendering the soft domain a dark color in the TEM image. The domain size in Figure 4-2 is 10~20nm, which is consistent with other observations on various types of TPUs (e.g., [4-5][4-6][4-7]). For instance, Koutsky et al. [4-7] observed domain size of 3nm~10nm for a polyester based polyurethane and 5nm~10nm for a polyether based polyurethane; Chen-Tsai et al.[4-8] observed a size of hard domains to be about 11nm and the inter-domain distance of 13nm for a PBD/TDI/BD based polyurethane. The DSC test was conducted over the temperature range from -70 °C to 200 °C. The two distinct changes of the slopes in the curve (Figure 4-3) correspond to two transition temperatures, verifying the two-phase structure of TPUs. The first transition temperature (about -40°C) marks the change of soft domain from glassy state to rubbery state, while the second transition temperature (about 70°C) represents the thermal dissociations of hydrogen bonds.

The presence of hard domain in segmented polyurethane is very important to the mechanical properties. In segmented polyurethanes, hard domains play the role of physical crosslinks, playing a role similar to crosslinks in vulcanizates and imparting the material's elastomeric behavior. Since hard domains also occupy significant volume and are stiffer than soft domains, they also function as effective nanoscale fillers and render a material behavior similar to that of a composite. At room temperature, the soft domain is above its glass transition temperature and imparts the material its capability of rubber-like behavior; the hard domain is below its glassy or melt transition temperature and is thought to govern the hysteresis, permanent deformation, high modulus, and tensile strength. Generally, TPUs have high tear strength, toughness, abrasion resistance, and resistance to polar solvents[4-9][4-10].

A wide variety of property combinations can be achieved by varying the molecular weight of the hard and soft segments, their ratio, and chemical type. For instance, shore

hardness ranging from 60A to 80D can be achieved. At present, thermoplastic polyurethanes are an important group of polyurethane products because of their advantage in abrasion and chemical resistance, excellent mechanical properties, blood and tissue compatibility, and structural versatility.

4.2 Stress-Strain Behavior of Thermoplastic Polyurethane

The stress-strain behavior of TPUs demonstrates strong hysteresis, rate dependence, and cyclic softening effects. In this section, a series of uniaxial compression tests were conducted to identify these features.

4.2.1 Test Descriptions

Uniaxial compression tests were conducted using a computer controlled servo-hydraulic uniaxial compression test machine, Instron model 1350. The sample material is thermoplastic polyurethane supplied by Caterpillar, Inc. with durometer hardness value of 92A immediately after production and about 94A after 1 year shelf life at room temperature. Sheets of the material of about 3mm in thickness were cut into cylinders of about 12mm diameter using a die cutter. To eliminate potential buckling, the sample height to diameter ratio should be less than 1; and also the height to diameter ratio should be at least 0.5 to reduce any effects from barreling due to the frictional interaction with the compression platens of the testing machine. Therefore, two cylinders were stacked to form one sample for a test. Teflon sheets were placed between the sample and the fixtures to reduce the friction.

The specimens were subjected to constant true strain rate loading-unloading cycles and the true stress vs. true strain curve was documented for each test. The true strain is defined as the logarithm of the compression ratio determined as the current height over the initial height, where the current height of the sample is monitored during testing using an extensometer. Height measurements are used to form a feedback loop with the actuator to precisely define and control the displacement history such that constant strain true rate conditions are achieved. The true stress is defined as the compression force divided by the current cross-sectional area of the sample; the current area is computed using the height measurement and assuming the material to be incompressible. Such

assumption on the material compressibility is reasonable for elastomeric materials since this type of material demonstrates very little volume change during axial deformation.

TPU samples exhibit a certain amount of permanent set after each loading-unloading cycle. The dimensions (diameter and height) of the samples were measured after each loading-unloading cycle to ensure that the true stress-true strain curves always started from the new unloaded specimen height for each cycle. The measurement of the dimensions took about 2~3 minutes, including re-positioning the sample on the compression platen and replacing the Teflon sheets whenever necessary.

4.2.2 Hysteresis

Figure 4-4 shows the true stress-true strain curves from two uniaxial compression tests on two fresh samples loaded to two different maximum strains, i.e. $\varepsilon_{max} = 0.5$ and $\varepsilon_{max} = 1.0$, respectively. The loading curves show an initially stiff response, followed by rollover at a strain of about 0.15, and stiffen again after a strain of 0.70. The unloading paths show a large hysteresis loop. Additional recovery occurs with time after unloading. The residual strains were measured approximately 1 minute after the tests and were found to be $\varepsilon^r = 0.02$ for the $\varepsilon_{max} = 0.5$ test, and $\varepsilon^r = 0.062$ for the $\varepsilon_{max} = 1.0$ test.

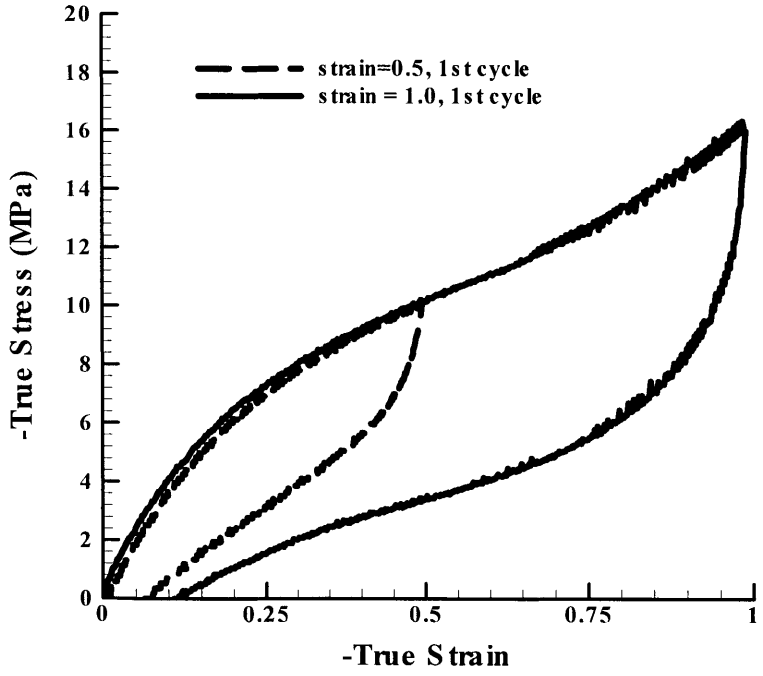

Figure 4-4: Uniaxial compression tests on fresh sample at strain rate $\dot{\varepsilon} = 0.01/s$, to different maximum strains ($\varepsilon_{max} = 0.5$ and $\varepsilon_{max} = 1.0$, respectively).

4.2.3 Rate-Dependence

Figure 4-5 shows the true stress-true strain curves to $\varepsilon_{max} = 1.0$ at three different strain rates, i.e. $\dot{\varepsilon}_1 = 0.01/s$, $\dot{\varepsilon}_2 = 0.05/s$, and $\dot{\varepsilon}_3 = 0.1/s$. For the loading portions of the curves, the higher the strain rate, the larger the stress. The unloading curves from different strain rate tests are about the same, suggesting that unloading behavior has less rate dependence than loading behavior. The residual strains were measured to be $\varepsilon^r = 0.062$ for the $\dot{\varepsilon}_1 = 0.01/s$ test, $\varepsilon^r = 0.046$ for the $\dot{\varepsilon}_2 = 0.05/s$ test, and $\varepsilon^r = 0.043$ for the $\dot{\varepsilon}_2 = 0.1/s$ test.

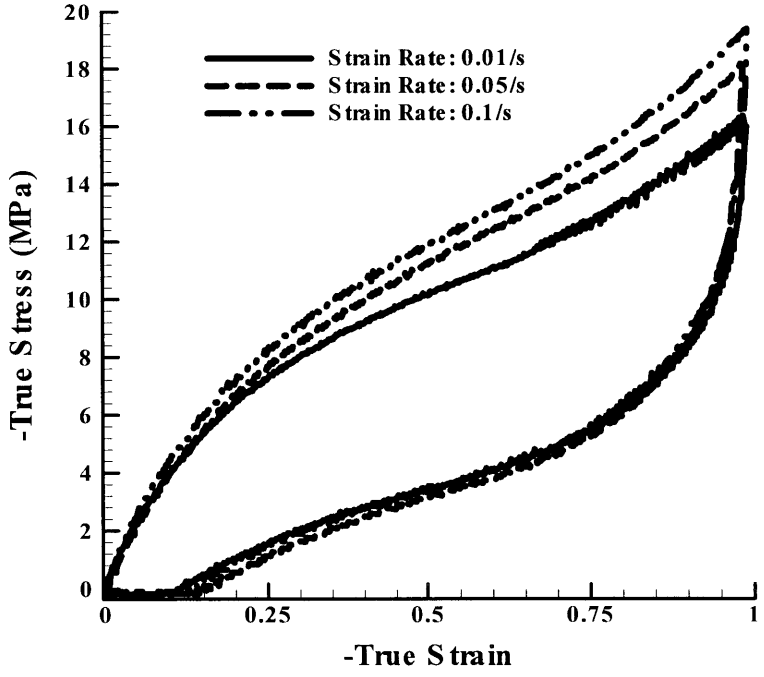

Figure 4-5: Uniaxial compression tests at three different strain rates.

During the process of loading and unloading, if the test is suspended, relaxation either in stress (stress relaxation when the strain is held constant) or in strain (creep when the stress is held constant) will be observed for TPUs. Stress relaxation tests were conducted during the course of loading-unloading cycles where the sample was compressed to a maximum strain of 1.0 at a strain rate of 0.1/s with intermittently pausing compression

for 60s at strains of 0.2, 0.4, 0.6 and 0.8 during both loading and unloading. Figure 4-6(a) shows the applied strain history. Figure 4-6(b) shows the corresponding true stress-time curve for the test on a fresh sample. During each hold period, the largest amount of stress relaxation occurs in 5~10s. The material time constant is thus determined to be about 2~5 seconds. During loading, the stress is observed to decrease during the strain hold period; whilst during unloading, the stress is observed to increase during the strain holding period. This behavior is a characteristic of the time dependent behavior of elastomeric materials. (see, for example, Bergstrom and Boyce[4-11], and Lion[4-12])

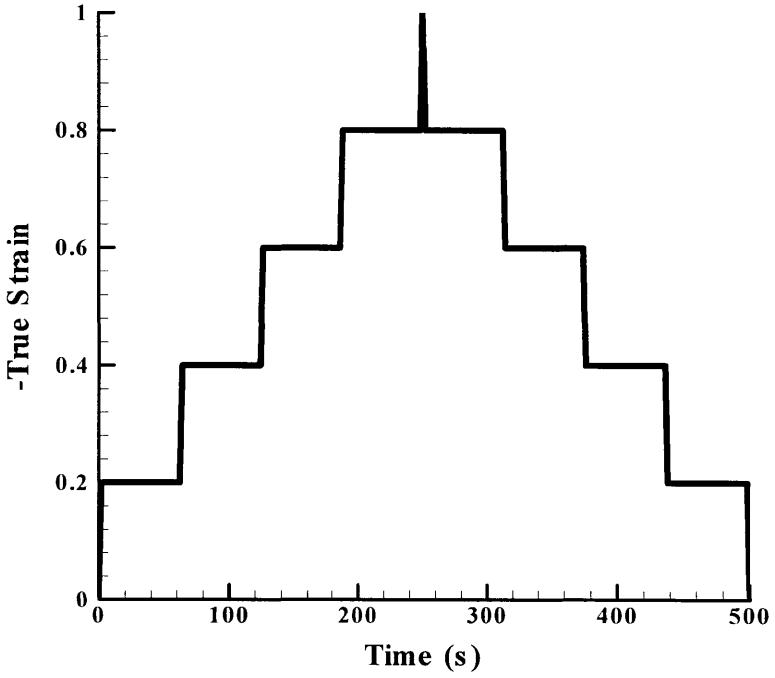

Figure 4-6(a)

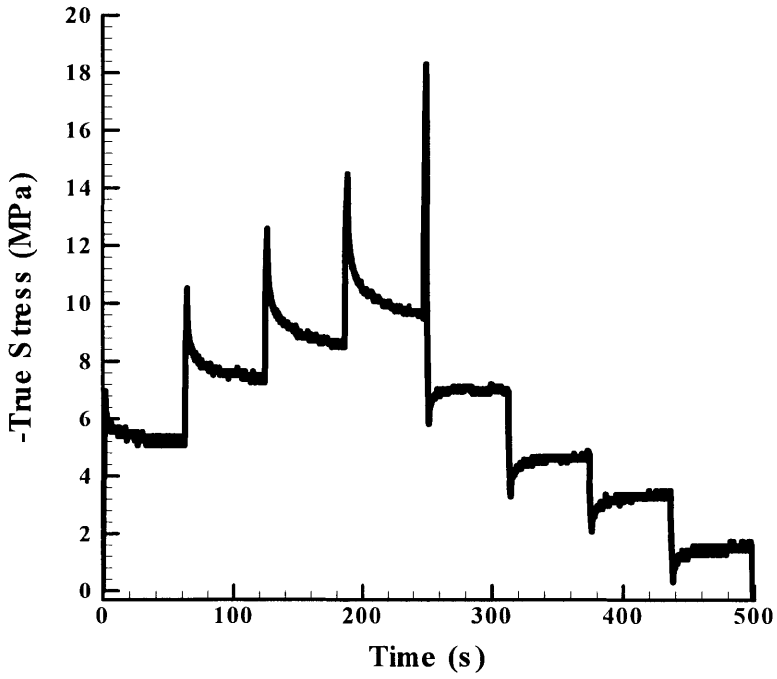

Figure 4-6(b)

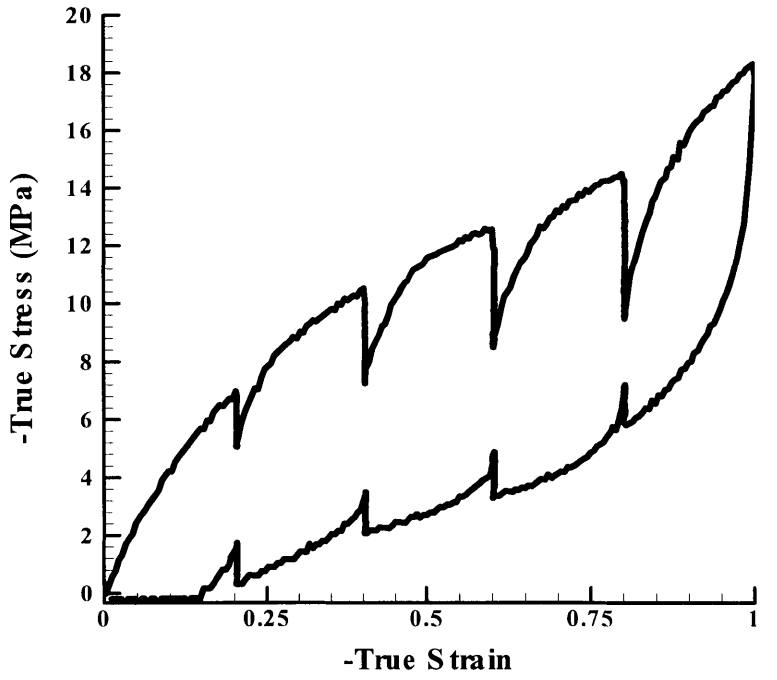

Figure 4-6(c)

Figure 4-6: (a) Schematics of loading history for stress relaxation tests; (b) True-stress vs. time curves for uniaxial compression test with a number of intermittently stops. (c) True-stress vs. time curves for the same test.

4.2.4 Cyclic Softening

Figure 4-7 shows the true stress-true strain curves from the cyclic loading-unloading tests with $\varepsilon_{max} = 1.0$ and $\dot{\varepsilon} = 0.01/s$. Several features are observed. First, in cyclic tests, strain-induced softening is observed after the first cycle, most obvious in the 2nd cycle test, as demonstrated by the large decrease in stress level for any given strain from the 1st cycle test to the 2nd cycle test shown in Figure 4-7. Second, the cyclic softening effect is reduced, or the stress tends to stabilize, after a few cycles. In other words, the stress difference between the 2nd cycle and the 4th cycle is much smaller than the difference between the 1st and the 2nd cycle tests. Third, the cyclic strain softening effect is significant in the middle range of the strain, and as the strain upon reloading approaches the maximum strain, the stress tends to approach the stress level of the 1st cycle. Fourth, the unloading paths after given strains all follow the same curve, independent of cycle number. Last, the residual strain occurs predominately for the first cycle test, and no significant height changes were observed from the tests after the 1st test. In the rest of this chapter, the test whereupon the stress does not show significant decrease from previous cycles will be referred as the stabilized test, e.g. in the current tests, the 4th test is the stabilized test.

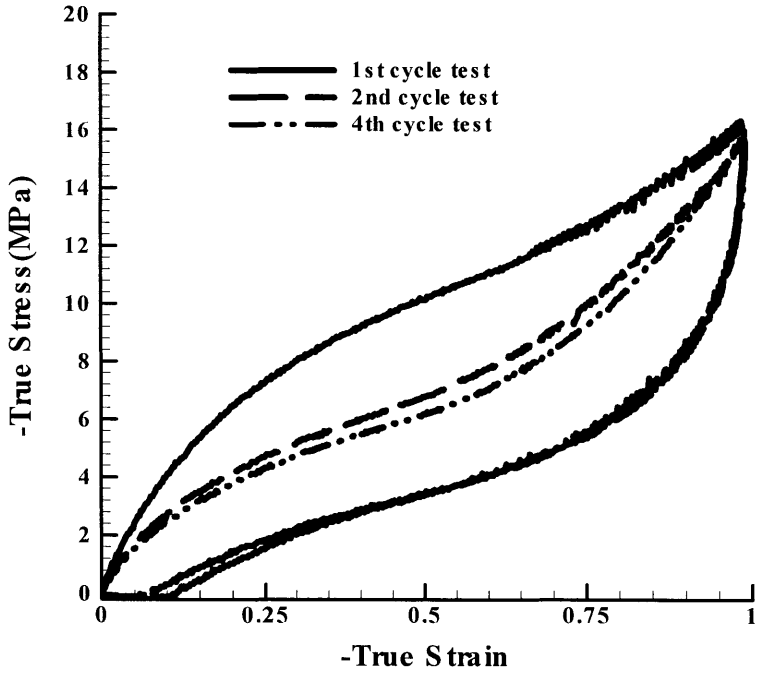

Figure 4-7: Cyclic uniaxial compression tests at strain rate $\dot{\varepsilon} = 0.01/s$.

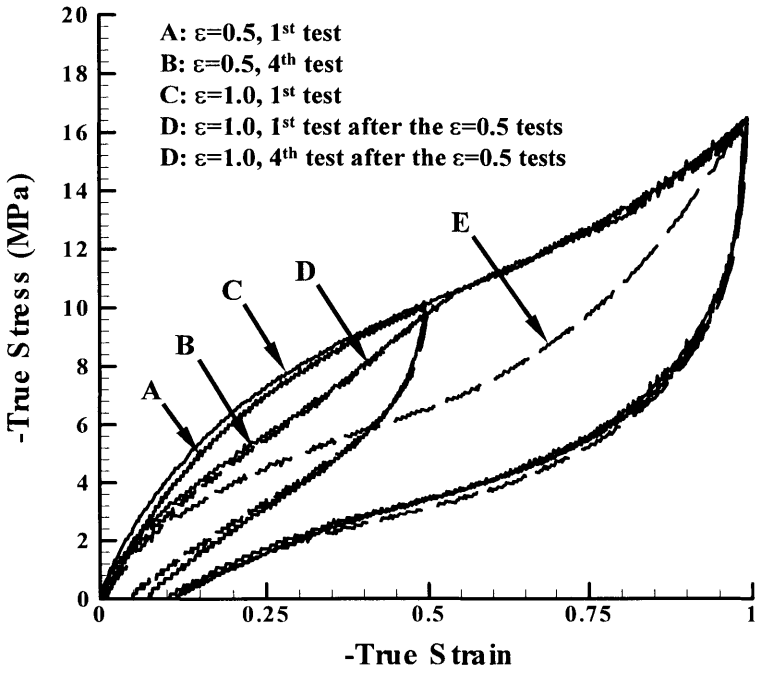

Figure 4-8: Uniaxial compression tests with cyclic loading to different maximum strains. The strain rate is $\dot{\varepsilon} = 0.01/s$

The cyclic softening was further explored by tests with cyclic strain to different maximum levels. Two uniaxial compression tests with $\varepsilon_{max} = 0.5$ and $\varepsilon_{max} = 1.0$ were conducted on two fresh samples, respectively. The true stress-true strain curves shown earlier in Figure 4-4 are repeated in Figure 4-8. The sample strained to $\varepsilon_{max} = 0.5$ was then subjected to cyclic loading-unloading with $\varepsilon_{max} = 0.5$. The true stress-true strain curves tend to stabilize after the 4th cycle, as shown in Figure 4-8. This sample was then tested with $\varepsilon_{max} = 1.0$. As illustrated in Figure 4-8, upon straining to $\varepsilon_{max} = 1.0$ after a previous excursion to $\varepsilon_{max} = 0.5$, the true stress-true strain curve for $\varepsilon < 0.5$ moves along the previously stabilized softened curve; as the strain approaches 0.5, the stress approaches the previous maximum stress. After $\varepsilon = 0.5$, the true stress-true strain curve follows the course shown by the fresh sample test with $\varepsilon_{max} = 1.0$, and the material exhibits the same behavior as the fresh material. The cyclic tests with $\varepsilon_{max} = 1.0$ result in the stress-strain behavior being softened to the new stabilized curve as defined by

$\varepsilon_{max} = 1.0$ cycle tests on the fresh sample. These variations in the stress-strain behavior of the material demonstrate the strong dependence of the material behavior on the strain history.

The softening with strain history is often observed in unfilled and filled rubbers, and is referred as the Mullin's effect ([4-13][4-14][4-15][4-16]). A similar phenomenon has also been observed in thermoplastic vulcanizates[4-17][4-18] and segmented polyurethanes[4-19]. Typically, the uniaxial stress-strain curve remains unchanged at strain levels above the previous maximum strain, but experiences a substantial softening below this maximum strain. The higher the previously attained maximum strain, the greater the subsequent loss of stiffness. Almost all of the loss in stiffness takes place during the first deformation cycle and steady-state response is attained in very few cycles.

4.2.5 Equilibrium Paths

In the stress relaxation tests, the stress relaxes towards an equilibrium state during the holding periods (Figure 4-6(b)(c) and 4-9(a)(b)). Bergstrom and Boyce have demonstrated this equilibrium state is independent of the strain rate and only depends on the current state of strain and loading history[4-14]. Figure 4-9 shows the stress relaxation during the 1st cycle and the 4th cycle tests after cycling between strains of 0.0 and 1.0. In these tests, depending on which cycle number, the stress tends to stabilize at two distinct equilibrium paths after 60 seconds relaxation for the fresh sample and the cycled sample. Further strain relaxation can be expected if the relaxation time is longer, but the difference between the two stabilized values is so significant that simply accounting for such a difference as the result of insufficient idling time is unrealistic. The relaxed value at any strain depends upon the maximum strain the material has experienced on its prior loading history. During unloading the increase in stress at each hold period is the same for both the 1st cycle and the 4th cycle tests since both have been strained to a strain of 1.0. The stress difference between the stabilized stress at loading and unloading holding periods are fairly small for the 4th cycle test. These observations strongly imply that the unloading stress and the loading stress (except the 1st loading) converge to the same equilibrium path but this path depends on the maximum strain experienced on the loading history. Precisely determining the equilibrium paths for the 1st

cycle test and the stabilized test, however, is difficult because of ambiguity in the concept of "long enough time for relaxation". For the first loading, equilibrium paths were determined by finding the point where another 10% stress relaxation would occur at the same strain. The equilibrium path for the relaxation tests on a previously loaded sample is determined by simply finding the midpoint of the points of the same strains on the loading and the unloading paths of the stabilized test (the 4^{th} cycle test), assuming that the set points under the same strain would converge at their middle points if given infinite time.

Comparing the simple monotonic loading-unloading cyclic tests with $\varepsilon_{max} = 0.5$ (Figure 4-8), we conclude that the stabilized equilibrium path with $\varepsilon_{max} = 0.5$ must be stiffer than the stabilized equilibrium path determined from the test with $\varepsilon_{max} = 1.0$, since the unloading curve in Figure 4-8 shows a stiffer response than the stabilized equilibrium path determined by the relaxation test with $\varepsilon_{max} = 1.0$. Therefore, the degree of softening of the stabilized equilibrium path increases with the increase in the prior maximum strain experienced during the overall loading history.

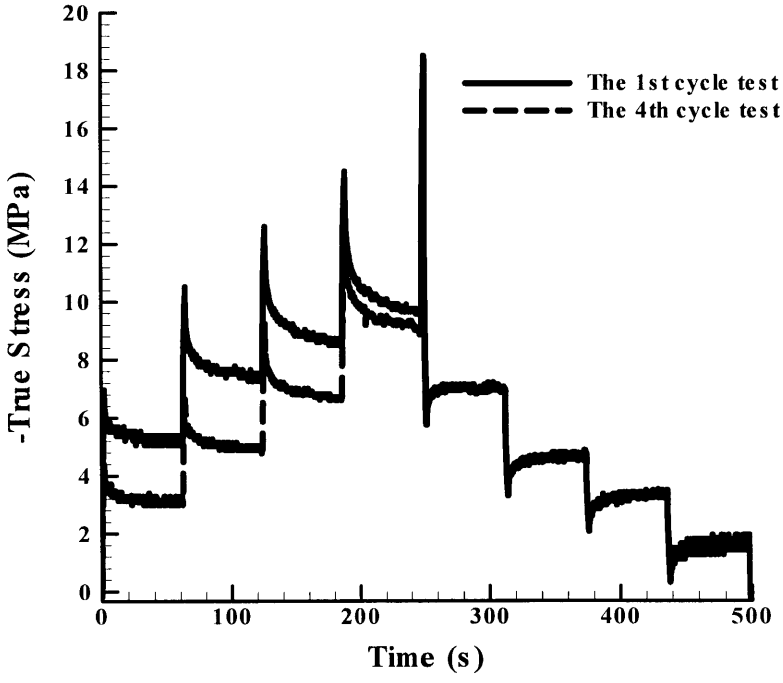

Figure 4-9(a)

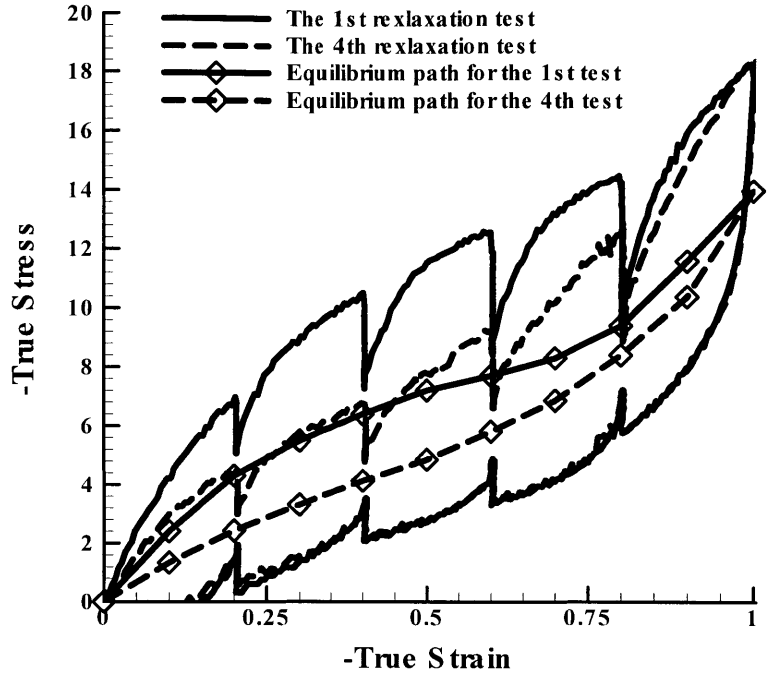

Figure 4-9(b)

Figure 4-9: Uniaxial compression test with a number of intermittently stops, (a) true-stress vs. time curves, and (b) true-stress vs. true-strain curves and the equilibrium path.

4.3 Constitutive Model for Thermoplastic Polyurethane

4.3.1 A review

A constitutive model for the large strain deformation of TPUs should address the three salient features of the material behavior: 1. Nonlinear large strain elastomeric behavior; 2.Rate dependence; 3.Softening of the equilibrium paths during cyclic tests.

The experimental data indicates that the stress-strain behavior can be decomposed into a time-independent equilibrium path and a time-dependent departure from the equilibrium path, as illustrated in Figure 4-10. The constitutive model developed by Boyce et al[4-20] for the stress-strain behavior of thermoplastic vulcanizates (TPVs) is used here as a starting point of the new constitutive model. The equilibrium part of the stress-strain behavior acts as the backbone of the overall material stress-strain behavior and originates from the entropy change of long molecular chains in the amorphous soft

domain due to orientation of molecular network with deformation. The rate-dependent part is taken to originate from the concomitant internal energy change due to elastic deformation of the hard domains as well as their visco-plastic deformation. The viscoplastic response tends to relax the elastic deformation and hence produces the relaxation of the stress-strain behavior to the equilibrium behavior with time. As the strain rate approaches an infinitesimal value, the hard domain elastic deformation will be fully relaxed and the deviation from the equilibrium path will diminish. The viscoplastic behavior comes from energy dissipation sources; potential sources include plastic slip in hard domains, the breakage of hydrogen bonds in the hard domain, the frictional behavior as two hard domains pass each other, and the interaction between soft and hard domains. In this paper, all of these energy dissipation behaviors are lumped into a single viscoplastic constitutive element.

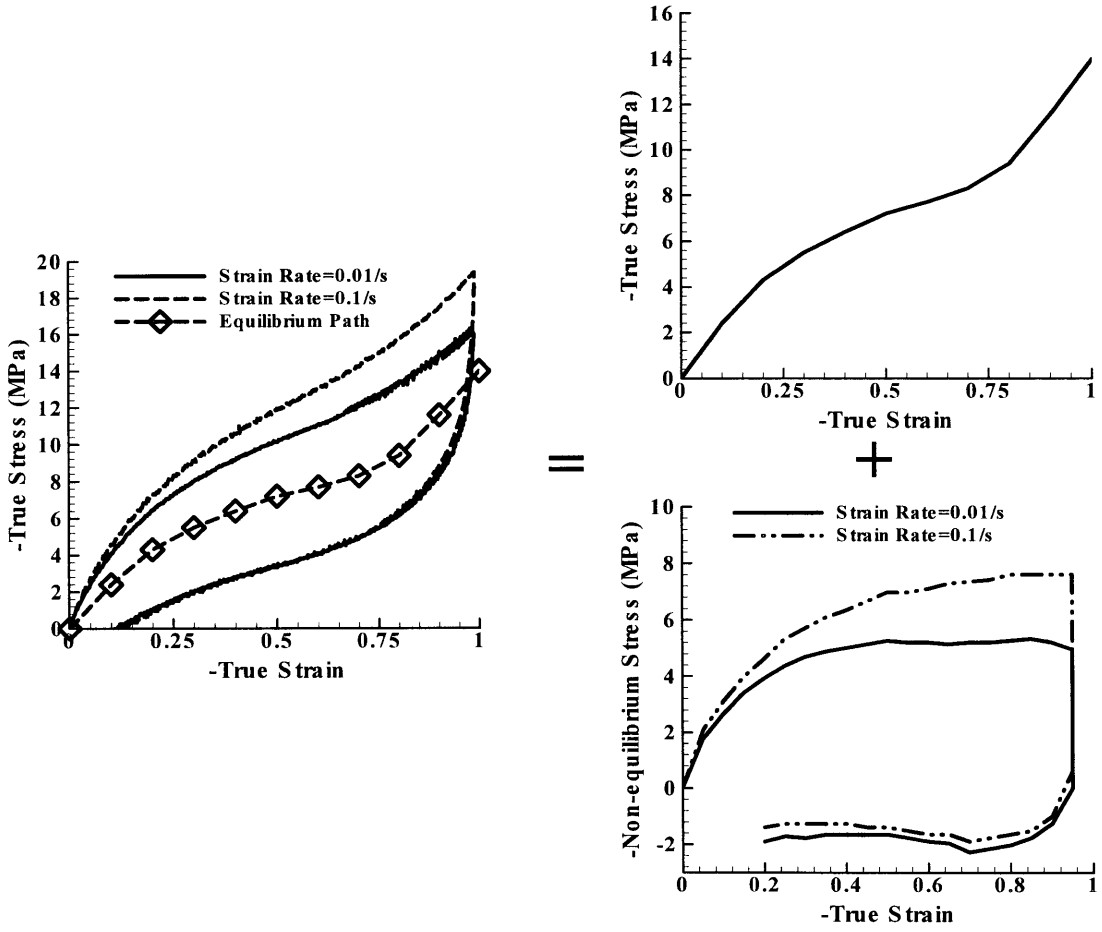

Figure 4-10: Decomposition of material behavior into a rate-independent equilibrium part and a rate dependent part.

Within this framework of decomposition of material behavior into an equilibrium component and a rate dependent deviation from equilibrium, we attribute the cyclic softening behavior to be due to the softening of the equilibrium path. In rubbery material, the softening of the equilibrium path is called "Mullins' Effect", so named due to the comprehensive study of this behavior by Mullins observed in unfilled and filled rubbers during the 1950s and the 1960s ([4-13] and [4-21]~[4-24]). The advantage of the addition of reinforcing filler into rubber is the increase in the stiffness and strength of the vulcanizate. This increase, however, is reduced and may be substantially destroyed by deformation. The attempts to understand this softening behavior date back to the 1950s. Although Mullins identified cyclic softening to occur in both unfilled and filled elastomers, its effect is far more pronounced in filled elastomers and therefore generally it is identified to be a filled elastomer phenomenon. At present, most of the theories are based on essentially two explanations. The first theory originates from Blanchard and Parkinson[4-25] and Bueche[4-26][4-15], who considered the increase in stiffness produced by fillers to be a result of rubber-filler attachment providing additional restrictions in the crosslinked rubber network. They attributed the softening to the breakdown or loosening of some of these attachments. Bueche[4-26][4-15], Dannenberg[4-27], and Rigbi[4-28] generalized the softening to be a result of strain-induced relative motion of carbon and rubber, and in some cases local separation of carbon black particles and rubber. Simo[4-29], Govindjee and Simo[4-16][4-30], and Miehe and Keck[4-31], Lion[4-12][4-32] extended Bueche's idea and developed damage based constitutive models to simulate the material behavior within the framework of large strain continuum mechanics. Ogden and Roxburgh[4-33][4-34], and Dorfmann and Ogden[4-35] developed a phenomenological model using a damage function without considering the underlying physical structure of the material. The second theory is due to Mullins, Tobin, Harwood, and Payne[4-13][4-21][4-22][4-23], who treated filled rubbers as a composite system and proposed the concept of amplified strain. In filled elastomers, due to the existence of stiffer fillers, usually carbon black, the strain, or stretch, is magnified by an amplification factor of X due to the amplification of the strain in the elastomer domains needed to accommodate the applied strain because of the very low strain in the stiffer filler domains. For uniaxial tension loading, the amplified material

stretch is $\Lambda = 1 + X(\lambda - 1)$. X generally has the form of

$$X = 1 + 2.5v_f + 14.1v_f^2, \qquad (4.1)$$

and for dilute solution, $X \approx 1 + 2.5v_f$. These researchers proposed that the cyclic strain softening was a property of the unfilled vulcanizate and was magnified through the amplified strain for filled rubbers. They further related strain softening to be a result of quasi-irreversible rearrangement of molecular networks due to localized nonaffine deformation resulting from short chains reaching the limit of their extensibility. This nonaffine deformation resulted in a displacement of the network junctions from their initial state, which thus produced some form of rearrangements of hard and soft domains in the elastomeric phase with strain, acting to increase the effective volume fraction of soft domain.

As demonstrated in the previous section, segmented polyurethanes also show a cyclic softening behavior. Trick[4-19] first reported the softening in segmented polyurethane. It is generally believed the domain structure of segmented polyurethane is responsible for the softening, the hysteresis behaviors and corresponding energy dissipation. Replacing physical crosslinks in segmented polyurethanes by disrupting the hard domain structure and forming chemical crosslinks was shown to reduce the softening and hysteresis; however, this also resulted in a loss in modulus and tensile strength[4-36]. A number of experimental studies were conducted to investigate the relationship between mechanical properties and material morphology ([4-37]~[4-47]). Bonart and coworkers[4-37][4-38][4-39] first systematically studied the morphology change during deformation using X-Ray scattering. They and, more recently, Yeh et. al.[4-46] using both SAXS and WAXD found that stress was not homogeneously distributed in the soft domains during deformation, and consequently, the stress distribution in soft domains around each hard domain could lead to a torque to rotate the hard domains and to minimize the local stress. They also found that at large stretch, the hard domain would break down to further accommodate stretch. For segmented polyurethanes with higher concentrations, the interconnected hard domains had profound influence on the softening and hysteresis. Sequela and Prudhomme[4-48] in their study on tri-block copolymer and Sung et al[4-42] in their study on polyurethaneureas found that polymers with less interconnected hard

domains showed reduced softening and hysteresis. Coopers and coworkers[4-4] found that, during tensile deformations, the hard domains were moved into a position where their longer dimensions were predominantly oriented perpendicular to the stretching directions, i.e., a configuration where the hard domains appeared to align perpendicular to the applied stress. To achieve the high degree of hard block orientation, it was necessary that the irregularly shaped hard domain underwent plastic deformation. Such process was accompanied by the breakage and reformation of hydrogen bonds in hard domain. At sufficiently high strains, hard domains might break into smaller units[4-4].

Based on the concept of amplified strain, Mullins and Tobin[4-24] in their very early work suggested that the softening in filled rubber was due to the decrease of volume fraction of hard domain, v_f, as a result of conversion of hard domain to soft domain. However, this idea seems to be abandoned in later work of others, probably because of the vagueness in the definition of these hard domains and soft domains in rubber vulcanizates and how the conversion occurs. The concept of phase transition has been used by Wineman and coworkers[4-49][4-50], and Beatty and coworkers[4-51][4-52][4-53] to develop constitutive models to study stress softening. However, the mechanism for the stress softening is not clear in these models. Recently, a series of micro-mechanics study on filled elastomers and filled polymers were conducted by Boyce and coworkers[4-54][4-55][4-17][4-18]. Bergstrom and Boyce[4-54] revealed that for randomly distributed filled particles, some of the rubber became trapped among hard particles and could not deform, thus resulting in the effective fraction of stiff particles to be larger than the physical fraction, so named "occluded volume" effect postulated by these workers and others [4-56] in filled elastomers. In the study of cyclic softening in thermoplastic vulcanizate, where the vulcanizates are the fillers, Boyce et al[4-17][4-18] showed that the cyclic softening is due to the gradual evolution in particle/matrix configuration during previous loading cycles. The plastic deformation of the contiguous thermoplastic phase acted to "release" vulcanizate particles creating a pseudo-continuous vulcanizate phase and thus a softer response during subsequent cycles. Although the material in the latter is a system of soft fillers/hard matrix, opposite to filled rubbers and TPUs, which are hard fillers/soft matrix, their research does enlighten the evolution of the filler/matrix structure and their relative configuration in filled rubbers and TPUs.

In this chapter, inspired by the experimental observations of Bonart[4-37][4-38][4-39], Cooper[4-4][4-36], and Sung[4-40][4-41][4-42], and theoretical analysis of Boyce and coworkers, we continued Mullins' early idea, and propose a constitutive model where the softening of the equilibrium path is due to evolution of the effective volume fraction of the soft domain during the deformation process, upon which the occluded soft material is released to carry load due to the relative motions and deformation of hard domains.

4.3.2 Constitutive Model Description

The model requires three constitutive elements, illustrated schematically in Figure 4-11 for a one-dimensional rheological analog to the elastomer deformation model. The viscoelastic-plastic component consists of a linear elastic spring characterizing the initial elastic response due to internal energy change, and a nonlinear viscoplastic dashpot capturing the rate and temperature dependent behavior of the material. The equilibrium behavior is modeled with the hyperelastic rubbery spring component capturing the entropy change due to molecular orientation of soft domains and is responsible for the major part of strain stiffening/hardening and cyclic softening. We note that in the actual material, there are constant interchanges and interplays between deformations in the soft and hard domains. Here, we average out this interplay by taking the two elements to be "in parallel" in the one-dimensional analog which, in turn, corresponds to subjecting both elements (the rubbery spring element and the viscoelastic-plastic elements) to the same deformation in the general three dimensional case. In the following, superscript N denotes the variables acting on the hyperelastic rubbery spring, whilst superscript V denotes the variables acting on the viscoelastic-plastic component. Due to the parallel arrangement of these components,

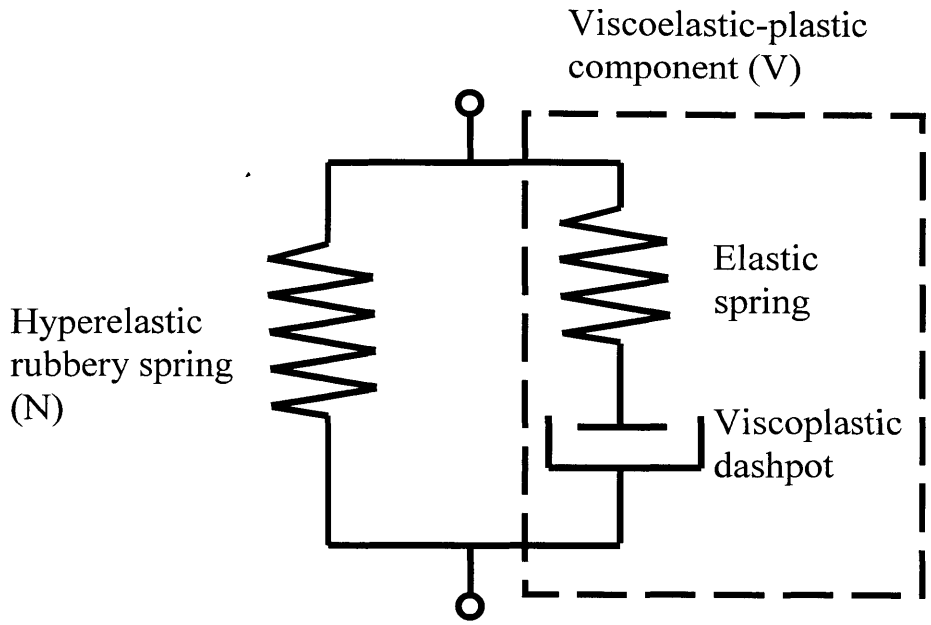

Figure 4-11: One-dimensional schematics of the constitutive model

$$\mathbf{F}^N = \mathbf{F}^V = \mathbf{F}, \tag{4.2}$$

where $\mathbf{F}$ is the deformation gradient; $\mathbf{F}^N$ is the deformation gradient acting on the hyperelastic rubbery spring, and $\mathbf{F}^V$ is the deformation gradient acting on the viscoelastic-plastic component. The total Cauchy stress is thus given by

$$\mathbf{T} = \mathbf{T}^N + \mathbf{T}^V. \tag{4.3}$$

$\mathbf{T}^N$ is the portion of the stress originating from the hyperelastic rubbery behavior; $\mathbf{T}^V$ is the portion originating from the viscoelastic-plastic (hard) domains. The rubbery and viscoelastic-plastic element each require constitutive models as described below.

4.3.3 Hyperelastic Rubbery Network Softening Spring

$\mathbf{T}^N$, the stress acting on the hyperelastic rubbery spring, captures the resistance to entropy change in the soft domain due to molecular network orientation, and is modeled using a modified Arruda-Boyce model detailed below.

Besides behaving as physical crosslinks, the hard domains also occupy a significant volume serving as effective fillers in the material[4-10]. This suggests that it is reasonable to model the equilibrium behavior of TPUs using the methodology for composites. Here, the soft domain is treated as the matrix with effective volume fraction

of v_s, and the hard domain is treated as fillers with effective volume fraction of v_h. We emphasis that v_s and v_h should be regarded as effective volume fraction and are different from the actual volume fractions calculated from the material composition of soft and hard segments. This difference will be discussed in more detail following the presentation of the model for the hyperelastic rubbery spring.

The estimation of the overall behavior of particulate filled materials can be traced back to Einstein[4-58][4-58], who derived the increase in viscosity for a dilute solution of rigid spherical particles in a viscous fluid. His approach was later applied by Smallwood[4-59] to predict the effective small strain Young's modulus $\langle E \rangle$ of a rigid particle filled solid,

$$\langle E \rangle = E_m \left(1 + 2.5 v_f\right), \tag{4.4}$$

where E_m is the Young's modulus of the matrix material and v_f is the volume fraction of the rigid filler. A number of attempts have been conducted to incorporate interactions between neighboring particles to predict the effective modulus of a composite with a high volume fraction of rigid filler. For instance, one of the most cited models for spherical rigid fillers is the Guth-Gold model[4-60][4-61][4-62],

$$\langle E \rangle = E_m \left(1 + 2.5 v_f + 14.1 v_f^2\right), \tag{4.5}$$

And for non-spherical particles, the Guth model[4-62]

$$\langle E \rangle = E_m \left(1 + 0.67 g_f v_f + 1.62 g_f^2 v_f^2\right), \tag{4.6}$$

where g_f is the factor to characterize the shape of fillers, and is typically found to be between 4 and 10. A good review of these models and other general composite theory of rigid particle filled materials can be found in Bergstrom and Boyce[4-54].

The above models are essentially developed for small strain predictions. At large deformation, Mullins and Tobin[4-24] introduced the notion of amplified strain, $\Lambda = 1 + X(\lambda - 1)$ for the case of uniaxial loading, where λ is the applied axial stretch, Λ is the amplified stretch (the average stretch in the matrix) and depends on the volume fraction of fillers; X is the amplification factor and depends on filler content. Following their procedure, the stress-strain behavior of a particle filled elastomer is then obtained by replacing λ by Λ in the constitutive model. In the Mullins and Tobin work[4-24], it is

the uniaxial stretch being amplified. Bergstrom and Boyce[4-54] extended this theory to a general three dimensional deformation state, where the first invariant of the stretch $I_1 = \lambda_1^2 + \lambda_2^2 + \lambda_3^2$ is amplified by

$$\langle I_1 \rangle_m = X\left(\langle I_1 \rangle - 3\right) + 3, \tag{4.7}$$

where $\langle I_1 \rangle_m$ is the average I_1 in the matrix, and $\langle I_1 \rangle$ is the overall macroscopic I_1 of the composite material. X depends on the shape and properties of fillers, and interactions among particles, and can take a general polynomial form of $X = 1 + av_f + bv_f^2$. The amplified $\langle I_1 \rangle_m$ thus can be applied to any I_1 based hyperelastic model. For a neo-Hookean matrix with rigid particles, the strain energy density of the composite $\langle W \rangle$ is found from the strain energy of the matrix $\langle W_m \rangle$ and is given as

$$W = \left(1 - v_f\right)\langle W_m \rangle = \left(1 - v_f\right)\frac{\mu_m}{2}\left[\langle I_1 \rangle_m - 3\right] = \left(1 - v_f\right)X\frac{\mu_m}{2}\left(I_1 - 3\right). \tag{4.8}$$

For X being capable to model dilute solution and high concentrations, it must satisfy $\left(1 - v_f\right)X \to \left(1 + 2.5v_f\right)$ as $v_f \to 0$, resulting in $a = 3.5$. We hereby take

$$X = 1 + 3.5v_f + bv_f^2, \tag{4.9}$$

where b is a coefficient depending on the nature of the dispersion of particle in the matrix. The amplified chain stretch can be obtained as

$$\Lambda_{chain} = \sqrt{\frac{\langle I_1 \rangle_m}{3}} = \sqrt{X\left(\lambda^2 - 1\right) + 1}. \tag{4.10}$$

where $\lambda^2 = I_1/3$. The Langevin chain based Arruda-Boyce eight chain model[4-63] captures the hyperelastic behavior of elastomers up to large stretch and is used here to represent the equilibrium behavior of the material. The Arruda-Boyce eight chain model as modified by amplified strain generates[4-14]

$$\mathbf{T}^N = \frac{1}{J}v_s X \mu_r \frac{\sqrt{N}}{\Lambda_{chain}}\mathcal{L}^{-1}\left(\frac{\Lambda_{chain}}{\sqrt{N}}\right)\overline{\mathbf{B}}', \tag{4.11}$$

where

$J = \det\left[\mathbf{F}^N\right]$,

$\overline{\mathbf{B}} = \overline{\mathbf{F}}^N \overline{\mathbf{F}}^{NT}$,

$$\overline{\mathbf{F}}^N = \frac{1}{J^{1/3}}\mathbf{F}^N,$$

$$\overline{\mathbf{B}}' = \overline{\mathbf{B}} - \frac{1}{3}tr(\overline{\mathbf{B}})\mathbf{I},$$

$$\Lambda_{chain} = \sqrt{X(\lambda_{chain}^2 - 1)^2 + 1},$$

$$X = 1 + 3.5(1 - v_s) + b(1 - v_s)^2,$$

$$\lambda_{chain} = \left(\frac{1}{3}tr[\overline{\mathbf{B}}]\right)^{1/2},$$

μ_r is the initial modulus of the matrix material, N is the number of rigid molecular units between entanglements and crosslinks (in the form of physical crosslink for TPUs) in the soft domains. In this model, $\mathbf{F}^N$ will potentially contain a small volumetric strain, which is taken out through $\overline{\mathbf{F}}^N = \frac{1}{J^{1/3}}\mathbf{F}^N$. $\overline{\mathbf{B}}$ is the left Cauchy-Green tensor, and $\overline{\mathbf{B}}'$ is the deviatoric part of $\overline{\mathbf{B}}$ so that the initial stress free condition is satisfied. $\lambda_{chain} = \sqrt{I_1/3}$ is a scalar equivalent macroscopic stretch and Λ_{chain} is amplified chain stretch. Eqn (4.11) takes the form for a compressible material, but the bulk resistance to volumetric strain (i.e. the bulk modulus) will be lumped into the viscoelastic-plastic component which acts in parallel with the rubbery spring element. Note that v_f in eqn (4.9) is replaced by $1 - v_s$. $\mathcal{L}$ is the Langevin function defined as

$$\mathcal{L}(\beta) = \coth(\beta) - \frac{1}{\beta}.$$

The contribution to the overall initial Young's modulus from the rubbery hyperelastic spring can be obtained as

$$E_0 = 3v_s X\mu_r\left(1 + \frac{40425}{67375N} + \frac{39501}{67375N^3} + \frac{42039}{67375N^4} + \cdots\right). \qquad (4.13)$$

In a TPU, the effective volume fraction v_s for the soft domain is not equal to the volume fraction of soft segments calculated from the material chemistry. In fact, on the one hand, phase separation in TPUs is generally incomplete and there exist non-clustered hard segments, resulting in a smaller volume fraction of hard domain than that obtained

from composition calculation; on the other hand, some of the soft domain material are occluded by the hard domains, resulting in an increase in the effective hard domain volume fraction to contribute to stiffen the material overall behavior. The latter will dominate the small to middle deformation, whereas the first causes the effective soft domain volume fraction to possibly become larger than the segment composition calculation at large deformations when all of the soft domain has been released from the occlusion and some isolated hard segment may also resolve in soft domains. Here, we take v_s to evolve with deformation where initially occluded regions of soft domains are gradually released with deformation. We model this evolution to be driven by the local chain stretch, Λ_{chain}, in the soft domain. Therefore, v_s is modeled to increase with increasing Λ_{chain}, and thus the amplification X decreases with increasing Λ_{chain}. It is thus reasonable to assume v_s varies from an initial value v_{s0} to a saturation value v_{ss} as the local chain stretch Λ_{chain} reaches the locking stretch of the chain, $\Lambda_{chain}^{locking}$. The evolution of v_s is taken to obey the following rule:

$$v_s = v_{ss} - (v_{ss} - v_{s0})\exp\left(-A\frac{\Lambda_{chain} - 1}{\Lambda_{chain}^{lock} - \Lambda_{chain}}\right), \qquad (4.14)$$

where A is a parameter that characterizes how fast v_s evolves toward the saturation value v_{ss} with increasing Λ_{chain}. Note that eqn(4.14) is analogous to the rate form of the evolution rule commonly used in damage mechanics and plasticity, but satisfies the conditions that as $\Lambda_{chain} = 1$, $v_s = v_{s0}$, and as $\Lambda_{chain} \to \Lambda_{chain}^{lock}$, $v_s \to v_{ss}$.

We also assume that as soon as an occluded soft domain is released from the hard domain, it will not relapse to the original occluded configuration upon unloading, i.e. the configuration change of hard domain is taken to be permanent (In reality, there is a very long time constant to recover back to the original state. This recovery time constant is far greater than the time period of interest here and we thus take the softening to be irresversible). v_s thus remains at its value attained at the maximum chain stretch before unloading. Evolution in v_s will be re-activated as the local chain stretch exceeds the previous maximum chain stretch, i.e. when $\Lambda_{chain} > \Lambda_{chain}^{\max}$.

4.3.4 Viscoelastic-plastic Element

The stress acting on the viscoelastic-plastic component is $\mathbf{T}^V$, determined from the elastic spring in the viscoelastic-plastic component, where the elastic deformation gradient is $\mathbf{F}^{Ve}$. The stress $\mathbf{T}^V$ is

$$\mathbf{T}^V = \frac{v_i}{\det \mathbf{F}^{Ve}} \mathbf{L}^e \left[\ln \mathbf{V}^{Ve} \right], \tag{4.15}$$

where $\mathbf{L}^e$ is the fourth-order tensor modulus of elastic constants and $\mathbf{V}^{Ve}$ is the left stretch tensor of the elastic deformation gradient obtained from the polar decomposition $\mathbf{F}^{Ve} = \mathbf{V}^{Ve}\mathbf{R}^{Ve}$, where $\mathbf{R}^{Ve}$ is the rotation tensor of the elastic deformation gradient. v_i is an effective volume fraction of hard domain accounting for the interaction between soft and hard domains. It should be noted that a TPU is not a composite material, even though the methodology for composite material is used here. Since the viscoelastic-plastic component models the material initial elastic behavior and lumped energy dissipation, the combination of these behaviors is believed to relate to the hard domain and soft-hard domain interactions. We assume $v_i = 1 - f v_s$, where f is a material parameter, implying v_i is related to v_s through a parameter f featuring the interactions between soft domain and hard domain.

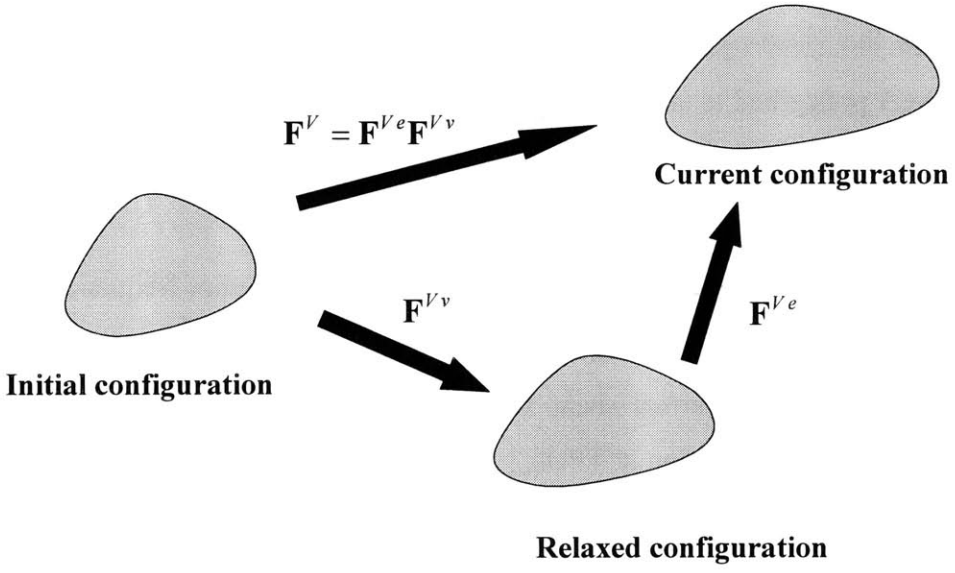

Figure 4-12: Schematic of decomposition of $\mathbf{F}^V$ into elastic and visco-plastic parts.

To obtain $\mathbf{F}^{Ve}$, $\mathbf{F}^{V}$ is further decomposed into elastic and visco-plastic parts (Figure 4-12)

$$\mathbf{F}^{V} = \mathbf{F}^{Ve}\mathbf{F}^{Vv}. \tag{4.16}$$

The corresponding decomposition of the velocity gradient is

$$\mathbf{L}^{V} = \dot{\mathbf{F}}^{V}\mathbf{F}^{V-1} = \dot{\mathbf{F}}^{Ve}\mathbf{F}^{Ve-1} + \mathbf{F}^{Ve}\dot{\mathbf{F}}^{Vv}\mathbf{F}^{Vv}\mathbf{F}^{Ve-1}. \tag{4.17}$$

The velocity gradient of the relaxed configuration is given by

$$\mathbf{L}^{Vv} = \dot{\mathbf{F}}^{Vv}\mathbf{F}^{Vv-1} = \mathbf{D}^{Vv} + \mathbf{W}^{Vv}, \tag{4.18}$$

where $\mathbf{D}^{Vv}$ and $\mathbf{W}^{Vv}$ are the rate of stretching and the spin, respectively. We take $\mathbf{W}^{Vv} = \mathbf{0}$ with no loss in generality as shown in Boyce et al[4-64]. The visco-plastic stretch rate $\mathbf{D}^{Vv}$ is constitutively prescribed to be

$$\mathbf{D}^{Vv} = \frac{\dot{\gamma}^{v}}{\sqrt{2}\bar{\tau}_{V}}\bar{\mathbf{T}}^{V\prime}, \tag{4.19}$$

where $\bar{\mathbf{T}}^{V}$ is the stress acting on viscoelastic-plastic component in its relaxed configuration ($\bar{\mathbf{T}}^{V} = \mathbf{R}^{Ve^{T}}\mathbf{T}^{V}\mathbf{R}^{Ve}$). and the prime denotes the deviator; $\bar{\tau}_{V}$ is the equivalent shear stress and

$$\bar{\tau}_{V} = \left[\frac{1}{2}\bar{\mathbf{T}}^{V\prime} \bullet \bar{\mathbf{T}}^{V\prime}\right]^{1/2}. \tag{4.20}$$

$\dot{\gamma}^{v}$ denotes the visco-plastic shear strain rate of the viscoplastic component, and is constitutively prescribed to take the form

$$\dot{\gamma}^{v} = \dot{\gamma}_{0}\exp\left[-\frac{\Delta G}{k\Theta}\left\{1-\left(\frac{\bar{\tau}_{V}}{s}\right)\right\}\right], \tag{4.21}$$

where $\dot{\gamma}_{0}$ is the pre-exponential factor proportional to the attempt frequency; ΔG is the zero stress level activation energy, k is Boltzmann's constant and Θ is absolute temperature. s is the athermal shear strength, which represents the resistance to the visco-plastic shear deformation in TPUs.

The true stress-true strain curve including relaxation periods (Figure 4-9) shows the amount of stress decrease during loading strain holding periods is larger than the amount of stress increase during unloading holding periods. Such effect is significant during the 1st cycle test. This suggests that there may be a different rate-dependent mechanism

operative during unloading. Although the mechanism is unclear yet, a possible conjecture is that such mechanism change is related to the configuration change of soft and hard domains as evidenced by Estes et al[4-4]. During the loading course, the hard domain clusters will irreversibly change their configuration to accommodate local deformation by breaking and reforming the hydrogen bonds. During unloading and reloading, the hard domain will remain in the configuration that formed during the previous maximum loading. From equation (4.21), for the same shear strain rate at loading and unloading, the unloading path has a lower driving stress $\bar{\tau}_V$, therefore its resistance s for unloading must be smaller than that for loading. We propose the following evolution rule as a first step to capture this behavior,

$$s_1 = \left(\frac{v_h}{v_{h0}}\right)^n s_0 . \tag{4.22}$$

4.4 Parameter Identification for the Constitutive Model

4.4.1 Material Parameter Summary

The deformation behavior of TPU is not trivial: It is highly nonlinear; it is rate dependent; it is hysteretic; and it softens with cyclic loading where the degree of softening depends on the maximum strain level reached in prior cycles. The new constitutive model captures all of these behaviors but requires 13 material parameters. The material parameters are listed in the following table, together with their corresponding material behavior and equations.

Due to the ability to systematically break down the stress-strain behavior, a systematic procedure for determining values for the material parameters can be identified. The three constitutive elements in the model each account for different material behaviors, i.e. the hyperelastic rubbery softening spring for equilibrium behavior, and the evolution of effective volume fraction of soft domains for the softening of equilibrium paths, the linear elastic spring accounting for the initial stiffness of the time dependent behavior, and the viscoplastic dashpot accounting for the rate dependent behavior. It is thus possible to identify these parameters associated with different features of the material behavior.

Table 4-1. Material parameters in the constitutive model.

Hyperelastic Rubbery Spring Element	Hyperelastic "filler" effect	μ, N,	$\mathbf{T}^N = \frac{1}{J} v_s X \mu_r \frac{\sqrt{N}}{\Lambda_{chain}} \mathcal{L}^{-1}\left(\frac{\Lambda_{chain}}{\sqrt{N}}\right)\overline{\mathbf{B}}'$
		b	$X = 1 + 3.5(1 - v_s) + b(1 - v_s)^2$
	Cyclic Softening	v_{s0}, v_{ss}, A	$v_s = v_{ss} - (v_{ss} - v_{s0})\exp\left(-A\frac{\Lambda_{chain} - 1}{\lambda_{chain}^{lock} - \Lambda_{chain}}\right)$
Linear Spring Element		E, ν	$\mathbf{T}^V = \frac{v_i}{\det \mathbf{F}^{Ve}} \mathbf{L}^e\left[\ln \mathbf{V}^{Ve}\right]$
		f	$v_i = 1 - f v_s$
Viscoplastic Dashpot Element	Time Dependence	$\dot{\gamma}_0$, ΔG	$\dot{\gamma}^v = \dot{\gamma}_0 \exp\left[-\frac{\Delta G}{k\Theta}\left\{1 - \left(\frac{\bar{\tau}_V}{s}\right)\right\}\right]$
	Cyclic Softening	s_0, n	$s = \left(\frac{v_h}{v_{h0}}\right)^n s_0$

4.4.2 Material Parameter Identification for Hyperelastic Rubbery Softening Spring

The material parameters associated with the hyperelastic rubbery component of the constitutive model can be determined using two equilibrium paths (the 1st cycle test and the 4th cycle test after cyclic loading to a strain of 1.0) presented in Figure 4-13. The initial Young's moduli for these two curves are measured from the initial slopes of the curves, $E_0^0 \approx 24MPa$ and $E_0^1 \approx 17MPa$, where E_0^0 denotes the initial Young's modulus for the 1st cycle equilibrium path, and E_0^s denotes the initial Young's modulus for the stabilized equilibrium path after a maximum cyclic strain of 1.0. In the following, a superscript 0 denotes the variables for the 1st cycle equilibrium, and a superscript s denotes the variables for the stabilized equilibrium path. The ratio is $E_0^0/E_0^s = 1.4$, and from eqn. (4.13),

$$\frac{E_0^0}{E_0^c} = \frac{v_s^0 X^0}{v_s^s X^s} = \frac{v_s^0\left[1+3.5\left(1-v_s^0\right)+b\left(1-v_s^0\right)^2\right]}{v_s^s\left[1+3.5\left(1-v_s^s\right)+b\left(1-v_s^s\right)^2\right]} \tag{4.24}$$

where $v_s^0 = v_{s0}$; v_s^s is effective volume fraction of soft domain at $\varepsilon = 100\%$, and remains constant during the 4th cycle test.

The chemical composition of the TPU used in the current study is 57% soft segment and 43% hard segment. Therefore, based on the argument in the discussion of the effective volume fraction, it is reasonable to assume that $v_{s0} = 0.4$ and $v_{ss} = 0.8$. Since in the test, the TPU shows increase in its stiffness at $\varepsilon = 100\%$, meaning a large strain is approached, it is thus reasonable to assume $v_s^s \approx 0.7$ for the purpose of parameter estimation. Note that this value is subjected to change during material parameter fitting, and it is assumed here only for the purpose of material parameter estimation. Using $v_s^0 = 0.4$, and $v_s^s = 0.7$, we obtained from eqn.(4.24) $b \approx 13$. Thus $X^0 = 3.832$ and $X^s = 2.58$.

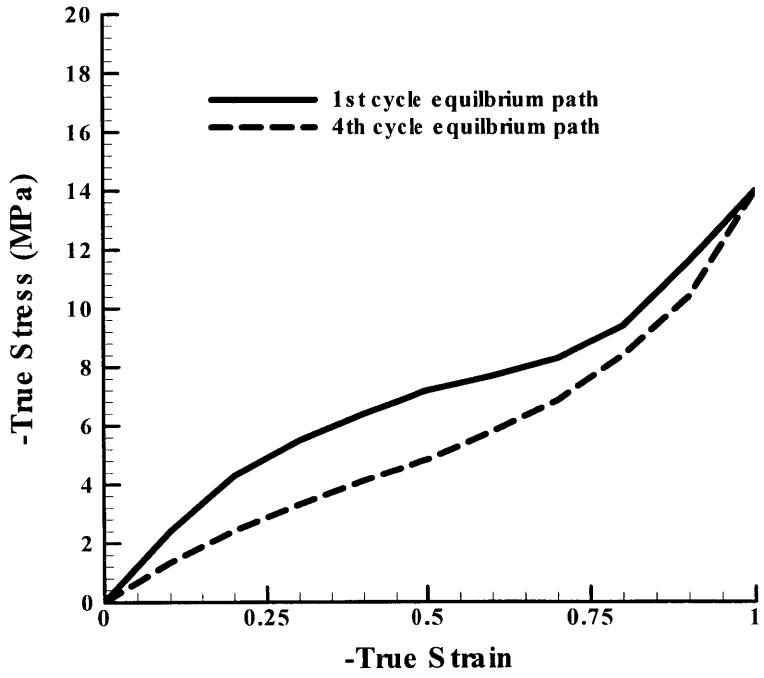

Figure 4-13: Equilibrium paths from the 1st relaxation test and the 4th relaxation test.

Since in the 4th cycle test, both v_s and X remain constant, it is convenient to use the stabilized equilibrium path to determine parameters μ and N in the Arruda-Boyce

model[4-56]. We found $\mu = 0.52MPa$ and $N = 5.26$. The locking chain stretch hence is $\lambda_{chain}^{locking} = \sqrt{N} = 2.3$.

In a uniaxial compression test, the compression ratio in the axial direction is λ_1 and is related with compression strain ε by $\lambda_1 = e^{-\varepsilon}$. Assuming material is incompressible, the lateral stretch ratios are $\lambda_2 = \lambda_3 = \sqrt{1/\lambda_1}$. Then the macroscopic equivalent stretch is

$$\lambda_{chain} = \sqrt{\frac{\lambda_1^2 + \lambda_2^2 + \lambda_3^2}{3}} = \sqrt{\frac{e^{-2\varepsilon} + 2e^{\varepsilon}}{3}} \approx \sqrt{\frac{2e^{\varepsilon}}{3}} \qquad (4.25)$$

For $\varepsilon = 100\%$, $\lambda_{chain} \approx 1.35$. The amplified chain stretch ratio is thus $\Lambda_{chain} = 1.77$. From eqn (4.14), we obtained $A \approx 1.0$.

The parameters obtained above provide the estimations, and are used as a guide to attain the material parameters by fitting the curve with the modified Arruda-Boyce model. Figure 4-14 shows the curve fitting using the following parameters

$$\mu = 1.70MPa,\ N = 5.26,\ b = 10,\ A = 3.0,\ v_{s0} = 0.4,\ v_{ss} = 0.8.$$

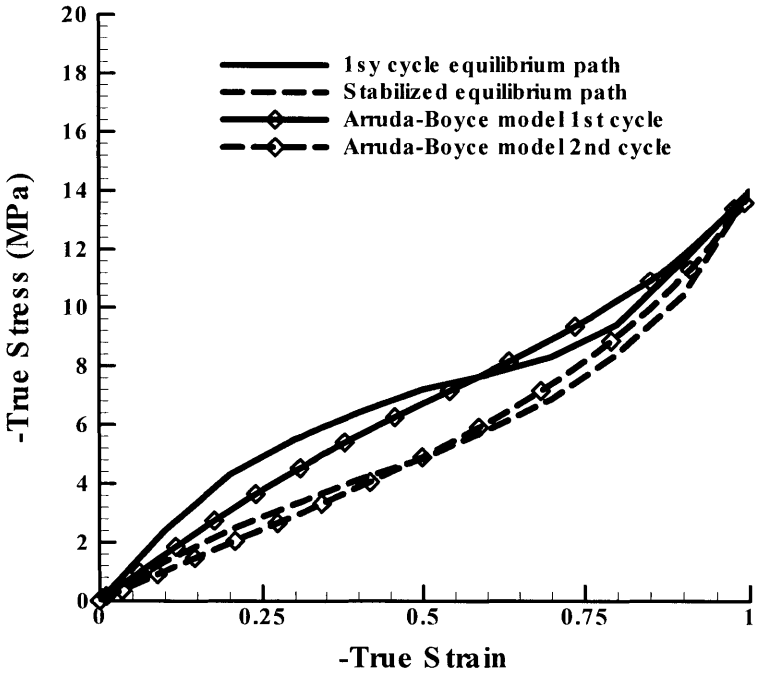

Figure 4-14: Material parameter identification for the rubbery hyperelastic spring.

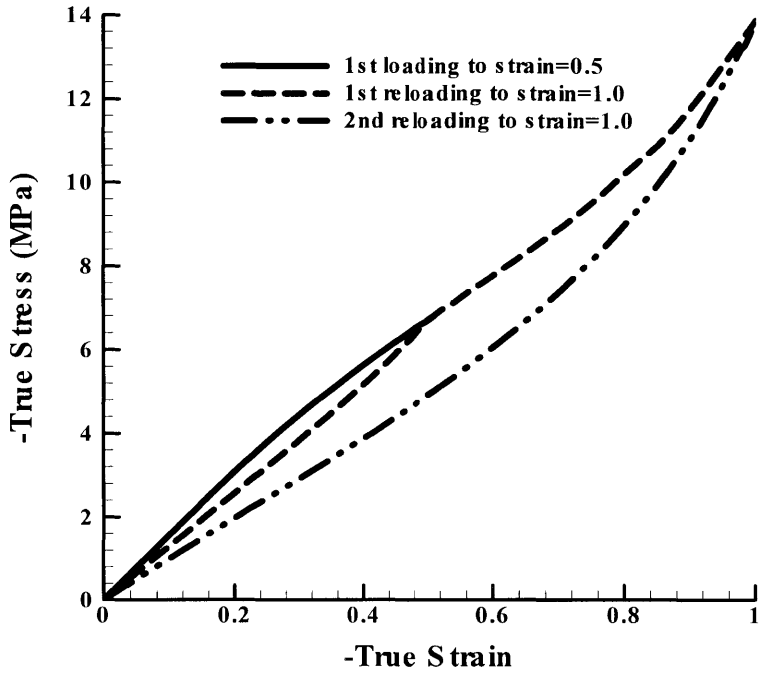

Figure 4-15(a)

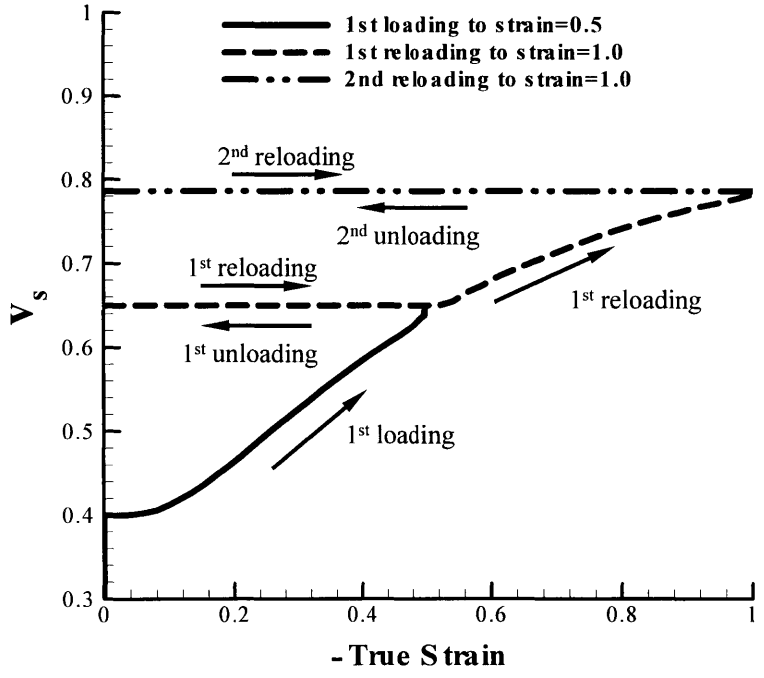

Figure 4-15(b)

Figure 4-15: Numerical simulations of equilibrium behavior during cyclic loadings to a maximum strain of 0.5 for first cycle, then reloading to 1.0 for two cycles: (a) The stress-strain behavior; (b) The variation of effective volume fraction of soft domain.

The obtained parameters for the equilibrium path were used to simulate the tests where the sample is subjected to three load-unloading cycles: the first one to a maximum strain of 0.50, whereas the last two to a maximum strain of 1.0. Figure 4-15 shows the numerical simulations. Clearly, the loading to the maximum strain of 0.50 shows less softening in the stress-strain behavior than that with the maximum strain of 1.0.

4.4.3 Material Parameter identification for viscoelastic-plastic component

From the one dimension simplification of eqn.(4.3), the stress acting on the viscoelastic-plastic component T^V is determined by

$$T^V = T - T_0. \tag{4.26}$$

The elastic modulus E_v for the elastic spring in the viscoelastic-plastic component can be determined since the initial Young's modulus of the material is the summation of the contributions from hyperelastic rubbery spring and the elastic spring. The initial overall Young's modulus is measured from the true stress-true strain curve in Figure 4-7, $E \approx 55MPa$. Hence, $E_v = E - E_0 \approx 35MPa$. Poisson's ratio is chosen as $\nu = 0.49$ to ensure small material compressibility. f is chosen as $f = 0.5$ as an estimation.

For the material parameters associated with the viscoplastic dashpot element, s_0, ΔG ,and $\dot{\gamma}_0$ can be determined using the loading curve, thus leaving n to be decided solely by the unloading and reloading curves. From eqn.(4.26), T^V vs ε plots for the tests at difference strain rates are constructed, as shown in Figure 4-16(a).

The equivalent shear strain γ and shear stress τ are related to strain and stress in uniaxial compression tests by

$$\gamma = \sqrt{3}\varepsilon,\ \tau = \frac{1}{\sqrt{3}} T^V \tag{4.27}$$

The equivalent visco-plastic shear strain is obtained by subtracting the elastic shear deformation from the total equivalent shear strain

$$\gamma^v = \gamma - \tau / G, \text{ where } G = E/3 \tag{4.28}$$

The equivalent visco-plastic shear stress and shear strain curves at different strain rate hereby are constructed for the loading path (Figure 4-16(b)).

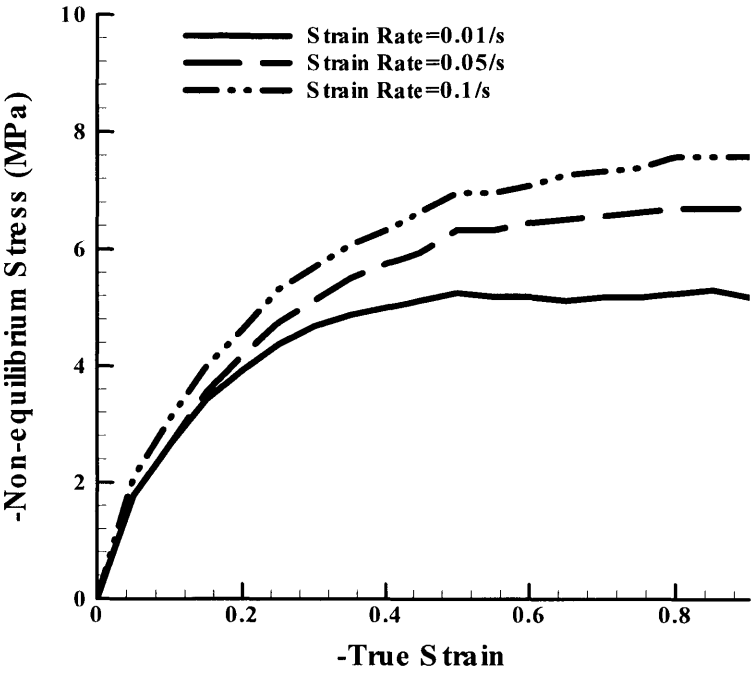

Figure 4-16(a)

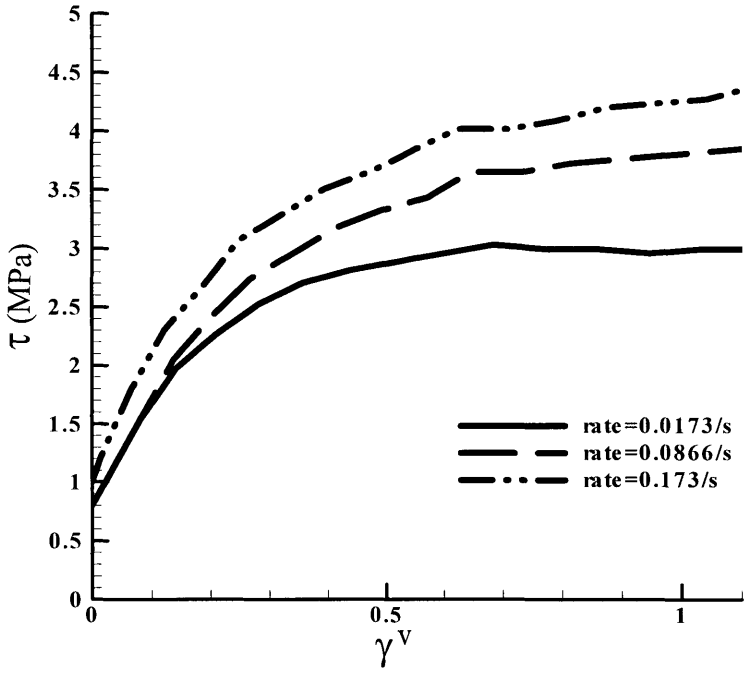

Figure 4-16(b)

Figure 4-16: (a) T^{V} vs ε plots at different strain rates; (b) τ - γ^{v} plots at different strain rates.

Eqn(4-21) describes the viscoplastic flow rate and can be rewritten as

$$\tau = c \ln \dot{\gamma}^v + b, \tag{4.29}$$

$$c = \frac{s}{D},\ b = \frac{s}{D}\left(D - \ln \dot{\gamma}_0\right),\ D = \frac{\Delta G}{k\Theta}. \tag{4.30}$$

Eqn. (4.29), together with Figure 4-16(b), provides insight into the evolution of s during deformation. Indeed, a detailed evolution rule for s can be identified by constructing τ vs $\dot{\gamma}^v$ curves at a number of γ^v from Figure 4-16(b), and then investigating the variation of the slopes and interception of the curves with respect of γ^v. Here, for the sake of brevity, we assume s_0 is a constant value, $s = s_0$, during the loading course. As shown in the results, such simplification generally can give good predictions of the stress-strain behavior of the material.

From Figure 4-16(b), the equivalent shear stress at each equivalent shear strain rate approximates to a constant value at large equivalent shear strain. For $\dot{\gamma}_1^v = 0.0173/s$ (from $\dot{\varepsilon} = 0.01/s$), $\tau_1 = 2.9MPa$; for $\dot{\gamma}_2^v = 0.0866/s$ (from $\dot{\varepsilon} = 0.05/s$), $\tau_2 = 3.8MPa$; for $\dot{\gamma}_3^v = 0.173/s$ (from $\dot{\varepsilon} = 0.1/s$), $\tau_3 = 4.3MPa$. Using least square fit gives $c = 0.60, b = 5.3$.

From eqn (4-30), we obtain

$$\dot{\gamma}_0 = e^{D-8.3}, \tag{4.31a}$$

$$D = \frac{s_0}{0.60}. \tag{4.31b}$$

Using a kinked model, Argon[4-65] and Argon and Bessonov[4-66] predicted for a wide range of glassy polymers,

$$s = \frac{0.077G}{1-v}. \tag{4-32}$$

Although the resistance to flow is a more complicated mechanism in the TPU, we use this expression as a guideline. From eqn(4-22), $s \sim 1.76MPa$. $s_0 = 1.76MPa$ is thus used as a starting point for identifying material parameters. s_0, ΔG, and $\dot{\gamma}_0$ can be determined using the loading curve. Parameter n is thereafter determined by simply best fitting the unloading and reloading curves.

4.5 Results

The material parameters are identified for the TPU tested in this study by following the procedure outlined above and are listed in Table 4-2.

Table 4-2: Material parameters.

Hyperelastic Rubbery Spring					
μ_r	N	b	A	v_{s0}	v_{ss}
(MPa)					
1.70	5.26	10	3.0	0.4	0.8

Viscoelastic-plastic Component						
Linear Elastic Spring			Viscoplastic Dashpot			
E_0	ν	f	s_0	ΔG	$\dot{\gamma}_0$	n
(MPa)			(MPa)	$(10^{-19} J)$		
35	0.49	0.5	4.55	0.41	2.26	3.0

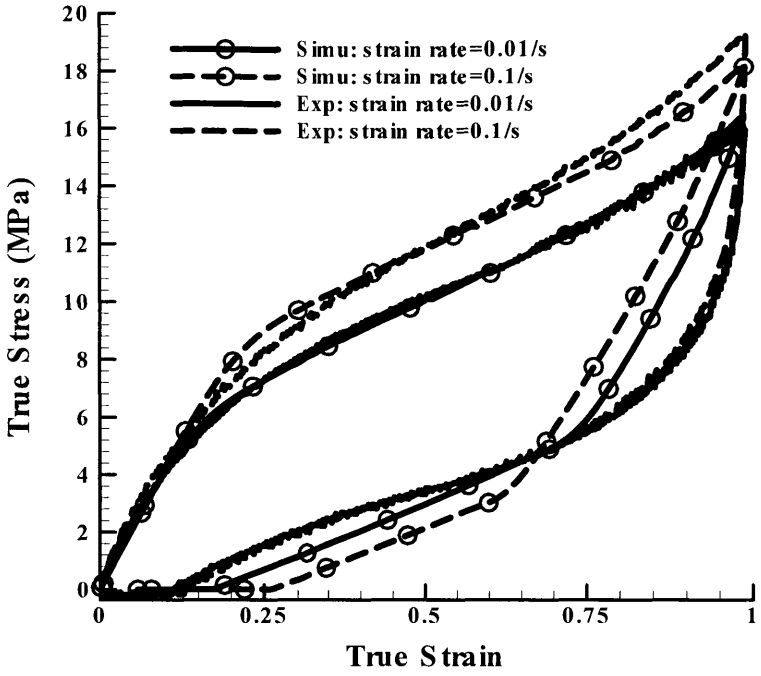

Figure 4-17(a)

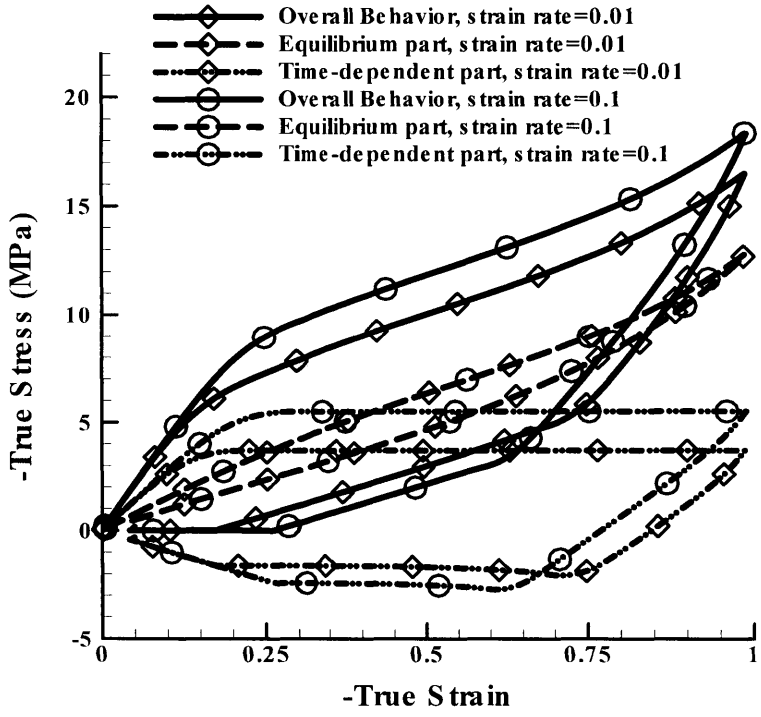

Figure 4-17(b)

Figure 4-17: (a) True Stress-true strain curves for uniaxial compression tests; (b) Decompositions of the stress-strain behavior into an equilibrium part and a time dependent part.

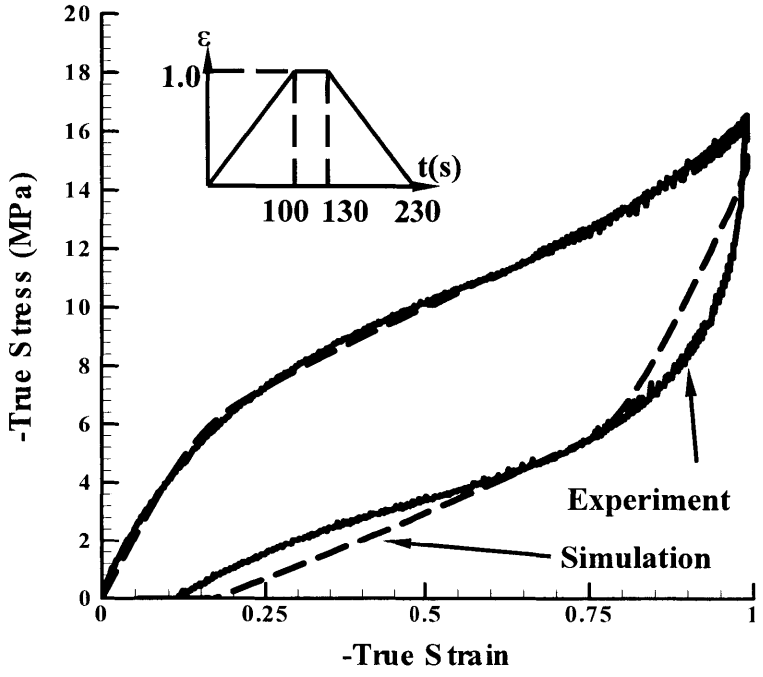

Figure 4-18: True Stress-true strain curves for uniaxial compression test with $\dot{\varepsilon} = 0.01/s$ and 30 seconds delay before unloading. The inset shows the true strain loading history.

Uniaxial compression tests at different constant strain rates on fresh samples are simulated to verify the proposed constitutive model. Figure 4-17(a) shows the simulated stress-strain curves for the tests at $|\dot{\varepsilon}| = 0.01s^{-1}$ and $|\dot{\varepsilon}| = 0.1s^{-1}$, respectively. The experimental curves are also presented in the figure for comparisons. The simulated results agree very well with the experimental loading curves and capture the stress response at different strain rates. Figure 4-17(b) shows the one dimensional decomposition of the material stress-strain behavior into an equilibrium part and a time dependent part. In Figure 4-17(b), the equilibrium parts for the tests at different strain rates follow the same course. This observation verifies the fact that the equilibrium part is independent of the strain rate and the methodology of material behavior decomposition. The proposed model does not fully capture the feature that the unloading curves follow the same path for the tests at different strain rate, but the difference is small. Improvement can be achieved by allowing certain small amount of time before unloading. Figure 4-18 shows the true stress-true strain curve from the simulation when a

30 second delay before unloading is used. To precisely capture the feature in unloading, however, the unloading mechanism should be subjected to a more detailed study, where additional material parameters are expected.

Simulations on cyclic loading-unloading tests were also conducted. Recall that the TPU sample showed residual strain (permanent set) after each cycle of test. In the experiments, the dimensions of the sample (diameter and height) were measured each time before the test, and were used as the new dimension for the sample so that the true stress-true strain curves always started from the new unloaded specimen height for each cycle. Such a process of having the true stress-true strain curve begin at the origin by measuring the dimensions before each test corresponds to simply shifting the true stress-true strain curves based on the fresh sample dimension leftward by the amount of residual strain ε^r. In simulations, the true stress-true strain curves were first obtained based on the initial dimensions of the sample and were then shifted leftward by the amount the residual strain after 2 minutes idling time between the two cyclic simulations, so chosen corresponding to the 2 minute period between cycles used to measure the dimension change and reposition the sample on the platen for the next cycle of loading. Figure 4-19(a) shows the loading history for the test with $\varepsilon_{\max} = 1.0$ and $|\dot{\varepsilon}| = 0.1 s^{-1}$. Due to the shift of the curve, the second cycle simulation was loaded to the strain $1 + \varepsilon^r$, where ε^r is the residual strain measured from the first cycle simulation.

Simulations on cyclic loading-unloading tests were conducted at a strain rate of $|\dot{\varepsilon}| = 0.01 s^{-1}$ (Figure 4-19(b)) and $|\dot{\varepsilon}| = 0.1 s^{-1}$ (Figure 4-19(c)). The model very well captures the loading paths for both loading and re-loading tests at both strain rates. As expected, the unloading paths show relative larger error; especially the one with $|\dot{\varepsilon}| = 0.1 s^{-1}$ which shows the largest deviation from experiments. The residual strains after 2min idling time in the simulation were about 0.05, which was very close to the residual strain of 0.04~0.06 observed in the experiments. Figure 4-19(d) and (e) show the one dimensional decomposition of the material stress-strain behavior into an equilibrium part and a time dependent part for each cycle of the tests. From Figure 4-19(d) and (e), the equilibrium parts during loading and unloading for the second cycle follow the same path, implying they do not soften in the second loading cycle. It is also noticed that for a

given the cycle, the equilibrium paths are same for the different rate tests as long as the maximum strains reached are same.

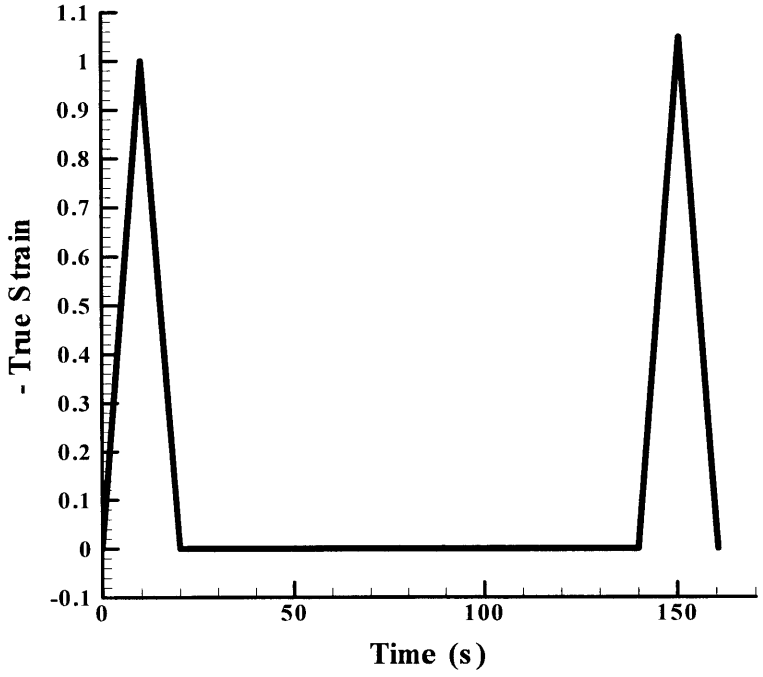

Figure 4-19(a)

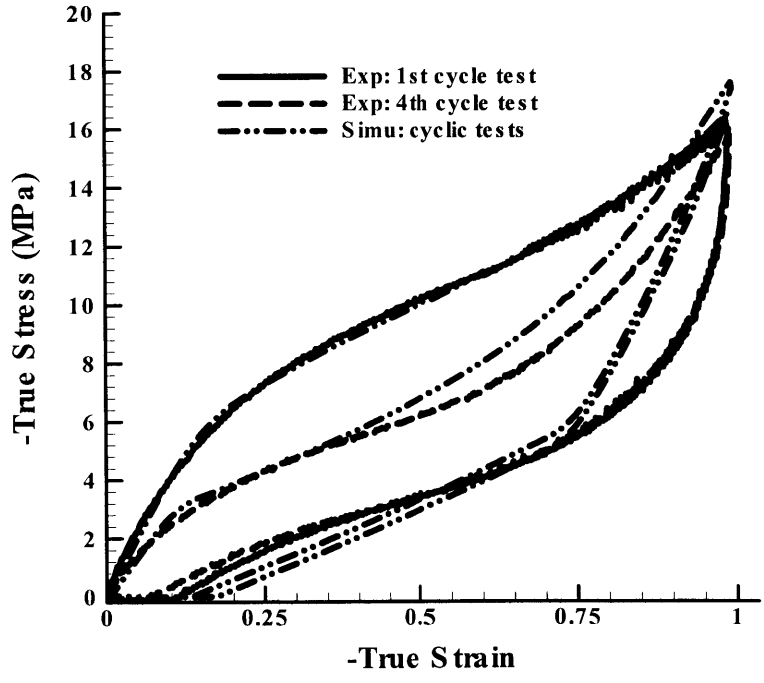

Figure 4-19(b)

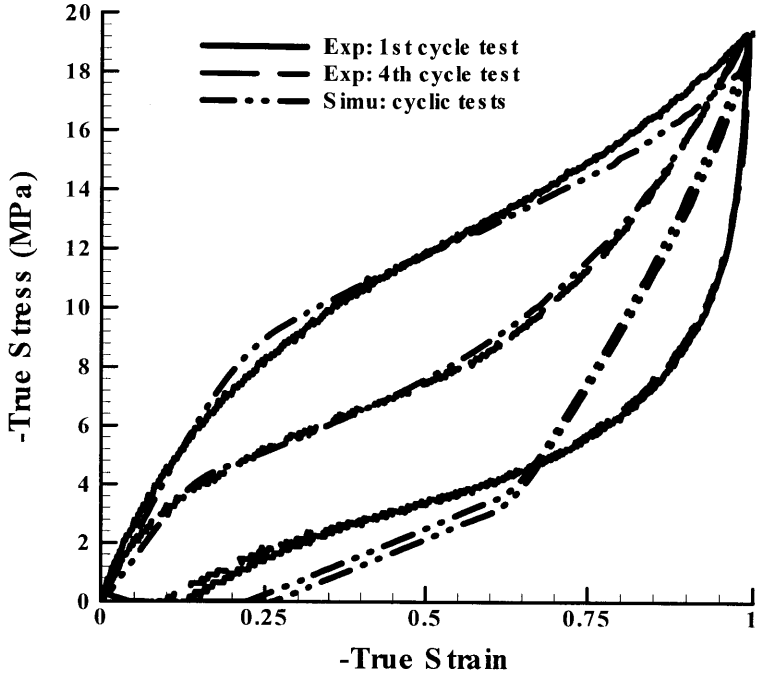

Figure 4-19(c)

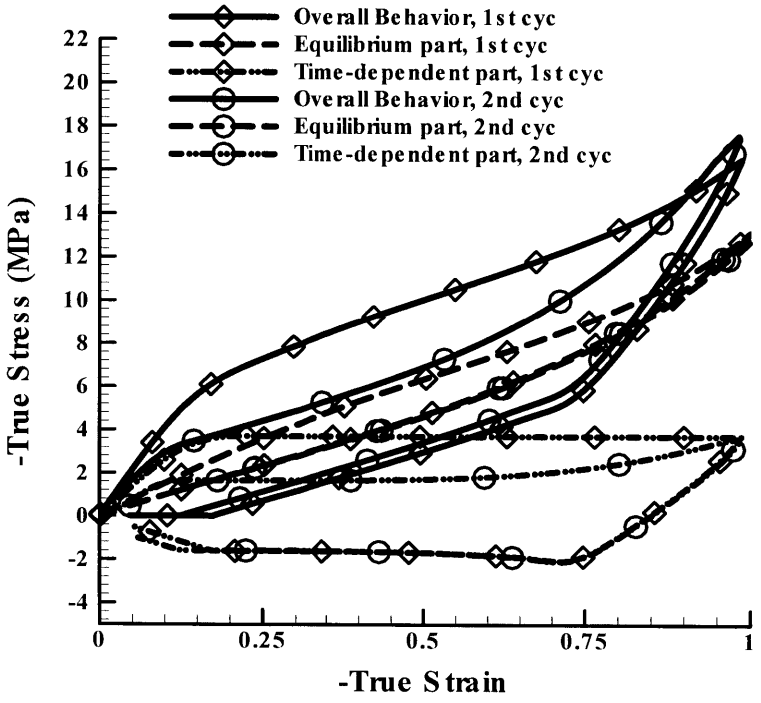

Figure 4-19(d)

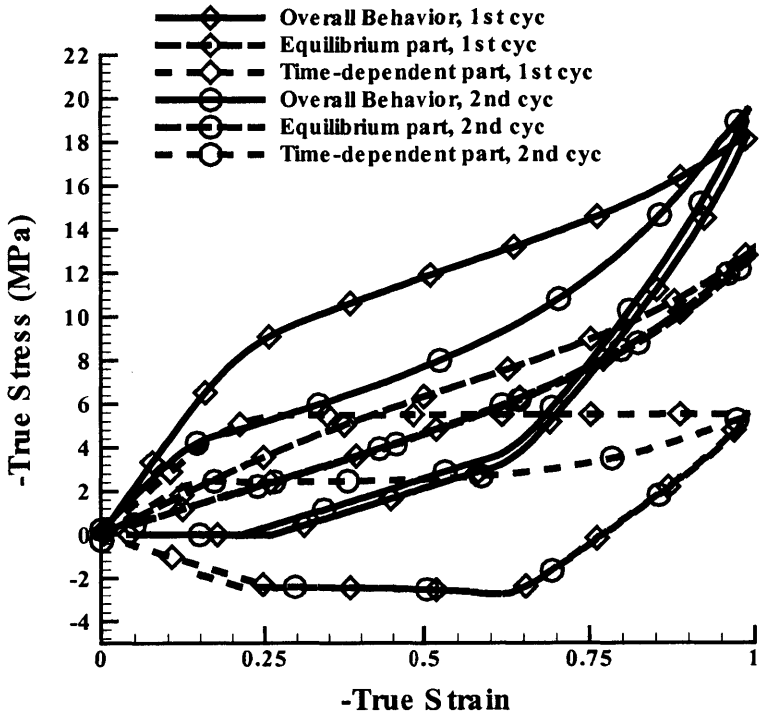

Figure 4-19(e)

Figure 4-19: Numerical simulation on cyclic loading tests: (a) loading history; Stress-strain behavior for (b) $\dot{\varepsilon} = 0.01/s$; and (c) $\dot{\varepsilon} = 0.1/s$; Decompositions of the stress-strain behavior into an equilibrium part and a time dependent part for (d) $\dot{\varepsilon} = 0.01/s$; and (e) $\dot{\varepsilon} = 0.1/s$.

Figure 4-20(a) shows the cyclic loading to different maximum strains, i.e. the sample was subjected to three loading-unloading cycles: the first cycle was loaded to $\varepsilon_{max} = 0.05$, and the second and the third cycles were loaded to $\varepsilon_{max} = 1.0$. The strain rate for these cyclic tests is $\dot{\varepsilon} = 0.01/s$. The corresponding experimental results are also presented in the figure. The numerical simulations adequately capture the softening effects during the cyclic tests. It is noted that the experimental results used to obtain material parameters do not include the tests with loading to $\varepsilon_{max} = 0.5$, but the model predicts the softening response corresponding to 0.5 strain, catches up the stress response after the strain exceeds 0.5. Figure 4-20(b) and (c) the equilibrium parts and the time dependent parts for each cycle of the tests. From Figure 4-20(b), the equilibrium part of the second loading cycle first follows the softened course determined by previous loading with $\varepsilon_{max} = 0.5$, then follows the course determined by fresh sample. For the third

loading cycle, the equilibrium part coincide with the one determined by the second loading cycle. These observations together with the observations from Figure 19(d) and (e) verify the fact that the softening of equilibrium part is independent of the strain rate and is dependent of the maximum strain reached in previous tests.

Figure 4-20(d) shows the evolution of the effective volume fraction of soft domain during this deformation course. The v_s evolves with strain from the original $v_{s0} = 0.4$ and reaches $v_s = 0.66$ at $\varepsilon_{\max} = 0.5$. Such value of v_s is retained until the strain exceeds 0.5 upon reloading, whereupon v_s starts increasing again.

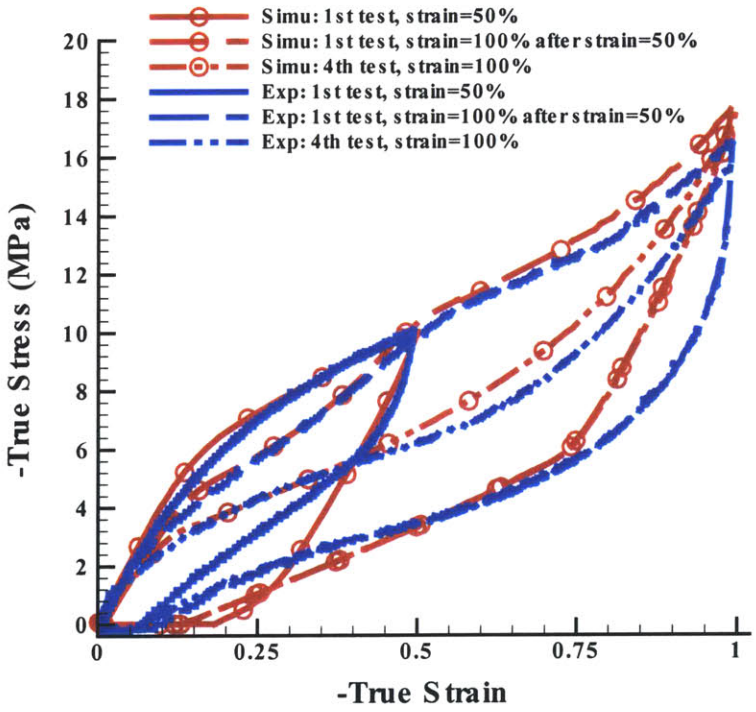

Figure 4-20(a)

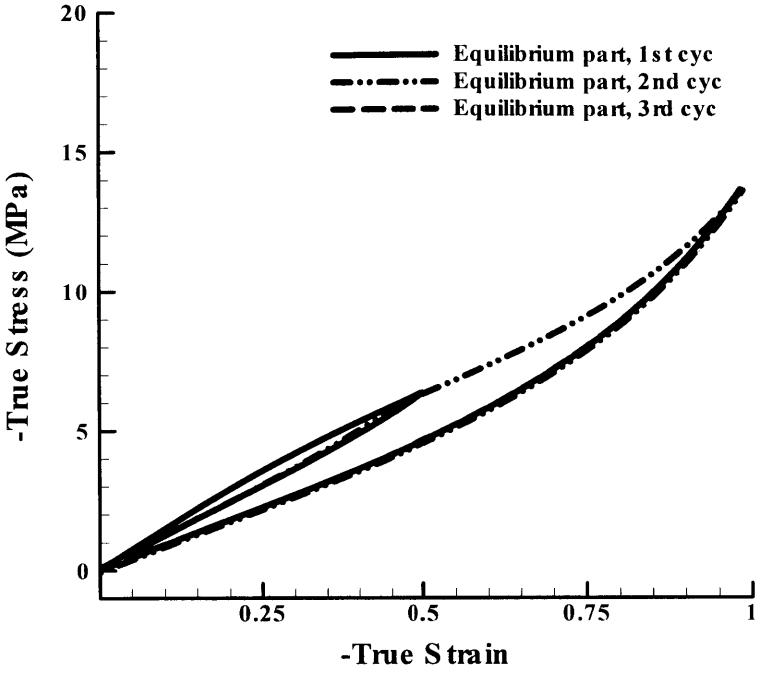

Figure 4-20(b)

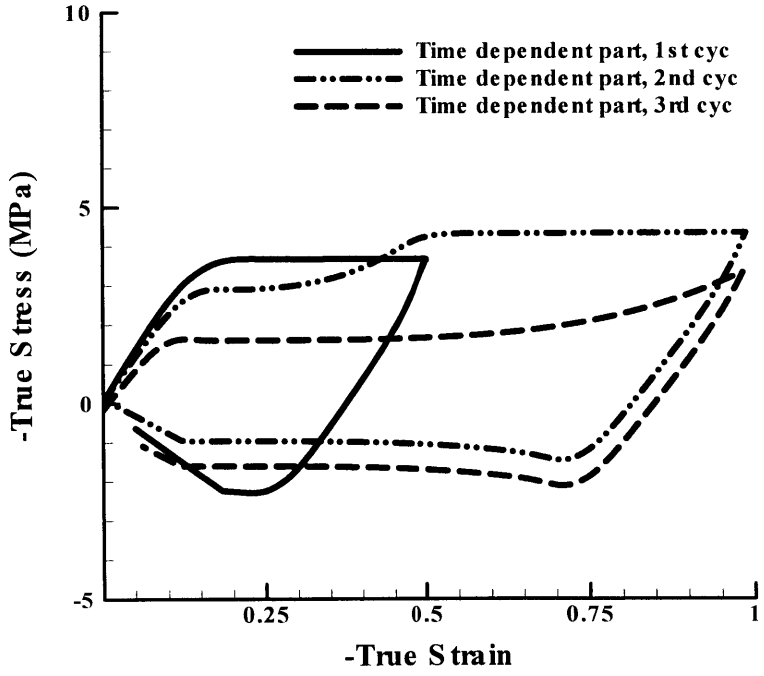

Figure 4-20(c)

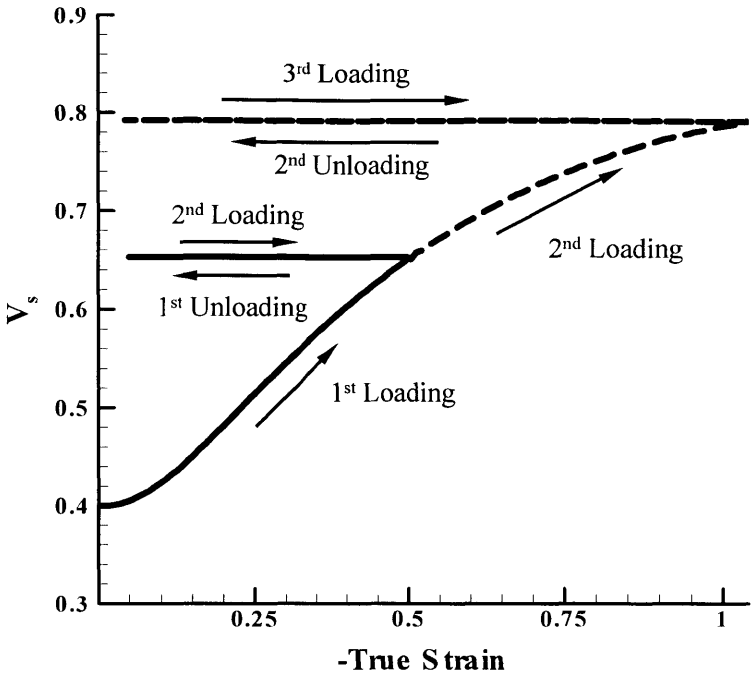

Figure 4-20 (d)

Figure 4-20: cyclic loading to different maximum strains, i.e. $\varepsilon = 50\%$ first, then $\varepsilon = 100\%$ with strain rate of $\dot{\varepsilon} = 0.01/s$. (a) true stress-true strain curve; (b) The equilibrium parts and (c) The time dependent parts; (e) evolution of effective volume fraction of soft domain.

Figure 4-21 shows the numerical simulation of the relaxation test at $\dot{\varepsilon} = 0.1/s$. For the first cycle (Figure 4-21(a)), the numerical simulation captures the decrease/increase of the stress during each hold period, except for the stop at $\varepsilon = 80\%$ during unloading due to relative slow stress drop at the transition from loading to unloading in the simulation. Since a constant athermal shear resistance is used in the current model, the model generally gives about constant stress decrease/increase at each stop. For the stabilized relaxation test, the numerical simulation (Figure 4-21(b)) captures the stress decrease/increase, but gives relatively large or fast stress changes. Figure 4-21(c) and (d) show the one dimensional decomposition of the material stress-strain behavior into an equilibrium part and a time dependent part for each cycle of the tests. This decomposition clearly shows that the stress relaxation is due to the relaxation of the time-dependent part while the equilibrium part does not change during the holding period.

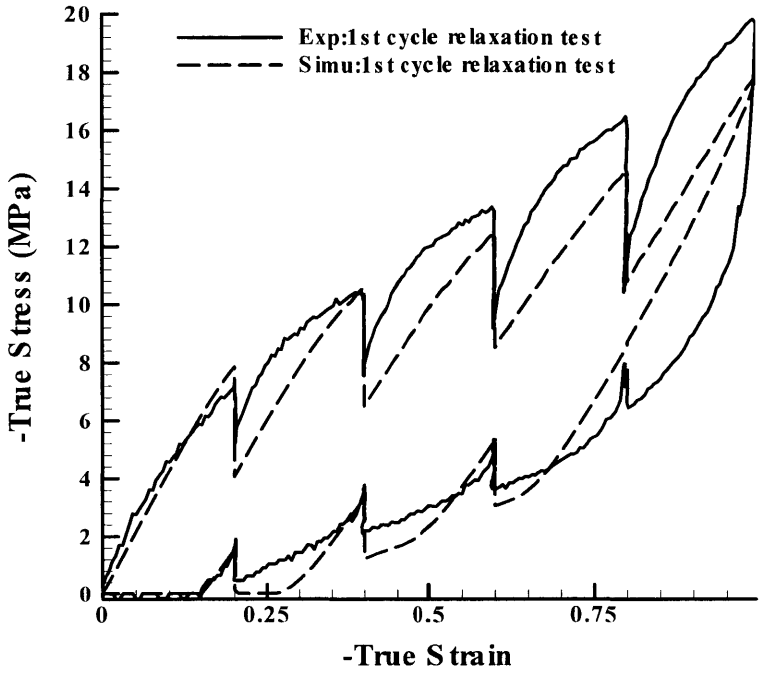

Figure 4-21(a)

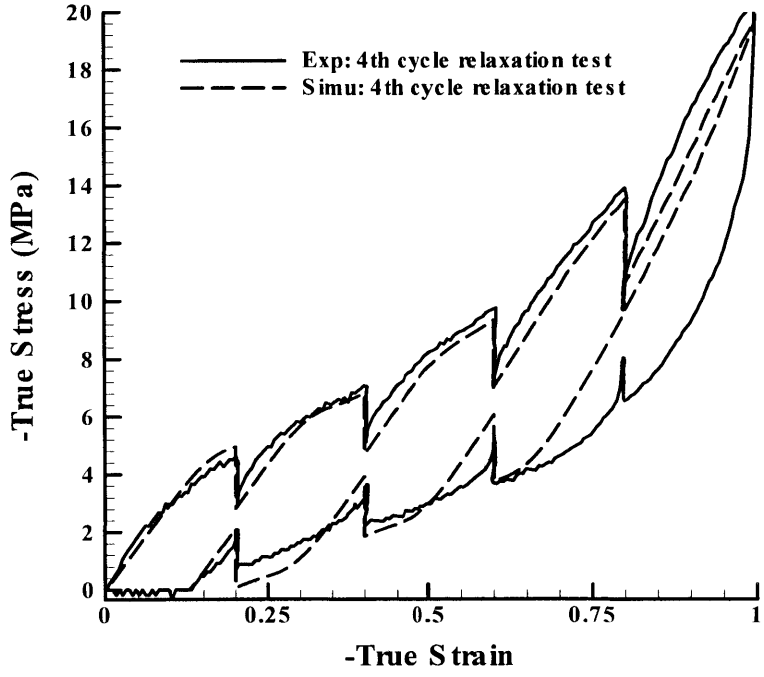

Figure 4-21(b)

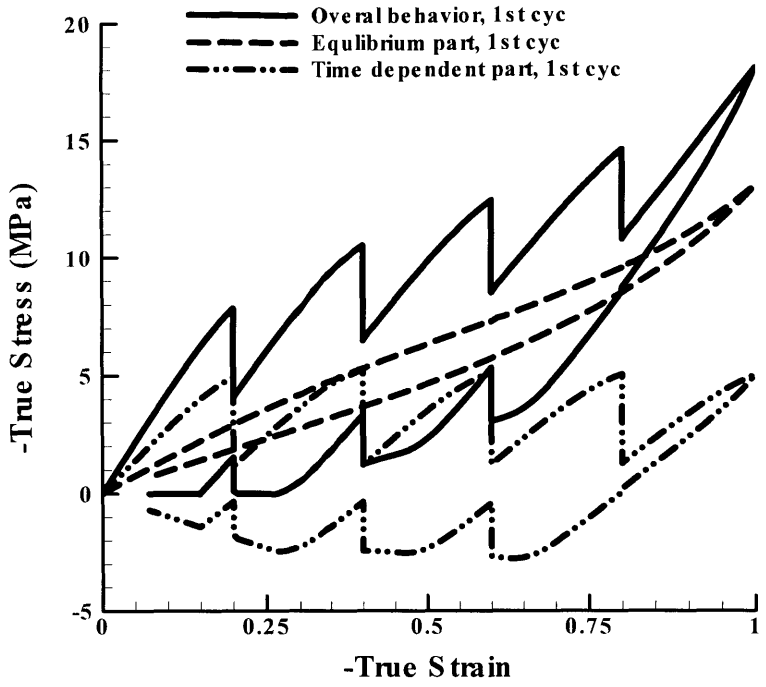

Figure 4-21(c)

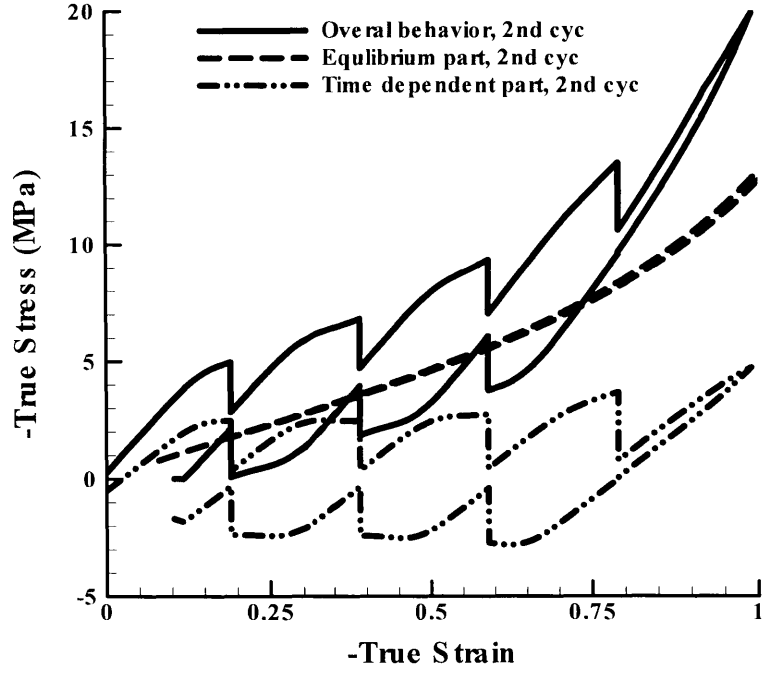

Figure 4-21(d)

Figure 4-21: Numerical simulations on relaxation test: (a) 1st cycle; (b) stabilized curves; Decomposition the material stress-strain behavior into (c) an equilibrium part and (d) a time dependent part.

4.6 Summary and Future Work

A constitutive model accounting for the rate dependent hysteresis behavior of polyurethane materials and the Mullins' cyclic softening behavior is presented in this chapter. The constitutive model decomposes the material behavior into a rate-independent equilibrium part and a rate-dependent viscoelastic-plastic part. For the the softening of equilibrium path, the model adopts the concept of amplified strain, and takes the strain amplification factor to evolve with loading history due to structure reorganization of the soft and hard domains to effectively increase the volume fraction of effective soft domain. Comparison of numerical simulations of uniaxial compression tests with experimental data verifies the proposed constitutive model. The model adequately captures the Mullin's effect and rate dependent behavior of the TPUs, and captures the strain relaxation behavior of the material.

It is believed that during large deformation of TPUs, the underlying material structure will undergo significant changes, such as reorientation of molecular network, damage development and recovering. As the result of such change, the rate dependent parameter should evolve with the deformation. The underlying physical process for these evolution rules is not clear. The softening effects can also demonstrate certain amount of anisotropy. In the future, multi-scale modeling, together with advanced experiments monitoring material structure change, should be used to explore these important aspects.

References

[4-1] Schollenbenger, C.S., Scott, H., Moore, G.R., Polyurethane VC, a virtually crosslinked elastomer, Rubber World, 137, 1958, pp549.

[4-2] Petrovic, Z., Ferguson, J., Polyurethane elastomers. Prog. Polym. Sci., 16, 1991, pp695-836.

[4-3] Wang, C.B., Cooper, S.L., Morphology and properties of segmented polyether polyurethaneureas, Macromol. 16, 1983, pp775-786.

[4-4] Estes, G.M., Seymour, R.W., Cooper, S.L., Infrared studies of segmented polyurethane elastomers. II, Macromol., 4, 1971, pp452-457.

[4-5] Cooper, S.L., Tobolsky, A.V., Textile Research J., 36, pp800, 1966.

[4-6] Estes, G.M., Seymour, R.W., Huh, D.S., Cooper, S.L., Polymer. Engr. Sci., 9, pp383, 1969.

[4-7] Koutsky, J.A., Hien, N.V., Cooper, S.L., Some results on electron microscope investigations of polyether-urethane and polyester-urethane block copolymers, Polymer lett., vol.8, pp353-359, 1970.

[4-8] Chen Tai, C.H.Y., Thomas, E.L., MacKnight, W.J., Schneider, N.S., Structure and morphology of segmented polyurethanes. 3. Electron microscopy and small angle X-ray scattering studies of amorphous random segmented polyurethanes, Polym., 27, 1986, pp659.

[4-9] Hepburn, C., Polyurethane Elastomers, Applied Science, London, 1982.

[4-10] Petrovic, Ferguson, J., Polyurethane elastomers, Prog. Polym. Sci., 16, 1991, pp695.

[4-11] Bergström, J.S., Boyce, M.C., Constitutive modeling of the large strain time-dependent behavior of elastomers, J. Mech. Phys. Solids, 46, 1998, pp931-954.

[4-12] Lion, A., A constitutive model for carbon black filled rubber, experimental investigation and mathematical representation. Continuum Mech. Thermodyn., 6, 1996, pp153-169.

[4-13] Mullins, L., Tobin, N.R., Stress softenings in natural rubber vulcanizates, Part I, J. Appl. Polymer Sci., 9, 1965, pp2993-3010.

[4-14] Mullins, L., Softening of rubber by deformation, Rubber Chem. Tech., v42, 1969, pp339-362.

[4-15] Bueche, F., Mullins effect and rubber-filler interaction. J. Appl. Polym. Sci., 5, 1961, pp271-281.

[4-16] Govindjee, S., Simo, J., Transition from micro-mechanics to computationally efficient phenomenology: carbon black filled rubbers incorporating Mullins' effect. J. Mech. Phys. Solids, 40, 1992, pp213-233.

[4-17] Boyce, M.C., Socrate, S., Yeh, O.C., Kear, K., Shaw, K., Micromechanisms of Deformation and Recovery in Thermoplastic Vulcanizates, J. Mech. Phys. Solids, 49, 2001, pp.1073-1098.

[4-18] Boyce, M.C., Yeh, O.C., Socrate, S., Kear, K., Shaw, K., Micromechanisms of the Cyclic Softening in Thermoplastic Vulcanizates, J. Mech. Phys. Solids, 49,

2001, pp. 1343-1360.

[4-19] Trick, G.S., J. Polym. Sci., 3, 1960, pp252.

[4-20] Boyce, M.C., Kear, K., Socrate, S., Shaw, K., Deformation of thermoplastic vulcanizates, J. Mech. Phys. Solids, Vol.49 (2001), pp1073-1098.

[4-21] Harwood, J.A.C., Mullins, L., Payne, A.R., Stress softening in natural rubber vulcanizates, Part II. 9, 1965, pp3011-3021.

[4-22] Harwood, J.A.C., Payne, A.R., Stress softening in natural rubber vulcanizates, Part III., J. Appl. Polymer Sci., 10, 1966, pp315-324.

[4-23] Harwood, J.A.C., Payne, A.R., Stress softening in natural rubber vulcanizates, Part IV., J. Appl. Polymer Sci., 10, 1966, pp1203-1211.

[4-24] Mullins, L., Tobin, N.R., Theoretical model for the elastic behavior of filler-reinforced vulcanized rubber, Rubber Chem. Technol., v30, 1957, pp555-571.

[4-25] Blanchard, A.F., Parkinson, D., Ind. Eng. Chem., 44, 1952, pp799.

[4-26] Beuche, F., J. Appl. Polym. Sci., 4, pp107.

[4-27] Dannenberg, E.M., The effects of surface chemical interactions on the properties of filler-reinforced rubbers. Rubber Chem. Tech., 48, 1974, pp410-444.

[4-28] Rigibi, Z., Adv. Poly. Sci., 36, 1980, pp21.

[4-29] Simo, J.C., On a fully three-dimensional finite-strain viscoelastic damage model: formulation and computational aspects, Compu. Method Appl. Mech. Eng., 60, 1987, pp153-173.

[4-30] Govindjee, S., Simo, J., A micro-mechanically based continuum damage model for carbon black-filled rubbers incorporating Mullin's effect. J. Mech. Phys. Solids, 39, 1991, pp87-112.

[4-31] Miehe, C., Keck, J., Superimposed finite elastic-viscoelastic-plastoelastic response with damage in filled rubbery polymers. Experiments, modeling and algorithmic implementation, J. Mech. Phys. Solids, 48, 2000,pp323-365.

[4-32] Lion, A., a physically based method to represent the thermo-mechanical behavior of elastomers, Acta Mechanica, 123, 1997, pp1-25.

[4-33] Ogden, R.W, Roxburgh, D.G., a pseudo-elastic model for the Mullins effect infilled rubber, Proc. R. Soc. Lond. A, 455, 1999, pp2861-2877.

[4-34] Ogden, R.W, Roxburgh, D.G., an energy-based model of the Mullins effect,

Proceedings of the First European Conference on Constitutive Models for Rubber, 1999, Belkema, Rotterdam.

[4-35] Dorfmann, A., Ordge, R.W., a pseudo-elastic model for loading, partial unloading and reloading of particle-reinforced rubber, Int. J. Solids Struct., 40, 2003, pp2699-2714.

[4-36] Cooper, S.L., Huh, D.S., Morris, W.J., in Encyclopedia of Polymer Science and Technolgy, Supplementary Volume, Wiley, New York, 1976, pp521.

[4-37] Bonart, R., J. Macromol. Sci., Phys, 1968, B2, pp115

[4-38] Bonart, R., Morbitzer, L., Hentze, G., X-ray investigations concerning the physical structure of cross-linking in urethane elastomers, II, J. Macromol. Sci. Phys., B3, 1969, 337-356.

[4-39] Bonart, R., Muller-Riederer, G., Colloid polym. Sci., 259, 1981, pp926-936.

[4-40] Sung, C.S.P., Hu, C.B., Wu, C.S., Properties of segmented poly(urethaneureas) based on 2,4-toluene diisocyanate, I. Macromol., 13, 1980, pp111-116.

[4-41] Sung, C.S.P., Smith, T.W., Sung, N.H., Properties of segmented poly(urethaneureas) based on 2,4-toluene diisocyanate, II. Macromol., 13, 1980, pp117-121.

[4-42] Sung, C.S.P., Smith, T.W., Hu, C.B., Sung, N.H., Hysteresis behavior in polyether poly(urethaneureas) based on 2,4-toluene diisocyanate, ethylenediamine, and poly(tetramethylene oxide). Macromol., 12, 1979, pp538-540.

[4-43] Wilkes, G.L., Abouzahr, S., SAXS studies of segmented polyesther poly(urethaneurea) elastomers, Macromol., 14, 1981, pp456-458.

[4-44] Kimura, I., Ishihara, H., Ono, H., Yashihara, N., Nomura, S., Kawai, H., Morphology and deformation mechanism of segmented poly(urethaneureas) in relation to spherulitic crystalline textures. Macromol., 7, 1974, pp355-363.

[4-45] Ishihara, H.; Kimura, I., Saito, K.; Ono, H. J. Macromol. Sci. Phys., 1974, B10(4), 591.

[4-46] Yeh, F., Hsiao, B.S., Sauer, B.B., Michel, S., Siesler, H.W., In situ studies of structure development during deformation of a segment poly(urethane-urea) elastomer. Macromol., 36, 2003, pp1940-1954.

[4-47] Sauer, B.B., Mclean, R.S., Brill, D.J., Londono, D.J., Morphology and orientation

during the deformation of segmented elastomers studied with small-angle X-ray scattering and atomic force microscopy. J. Ploym. Sci., 40, 2002, pp1727-1740.

[4-48] Sequela R., Prudhomme, J., Macromol., 11, 1978, pp1007.

[4-49] Rajagopal, K.R., Wineman, A.S., a constitutive model for nonlinear solids which undergo deformation induced microstructural changes, J. Plasticity, 8, 1992, pp385-395.

[4-50] Wineman, A.S., Huntley, H.E., numerical simulation of effect of damaged induced softening on the inflation of a circular rubber membrane, Int. J. Solids Struct., 31, 1994, pp3295-3313.

[4-51] Johnson, M.A., Beatty, M.F., the mullins effect in uniaxial extension and its influence on the transverse vibration of a rubber string, Comtinuum Mech. Thermodyn., 5, 1993, pp83-115.

[4-52] Johnson, M.A., Beatty, M.F., a constitutive equation for the Mullins effect in stress controlled uniaxial extension experiments, Comtinuum Mech. Thermodyn., 5, 1993, pp301-318.

[4-53] Beatty, M.F., Krishnaswamy, S., a theory of stress-softening in incompressible isotropic materials, J. Mech. Phys. Solids, 48, 2000, pp1931-1965.

[4-54] Bergstrom, J., Boyce, M.C., Mechanical behavior of particle filled elastomers, Rubber Chem. Tech., 72, 1999, pp633-pp656.

[4-55] Bergström, J.S., Boyce, M.C., Large strain time-dependent behavior of filled elastomers, Mechanics of Materials, Vol.32, 2000, pp627-644.

[4-56] Medalia, A.I., Kraus, G., Science and Technology of Rubber, Academic Press Inc., New York, 1994, pp387.

[4-57] Einstein, A., Ann. Physik. (Leipzig) 19, 1906, pp289.

[4-58] Einstein, A., Ann. Physik. (Leipzig) 34, 1911, pp591.

[4-59] Smallwood, H.M., J. Appl. Phys., 15, 1944, pp758.

[4-60] Guth, E., Gold, O., Phys. Rev., 53, 1938, pp53.

[4-61] Guth, E., Simha, R., Kolloid-Z, 74, 1936, pp266.

[4-62] Guth, E., J. Appl. Phys., 16, 1940, pp20.

[4-63] Arruda, E.M., Boyce, M.C., A Three-dimensional constitutive model for the large stretch behavior of elastomers, J. Mech. Phys. Solids, Vol.46, No.5, pp931-954.

[4-64] Boyce, M.C., Parks, D.M., Argon, A.S., Large inelastic deformation of glassy polymers, Part I: rate dependent constitutive model, Mechanics of Materials, Vol.7, 1988, pp15-33.

[4-65] Argon, A.S., A theory for the low temperature plastic deformation of glassy polymers, Philosophical Magazine, v.28, n.4, 1973, pp839-865.

[4-66] Argon, A.S., Bessonov, M.I., Plastic deformation in polyimides, with new implications on the theory of plastic deformation of glassy polymers, Philosophical Magazine,35, 1977, pp917-933.

Chapter 5

FEM Simulations of Micro Indentation and Scratching Tests

In this chapter, computational modeling studies on the mechanics of the micro indentation and scratching tests are conducted using the finite element method (FEM). The first section will introduce the models for the FEM simulations. The second section will compare the displacement and strain fields obtained by FEM with those obtained by image processing of the SEM micrographs from the in-situ micro indentation/scratching tests in Chapter 2. The third section studies the effects of the indentation depth, contact condition, and cyclic scratching on the mechanics of the scratching, and investigates the underlying mechanics and mechanism for the damage observed in the Zygo-SEM surface topography studies in Chapter 3. The fourth section conducts parametric studies on the mechanics of indentation and scratching by varying the parameters in the FEM model, i.e. the contact friction coefficient (or the adhesive force), the scratching speed, and the material properties. In section five, mechanics of the scratching tests on glass fiber filled TPUs is investigated by studying three representative orientations of the fiber in the material. Conclusions and future research directions will be discussed in the last section.

5.1 Physical and Numerical Model

5.1.1 Physical Model

The finite element model is developed to investigate the scratching tests, which were studied experimentally in Chapter 2 where direct observation of deformation of the material surface ABCD (Figure 5-1) was established. Figure 5-1(a) shows a schematic of the scratching test. Since the side surface ABCD is free of normal traction, the surface deformations observed in the in-situ tests are essentially in plane stress state. However, the goal of current research is to study the mechanics of abrasive wears, where the most critical deformations and stresses occur in the middle of the contact zone between an

abrasive particle and the material (the projection of line KL on the material surface EADH). In this regard, the problem of interest of current research is a plane strain one, and thus is modeled as a two-dimensional plane strain problem. Note that the in-plane displacement fields of surface ABCD will be nearly identical to the displacement fields of any interior parallel plane (most of which are in a plane strain state).

In the tests, the two ends of the sample (EFBA and HGCD) were fixed by two screws and the distance between them was about 15mm. The locations for indentations were generally at least 3mm away from one of the ends and the scratching distance was about 5~7mm. The indentation depth was less than 100μm whereas the thickness of the sample was about 3mm. A metal tape was used between the sample surface FBCG and the sample holder to ensure full contact between the two surfaces.

The model for FEM simulations is built based on the test geometry and the consideration of the computational efficiency. Figure 5-1(b) shows the schematics of the model for FEM simulations. The edge AB and CD are fixed in the x-direction but are allowed to move in the y-direction, i.e., $u_1\big|_{AB} = u_1\big|_{DC} = 0$. The back surface BC of the sample is fixed in both x and y directions. In simulations, the indentation depth is less than 100μm and scratching distance was 120-160 μm. The dimension of the model is chosen to be 3mm by 6mm (Figure 5-1(b)). The large ratio between the dimensions of the model and the applied displacement ensures that the model can provide boundary conditions similar to the real tests.

The material stress-strain behavior is modeled using the constitutive model developed in Chapter 4. The knife is modeled as a rigid surface of the wedge shape with a rounded tip based on the observation from the SEM micrograph of the knife tip (Figure 5-2(a)). The half angle of the tip is 15° and the tip radius is 3-8μm. Figure 5-2(b) shows the simplification of the knife geometry used in the finite element simulations. The tip radius used in simulation is 6μm.

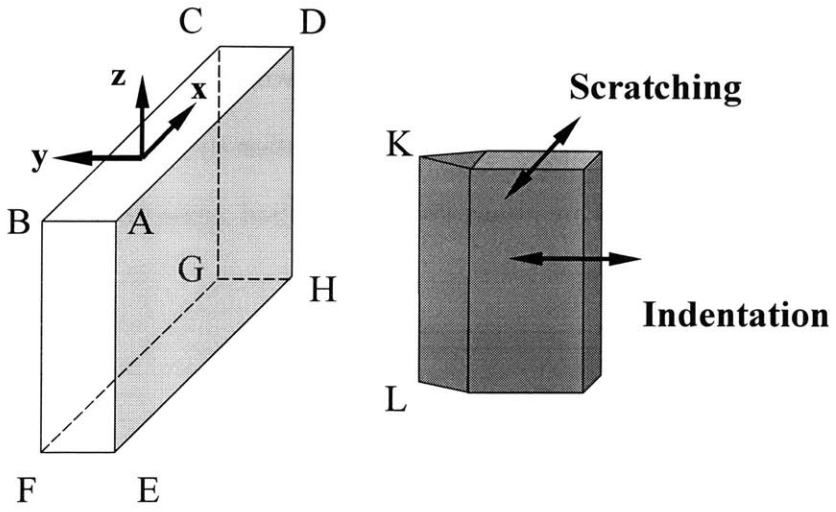

Figure 5-1(a)

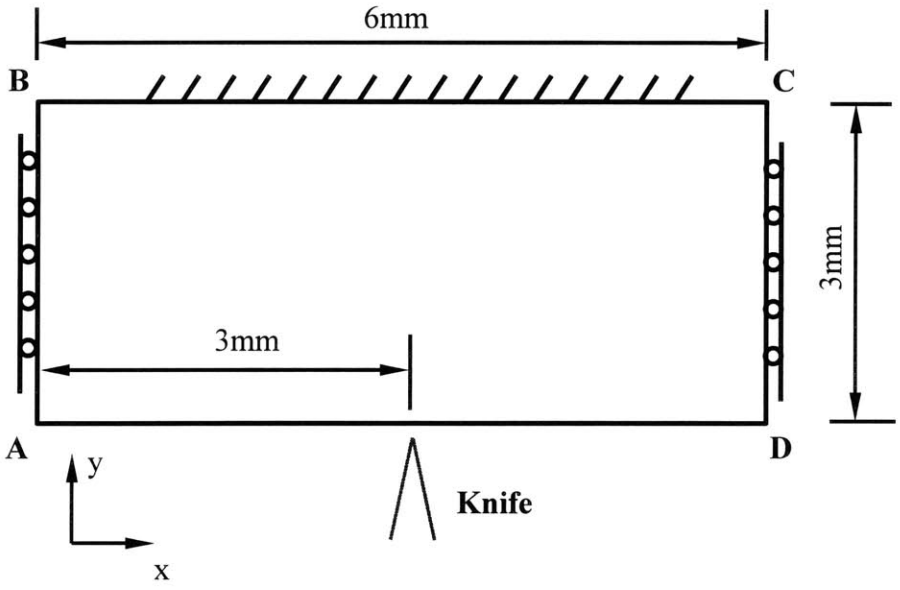

Figure 5-1(b)

Figure 5-1: Schematics (a) of scratching tests; (b) of the model for FEM simulations

The loading conditions used in simulations follow the same scheme as those in the tests (Figure 5-3). Indentation and scratching are realized by applying proper motions to the knife, i.e., a y-direction translation of the knife u_2 normal to the surface creates the indentation motion whereas an x-direction translation u_1 tangential to the surface creates the scratching motion. In figure 5-3, the indentation is first applied until a maximum indentation depth of $\delta_n^{\max}$ is reached. The indentation depth is then held constant and the

scratching is applied until a maximum scratching distance of δ_t^{max} is achieved. In the simulations of cyclic scratching, the knife is withdrawn by decreasing δ_n to zero from δ_n^{max}. The knife is then moved back to its original position by decreasing δ_t to zero from δ_t^{max}. The loading conditions in Figure 5-3 are applied again to generate the second indentation and scratching cycle.

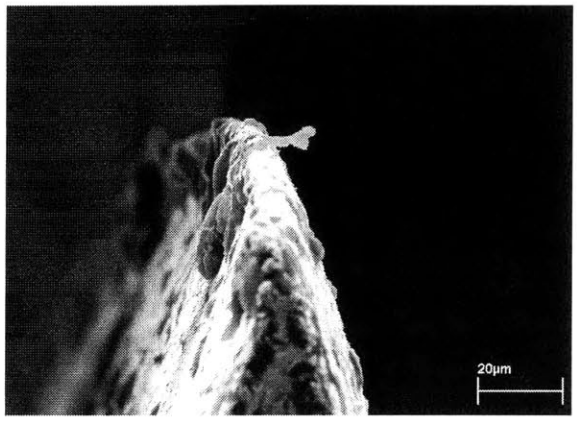

Figure 5-2(a)

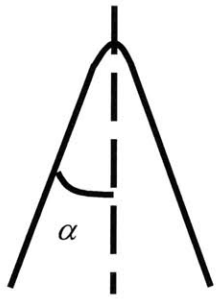

Figure 5-2(b)

Figure 5-2: (a) SEM micrograph of the knife; (b) Model for the knife.

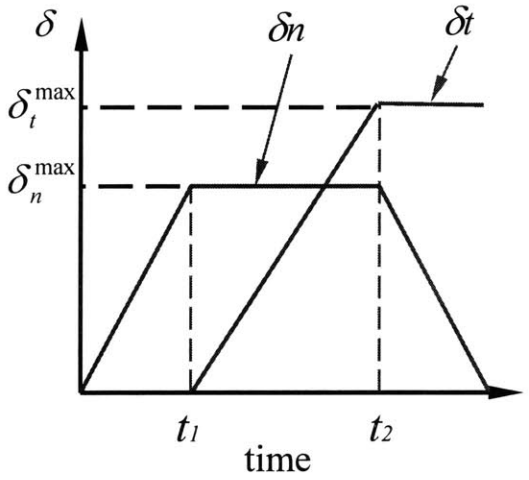

Figure 5-3: Knife displacement history.

5.1.2 FEM Model

The boundary value problem presented in Figure 5-1(b) is solved using the finite element software package ABAQUS. Plane strain quadratic hybrid continuum elements with

biquadratic interpolation of the displacement field and linear interpolation of pressure are used to model the elastomer. Figure 5-4(a) shows the mesh used for the simulations. It has 11202 nodes and 3670 elements. The mesh is refined near the contact region where large gradients in stress and strain prevail due to the large ratio between indentation depth and the knife tip radius. Several mesh densities were analyzed and an optimal mesh was finally chosen for use in all simulations.

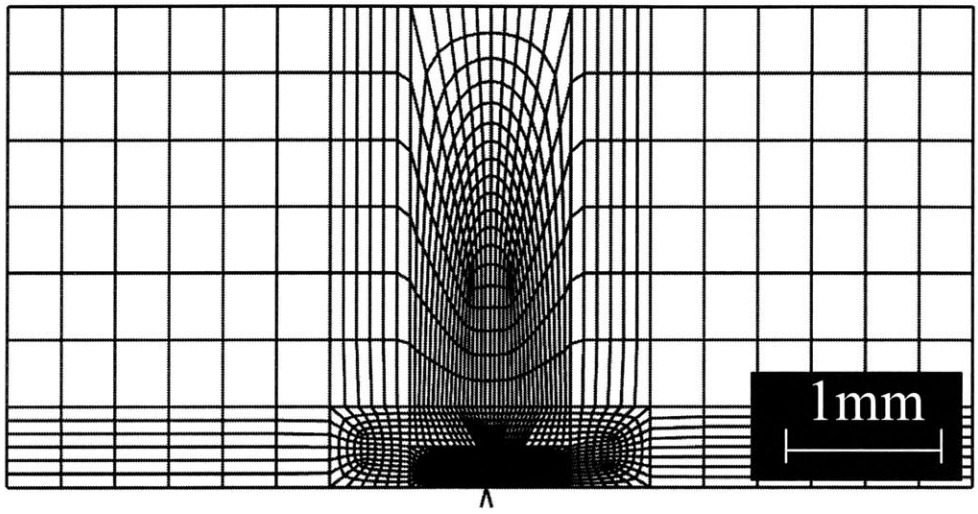

Figure 5-4(a)

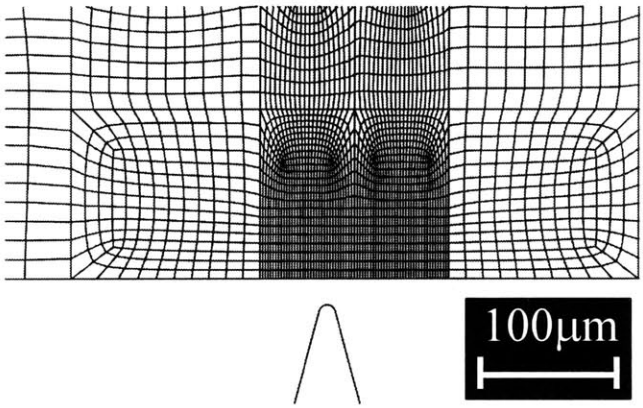

Figure 5-4(b)

Figure 5-4: (a) The mesh used for finite element simulations; (b) Refined mesh near the contact region.

The knife is modeled as a rigid contact surface since it is much stiffer than elastomers. Contact conditions are applied between the knife and the element surface where the contact occurs. A frictional coefficient of 0.1 is applied to simulate the real

contact conditions.

5.2 Comparisons with Experiments

Numerical simulation results are compared with observations from image processing of the deformation fields obtained in SEM micrographs. These comparisons provide verification of the FEM model.

5.2.1 δn=50μm for Unfilled TPU with Wedge-type Knife

A FEM simulation with indentation depth of $\delta_n = 50\mu m$ is first conducted. The indentation speed is $2\mu m/s$ and the scratching speed is $4\mu m/s$, corresponding to the speeds in the test. Figure 5-5(a) shows the normal/tangential force vs time curves. The corresponding curves from the test are also shown in Figure 5-5(b) for comparison. The FEM simulation nicely captures the overall reaction forces. During indentation, the normal force increases linearly. Upon scratching, the normal force experiences a decrease then becomes a constant. The tangential force increases first linearly then gradually bends over toward a constant force, resulting in an overall nonlinear increase in tangential force. Numerical simulation using Arruda-Boyce eight chain model (examples of such simulation are presented in the fourth section), which only captures the equilibrium behavior of elastomeric materials and does not account for the time dependence and stress relaxation, do not show such variations in normal and tangential forces. Therefore, such features are believed to be due to time dependent aspect of the material behavior.

Figure 5-5(c) shows the effective friction coefficient, defined as the ratio between the tangential force and the normal force. It is noticed that even though the contact friction coefficient used in the FEM model is only 0.10, the effective friction coefficient is predicted to be about 1.0, in agreement with the result from the test. Clearly, effective friction behavior of the scratching test is affected by the contact friction as well as other factors, such as material blocking, as will be discussed later.

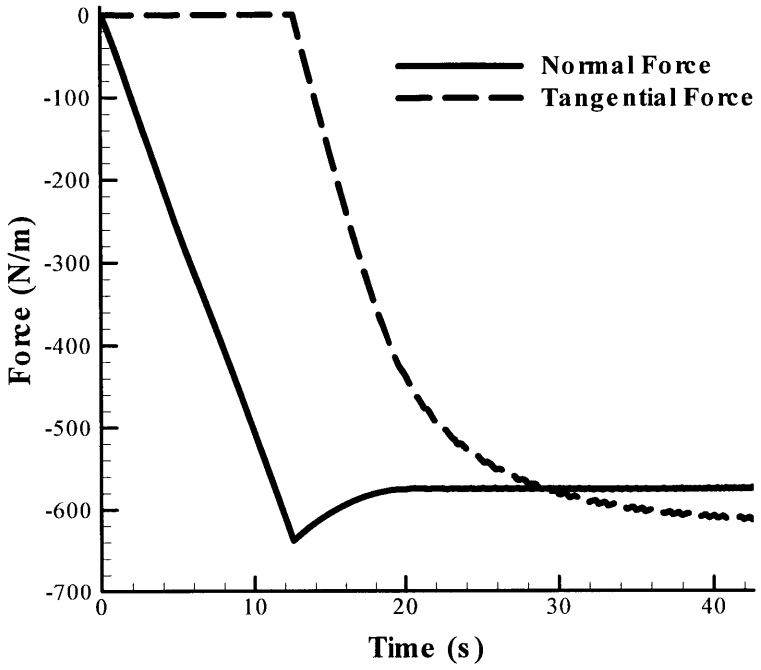

Figure 5-5(a)

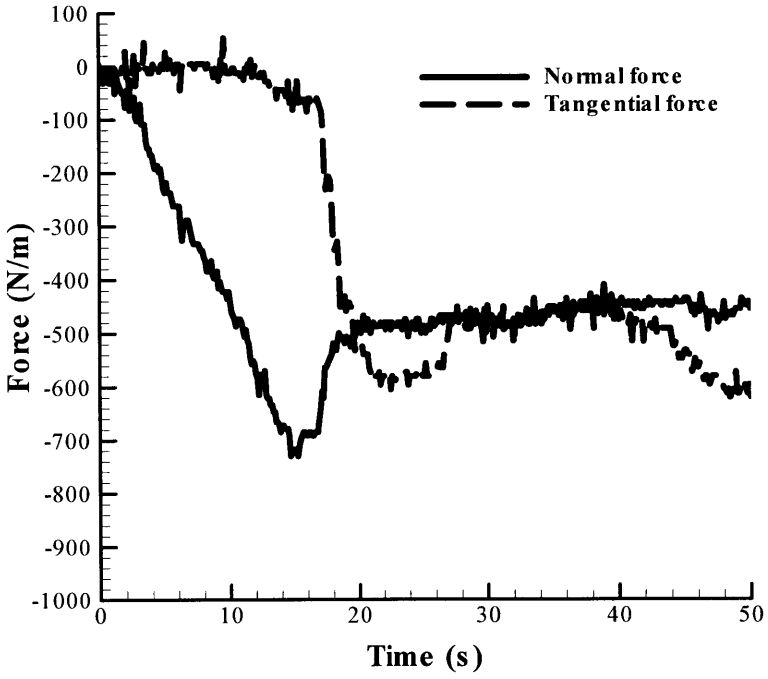

Figure 5-5(b)

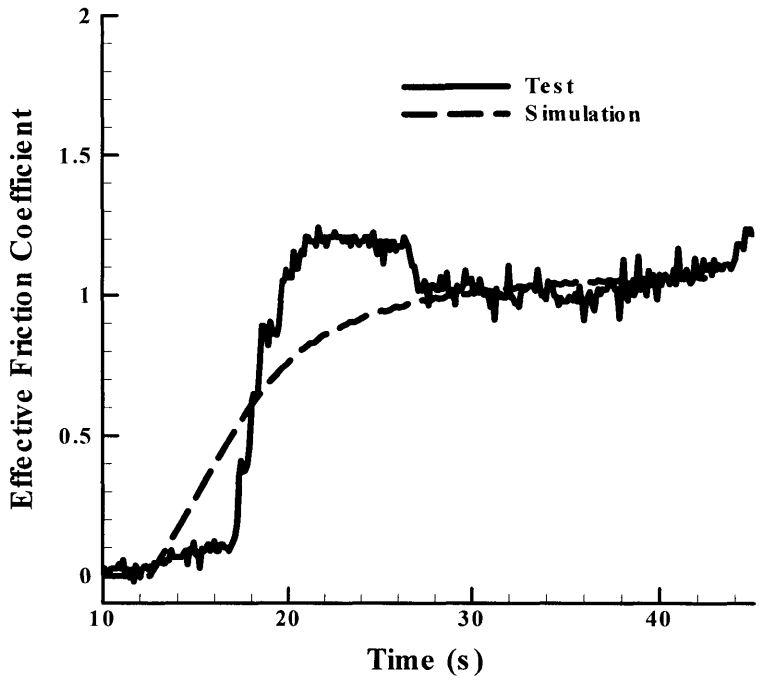

Figure 5-5(c)

Figure 5-5: Normal/tangential force vs time curves (a) from numerical simulations; (b) from tests; (c) Effective friction coefficient.

Contour plots in Figure 5-6 show the displacement fields immediately after the indentation, i.e., δn=50μm, δt=0μm. For the purpose of comparison with the results from the test, contour plots obtained from image processing of the SEM micrographs are also presented in Figure 5-6. In order to achieve better comparison, contour plots for the same variables are presented based on the same scale (In the remainder of this section, for the same purpose, contour plots for the same variables are presented based on the same scale). For the displacement u_1 (Figure 5-6(a) and (b)), the color changes from the blue for the displacement of -5μm to the red for the displacement of 5μm. For the displacement u_2 (Figure 5-6(c) and (d)), the red color represents the displacement of 30μm, where the blue represents the displacement of 7μm. Both numerical simulation and image processing give similar features of the displacement fields: The u_1 contour shows material being pushed in the horizontal direction with maximum displacement occurring along 45° lines away from the center line; The u_2 contour show the decrease of the displacement from the contact point to the far field. This excellent similarity between

the contour plots from the numerical simulation and the test verifies the numerical simulation results.

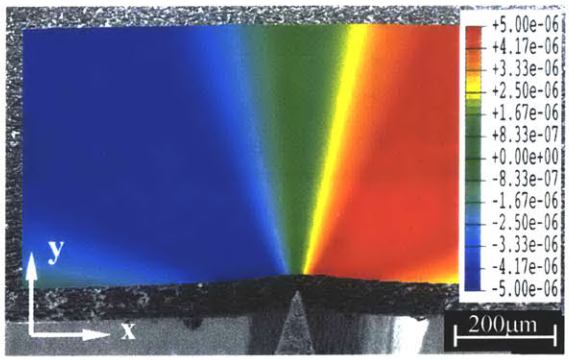

Figure 5-6(a)

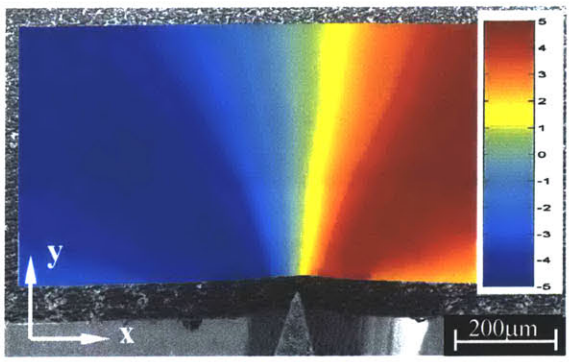

Figure 5-6(b)

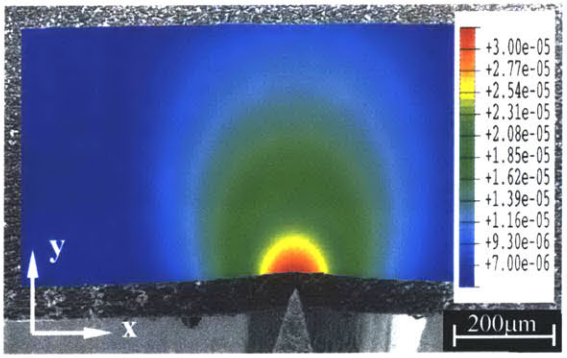

Figure 5-6(c)

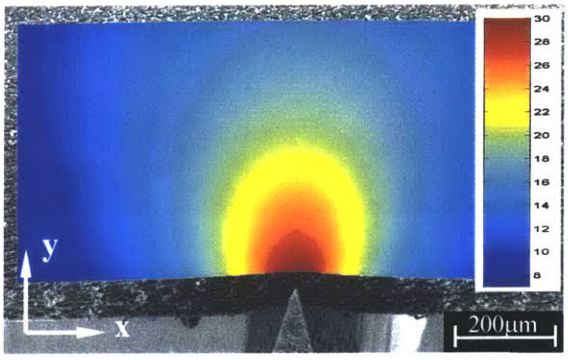

Figure 5-6(d)

Figure 5-6: Displacement fields for the indentation/scratching test with δn=50μm, δt=0μm: (a) u_1 contour from FEM simulation; (b) u_1 contour from image processing of SEM micrographs; (c) u_2 contour from FEM simulation; (d) u_2 contour from image processing of SEM micrographs.

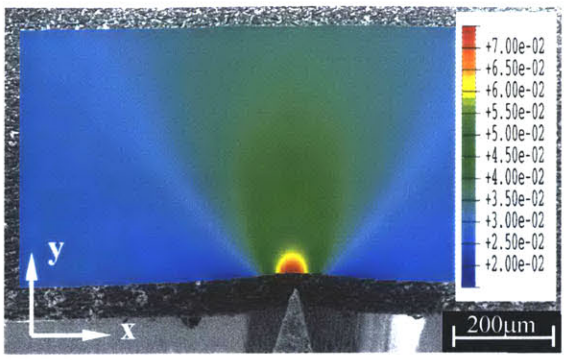

Figure 5-7(a)

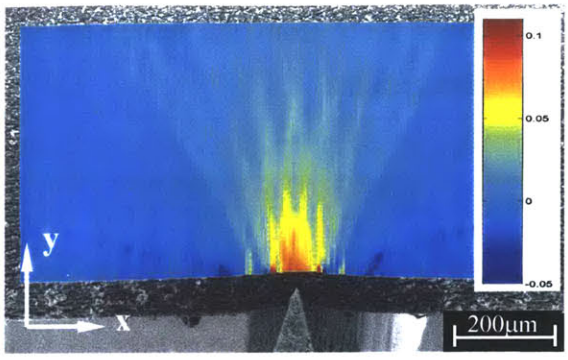

Figure 5-7(b)

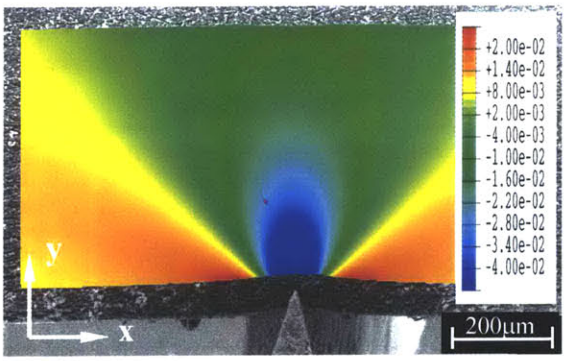

Figure 5-7(c)

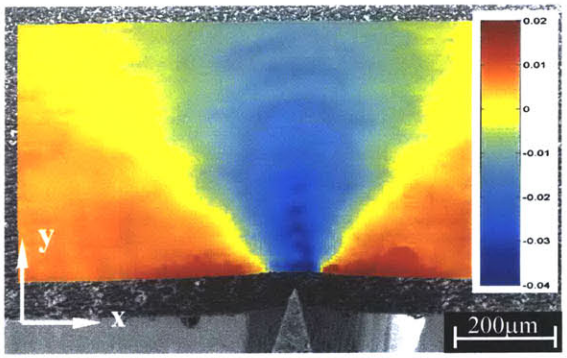

Figure 5-7(d)

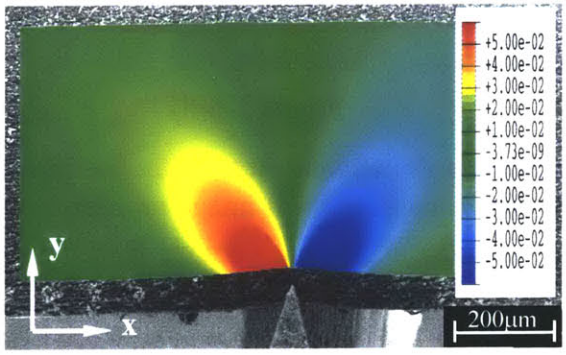

Figure 5-7(e)

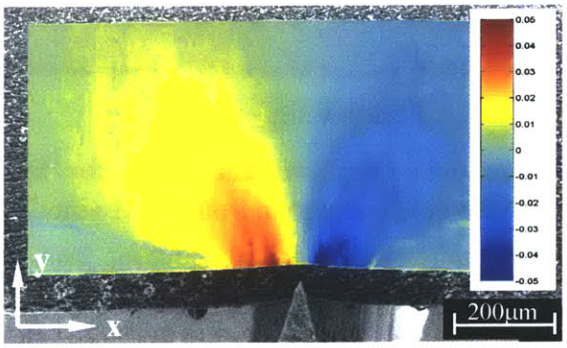

Figure 5-7(f)

Figure 5-7: Strain fields for the indentation/scratching test with δn=50μm, δt=0μm: (a) ε_{11} contour from FEM simulation; (b) ε_{11} contour from image processing of SEM micrographs; (c) ε_{22} contour from FEM simulation; (d) ε_{22} contour from image processing of SEM micrographs; (e) ε_{12} contour from FEM simulation; (f) ε_{12} contour from image processing of SEM micrographs.

The strain contour plots from both numerical simulations and image processing of SEM micrographs are presented in Figure 5-7. For the strain ε_{11} (Figure 5-7(a) and (b)), the blue color represents the strain of -0.02, whilst the red color represents the strain of

0.07. For the strain ε_{22} (Figure 5-7(c) and (d)), the blue color represents the strain ε_{22} of about -0.04, to the red for the strain ε_{22} of about 0.02. For the strain ε_{12} (Figure 5-7(e) and (f)), the blue color represents the strain of -0.05, to the red for the strain of 0.05. Due to the noise in the test results, the strain contour plots obtained from image processing show some un-smooth variations, most pronounced for ε_{11}. However, both numerical simulation and image processing give similar features of the strain fields: Below the contact point, the material is subjected to tensile strain along the horizontal direction and compression strain along the vertical direction. The strain decreases along the radial direction. The excellent similarity further verifies the capability of the numerical model to generate correct strain results.

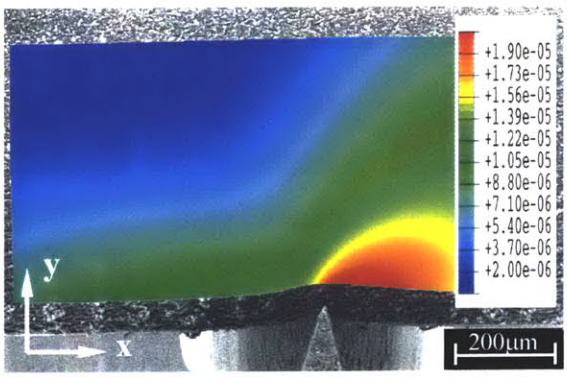

Figure 5-8(a)

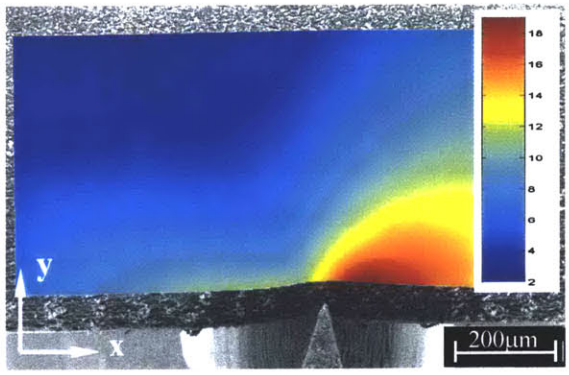

Figure 5-8(b)

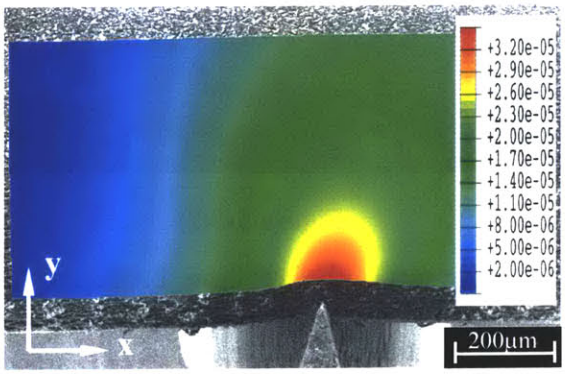

Figure 5-8(c)

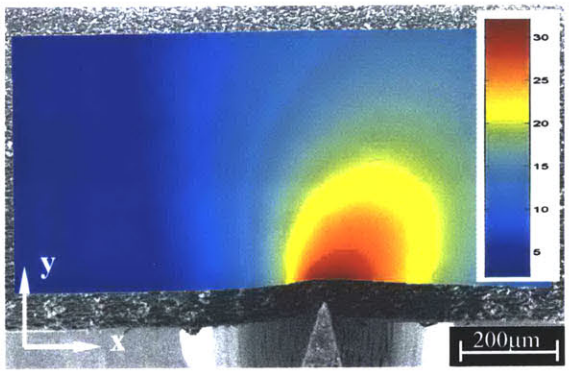

Figure 5-8(d)

Figure 5-8: Displacement fields for the indentation/scratching test with δn=50μm, δt=60μm: (a) u_1 contour from FEM simulation; (b) u_1 contour from image processing of SEM micrographs from; (c) u_2 contour from FEM simulation; (d) u_2 contour from image processing of SEM micrographs.

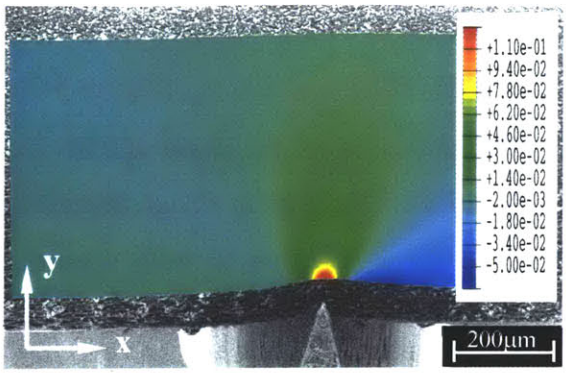

Figure 5-9(a)

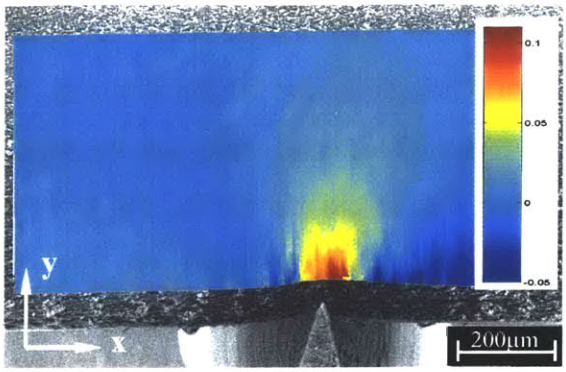

Figure 5-9(b)

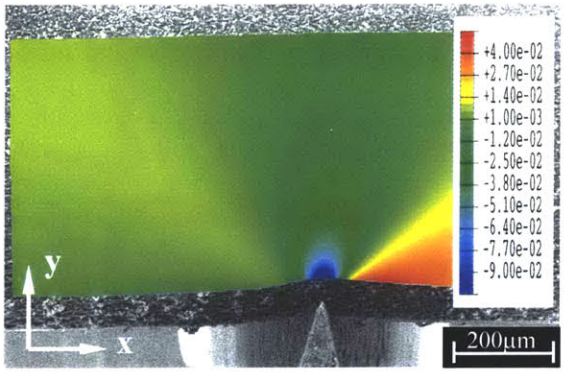

Figure 5-9(c)

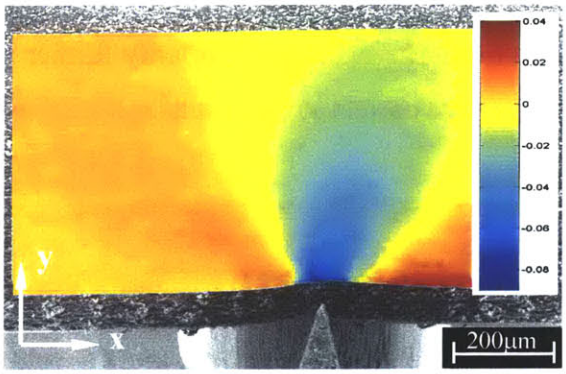

Figure 5-9(d)

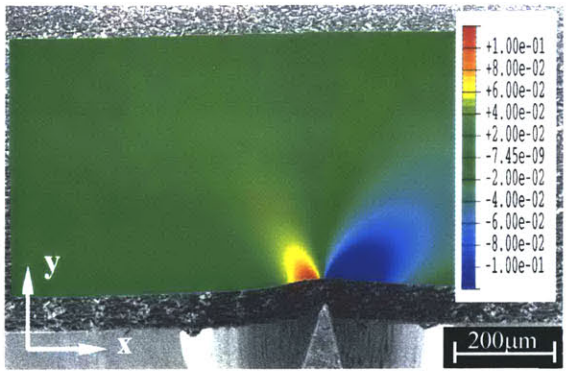

Figure 5-9(e)

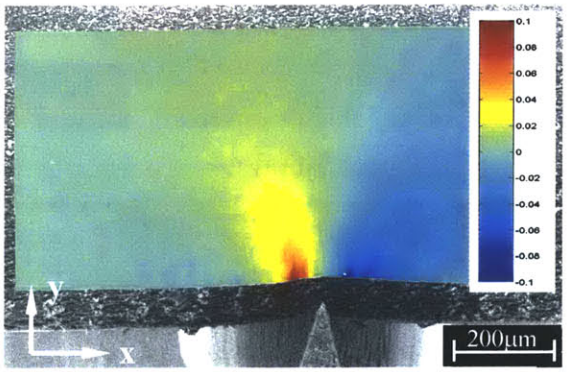

Figure 5-9(f)

Figure 5-9: Strain fields for the indentation/scratching test with δn=50μm, δt=60μm: (a) ε_{11} contour from FEM simulation; (b) ε_{11} contour from image processing of SEM micrographs; (c) ε_{22} contour from FEM simulation; (d) ε_{22} contour from image processing of SEM micrographs; (e) ε_{12} contour from FEM simulation; (f) ε_{12} contour from image processing of SEM micrographs.

Contour plots in Figure 5-8 show the displacement fields upon scratching, i.e., δn=50μm, δt=60μm. Contour plots obtained from both numerical simulation and image

processing of SEM micrographs are presented in Figure 5-8. For the displacement u_1 (Figure 5-8(a) and (b)), the scale ranges from 2μm (blue) to 19μm (red). For the displacement u_2 (Figure 5-8(c) and (d)), the scale ranges from 2μm (blue) to 32μm (red). Both numerical simulation and image processing give similarly biased displacement fields as the knife moves rightward: The horizontal displacements from FEM simulation and image processing show beautiful butterfly-like symmetric distributions about the line biased from the vertical line by about 30° to the left. The maximum horizontal displacements occur in front of the knife along the line of about 30° away from the horizontal direction, whereas the minimum displacement occurs along the line of about 30° away from the vertical direction. The vertical displacements also show features of biased displacement field: the symmetric lines are about 65° for both FEM results and about 62° for image processing results away from the horizontal direction. The excellent agreements between the directions of the symmetric lines for the biased displacement fields provide solid evidence that the proposed FEM can capture the material deformation behavior during scratching process.

Contour plots for the strain fields upon scratching, i.e., δn=50μm, δt=60μm are presented in Figure 5-9, where both FEM simulation results and the results of image processing of SEM micrographs are presented. For the strain ε_{11} (Figure 5-9(a) and (b)), the scale ranges from –0.05 (blue) to 0.11 (red). For the strain ε_{22} (Figure 5-9(c) and (d)), the scale ranges from –0.09 (blue) to 0.04 (red). For the strain ε_{12} (Figure 5-9(e) and (f)), the scale ranges from –0.10 (blue) to 0.10 (red). The unsymmetrical strain fields clearly demonstrated the biased deformation during scratching.

The remarkable similarity in the displacement and strain fields upon scratching between the FEM results and image processing of SEM micrographs verifies the predictions of the numerical model for scratching tests.

5.2.2 δn=80μm for Unfilled TPU with Wedge-type Knife

FEM simulation with indentation depth of δn=80μm was conducted. The indentation speed was 2μm/s and the scratching speed was 4μm/s, corresponding to the speeds in the test with 80μm. Figure 5-10(a) shows the normal/tangential force vs time curves. The

corresponding curves from the test are also shown in Figure 5-10(b) for comparison. The same features of the curves as those from the test and simulation with $\delta n=80\mu m$ are observed. The FEM simulation nicely captures the overall reaction forces.

Figure 5-10(c) shows the effective friction coefficient. It is noticed that even though the contact friction coefficient used the FEM model is only 0.10, the effective friction coefficient is predicted to be about 1.2, in agreement with the result from the test, but higher than the value in the case with $\delta n=50\mu m$. A detailed discussion about the effective friction behavior in scratching tests will be presented in section 4.

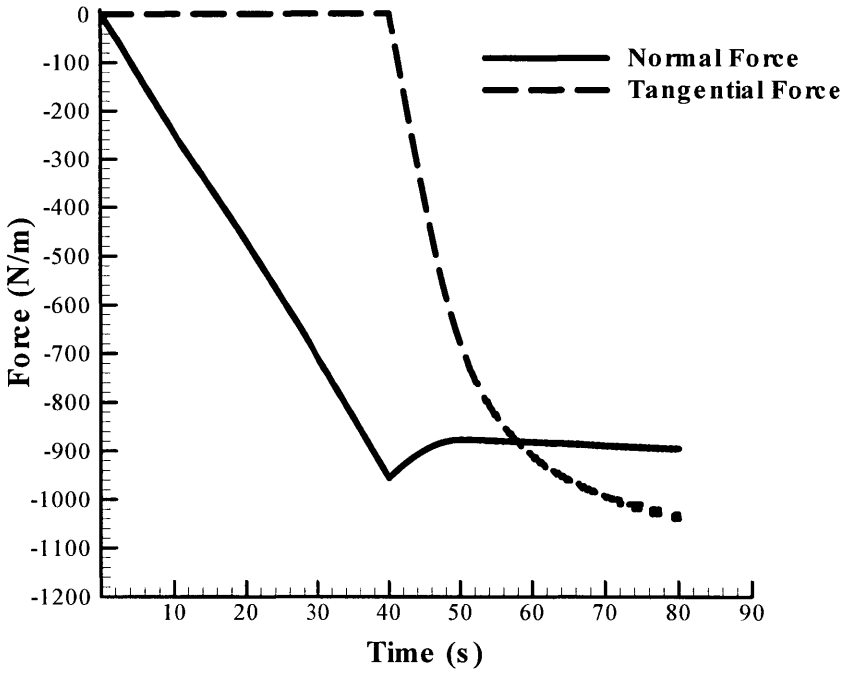

Figure 5-10(a)

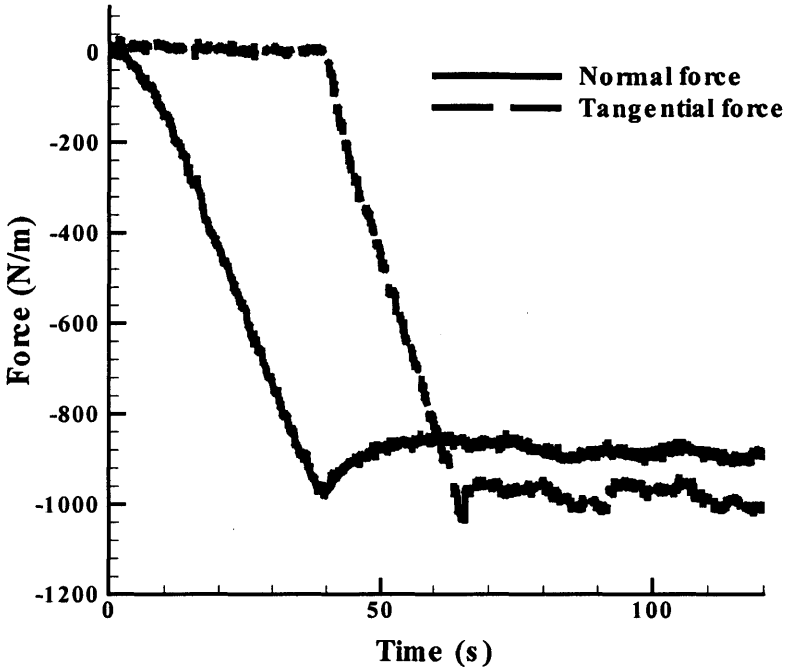

Figure 5-10(b)

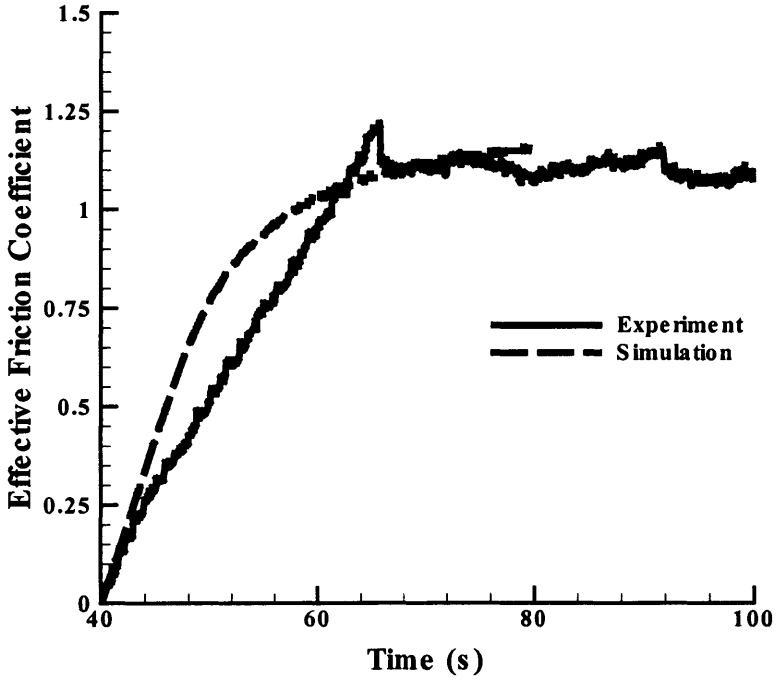

Figure 5-10(c)

Figure 5-10: Normal/tangential force vs time curves (a) from numerical simulations; (b) from tests; (c) Effective friction coefficient.

Contour plots in Figure 5-11 show the displacement field immediately after the indentation, i.e., δn=80μm, δt=0μm. For the displacement u_1 (Figure 5-11(a) and (b)), the color changes from the blue color for the displacement of -7μm to red color for the displacement of 7μm. For the displacement u_2 (Figure 5-11(c) and (d)), the blue represents the displacement of -12μm, whereas the red represents the displacement of 50μm. Both numerical simulation and image processing give similar distributions of the displacement fields: The u_1 contour shows material being pushed in the horizontal direction with maximum displacement occurring along 45° lines away from the center line; The u_2 contour shows the decrease of the displacement from the contact point to the far field. This similarity between the contour plots from the numerical simulation and the test verifies the capability of the proposed model to simulate even more severe deformation, i.e. the test with the indentation depth of δn=80μm.

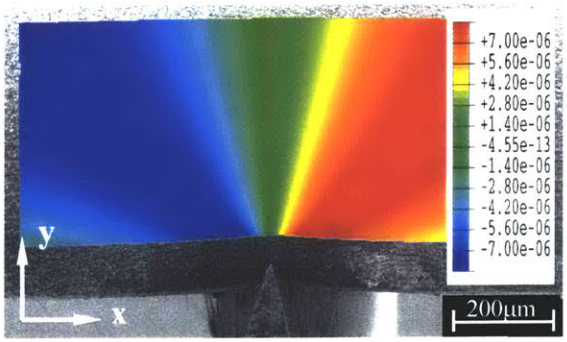

Figure 5-11(a)

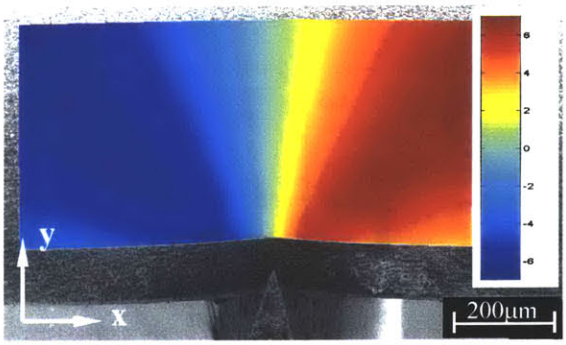

Figure 5-11(b)

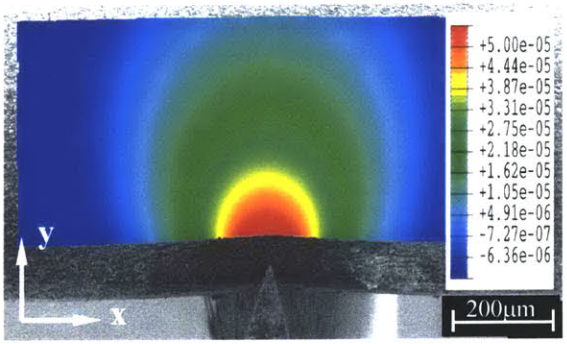

Figure 5-11(c)

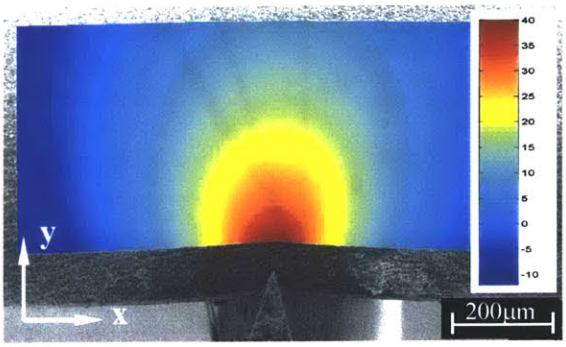

Figure 5-11(d)

Figure 5-11: Displacement fields for the indentation/scratching test with δn=80μm, δt=0μm: (a) u_1 contour from FEM simulation; (b) u_1 contour from image processing of SEM micrographs from the test; (c) u_2 contour from FEM simulation; (d) u_2 contour from image processing of SEM micrographs from the test.

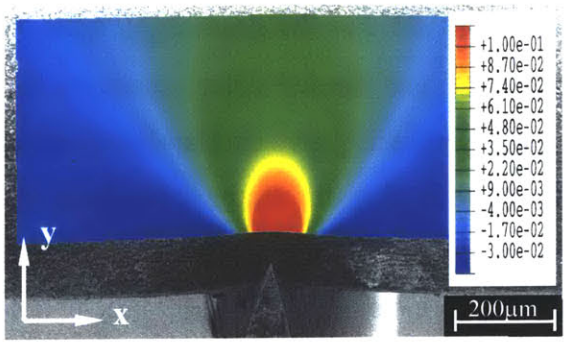

Figure 5-12(a)

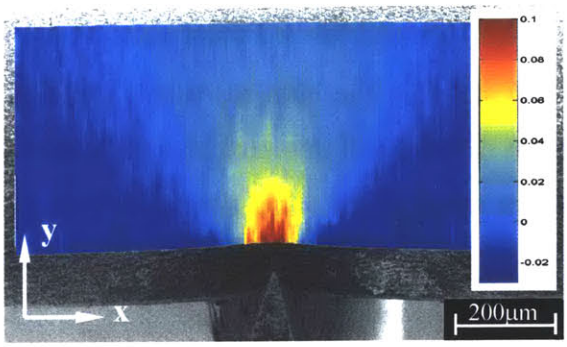

Figure 5-12(b)

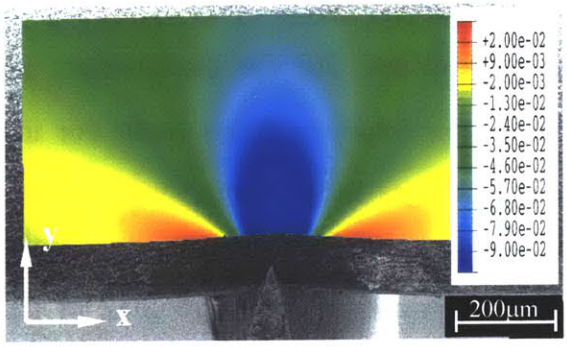

Figure 5-12(c)

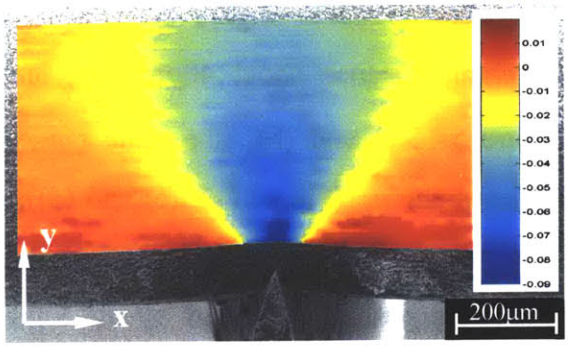

Figure 5-12(d)

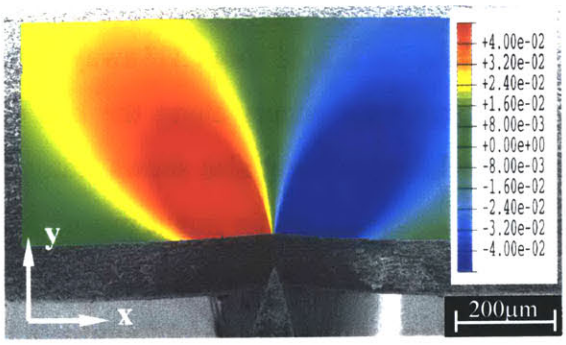

Figure 5-12(e)

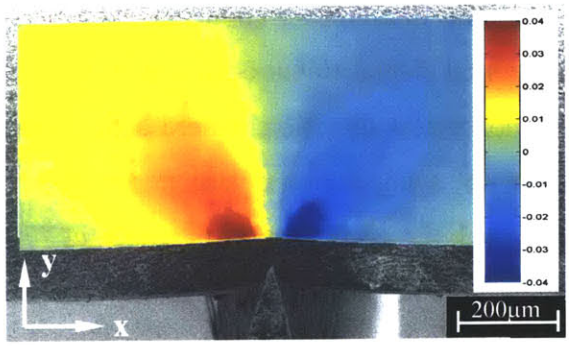

Figure 5-12(f)

Figure 5-12: Strain fields for the indentation/scratching test with δn=80μm, δt=0μm: (a) ε_{11} contour from FEM simulation; (b) ε_{11} contour from image processing of SEM micrographs; (c) ε_{22} contour from FEM simulation; (d) ε_{22} contour from image processing of SEM micrographs; (e) ε_{12} contour from FEM simulation; (f) ε_{12} contour from image processing of SEM micrographs.

The strain contour plots are presented in Figure 5-12. For the strain ε_{11} (Figure 5-12(a) and (b)), the blue represents the strain of –0.03, whilst the red color represents the strain of 0.10. For the strain ε_{22} (Figure 5-12(c) and (d)), the blue represents the strain of

about –0.09, and the red color represents the strain of 0.02. For the strain ε_{12} (Figure 5-12(e) and (f)), the blue represents the strain of –0.04, and the red color represents the strain of 0.04. Both numerical simulation and image processing give similar distributions of the strain fields: This similarity between the contour plots for strain fields from the numerical simulation and the image processing of SEM micrographs verifies the capability of the numerical model to generate correct strain results at a larger indentation depth.

Contour plots in Figure 5-13 show the displacement fields upon scratching at scratching distance about 40μm, i.e., δn=80μm, δt=40μm. For the displacement u_1 (Figure 5-13(a) and (b)), the scale ranges from -5μm (blue) to 20μm (red). For the displacement u_2 (Figure 5-13(c) and (d)), the scale ranges from 10μm (blue) to 40μm (red). The contours very nicely reveal the feature of the biased displacements where material is pushed rightward by the knife during scratching: The distribution of the horizontal displacements from both FEM simulation and image processing shows a symmetric distribution about the line about 45° left to the vertical line. The maximum horizontal displacement occurs in front of the knife along the line of about 31° away from the horizontal direction, whereas the minimum displacement occurs along the line of about 45° away from the vertical direction. The vertical displacement also shows features of biased: the symmetric lines are about 77° for FEM results and 75° for image processing away from the horizontal direction. The excellent agreements between the directions of the symmetric lines prove that the proposed FEM can capture the material deformation behavior during scratching process for even more sever deformation.

Contour plots for the strain fields upon scratching, i.e., δn=80μm, and δt=40μm, are presented in Figure 5-14. For the strain ε_{11} (Figure 5-14(a) and (b)), the scale ranges from –0.04 (blue) to 0.12 (red). For the strain ε_{22} (Figure 5-14(c) and (d)), the scale ranges from –0.25 (blue) to 0.04 (red). For the strain ε_{12} (Figure 5-14(e) and (f)), the scale ranges from –0.06(blue) to 0.04 (red).

The remarkable similarity in the displacement and strain fields upon scratching verifies the predictions of the numerical model for the simulations for the scratching test at a deeper indentation depth.

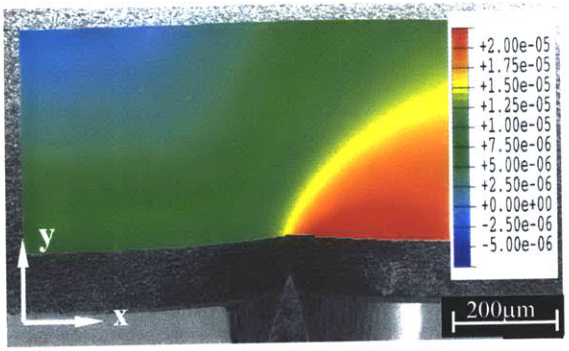

Figure 5-13(a)

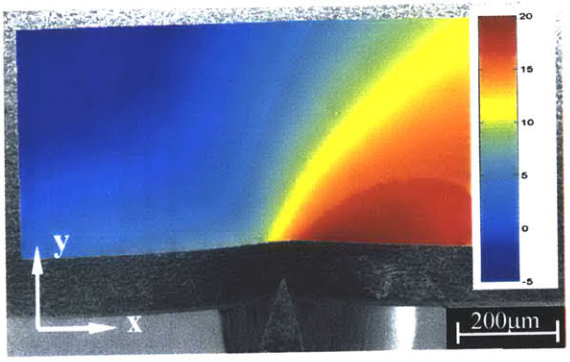

Figure 5-13(b)

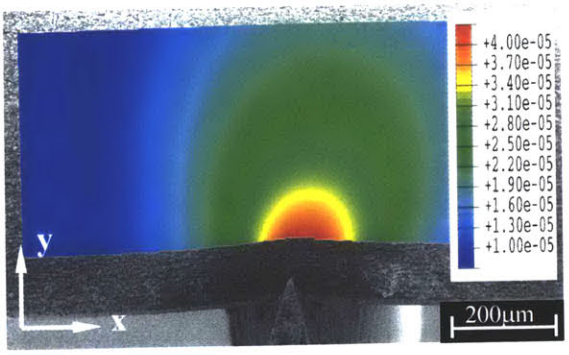

Figure 5-13(c)

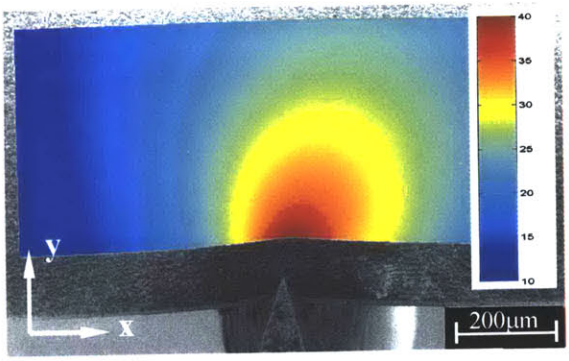

Figure 5-13(d)

Figure 5-13: Displacement fields for the indentation/scratching test with δn=80μm, δt=40μm: (a) u_1 contour from FEM simulation; (b) u_1 contour from image processing of SEM micrographs from the test; (c) u_2 contour from FEM simulation; (d) u_2 contour from image processing of SEM micrographs from the test.

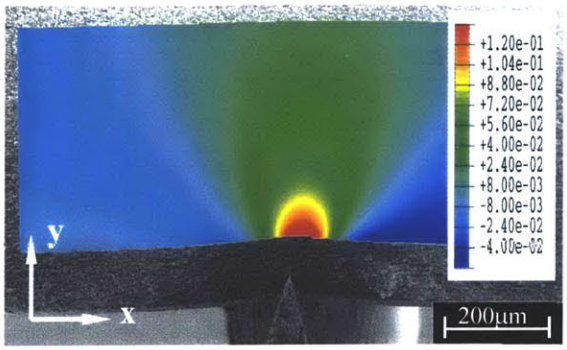

Figure 5-14(a)

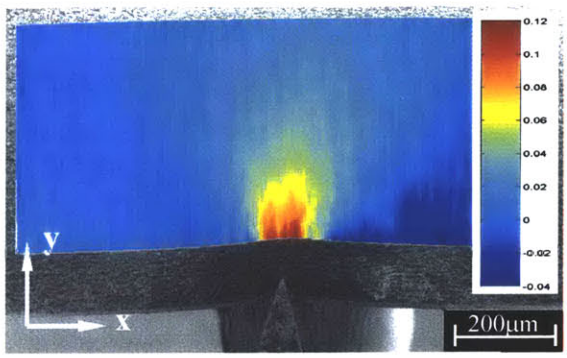

Figure 5-14(b)

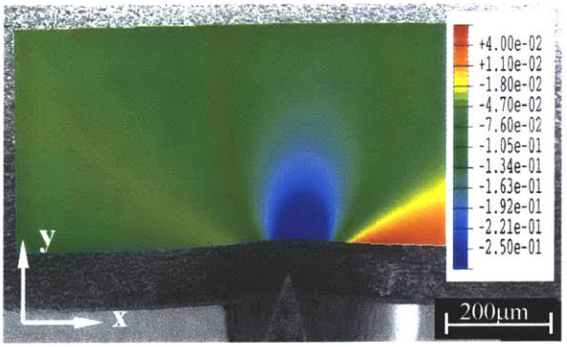

Figure 5-14(c)

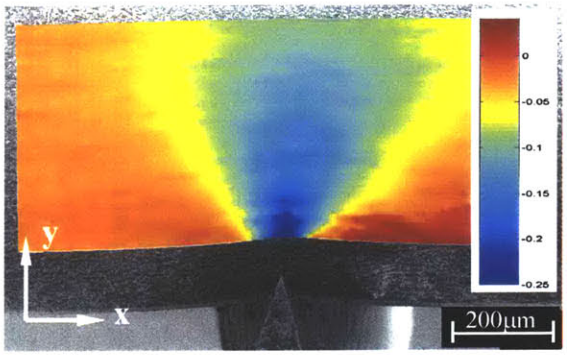

Figure 5-14(d)

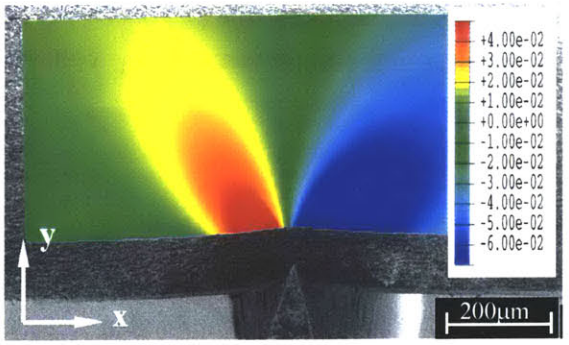

Figure 5-14(e)

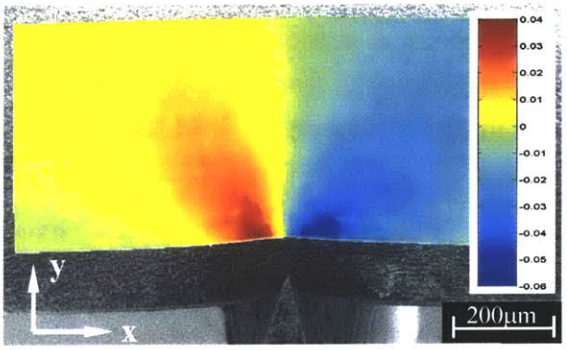

Figure 5-14(f)

Figure 5-14: Strain fields for the indentation/scratching test with δn=80μm, δt=40μm: (a) ε_{11} contour from FEM simulation; (b) ε_{11} contour from image processing of SEM micrographs from the test; (c) ε_{22} contour from FEM simulation; (d) ε_{22} contour from image processing of SEM micrographs from the test; (e) ε_{12} contour from FEM simulation; (f) ε_{12} contour from image processing of SEM micrographs from the test.

5.2.3 Indentation/Scratching Tests for Unfilled TPU with Bulk-type Knife

FEM simulation of the indentation/scratching test using a bulk-type knife was conducted.

In the test, the contact length (the length of the smooth surface) of the bulk-type knife was 10mm, the protrusion was about 60μm above the smooth surface, and the tip radius was about 15μm. Since the model used previously was 6mm in length, which could not cover the region of the contact between the bulk knife and the material, a larger model with the length of 15mm is built for the simulation with the bulk-type knife. Recall that such dimension was the same dimension as the effective sample length (the distance between the end surfaces of the sample) in the test. Figure 5-15 shows the mesh used in the study for the bulk-type knife scratching test.

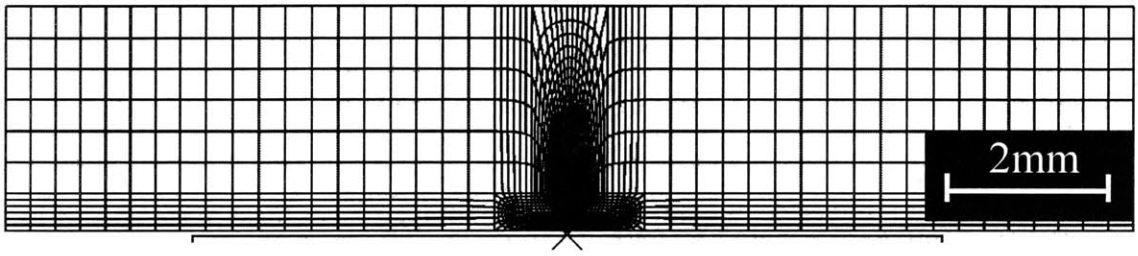

Figure 5-15(a)

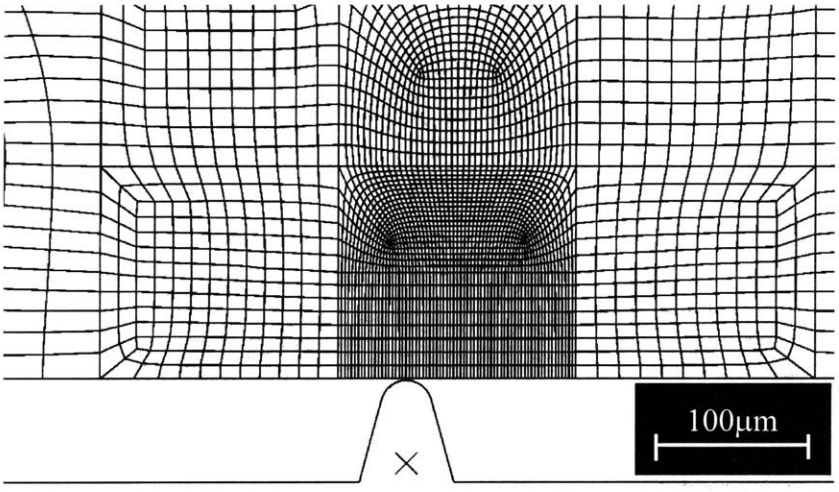

Figure 5-15(b)

Figure 5-15: The mesh used for the simulations of the indentation tests using the bulk-type knife: (a) Overall mesh; (b) Mesh near the protrusion.

In the test, due to the lack of the power of the stepper motor driving the scratching motion, the scratching speed falls to below 1μm/s. In the numerical simulations, however, in order to be consistent with above numerical simulations, we still use the

indentation speed of 2μm/s and the scratching speed of 4μm/s. As discussed in Chapter 2, because of the difficulties in measuring the displacement in the test with the bulk-type knife, the load control was used. The indentation and scratching marks on the sample were inspected after the tests to determined the real contact width. The average contact load in terms of N/m was then calculated and used as the load control in the simulations. Figure 5-16(a) shows the normal/tangential force vs time curves. The corresponding curves from the test are also shown in Figure 5-16(b) for comparison. The FEM simulation nicely captures the overall reaction forces. During indentation, the normal force increases at a small rate due to the small contact region between the protrusion and the material. As soon as the smooth surface of the bulk-type knife becomes in contact with the material, a dramatic increase in the slope of the normal force is observed due to the sudden increase in the contact area. Such feature, however, was not seen in the real tests because of the imperfect alignment of the smooth surface of the bulk-type knife to the material surface. Upon scratching, the normal force linearly decreases whereas the tangential force increases nonlinearly.

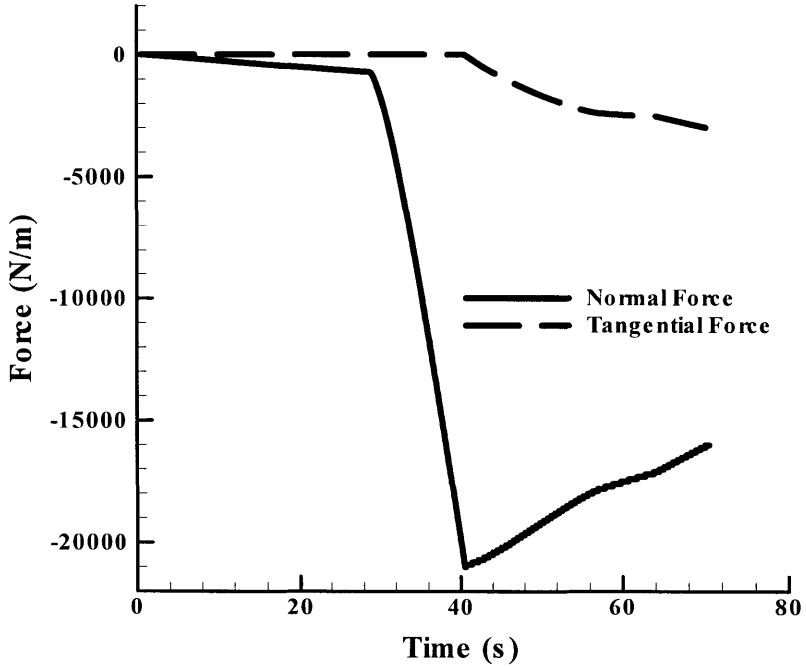

Figure 5-16(a)

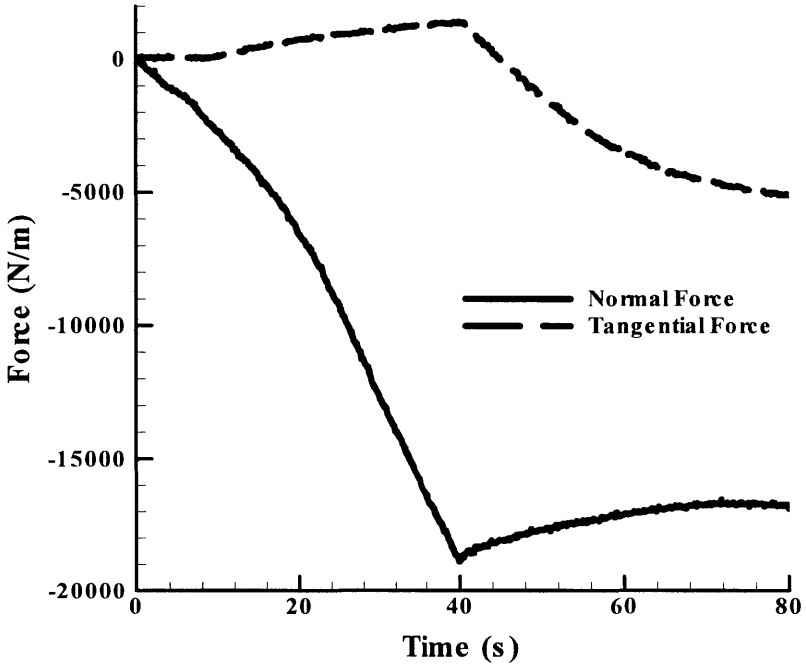

Figure 5-16(b)

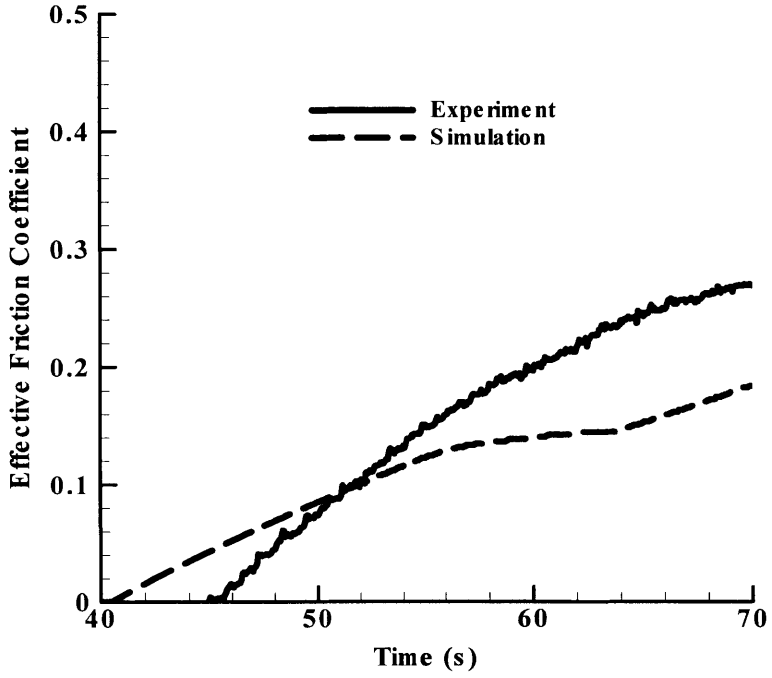

Figure 5-16(c)

Figure 5-16: Normal/tangential force vs time curves for the indentation using the bulk-type knife: (a) from numerical simulations; (b) from tests; (c) Effective friction coefficient.

Figure 5-16(c) shows the effective friction coefficient. It is noticed that even though the contact friction coefficient used the FEM model is only 0.10, the effective friction coefficient is predicted to be about 0.2.

Contour plots in Figure 5-17 show the displacement field immediately after the indentation, i.e., δt=0μm. For the displacement u_1 (Figure 5-17(a) and (b)), the color changes from the blue for the displacement of -5μm to red for the displacement of 5μm. For the displacement u_2 (Figure 5-17(c) and (d)), the blue represents the displacement of 20μm, whilst the red represents the displacement of 40μm. Due to the imperfect alignment between the bulk-type knife and the material, image processing gave asymmetric displacement field for u_1, where the basic features of the deformation field could not be retrieved. Numerical simulation gives a symmetric displacement field for u_1: The u_1 contour shows material being pushed in the horizontal direction with maximum displacement occurring along 40° lines away from the centerline. Recall that for the test using the wedge-type knife, the maximum displacement u_1 was along the 45° lines away from the center line. This difference in the distribution of u_1 is due to the constraint applied by the contact of the smooth surface with the material.

The strain contour plots from both numerical simulations and image processing of SEM micrographs are presented in Figure 5-18. For the strain ε_{11} (Figure 5-18(a) and (b)), the blue represents the strain of –0.01, whilst the red color represents the strain of 0.08. For the strain ε_{22} (Figure 5-18(c) and (d)), the blue represents the strain ε_{22} of –0.05, whereas the red color represents the strain of 0.02. For the strain ε_{12} (Figure 5-18(c) and (d)), the blue represents the strain of –0.04, whereas the red color represents the strain of 0.04. It is noticed that even though the strain contours from image processing show features of asymmetric distribution (the strains on the left side of the protrusion have higher magnitude than the right side) due to the asymmetric displacement field u_1 because of the imperfect alignment, both numerical simulation and image processing give similar overall distributions of the strain fields. This similarity between the strain contour plots from the numerical simulation and from the tests verifies the capability of the numerical model to result in correct strain fields for the indentation tests using the bulk-

type knife.

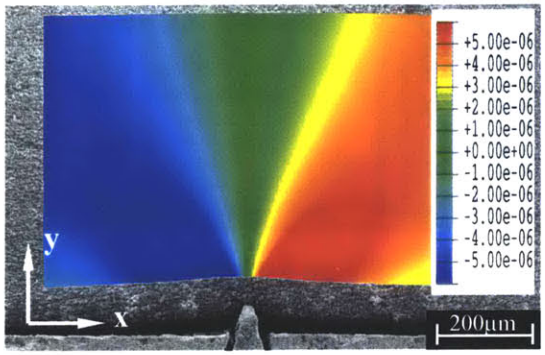

Figure 5-17(a)

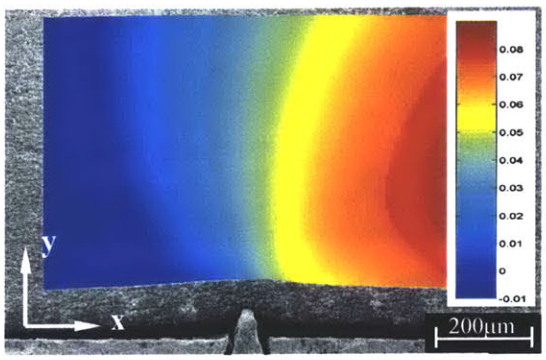

Figure 5-17(b)

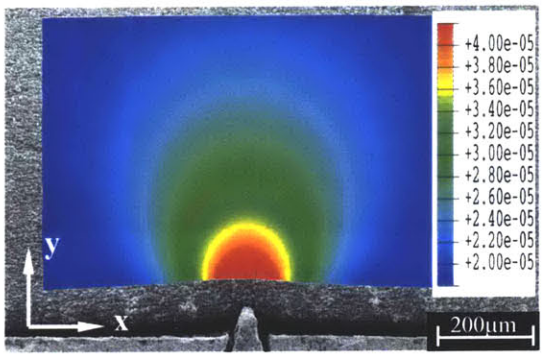

Figure 5-17(c)

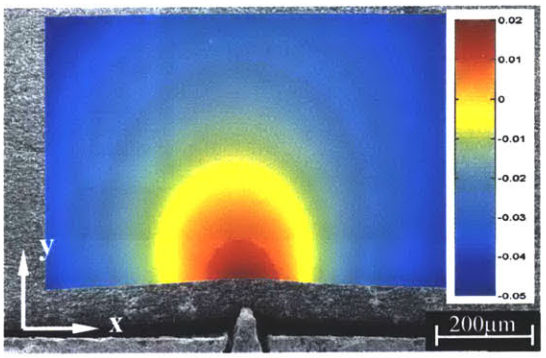

Figure 5-17(d)

Figure 5-17: Displacement fields for the indentation/scratching test with the bulk-type knife, δt=0μm: (a) u_1 contour from FEM simulation; (b) u_1 contour from image processing of SEM micrographs; (c) u_2 contour from FEM simulation; (d) u_2 contour from image processing of SEM micrographs.

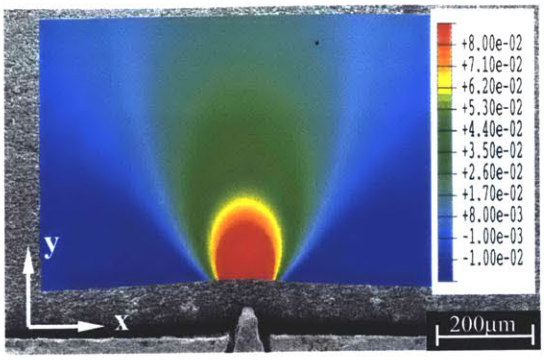

Figure 5-18(a)

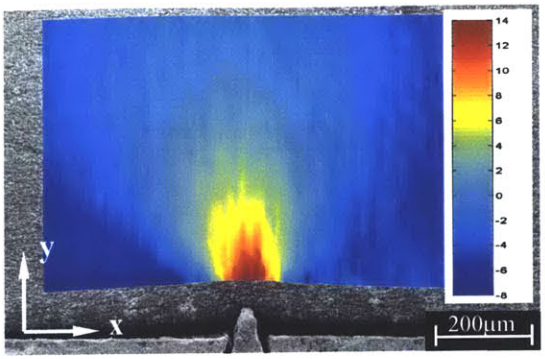

Figure 5-18(b)

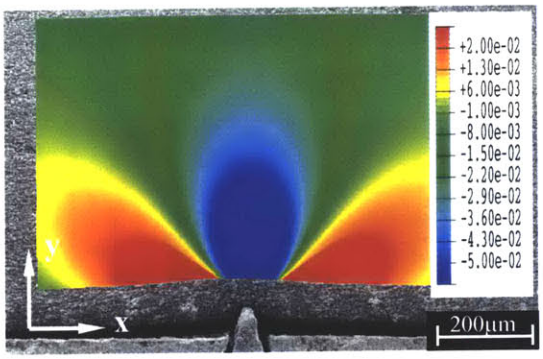

Figure 5-18(c)

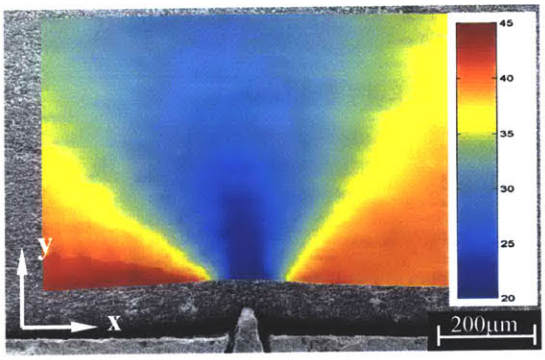

Figure 5-18(d)

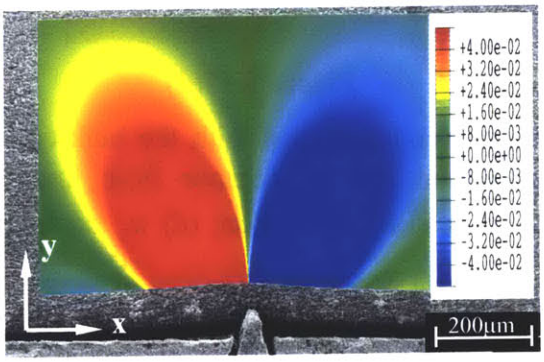

Figure 5-18(e)

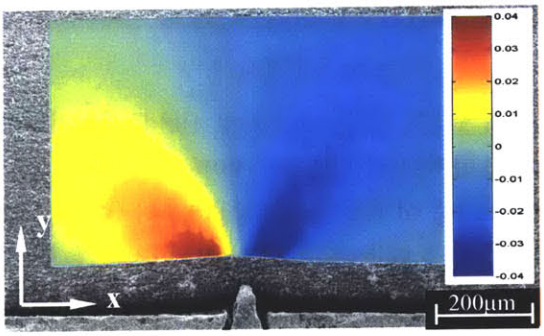

Figure 5-18(f)

Figure 5-18: Strain fields for the indentation/scratching test using the bulk-type knife, δt=0μm: (a) ε_{11} contour from FEM simulation; (b) ε_{11} contour from image processing of SEM micrographs from the test; (c) ε_{22} contour from FEM simulation; (d) ε_{22} contour from image processing of SEM micrographs from the test; (e) ε_{12} contour from FEM simulation; (f) ε_{12} contour from image processing of SEM micrographs from the test.

Contour plots in Figure 5-19 show the displacement fields upon scratching, i.e., δt=100μm. For the displacement u_1 (Figure 5-19 (a) and (b)), the scale ranges from 10μm (blue) to 50μm (red). For the displacement u_2 (Figure 5-19(c) and (d)), the scale

ranges from 10μm (blue) to 40μm (red). Both numerical simulation and image processing give similarly biased displacement fields as the knife moves rightward.

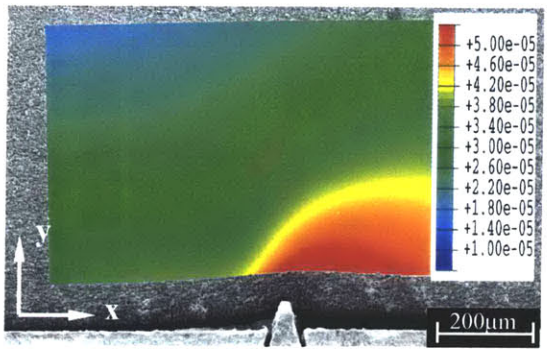

Figure 5-19(a)

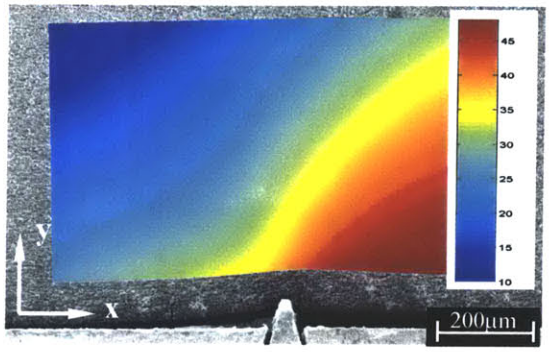

Figure 5-19(b)

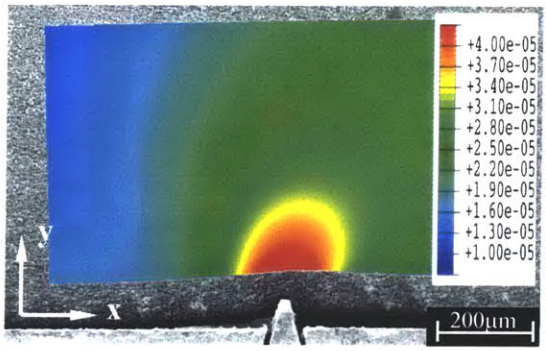

Figure 5-19(c)

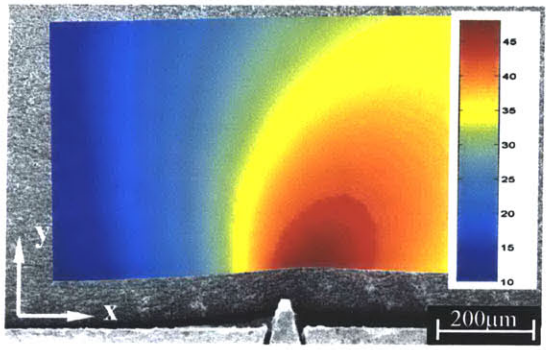

Figure 5-19(d)

Figure 5-19: Displacement fields for the indentation/scratching test with the bulk-type knife, δt=100μm: (a) u_1 contour from FEM simulation; (b) u_1 contour from image processing of SEM micrographs; (c) u_2 contour from FEM simulation; (d) u_2 contour from image processing of SEM micrographs.

Contour plots for the strain fields upon scratching, i.e., δt=100μm are presented in Figure 5-20, where both numerical simulation results and image processing of SEM micrographs are presented. For the strain ε_{11} (Figure 5-20(a) and (b)), the scale ranges from –0.03 (blue) to 0.08 (red). For the strain ε_{22} (Figure 5-20(c) and (d)), the scale ranges from –0.04(blue) to 0.02 (red). For the strain ε_{12} (Figure 5-20(e) and (f)), the scale ranges from –0.04(blue) to 0.03 (red).

The similarity in the displacement and strain fields upon scratching verifies the predictions of the numerical model for the simulations for the scratching test at a deeper

indentation depth.

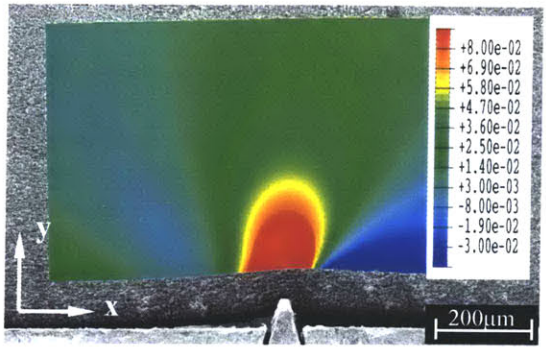

Figure 5-20(a)

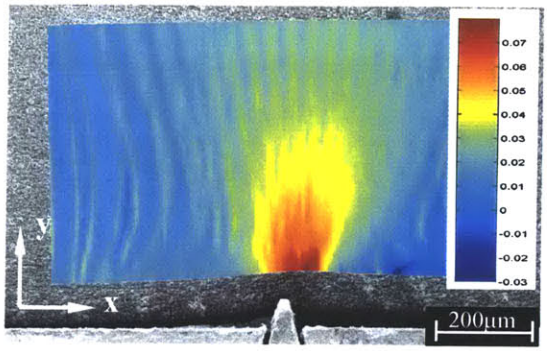

Figure 5-20(b)

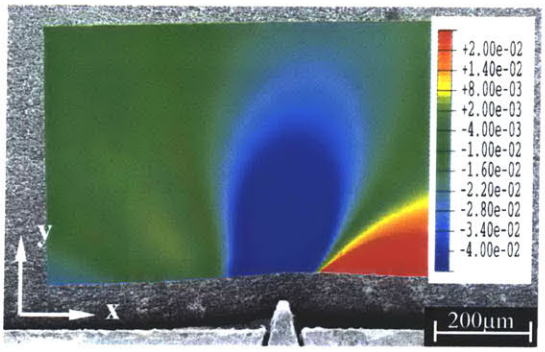

Figure 5-20(c)

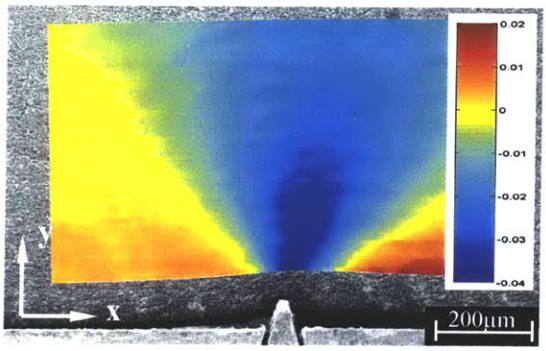

Figure 5-20(d)

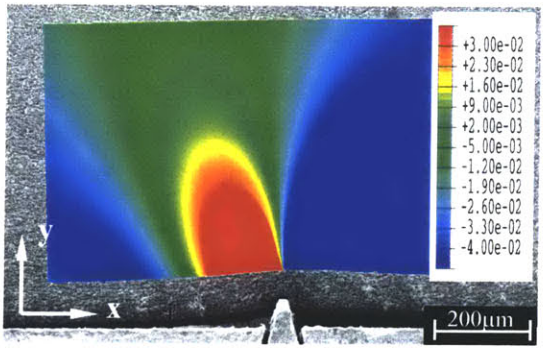

Figure 5-20(e)

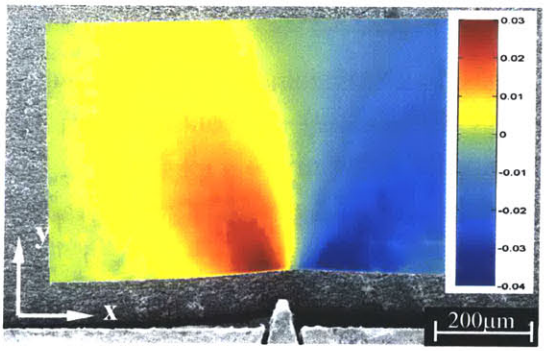

Figure 5-20(f)

Figure 5-20: Strain fields for the indentation/scratching test using the bulk-type knife, δt=100μm: (a) ε_{11} contour from FEM simulation; (b) ε_{11} contour from image processing of SEM micrographs from the test; (c) ε_{22} contour from FEM simulation; (d) ε_{22} contour from image processing of SEM micrographs from the test; (e) ε_{12} contour from FEM simulation; (f) ε_{12} contour from image processing of SEM micrographs from the test.

5.3 Mechanics of the Scratching Tests for Unfilled TPUs

5.3.1 Damage Criterion

During scratching process, the material undergoes complex multi-axial stress-strain state. However, few studies have been made on the failure of elastomers under multi-axial stress-strain state, largely because of the difficulty in designing and conducting proper experiments[5-1]. The study of the failure of elastomers under multi-axial stress-strain state is further complicated by the fact that the failure form depends on the state of applied stresses. For instance, rupture stress in uniaxial tension is highly dependent upon factors such as whether crystallization occurs under high strains, whereas the critical stress for failure under triaxial tension is solely dependent upon the modulus of elastomer[5-2][5-3][5-4]. Currently, no single criterion based on a simple relationship, such as the Tresca, von Mises, or modified forms, is generally applicable to the fracture of elastomers[5-1].

Gent and coworkers proposed[5-2][5-3][5-4] that under triaxial tension cavitation may occur as soon as the inflation pressure, defined as $p = (\sigma_{11} + \sigma_{22} + \sigma_{33})/3$, exceeded a critical pressure p_{cr}, which was given by

$$p_{cr} = \frac{5}{6}E, \tag{5.1}$$

where E was the elastic modulus of the rubber material. In this model, the crack initiation was treated as a consequence of an elastic instability of pre-existing cavities too small to be readily detected. It is noted that the applicability of this criteria depends on whether material is subjected to a triaxial or near triaxial tensile stress state. As will be shown later, the stress state in indentation and scratching process is mostly tensile in one direction and compression in another direction. Therefore, such a criteria is not applicable to the problem of current interest.

In the following, in order to provide the insight into the mechanics about possible damage initiation, we inspect two parameters: the maximum principal stress S_3 and limiting chain stretch ratio η.

The maximum principal stress indicates the severity of the stress in a multi-axial

stress state: When $S_3 > 0$, it represents the largest tensile stress; when $S_3 < 0$, it represents the minimum compression stress. It is thought that very large maximum principal stress may result in the damage in the form of tensile rupture.

Limiting chain stretch ratio η is defined as

$$\eta = \frac{\Lambda_{chain}}{\sqrt{N}}, \tag{5.2}$$

where Λ_{chain} is the amplified chain stretch defined by eqn.(4-11) and depicts the stretch ratio of molecular chains in the soft domain of TPUs; N is the number of rigid molecular units between entanglements and crosslinks whereas $\sqrt{N}$ represents the maximum stretch ratio that a molecular chain can sustain, or the chain extensibility. Clearly, as $\eta \to 1$, chain breakage may occur.

5.3.2 Effects of Indentation Depth

Numerical simulations of the scratching tests with indentation depths of δn=50μm and δn=80μm were conducted. In the both simulations, the indentation speed was 2μm/s whereas the scratching speed was 4μm/s. Figure 5-21 shows the normal and tangential force vs time curves for both cases. In Figure 5-21, for the purpose of comparison, the abscissa has a normalized time scale t^*, defined as

$$t^* = \begin{cases} t/t_1 & for \quad t < t_1 \\ 1 + (t - t_1)/t_2 & for \quad t_1 < t < t_2 \end{cases}, \tag{5.3}$$

where t_1 is the time for the indentation, and t_2 is the time for the scratching for a given scratching distance. For the simulations of δn=50μm, $t_1 = 25s$ and for the simulations of δn=80μm, $t_1 = 40s$. The scratching distance for δn=50μm simulation was 120μm whereas for δn=80μm simulation was 160μm. t_2 was chosen as 30s.

In Figure 5-21, the maximum normal force per unit length is 588 N/m for δn=50μm and 956N/m for δn=80μm. During scratching, the normal forces are stabilized at 553N/m for δn=50μm and 895N/m for δn=80μm, i.e., the normal forces decreases about 6.3% for δn=50μm and about 6.8% for δn=80μm. The tangential forces increase initially linearly then gradually bend over toward different constant values, depending on the indentation

depth. For δn=50μm, the stabilized value is approximately 584N/m, and for δn=80μm, it is approximately 1040N/m. It is also noticed that it takes a longer time (or distance) for the tangential force to achieve a stabilized value for the δn=80μm simulation than for the δn=50μm simulation. Since the process of the tangential force achieving a constant value corresponds to the transition from stick phase to slip phase, the test with deeper indentation depth should have longer transition time or distance.

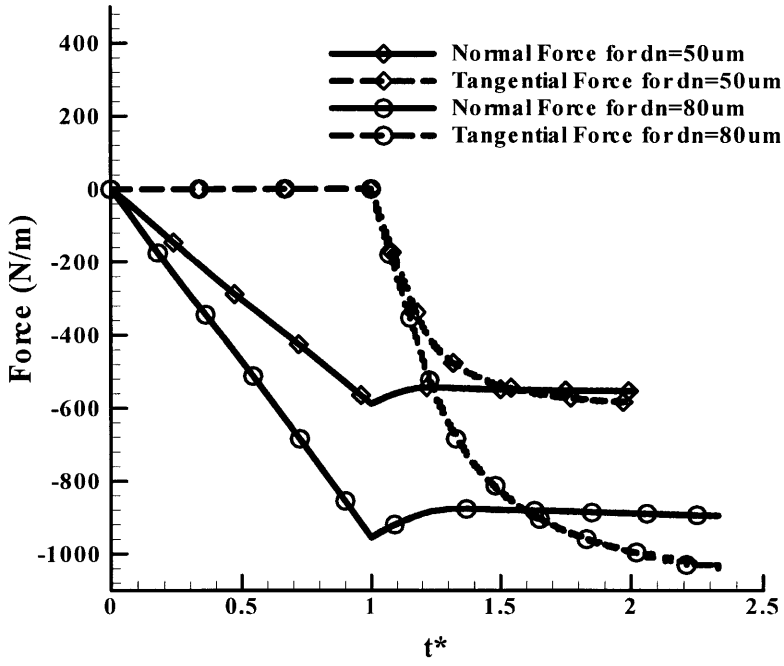

Figure 5-21: Normal/tangential force vs. t^* curves from numerical simulations for the indentation tests with δn=50μm and δn=80μm.

To further investigate the mechanics, the contour plots for the maximum principal stress S_3 and the limiting chain stretch ratio η (where $\eta = \Lambda_{chain}/\sqrt{N}$) at different scratching distances are presented in Figure 5-22 and Figure 5-23 for δn=50μm and δn=80μm, respectively.

Figure 5-22 shows the contour plots of the maximum principal stress S_3 and the limiting chain stretch ratio η for the simulation with δn=50μm. Upon indentation, i.e., δn=50μm, δt=0μm (Figure 5-22(a) and (b)), the material symmetrically conforms to the knife tip with the conformation length of about 20μm. The largest S_3 occurs about 2-

5μm underneath the contact surface instead of on the contact surface due to the constraint applied by the frictional force. It is also noticed that upon indentation, the material on the contact surface is subjected to compression stress. The largest value of S_3 is 3.98MPa. The largest limiting chain stretch ratio η, however, occurs on the contact surface with $\eta^{max} = 0.79$. The difference between the locations for the largest maximum principal stress and the largest limiting chain stretch ratio is because η is a parameter identifying the molecular chain stretch in the multi-axial strain state and its largest value is not necessary to occur at the same place as the largest maximum principal stress. In this case, the largest limiting chain stretch occurs at the location where the compression stress prevails.

Upon scratching (Figure 5-22(c) and (d)) with the scratching distance of δt=30μm, the material conformation to the knife tip is biased: the material on the left side of the knife loses contact with the knife whereas the material on the right side still contacts with the knife tip. Accompanying the bias of the material conformation to the knife tip, the location for the largest maximum principal stress moves to the contact surface and behind the knife tip whereas location for the maximum limiting chain stretch ratio moves to the position ahead of the knife tip. With the scratching distance of δt=30μm, the largest maximum principal stress increases dramatically to 17.5MPa whereas the largest limiting chain stretch ratio increases moderately to 0.86. It is also noticed that the location of the largest limiting chain stretch ratio occurs in the region where the material is subjected to compression.

Upon further scratching (Figure 5-22(e) and (f)) with the scratching distance of δt=100μm, the material conformation to the knife tip is further biased: the material on the left side of the knife totally loses contact whereas the material on the right side still contacts with the knife tip. Residual deformation due to indentation and scratching is also observed behind of the knife. During this process, the location for the largest maximum principal stress moves to the material surface and behind the knife tip whereas location for the maximum limiting chain stretch ratio moves to a position ahead of the knife tip. It is also observed that very large maximum principal stress prevails over a relatively large region of the material surface behind the knife tip. At the scratching distance of

δt=100μm, the largest maximum principal stress decreases dramatically to 8.81MPa whereas the largest limiting chain stretch ratio also decreases to 0.84.

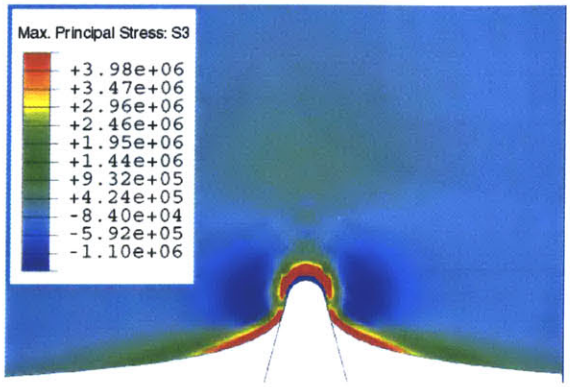

Figure 5-22(a)

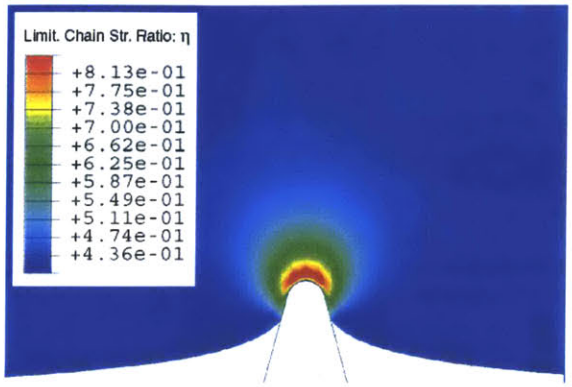

Figure 5-22(b)

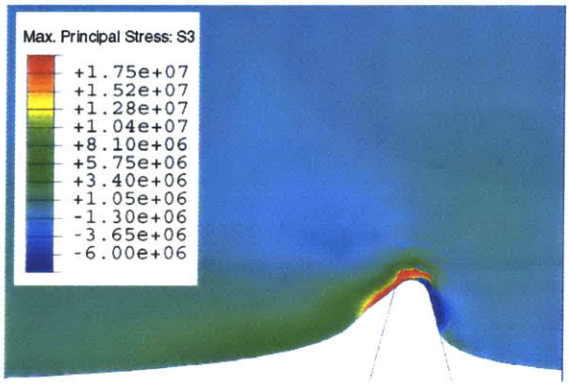

Figure 5-22(c)

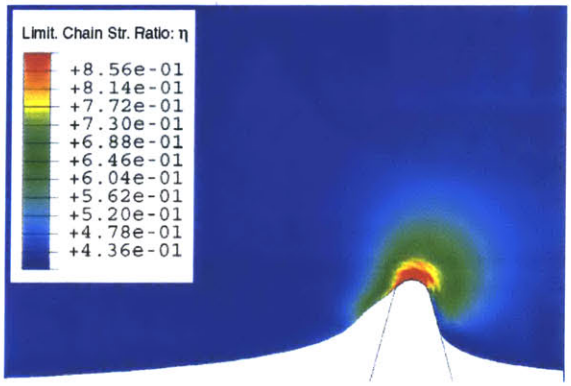

Figure 5-22(d)

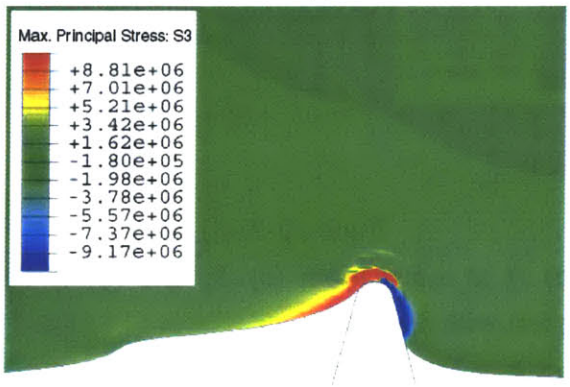

Figure 5-22(e)

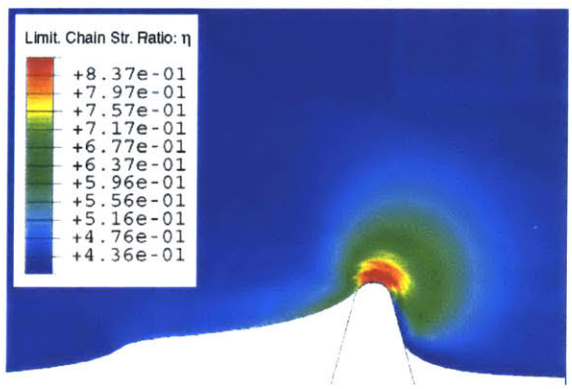

Figure 5-22(f)

Figure 5-22: Contour plots for (a) S_3 and (b) η at indentation; (c) S_3 and (d) η at δt=30μm; (e) S_3 and (f) η at δt=100μm for the test with δn=50μm.

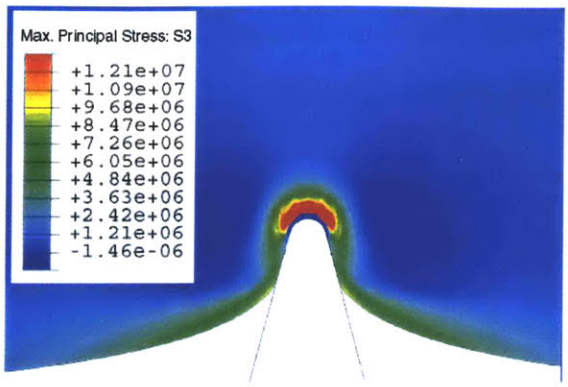

Figure 5-23(a)

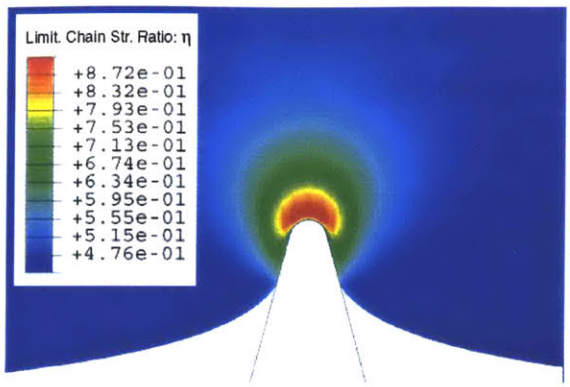

Figure 5-23(b)

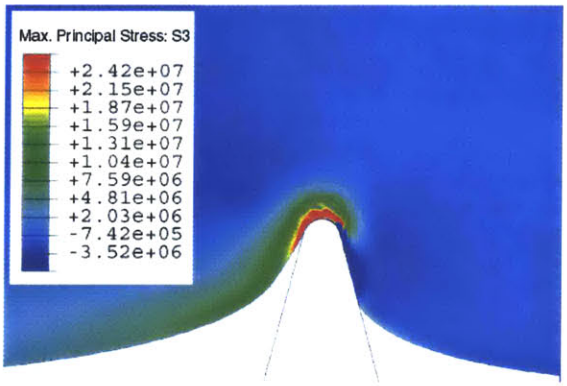

Figure 5-23(c)

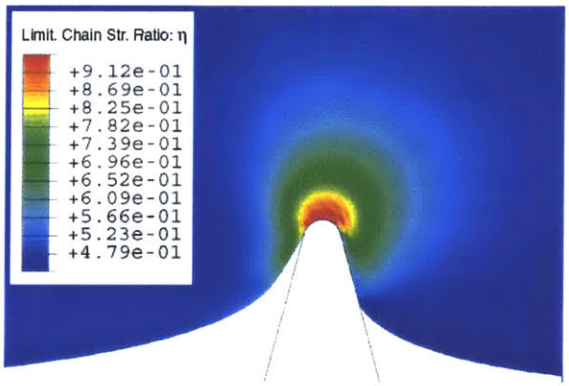

Figure 5-23(d)

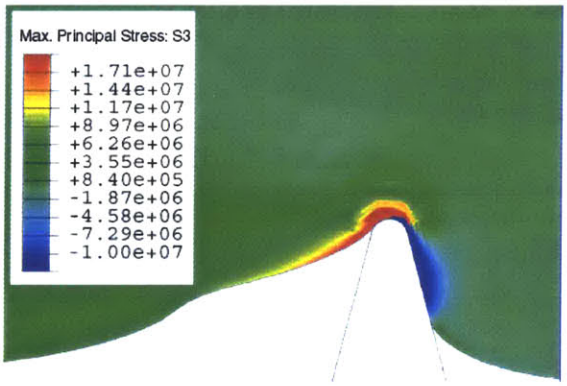

Figure 5-23(e)

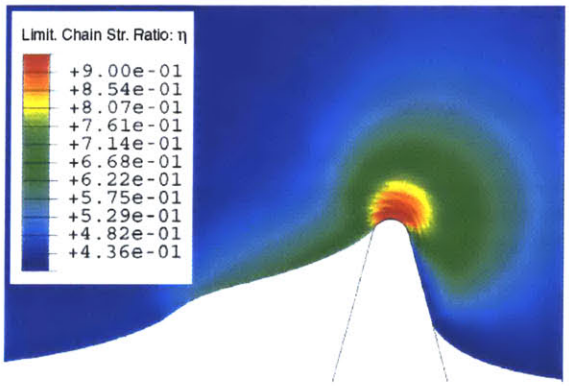

Figure 5-23(f)

Figure 5-23: Contour plots for (a) S_3 and (b) η at indentation; (c) S_3 and (d) η at δt=30μm; (e) S_3 and (f) η at δt=100μm for the test with δn=80μm.

Figure 5-23 shows the contour plots of the maximum principal stress S_3 and the limiting chain stretch ratio η for the simulation with δn=80μm. Upon indentation, i.e., δn=80μm, δt=0μm (Figure 5-23(a) and (b)), the material symmetrically conforms to the knife tip with the conformation length of about 30μm. The largest S_3 occurs underneath the contact surface and the largest limiting chain stretch ratio η occurs on the contact

surface with $\eta^{max} = 0.87$. The largest value of S_3 is 12.1MPa, which is about 300% greater than the largest value of S_3 for δn=50μm. The large increase in S_3 indicates the molecular chain under the knife tip may undergo stretch near its limiting extensibility.

Upon scratching (Figure 5-23(c) and (d)) with the scratching distance of δt=30μm, the material conformation to the knife tip is biased: the material on the left side of the knife loses contact with the knife whereas the material on the right side still contacts with the knife tip. The location for the largest maximum principal stress moves to the contact surface and behind the knife tip whereas the location for the maximum limiting chain stretch ratio moves to a place ahead of the knife tip. With the scratching distance of δt=30μm, the largest maximum principal stress increases dramatically to 24.2MPa whereas the largest limiting chain stretch ratio increases to 0.90.

Upon further scratching (Figure 5-23(e) and (f)) with the scratching distance of δt=100μm, the material conformation to the knife tip is further biased: the material on the left side of the knife totally loses contact with the knife whereas the material on the right side still contacts with the knife tip. During this process, the location for the largest maximum principal stress moves to the material surface and behind the knife tip whereas the location for the maximum limiting chain stretch ratio moves to a location ahead of the knife tip. It is also observed that large maximum principal stress prevails over a relatively large region of the material surface behind the knife tip. With the scratching distance of δt=100μm, the largest maximum principal stress decreases to 17.1MPa whereas the largest limiting chain stretch ratio maintains about the same level, $\eta^{max} = 0.90$.

The contour plots in Figure 5-22 and Figure 5-23 show that accompanying the change of the conformation of the material to the knife tip, the largest maximum principal stress and the largest limiting chain stretch ratio changes. To further illustrate the variations of the largest maximum principal stress and the limiting chain stretch ratio, Figure 5-24 shows the largest maximum principal stress and the largest limit chain stretch ratio vs. the scratching distance curves. The scratching distance is normalized by the indentation depth, i.e., the normalized scratching distance D^*

$$D^* = \frac{D}{\delta_n}, \tag{5.4}$$

where D is the scratching distance.

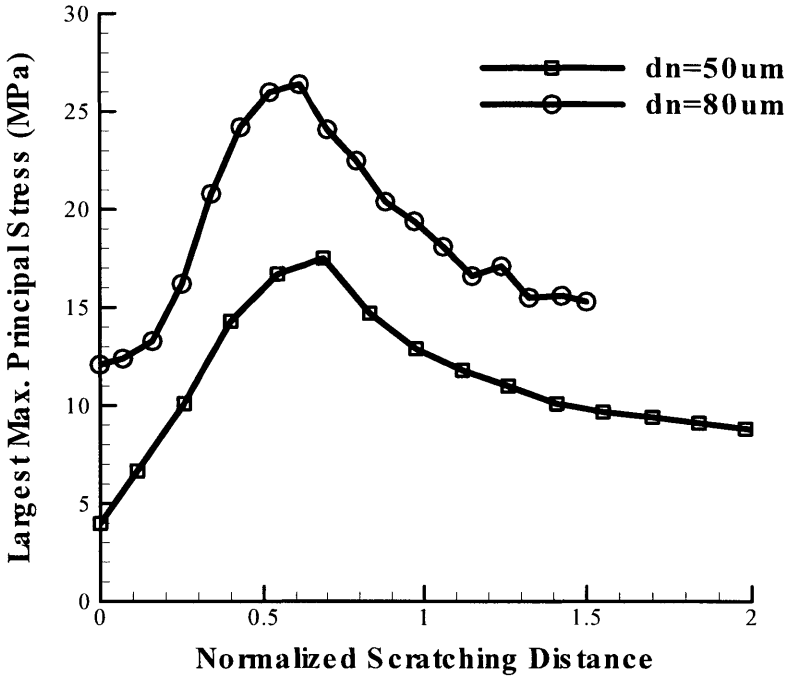

Figure 5-24(a)

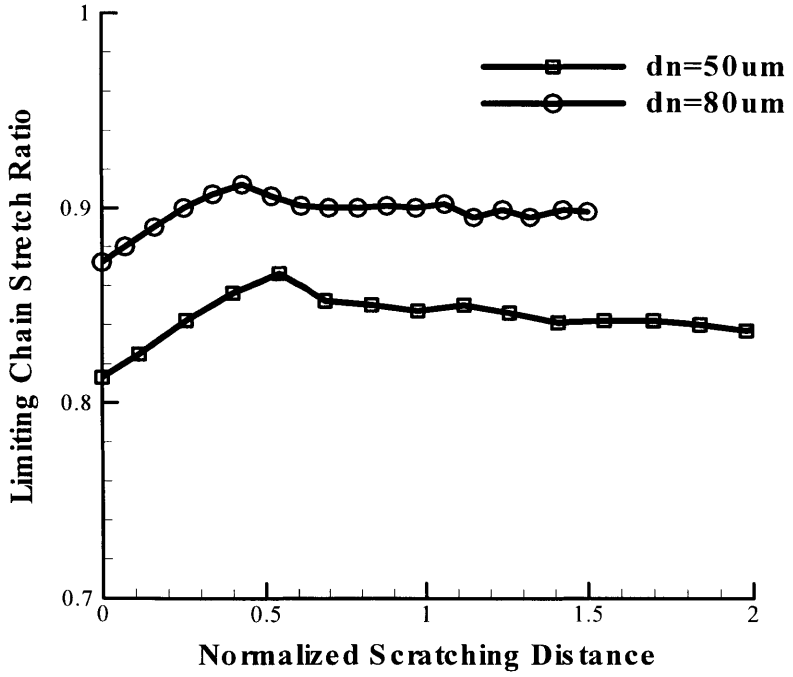

Figure 5-24(b)

Figure 5-24: The variations of (a) the largest maximum principal stress, and (b) the largest limiting chain stretch ratio with the normalized scratching distance.

From Figure 5-24, it is clear that upon scratching, the largest maximum principal stress increases first, then gradually decreases and tends to stabilize at a constant value, whereas the largest limiting chain stretch ratio increases then maintain the highest value during the scratching. The largest maximum principal stress for $\delta n=80\mu m$ is about 27MPa and is about 1.6 times higher than the one for $\delta n=50\mu m$, which is about 17MPa. The largest chain limiting stretch ratio is 0.91 $\delta n=80\mu m$ and 0.87 for $\delta n=50\mu m$. The combination of the large maximum principal stress and chain limiting stretch ratio in $\delta n=80\mu m$ may be responsible for the observations in Chapter 3 where surface damages were observed only for the test with $\delta n=80\mu m$ whereas the surface remained almost unchanged for the test with $\delta n=50\mu m$.

It is also noticed that for both simulations, the largest maximum principal stress occurs at a scratching distance equal to about 60% of the indentation depth. Such scratching distance is within the distance where the transition from the stick phase to the slip phase occurs. Therefore, the transition from the stick phase to the slip phase, marked by the change of the material conformation to the knife from a symmetric one to an asymmetric one, is the period where the damage is most likely to occur.

5.3.3 Effect of Contact Conditions

Numerical simulation of the scratching test using the bulk-type knife was conducted. The mesh shown in Figure 5-15 was used as the FEM model. In order to compare the results with the wedge-type knife, the geometry of the knife protrusion was chosen to be 50μm above the smooth surface and the tip radius to be 6μm. The normal displacement (including protrusion and overall compression) was 80μm. In the simulation, the indentation speed was 2μm/s whereas the scratching speed was 4μm/s.

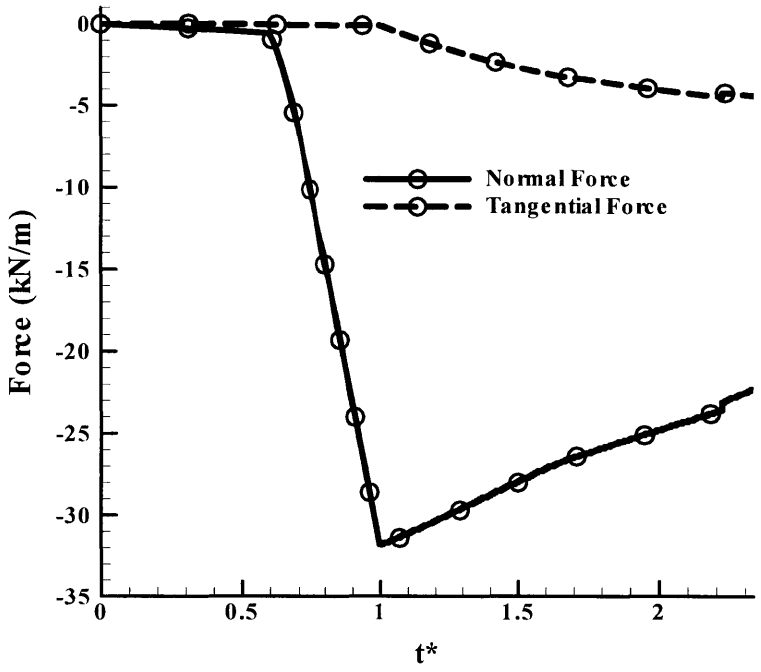

Figure 5-25(a)

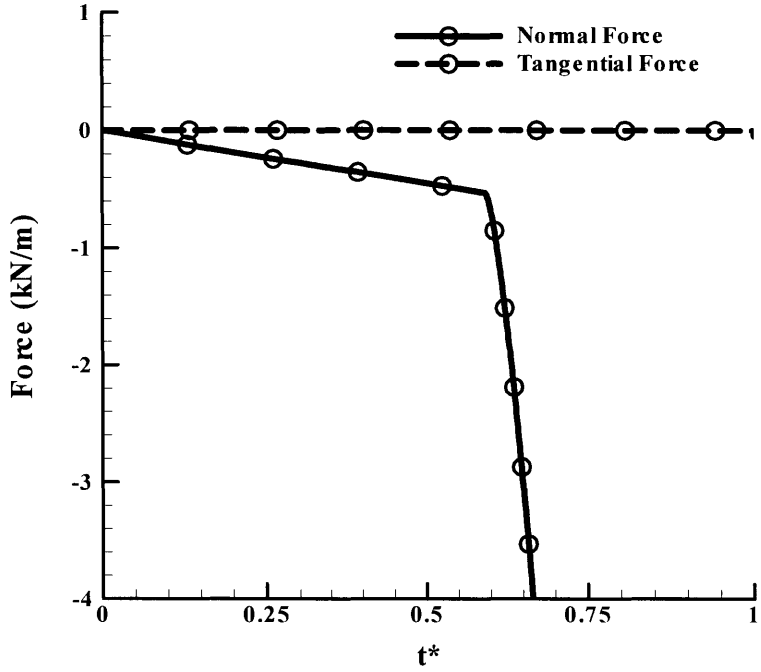

Figure 5-25(b)

Figure 5-25: Normal/tangential force vs. t^* curves from numerical simulations for the indentation tests with δn=80μm using the bulk-type knife. The tip radius of the protrusion is 6μm and the protrusion is 50μm above the smooth surface. (a) Overall curves; (b) Close-up look at the section of the curve as the smooth surface of the knife touches the material surface.

Figure 5-25 shows the normal/tangential force vs normalized time t^* curves. t^* is defined according to eqn.(5-3). During indentation, the normal force first increases at a small rate due to the small contact region between the protrusion and the material. As soon as the smooth surface of the bulk-type knife comes into contact with the material, a dramatic increase in the slope of the normal force is observed. The maximum normal force is 32kN/m. The average pressure on the surface contact is then calculated as 3.2MPa (the length of the smooth surface in the model is 10mm). Upon scratching, the normal force shows a decrease. Due to the limited length of the region with a refined mesh, the scratching distance in the FEM simulations was not long enough to reveal the stabilized value of the normal force. The tangential force, however, starts to bend over towards a constant value of about 5kN/m. It is also noticed, even though the frictional coefficient used in the simulation is 0.10, the effective friction coefficient, defined as the ratio between the tangential force and normal force, is larger than 0.10. For instance, at the end of the simulations, the ratio between the tangential force and the normal force is about 0.19. Since the curves show the trend of increasing tangential force and decreasing normal force, a larger effective frictional coefficient is expected for a longer scratching distance.

Figure 5-26 shows the contour plots of the maximum principal stress S_3 and the limiting chain stretch ratio η for the simulation with δn=80μm using the bulk-type knife. Upon indentation, i.e., δn=80μm, δt=0μm (Figure 5-26(a) and (b)), the material symmetrically conforms to the knife tip with the conformation length of about 30μm. The largest S_3 occurs underneath the contact surface and is 13.5MPa. The largest limiting chain stretch ratio η, however, occurs on the contact surface with $\eta^{max} = 0.91$. Compared with the corresponding values for the tests with δn=80μm using the wedge-type knife, these values are higher as a result of the constraint due to the frictional force between the smooth surface and the material. For the wedge-type knife, the material close to the knife moves toward the knife from both sides during the indentation, effectively reducing the severity of the deformation under the knife tip. For the bulk-type knife, however, such motion is constrained by the frictional force, resulting in a more severe deformation.

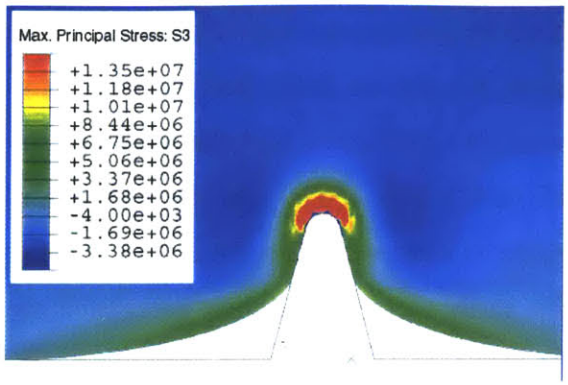

Figure 5-26(a)

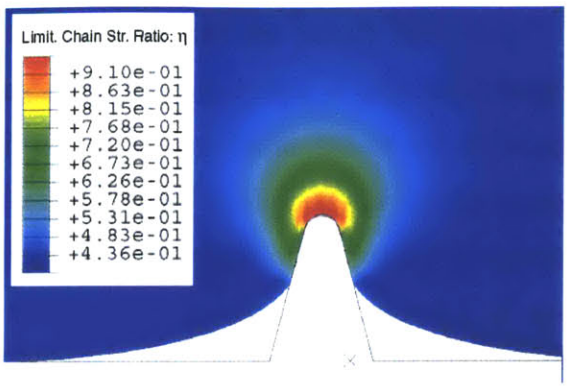

Figure 5-26(b)

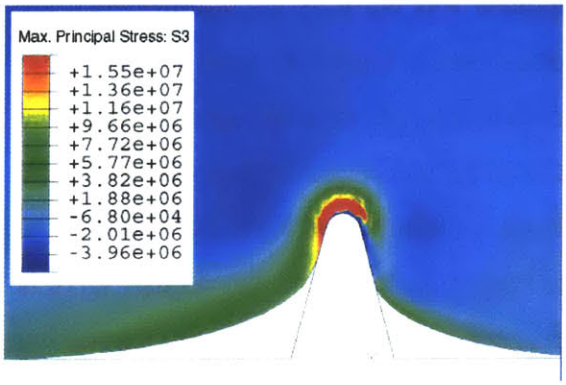

Figure 5-26(c)

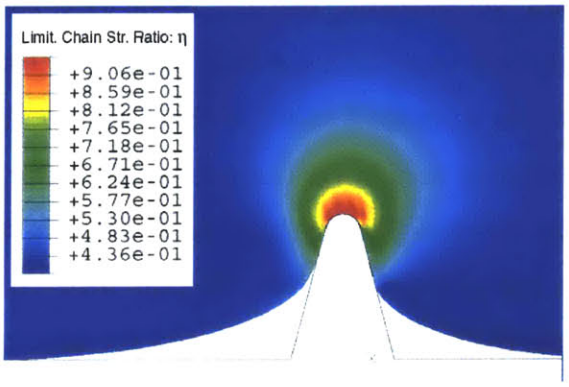

Figure 5-26(d)

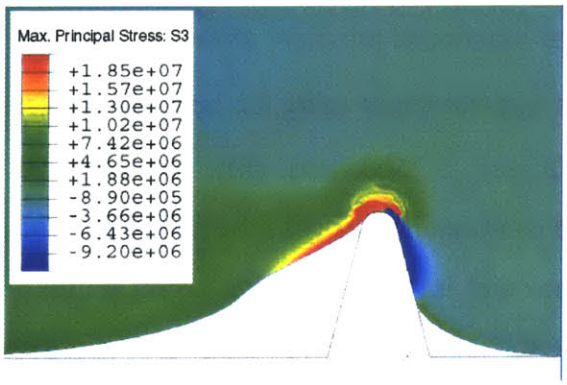

Figure 5-26(e)

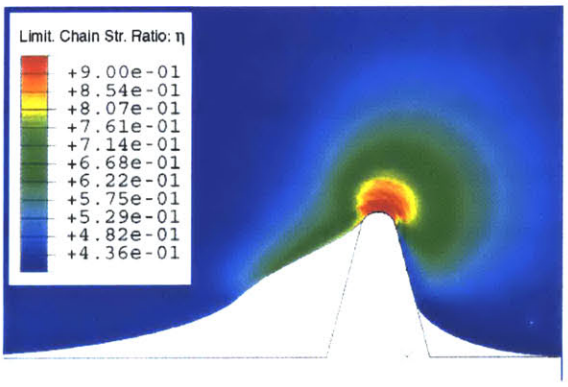

Figure 5-26(f)

Figure 5-26: Contour plots for (a) S_3 and (b) η at indentation; (c) S_3 and (d) η upon scratching δt=30μm; (e) S_3 and (f) η upon scratching δt=100μm for the test with δn=80μm using the bulk-type knife.

Upon scratching (Figure 5-26(c) and (d)) with the scratching distance of δt=30μm, the material conformation to the knife tip is biased and the change of the conformation

demonstrates the same features as those observed from the using the wedge-type knife. However, with the scratching distance of $\delta t=30\mu m$, the largest maximum principal stress increases slightly to 15.5MPa and the limiting chain stretch ratio remains about the same as the values immediately after the indentation.

Upon scratching (Figure 5-26(e) and (f)) to a scratching distance of $\delta t=100\mu m$, the material conformation to the knife tip is further biased and has the same features as those observed using the wedge-type knife. The residual deformation due to indentation and scratching is also observed behind the knife tip. At a scratching distance of $\delta t=100\mu m$, the largest maximum principal stress increases to 18.5MPa whereas the largest limiting chain stretch ratio decreases only slightly to 0.90.

To further illustrate the evolution of the largest maximum principal stress and the limiting chain stretch ratio, Figure 5-27 shows the largest maximum principal stress and the largest limit chain stretch ratio vs. the scratching distance curves. The scratching distance is normalized using the indentation depth of $\delta n=80\mu m$. The corresponding curves from the wedge-type knife test with $\delta n=80\mu m$ are also shown in the figure. Although immediately after the indentation the largest maximum principal stress for the test using the bulk-type knife is higher than the test using the wedge-type knife, the former shows a slow increase during scratching. In comparison to the test with $\delta n=80\mu m$ using the wedge-type knife, the largest maximum principal stress (20MPa) is about 7Mpa (25%) smaller than the latter and the limiting chain stretch ratio is about the same, implying that for the same overall indentation depth, the superposition of an overall pressure to the contact surface reduces the severity of the deformation during scratching. In comparison to the test with $\delta n=50\mu m$ using the wedge-type knife, the largest maximum principal stress (20MPa) is about 3MPa (17%) higher than the latter and the limiting chain stretch ratio is about 0.06 (7%) higher, implying that for the same size of the asperity, the superposition of an overall compression to the contact surface increases the severity of the deformation during scratching.

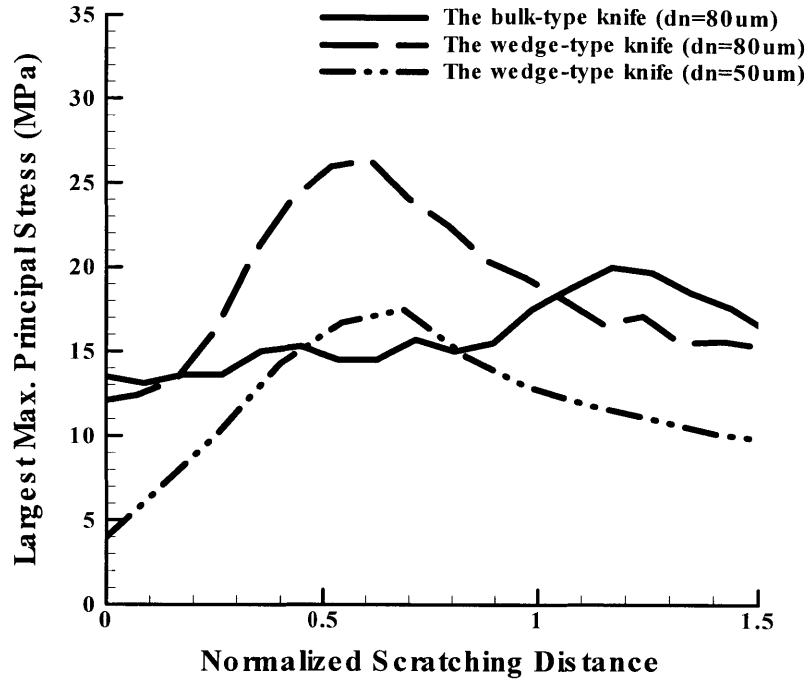

Figure 5-27(a)

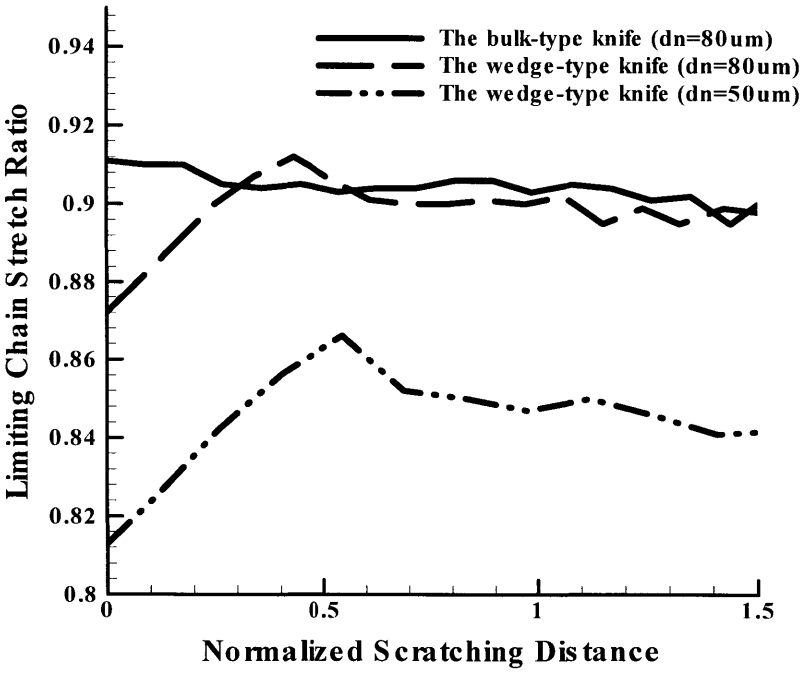

Figure 5-27(b)

Figure 5-27: The evolutions of (a) the largest maximum principal stress, and (b) the largest limiting chain stretch ratio with the normalized scratching distance.

5.3.4 Effects of Cyclic Scratching

Numerical simulations of the cyclic scratching tests using the wedge-type knife were conducted. The simulation on the fresh sample using the wedge-type knife with δn=80μm was first conducted following the loading condition defined in Figure 5-3. After the scratching, the knife was withdrawn by decreasing δ_n to zero, and then was moved back to its original position by decreasing δ_t to zero. The loading condition defined in Figure 5-3 was then applied again. Here, only the results for the second scratching are presented. The results for the first scratching are used here for the purpose of comparison.

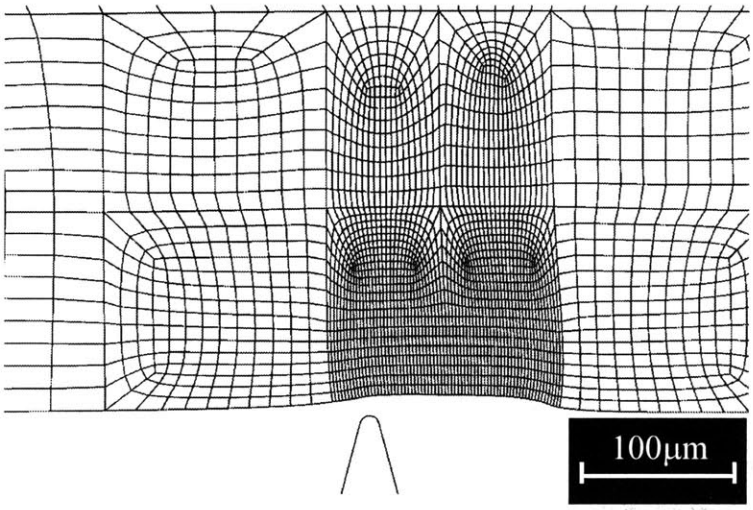

Figure 5-28: Residual deformation after withdrawing the knife back from the first scratching simulation with δn=80μm.

Figure 5-28 shows the deformed mesh after withdrawing the knife back from the first scratching simulation. Due to the large deformation during the first cycle of indentation and scratching, significant residual deformation is observed. After the first cycle of indentation and scratching, the material surface is 10-12μm under the original surface level. The mesh shown in Figure 5-28 is used for the second cycle indentation and scratching simulation.

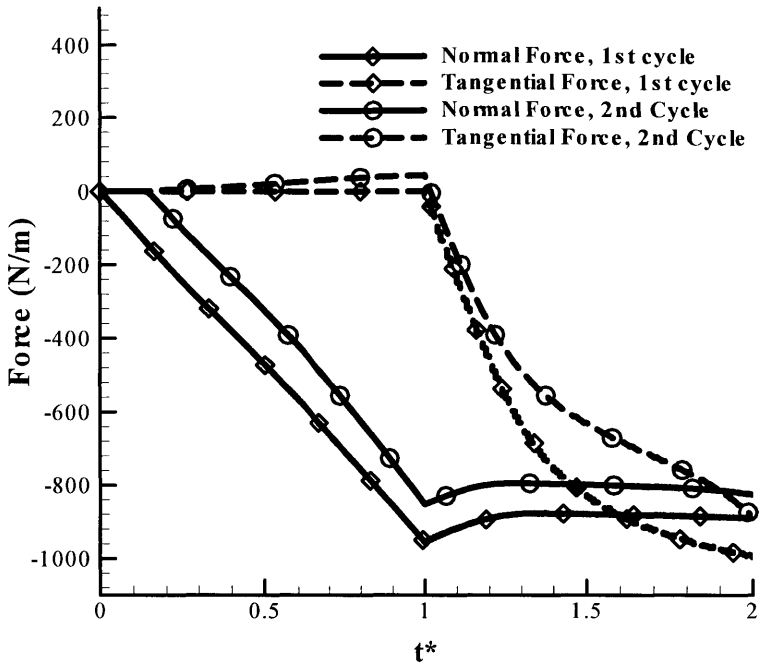

Figure 5-29: Normal/tangential force vs. t^* curves from numerical simulations for cyclic the indentation/scratching tests δn=80μm.

Figure 5-29 shows the normal/tangential force vs normalized time t^* curves. It is noticed that for the second indentation/scratching test, the variation in the normal/tangential force shows the similar overall features as those observed for the first cycle test. However, it also shows the features of material softening due to pre-loading. The normal and tangential forces for the second indentation/scratching test are smaller than those from the first cycle simulation. A positive tangential force is also observed during the second indentation. This is because the residual deformation after the first scratching test renders an asymmetric contact condition for the second indentation. From Figure 5-29, the asymmetric contact will push the knife rightward during the indentation, resulting a positive tangential reaction force of the knife.

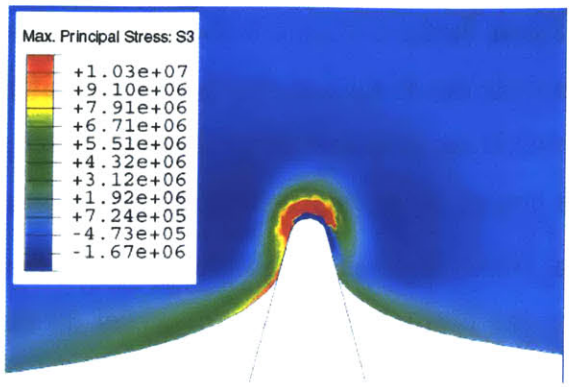

Figure 5-30(a)

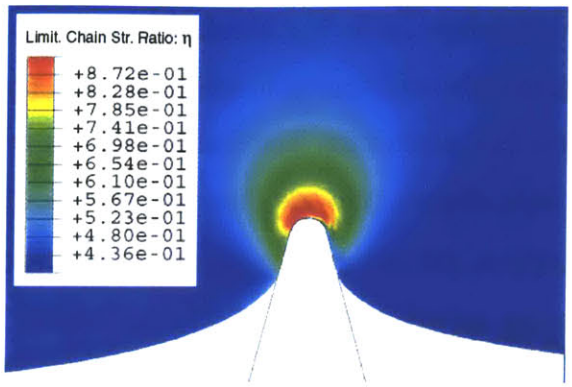

Figure 5-30(b)

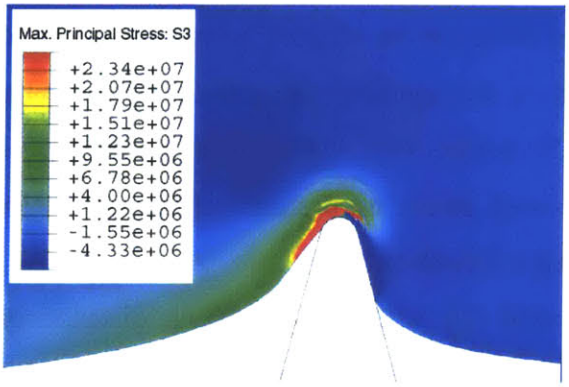

Figure 5-30(c)

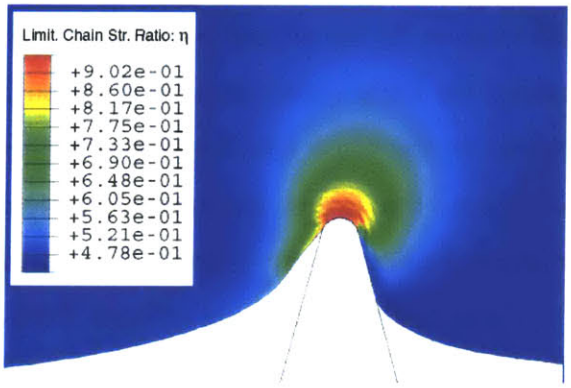

Figure 5-30(d)

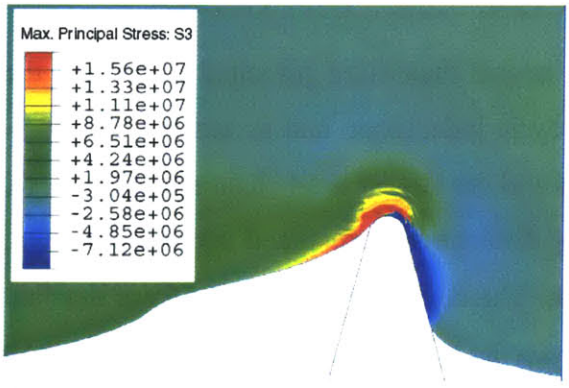

Figure 5-30(e)

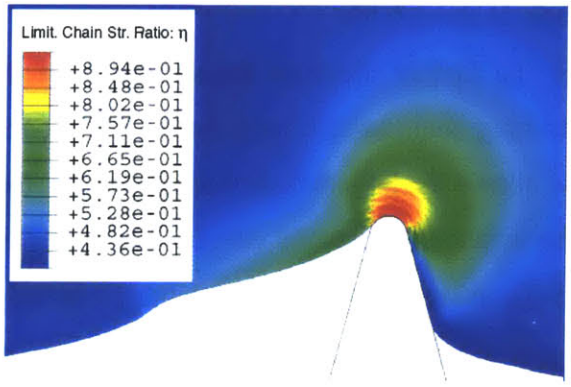

Figure 5-30(f)

Figure 5-30: Contour plots for (a) S_3 and (b) η at indentation; (c) S_3 and (d) η upon scratching δt=20μm; (e) S_3 and (f) η upon scratching δt=100μm for the second cycle scratching test with δn=80μm using the wedge-type knife.

Figure 5-30 shows the contour plots of the maximum principal stress S_3 and the limiting chain stretch ratio η for the second scratching test with δn=80μm using the

wedge-type knife. Upon indentation, i.e., δn=80μm, δt=0μm (Figure 5-30(a) and (b)), the material conformation to the knife tip is asymmetric due to the residual deformation after the first scratching. The distributions of the maximum principal stress and the limiting chain stretch ratio are thus asymmetric. The largest S_3 occurs underneath the contact surface and has the largest value of 10.3MPa, which is smaller than that from the first cycle indentation (12.1MPa). The largest limiting chain stretch ratio η occurs on the contact surface with $\eta^{\max} = 0.87$, which is the same as that from the first scratching test.

Upon scratching (Figure 5-30(c) and (d)) with the scratching distance of δt=30μm, the location for the largest maximum principal stress moves onto the contact surface and behind the knife tip whereas the location for the maximum limiting chain stretch ratio moves to the place ahead of the knife tip. However, with the scratching distance of δt=30μm, the largest maximum principal stress increases dramatically to 23.4MPa whereas the limiting chain stretch ratio increases moderately to 0.90.

Upon further scratching (Figure 5-30(e) and (f)) with the scratching distance of δt=100μm, the material conformation to the knife tip is further biased. The largest maximum principal stress decreases to 15.6MPa whereas the largest limiting chain stretch ratio is about 0.90.

To further illustrate the variations of the largest maximum principal stress and the limiting chain stretch ratio during the second cycle indentation and scratching, Figure 5-31 shows the largest maximum principal stress and the largest limit chain stretch ratio vs. the scratching distance curves. The scratching distance is normalized according to eqn. (5-3), using the indentation depth of δn=80μm. The corresponding curves from the first cycle scratching with δn=80μm are also shown in the figure. From Figure 5-31, the largest maximum principal stress for the second cycle scratching shows faster increase and has the largest value of about 24MPa, which is about 11% smaller than the largest value in the first cycle scratching. The limiting chain stretch ratio (Figure 5-31(b)) is generally the same as that in the first scratching test. Clearly, for the cyclic scratching tests, the largest maximum principal stress is still very high and the limiting chain stretch ratio remains the same, which may create the condition for the damage to initiate and propagate due to fatigue.

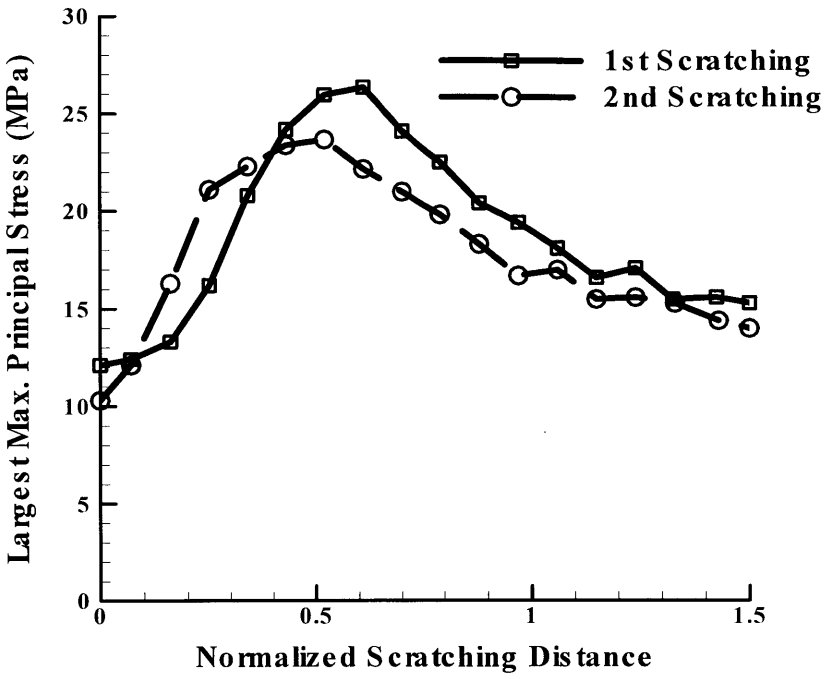

Figure 5-31(a)

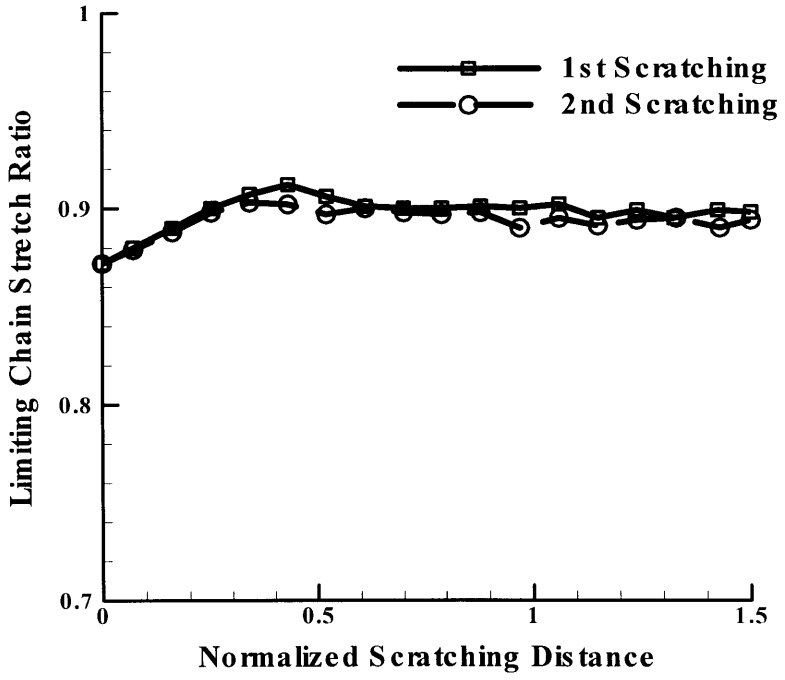

Figure 5-31(b)

Figure 5-31: The variations of (a) the largest maximum principal stress, and (b) the largest limiting chain stretch ratio with the normalized scratching distance.

5.4 Parametric Study of the Scratching Tests for Unfilled TPUs

In this section, parametric studies by varying contact friction force, scratching speed, and material properties of elastomers are conducted to identify and evaluate the influence of these factors on the abrasive wear performance of the material under various conditions.

5.4.1 Effects of Contact Friction Force

5.4.1.1 Effects of Contact Friction Force

It has been observed that the effective friction coefficient defined as the ratio between the tangential force and normal force demonstrated much higher values than the contact friction coefficients used in the FEM model. In addition, the contact friction force will affect the transition from the stick phase to slip phase, which has been shown accompanied by the increase of the largest maximum principal stress and the largest chain limiting stretch ratio, and has profound influence on the damage initiation during the scratching process. In this part, numerical simulations using three contact friction coefficients, i.e., $f = 0.00$, $f = 0.05$, $f = 0.10$, and $f = 0.20$ are conducted to investigate the effects of contact friction coefficients on the material behavior during scratching.

Figure 5-32(a) shows the normal/tangential force vs. time curves for the simulations using $f = 0.00$, $f = 0.05$, $f = 0.10$, and $f = 0.20$. During indentation, even with different contact friction coefficients, the normal forces are about identical for all the four cases. During scratching, the courses of the normal and the tangential forces for $f = 0.00$ and $f = 0.05$ are almost identical. The courses of the normal/tangential forces are the same for the four cases until $t^* > 1.2$ where the tangential force curves for $f = 0.00$ and $f = 0.05$ starts to bend over and deviate from the other two, and until $t^* > 1.28$, the tangential force curve for $f = 0.10$ starts to bend over and deviates from the curve for $f = 0.20$ (See Figure 5-32(b) for details). It is also noticed that even with $f = 0.00$, the effective friction coefficient is about 1.0. In comparison to the effective friction coefficient for $f = 0.20$, which is about 1.4, it is clear that factors not due to contact friction force account for much of the effective friction coefficient.

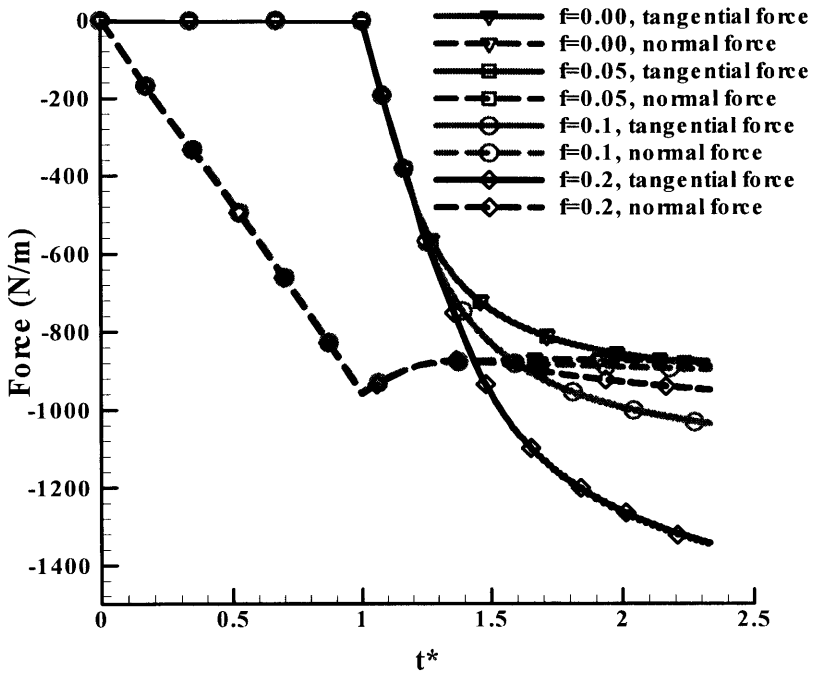

Figure 5-32(a)

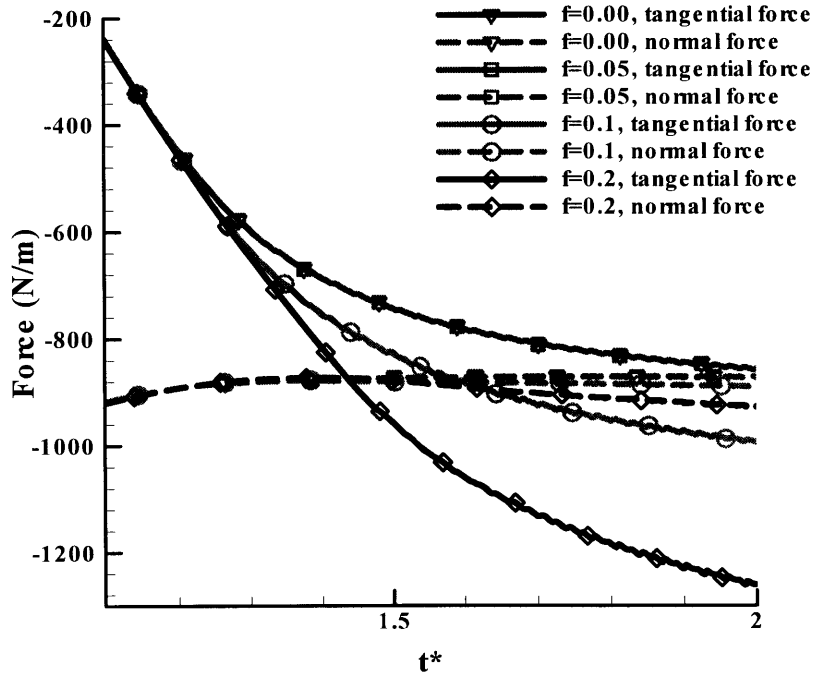

Figure 5-32(b)

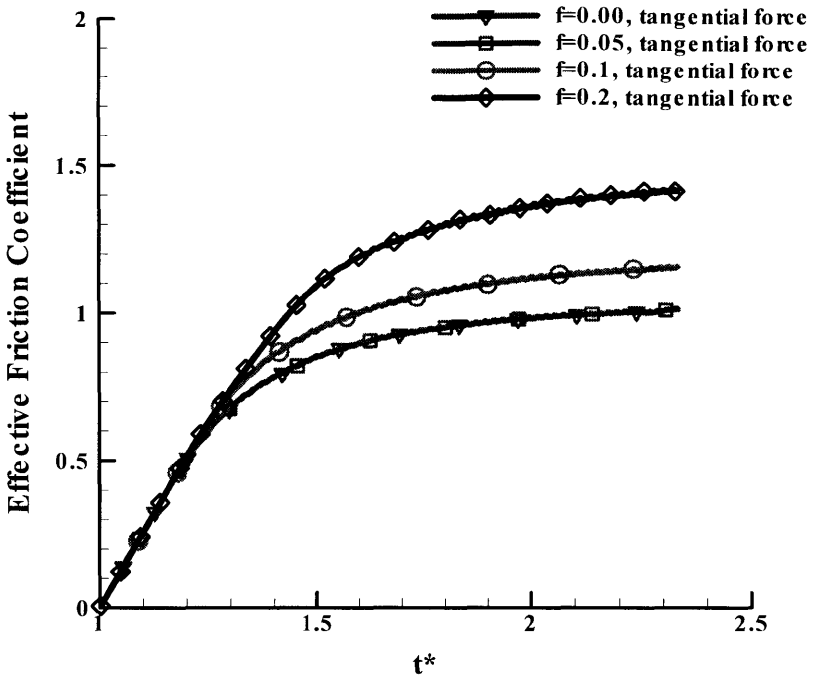

Figure 5-32(c)

Figure 5-32: Effects of contact friction coefficient on: (a) Normal/tangential force vs time curves; (b) Close-up look of the Normal/tangential force vs time curves during scratching; (c) Effective friction coefficient.

Figure 5-33(a) shows the effect of contact friction force on the variations of the largest maximum principal stress. Upon indentation, the simulation using $f = 0.00$ shows the greatest largest maximum principal value. As the contact friction force increases, the largest maximum principal stress decreases, Clearly, the presence of the frictional force constrains the deformation around the contact surface, and hence reduces the largest maximum principal stress during indentation. During scratching, the contact friction force raises the peak value of largest maximum principal stress significantly. For instance, as f increases from 0.05 to 0.20, the peak value of the largest maximum principal stress increases by 120%. It is also noticed that the contact friction force delays the peak value to occur at a longer scratching distance. Since the occurrence of the peak value corresponds to the transition from stick phase to slip phase, the larger contact frictional force lengthens the stick phase and stick distance, resulting in high stretch behind the knife and greater largest maximum principal stress.

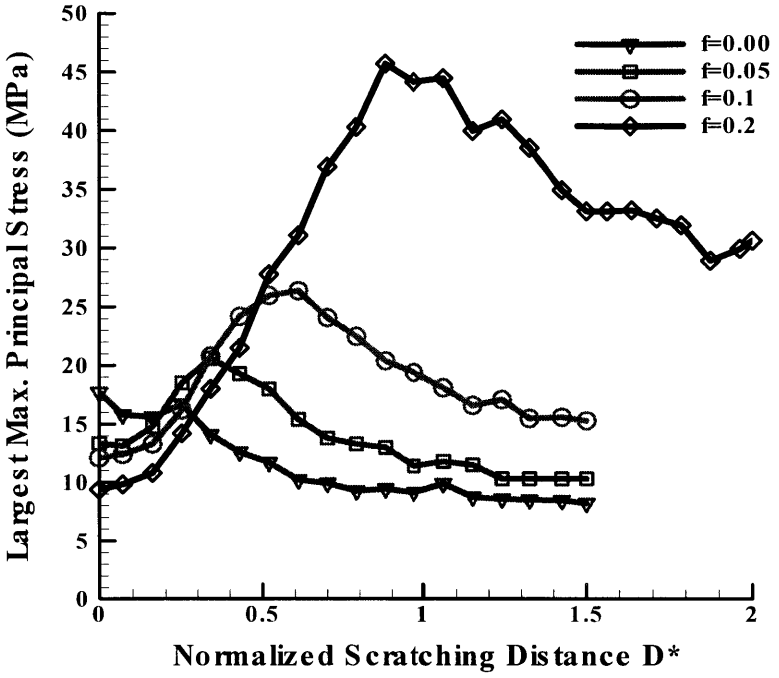

Figure 5-33(a)

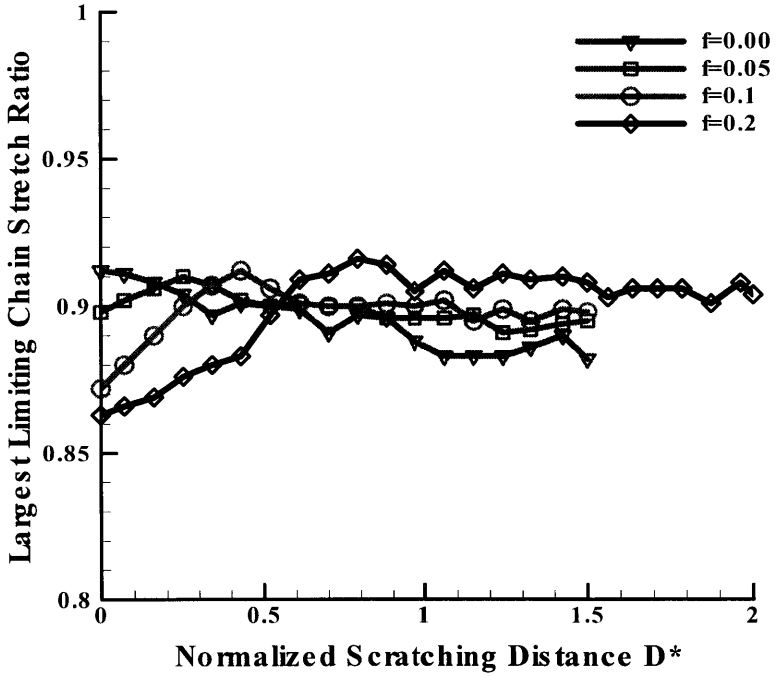

Figure 5-33(b)

Figure 5-33: Effects of contact friction coefficient on: The variations of (a) the largest maximum principal stress, and (b) the largest limiting chain stretch ratio with the normalized scratching distance.

Figure 5-33(b) shows the effect of contact friction force on the variations of the

largest limiting chain stretch ratio. From Figure 5-33(b), it is observed that increasing the contact friction force decreases the largest limiting chain stretch ratio upon indentation, whereas increases largest limiting chain stretch ratio during scratching.

5.4.1.2 Mechanism of Effective Friction Force

TPUs are well known for their low friction coefficients. However, large effective friction coefficients (defined as the ratio between the tangential force and normal force) were observed from both tests and numerical simulations of scratching. Moreover, as revealed in the previous part, even with contact frictional force being zero, a very large effective friction coefficient was observed. Clearly, the effective friction coefficient must be related with the stress-strain behavior features, i.e. cyclic softening and hysteresis, of TPUs. To further explore the mechanism for this phenomenon, the effective friction coefficient is studied in this part. For the sake of clarity, the contact frictional force is taken to be zero, i.e., $f = 0.00$.

In order to inspect the effects of cyclic softening, hysteresis and rate dependence on effective friction coefficients, three materials are studied: the first material (Material F1) is modeled using Arruda-Boyce model without cyclic softening; the second material (Material F2) is modeled using Arruda-Boyce model with cyclic softening; and the third material (Material A) is modeled using the constitutive model proposed in Chapter 4. Therefore, the difference between Material F1 and Material F2 is the presence of cyclic softening, whereas the difference between Material F2 and Material A is the presence of hysteresis and rate dependence.

Figure 5-34(a) and Figure 5-34(b) show the normal/tangential forces and effective friction coefficients. For Material F1, which has no softening, hysteresis, and rate dependence, without the presence of contact friction force, the tangential force is always zero and normal force is constant during scratching. With cyclic softening behavior, Material F2 shows small amount of decrease in normal force and small tangential force during scratching. Clearly, such differences in normal forces and tangential forces are due to cyclic softening. As cyclic softening, hysteresis, and rate dependence present, during scratching, Material A shows significantly larger tangential force and there is a relatively large decrease in normal force at beginning. The effective friction coefficient at slip

phase is zero for Material F1, about 0.1 for Material F2, and about 1.1 for Material A.

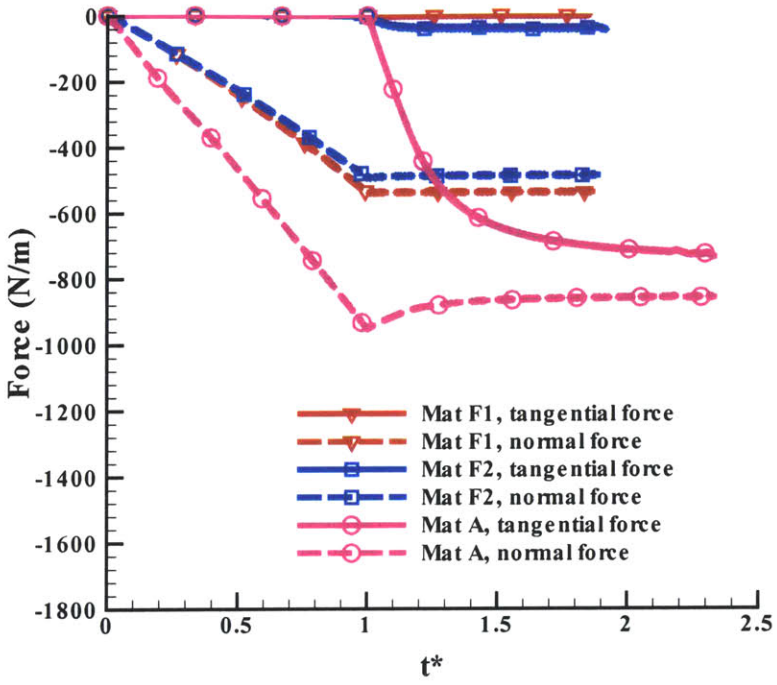

Figure 5-34(a)

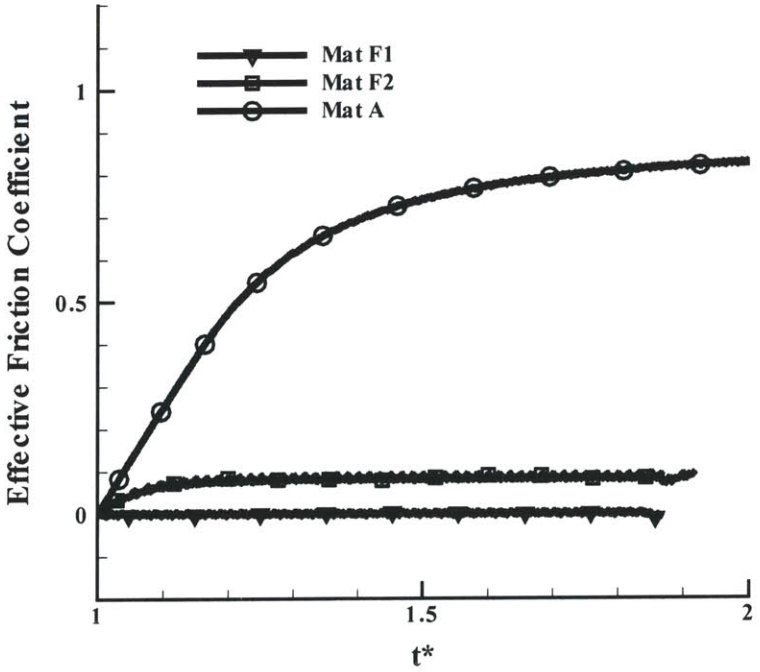

Figure 5-34(b)

Figure 5-34: (a) Normal/tangential force vs time curves; (c) Effective friction coefficient for Material F1, Material F2, and Mat A. The contact friction force used in simulations is zero, i.e., $f = 0.00$.

To further explore the mechanism of the effective friction coefficient, the contour plots of the maximum principal stress for the three materials during scratching $\delta_t = 30\mu m$ are presented in Figure 5-35.

From Figure 5-35, Material F1 shows a symmetric deformation and distribution of maximum principal stress. Such a symmetric deformation results in the balanced stress about the knife and zero tangential force. For Material F2, the deformation is biased and the material in front of the knife has larger conformation to the knife than the material behind the knife. Such a biased deformation results in a non-zero tangential force. For Material A, the deformation is highly biased: The material in front of the knife has very large conformation to the knife whereas the material behind the knife almost loses contact with the knife, resulting in a large tangential force.

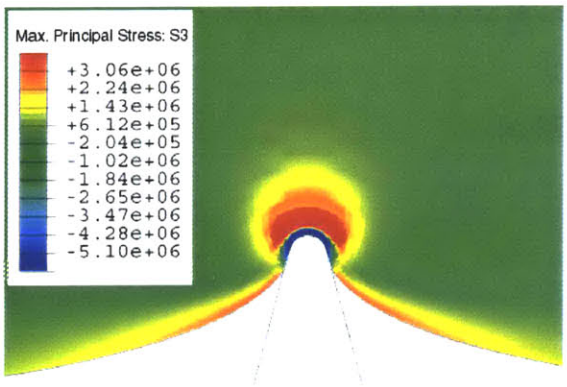

Figure 5-35(a)

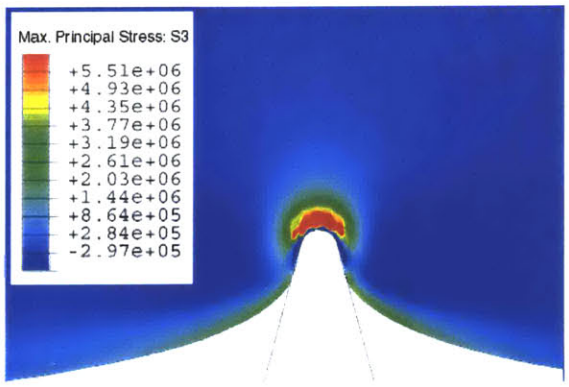

Figure 5-35(b)

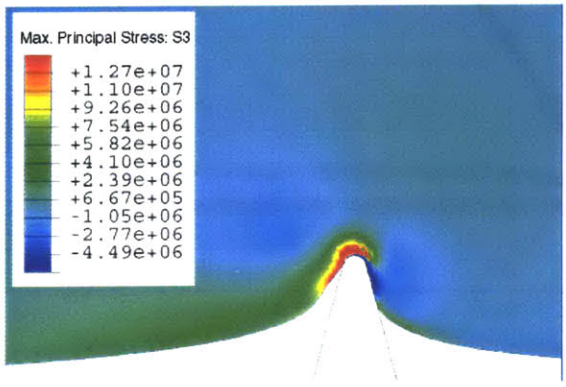

Figure 5-35(c)

Figure 5-35: Contour plots of maximum principal stress at $\delta_t = 34\mu m$ for (a) Material F1; (b) Material F2; (c) Material A.

During the scratching process, as the knife approaches and passes by a particular part of material, that part of material will undergo loading (as the knife approaches), then unloading (as the knife passes by). For TPU material, due to cyclic softening and hysteresis, for a given strain, the material has higher resistance to deformation in loading state that it does in unloading state. Clearly, in Figure 5-35, the material behind the knife undergoes unloading and has smaller resistance to deformation, whereas the material in front of the material undergoes loading and has larger resistance to deformations. Such a difference in the deformation resistance of the material in front and behind the knife causes the significant amount tangential force when cyclic softening, hysteresis and rate dependence present.

In pneumatic tire applications, the tangential force provides desired tire traction. The case of $f = 0.0$ is of special interest because it provides the situation of wet-sliding, where the adhesive force does not present and mechanism to provide traction has to be sought. It has been widely accepted that wet-sliding friction primarily comes from the bulk hysteretic energy dissipation[5-6][5-7][5-8]. It is been widely practiced in tire industry to use the loss tangent, $\tan\delta$, from dynamic viscoelasticity measurements at a low frequency of about 10Hz and at a specific low temperature to evaluate the wet traction performance of a tread compound using empirical relations. However, it is still unclear what is the mechanism for the relationship between the loss tangent $\tan\delta$ and tire traction. It is also desirable to have analytical tools to predict tire traction. The proposed mechanism and numerical simulation model together with the new constitutive model meet this demand and will be used to address the relationship between tire traction and viscoelasticity in the future.

5.4.2 Effects of Scratching Speeds

Effects of scratching speeds on the mechanics of scratching were studied by varying the scratching speed in the FEM simulations whereas the indentation speeds were the same. Figure 5-36(a) shows the normal/tangential force vs time curves for the simulations with three different scratching speeds, i.e., v=4μm/s, v=8μm/s, and v=16μm/s. Figure 5-36(b) shows the corresponding effective friction coefficient curves. From Figure 5-36(a), the normal forces are different as soon as the scratching starts and the higher the scratching

speed, the higher the normal force. The simulation with lower scratching speed v=4μm/s shows some initial decrease in the normal force until $t^* = 1.3$, after which the normal force increases; whereas the simulations with higher scratching speed v=16μm/s shows relatively smaller decrease in the normal force until $t^* = 1.2$, after which the normal force increases. The amount of decrease in the normal force decreases with increasing scratching speed. It is also noticed that the amount of the increase in the tangential force decreases with increasing scratching speed. For instance, the difference in tangential forces at $t^* = 2.0$ is about 40N/m for the tests with v=4μm/s and v=8μm/s, whereas the difference is about 20N/m for the tests with v=8μm/s and v=16μm/s. It is unclear yet whether a saturated tangential force can be achieved, but it seems that the increase in the tangential force will be less sensitive at higher speed than that at lower speed.

From Figure 5-36(a), the normal force increase at a faster rate than the tangential forces at higher scratching speed, resulting in the decrease in the effective friction coefficients, as indicated in Figure 5-36(b). From Figure 5-36(b), the effective friction coefficients for different scratching are indistinguishable until $t^* > 1.4$. It is also noticed that although the general trend is that the higher scratching speed, the lower the effective friction coefficient, the differences are generally small.

Figure 5-37 shows the effect of scratching speeds on the variations of the largest maximum principal stress and the largest limiting chain stretch ratio. From Figure 5-37(a), the peak value of the largest maximum principal stress increases with increasing scratching speed, i.e. for v=4μm/s, $S_3^p \approx 26MPa$, for v=8μm/s, $S_3^p \approx 28MPa$, and for v=16μm/s, $S_3^p \approx 30MPa$. However, the largest limiting chain stretch ratio does not show significant dependence on the scratching speed, as shown in Figure 5-37(b). Although Figure 5-37(b) only shows the dependence of largest value of the limiting chain stretch ratio on the scratching speed, it is reasonable to expect that the limiting chain stretch ratio is essentially independent upon the scratching speed, since limiting stretch ratio is related with the reorientation of molecular chain which occurs at a much higher rate than the scratching speed in current study.

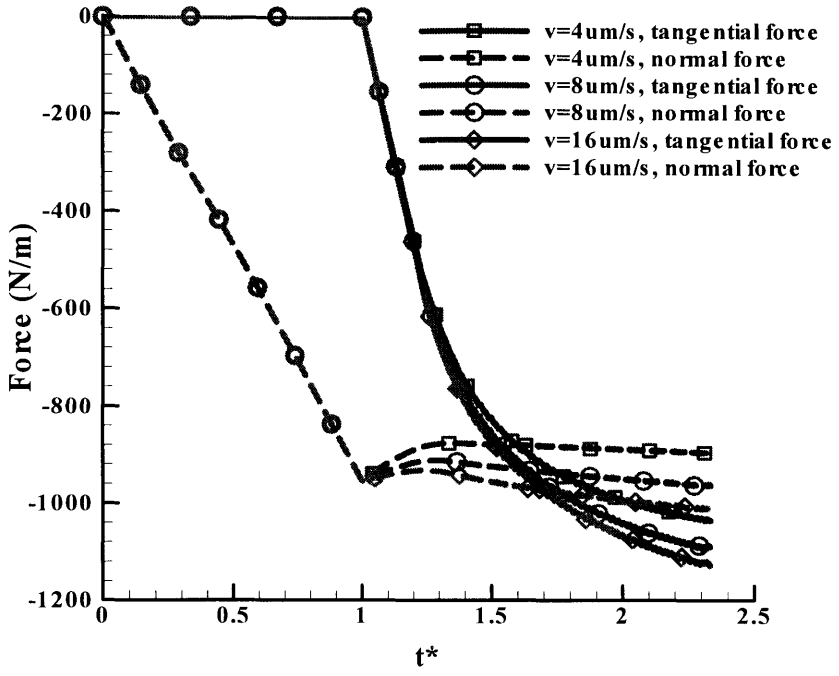

Figure 5-36(a)

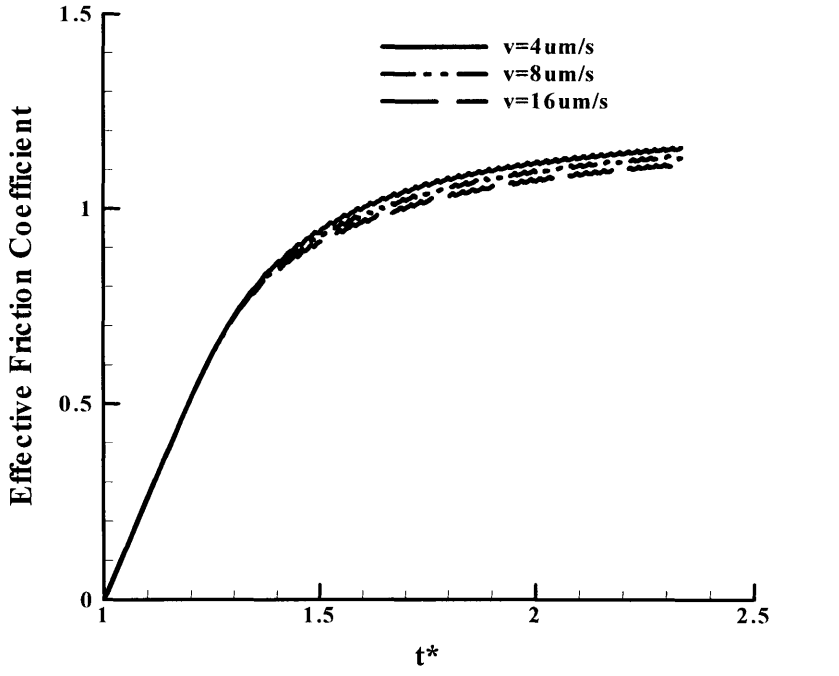

Figure 5-36(b)

Figure 5-36: Effects of scratching speed on: (a) Normal/tangential force vs time curves; (b) Effective friction coefficient.

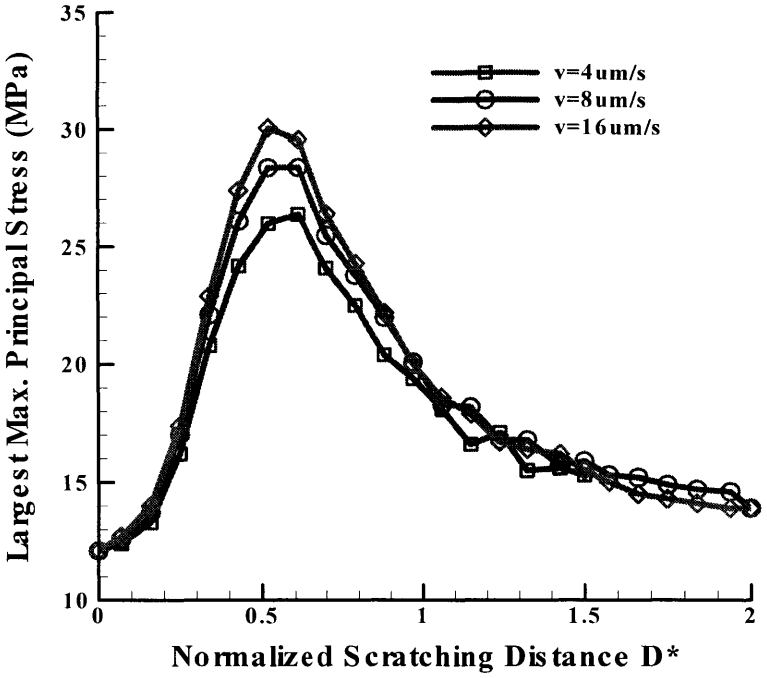

Figure 5-37(a)

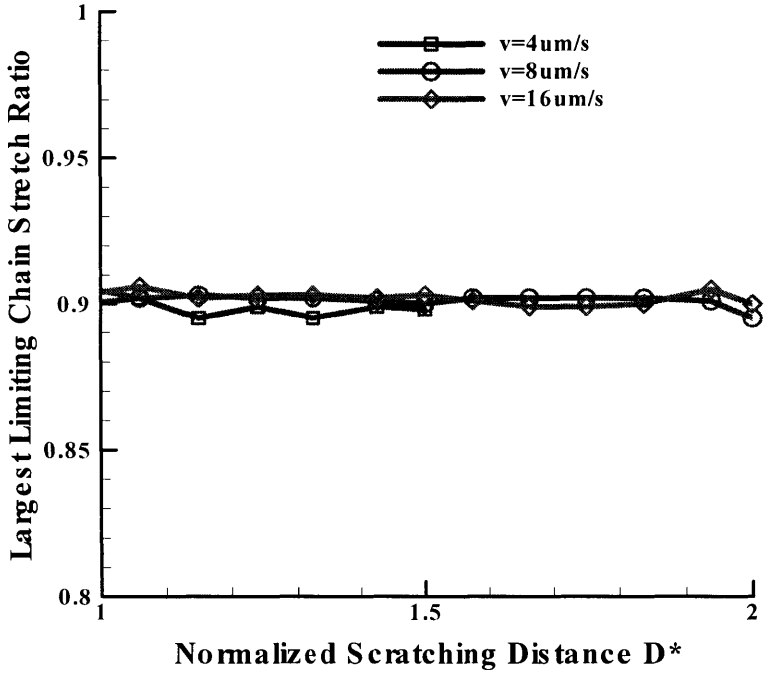

Figure 5-37(b)

Figure 5-37: Effects of scratching speed on: The variations of (a) the largest maximum principal stress, and (b) the largest limiting chain stretch ratio with the normalized scratching distance.

5.4.3 Effects of Material Properties

The stress-strain behavior of TPUs shows an initially stiff response, followed by rollover, then stiffen again during the loading course, whereas the unloading paths show a large hysteresis loop. The material also shows various dependences. The constitutive model proposed in Chapter 4 successfully captured the complicated behavior of the material and made it possible to inspect the effects of different aspects of material behavior on the deformation and mechanics by deliberately varying the material parameters in the constitutive model. In this part, the effects of hysteresis, initial modulus of the material stress-strain behavior, and the chain extensibility, on the mechanics of the scratching tests are investigated.

5.4.3.1 Effects of Hysteresis

Effects of hysteresis on the mechanics are studied by comparing the responses of materials with different level of hysteresis in their uniaxial compression stress-strain behaviors. Here, three materials are chosen: the first one (Material A) is the material discussed in Chapter 4, and the second material (Material B) is created by deliberately choosing material parameters to generate smaller hysteresis. To further investigate the effects of hysteresis, the third material to demonstrate the extremity of low hysteresis, i.e. the third material (Material EQ) is chosen to demonstrates equilibrium behavior of Material A and Material B. Material EQ is modeled by Arruda-Boyce 8 chain model and uses the same material parameters as those used in hyperelastic rubbery spring of Material A and Material B. As discussed in Chapter 4, the hysteresis and rate dependent behaviors are attributed to the three material parameters $\dot{\gamma}_0$, ΔG, and s_0 in the constitutive model. Therefore, Material B is chosen by only varying these parameters. Table 5-1 shows the material parameters for Material A and Material B. In Table 5-1, only parameters related with viscoplastic dashpot element in the constitutive model are presented, and other parameters in the material model are same for both Material A and Material B and are not shown for the seek of brevity. Figure 5-38 shows the true stress-true strain curves for the three materials. From the figure, the Material B shows lower hysteresis than the Material A does: the area between the loading and unloading curve for Material B is about 54% of the one for the Material A for the first cycle, and about 44%

for the second cycle.

Table 5-1: Material Parameters for Material A and Material B.

	s_0 (MPa)	ΔG $(10^{-19} J)$	$\dot{\gamma}_0$
Material A	4.55	0.41	2.26
Material B	2.275	0.41	4.52

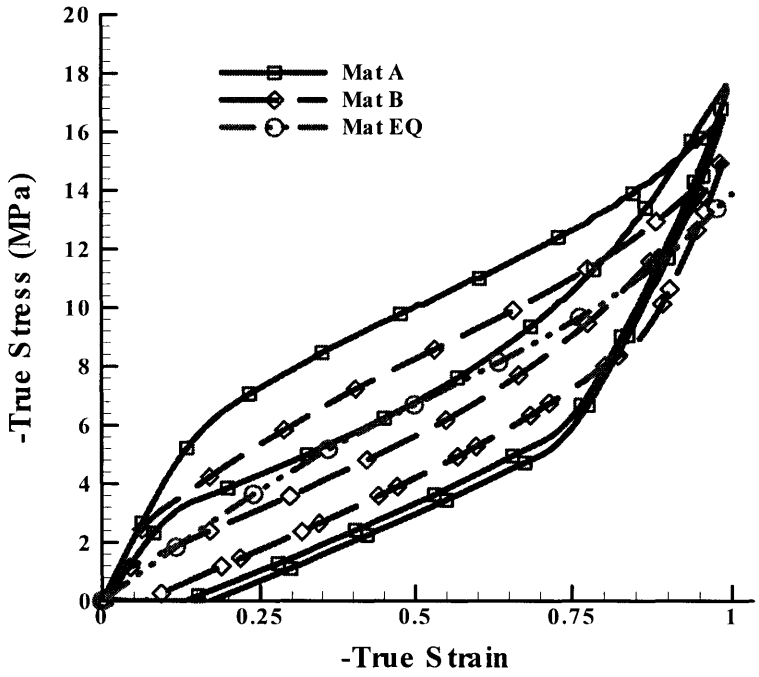

Figure 5-38: The true stress-true strain curves for Material A, Material B and Material EQ.

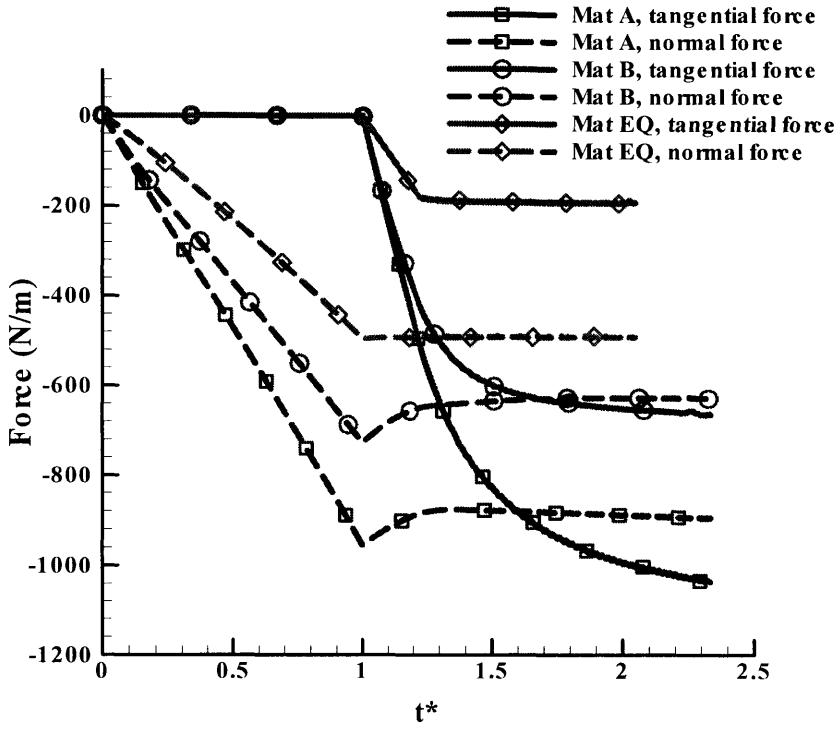

Figure 5-39(a)

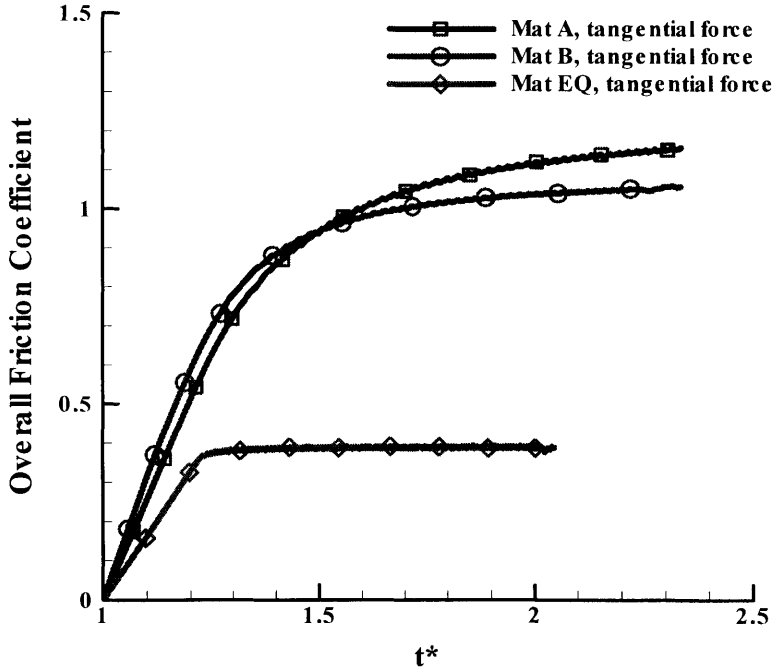

Figure 5-39(b)

Figure 5-39: Effects of rate dependence on: (a) Normal/tangential force vs time curves; (b) Effective friction coefficient.

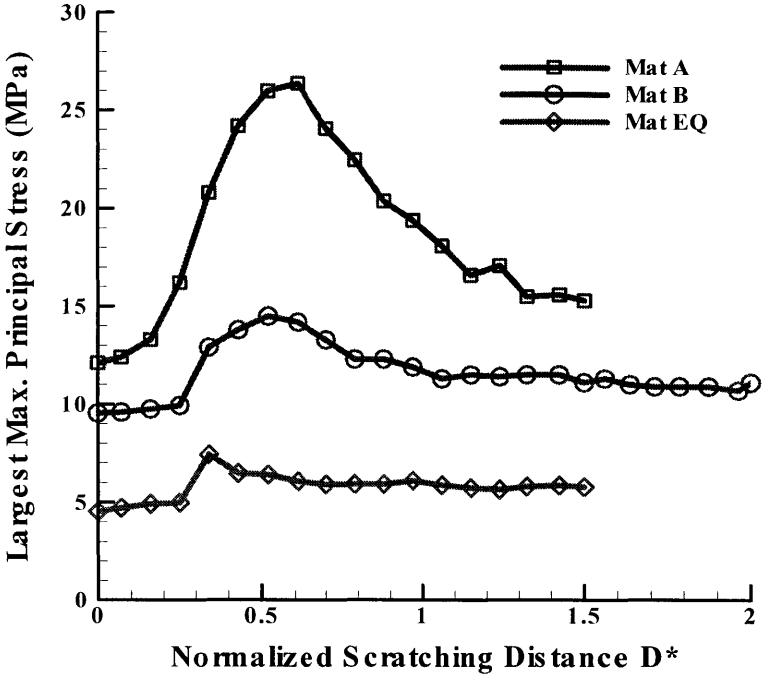

Figure 5-40(a)

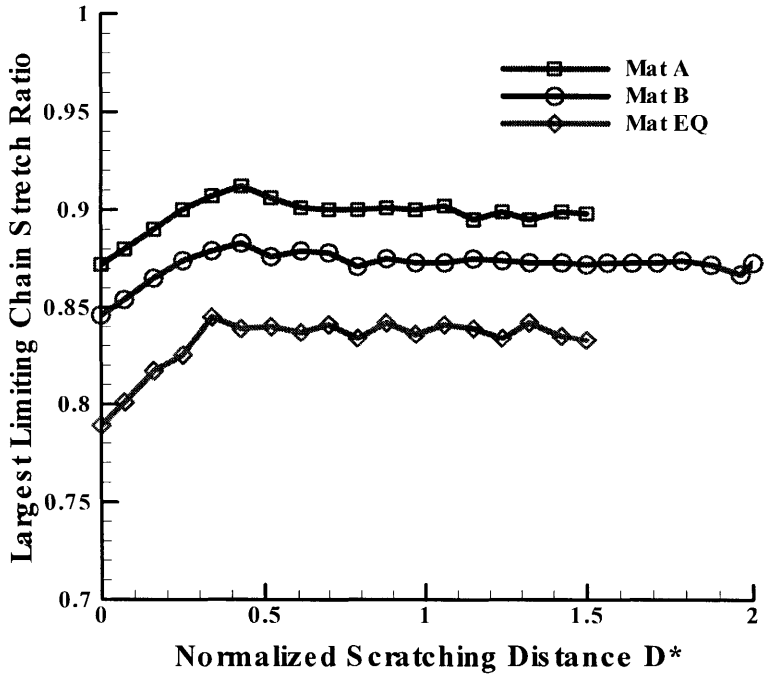

Figure 5-40(b)

Figure 5-40 Effects of rate dependence on: The variations of (a) the largest maximum principal stress, and (b) the largest limiting chain stretch ratio with the normalized scratching distance.

Figure 5-39(a) shows the normal/tangential forces from the simulations for the three materials and Figure 5-39(b) shows the effective friction coefficients. Reducing the hysteresis decreases both the normal force and the tangential force significantly. As indicated in Figure 5-39(a), reducing the hysteresis by about 50% in the material stress-strain behavior results in about 29% decrease in the normal force and about 35% decrease in the tangential force. As hysteresis is totally removed, the normal force does not show the feature of decreasing to a stabilized value during scratching and maintains the force value. The effective friction coefficient at $t^* = 2.33$ is about 1.1 for Material A whereas is about 1.0 for Material B, and is only 0.4 for Material EQ.

Figure 5-40(a) and Figure 5-40(b) shows the variations of the largest maximum principal stress and the largest limiting chain stretch ratio vs. the normalized scratching distance. Due to the decrease in the normal and tangential forces for Material B, the largest maximum principal stress is reduced significantly: the peak value for the largest maximum principal stress for Material B is about 15MPa, only about 55% of the value for Material A; the stable value for the largest maximum principal stress for Material B is about 12MPa, which is about 75% of that for Material A. Without hysteresis, the peak value of the largest maximum principal stress is only about 27% of that of Material A. The largest limiting chain stretch ratio is about 0.90 for Material A, 0.87 for Material B, and 0.84 for Material EQ. Clearly, reducing the rate dependence and hysteresis decreases the largest maximum principal stress significantly, and decreases the largest limiting chain stretch moderately.

5.4.3.2 Effects of Initial Young's Modulus

The effects of initial modulus E^0 of the material are studied in this part. From Chapter 4, it is known the initial modulus of the material has contributions from the hyperelastic rubbery spring and the elastic spring of the viscoelastic-plastic component. From eqn.(4-13), the initial Young's modulus for the hyperelastic rubbery spring is determined by the parameters μ and N. The initial Young's modulus for the elastic spring is E^v. Therefore, by varying any of these three parameters and any combinations of them will change the initial Young's modulus of the material. Here, we will study the effect of μ and E^v on the mechanics of the scratching test, and will leave the effect of N for the next. In this

part, three materials are studied: Material A studied in Chapter 4 is used here as a reference for comparison; Material C and D are created by varying μ and E^v. Table 5-2 lists the material parameters μ and E^v, and corresponding material initial Young's modulus E^0. Material C is chosen by doubling the μ of Material A and uses the same E^v. Material D uses the same E^v but doubling μ. The rest of material parameters for all the materials are the same and are not presented in the table for the sake of brevity.

Figure 5-41 shows the true stress-true strain curves for the materials studied in this part. It is noticed that parameters μ and E^v have different influences on the material stress-strain behaviors: E^v only changes the initial modulus of the material, resulting in the almost identical stress-strain behavior at large strains (Material A and Material C follow almost identical course at large strain), whereas μ changes both initial modulus as well as large strain behavior, as indicated by the greater stress response of Material C.

Table 5-2: Material Parameters for Material A, C, and D

	μ (MPa)	E^v (MPa)	E^0 (MPa)
Material A	1.7	35	48
Material C	3.4	35	64
Material D	1.7	70	77

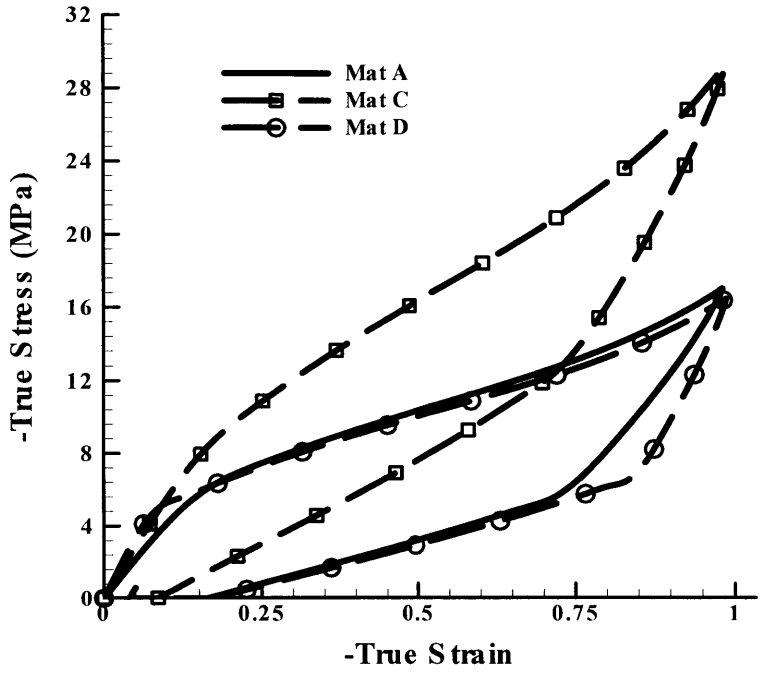

Figure 5-41: The true stress-true strain curves for Material A, Material C, Material D, and Material E.

Figure 5-42(a) shows the normal/tangential force vs. time curves from the simulations for the three materials. Increasing the initial Young's modulus generally increases both normal force and tangential force. However, increasing material stress response at small strain (Material D compared with Material A) increases the normal force moderately and tangential force significantly, whereas increasing material stress response at both small and large strain increases the normal and tangential forces significantly with normal force having much larger level of increase than the tangential force. The change of the normal force and tangential force is more clearly demonstrated by Figure 5-42(b), which shows the effective friction coefficient from the simulations for the four materials. Clearly, Material D, which doubles the modulus for the elastic spring in the viscoelastic-plastic component, results in the highest effective friction coefficient, whereas Material C, which doubles the initial modulus of the hyperelastic rubbery spring, generates the smallest effective friction coefficient. In practice, normal force provides loading carrying of the material, whereas the tangential force represents the resistance for the tangential motion and dissipation of the energy. Therefore, increasing only the modulus of hyperelastic

rubbery spring μ provide an effective way to increase both loading carrying as well as to reduce energy dissipation.

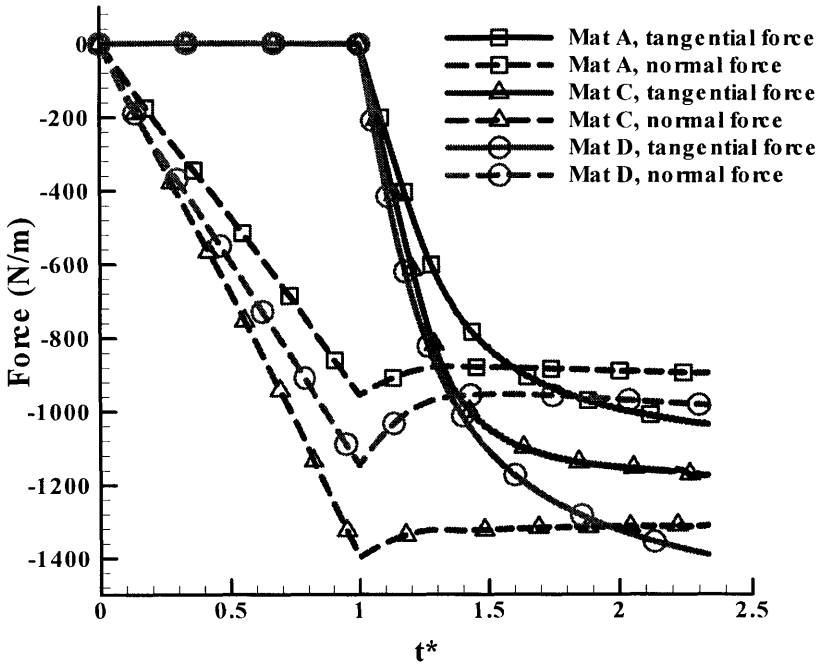

Figure 5-42(a)

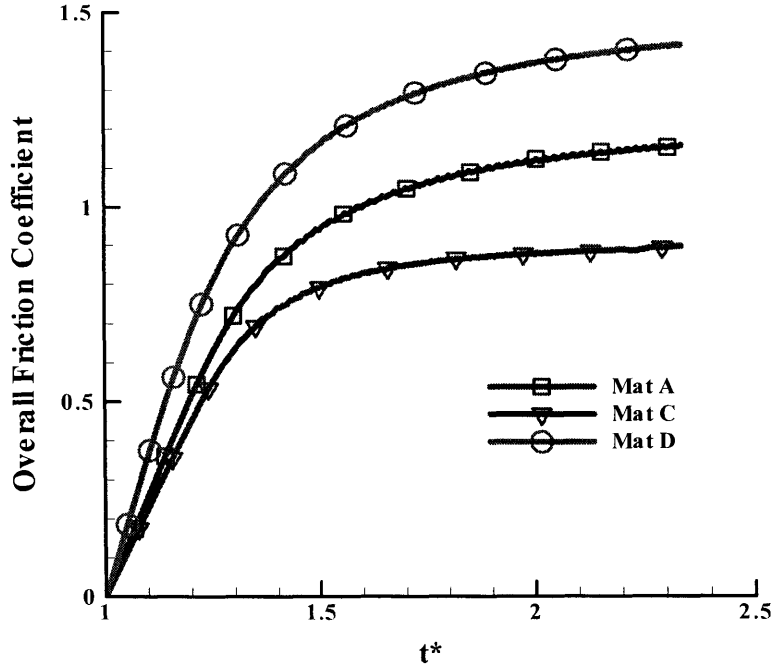

Figure 5-42(b)

Figure 5-42: Effects of material initial modulus on: (a) Normal/tangential force vs time curves; (b) Effective friction coefficient.

Figure 5-43(a) shows the variations of the largest maximum principal stress vs. the normalized scratching distance. It is found that the peak value of the largest maximum principal stress during scratching increases with increasing initial Young's modulus of material. Figure 5-43(b) presents the peak value of the largest maximum principal stress vs. the initial modulus of the materials curves, and shows an almost linear relationship between them,

$$S_3^{peak} = 0.21E^0 + 16. \qquad (5.5)$$

Figure 5-43(c) shows the variations of the largest limiting chain stretch ratio vs. the normalized scratching distance. From the figure, it is found that increasing the initial modulus of the hyperelastic rubbery spring reduces the largest limiting chain stretch ratio whereas increase the modulus of the elastic spring of the viscoelastic-plastic component increases the largest limiting chain stretch ratio. In this regard, increasing the initial modulus of the hyperelastic rubbery spring will benefit the abrasive wear performance of material.

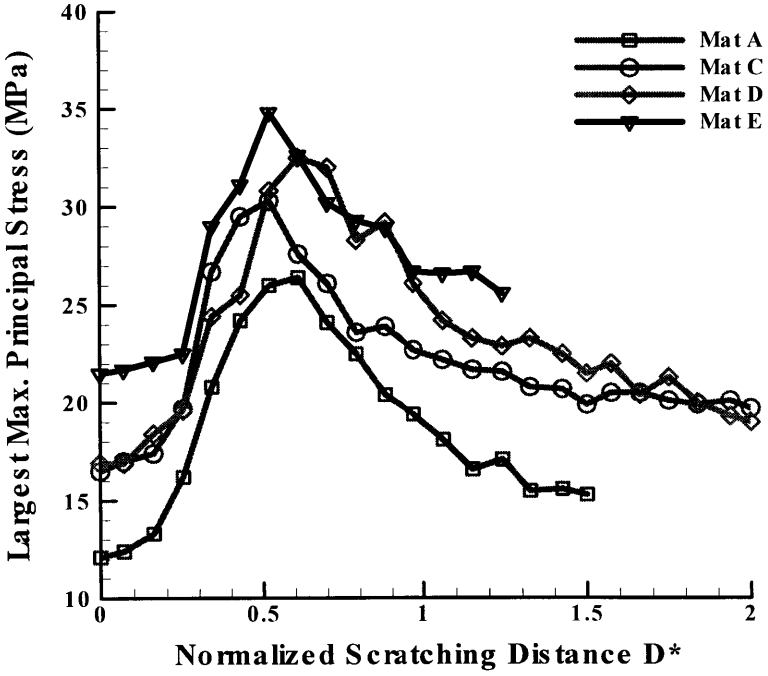

Figure 5-43(a)

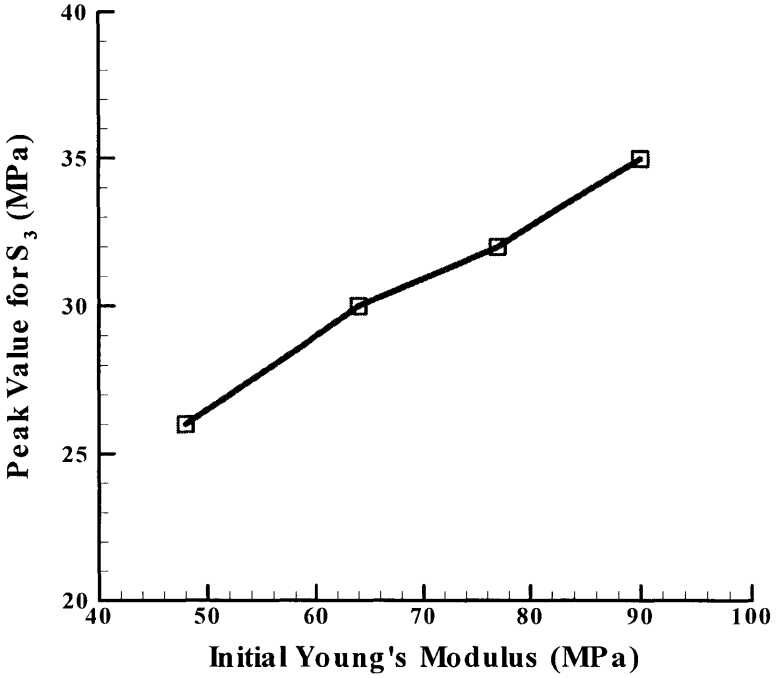

Figure 5-43(b)

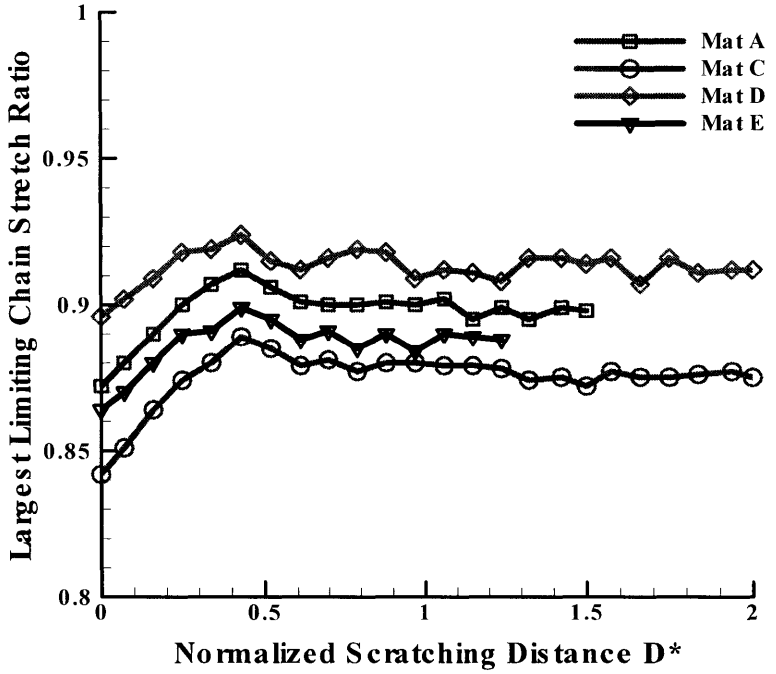

Figure 5-43(c)

Figure 5-43: Effects of material initial modulus on: The variations of (a) the largest maximum principal stress, and (b) Relation between the peak value of the largest maximum principal stress and the initial modulus of the material; (c) the largest limiting chain stretch ratio with the normalized scratching distance.

5.4.3.3 Effects of Chain Extensibility

The effects of chain extensibility, N, of the material are studied in this part. From Chapter 4, it is known the initial Young's modulus E_0^r of the hyperelastic rubbery spring is determined by the parameter μ and N by eqn. (4-13). Therefore, simply varying N will also change the initial modulus of the material. In order to isolate the effects of N from the effects of μ, the change of N is accompanied by the change of μ to maintain the same initial Young's modulus E_0^r for all the materials studied. Three materials are studied here: Material A studied in Chapter 4 is used as a reference for comparison; Material F and G are created by varying μ and N. Table 5-3 listed the material parameters μ and N, and corresponding initial Young's modulus E_0 of the hyperelastic rubbery spring. Material F is chosen by doubling the N of Material A whereas Material G uses the half of N of Material A.

Table 5-3: Material Parameters for Material A, F, and G.

	N	$\mu\,(MPa)$	$E_0^r\,(MPa)$
Material A	5.26	1.70	5.70
Material F	10.52	1.79	5.70
Material G	2.63	1.51	5.70

Figure 5-44 shows the true stress-true strain curves for the Material A, Material F, and Material G. It is noticed that the difference between the stress response of the materials becomes significant at relatively large strains: Material G shows a sharp increase in stress response after $\varepsilon = 0.60$, implying that molecular chain is stretched close to the chain extensibility. Material F shows smaller response stress at strain $\varepsilon = 1.00$ than Material A due to the larger chain extensibility of Material F.

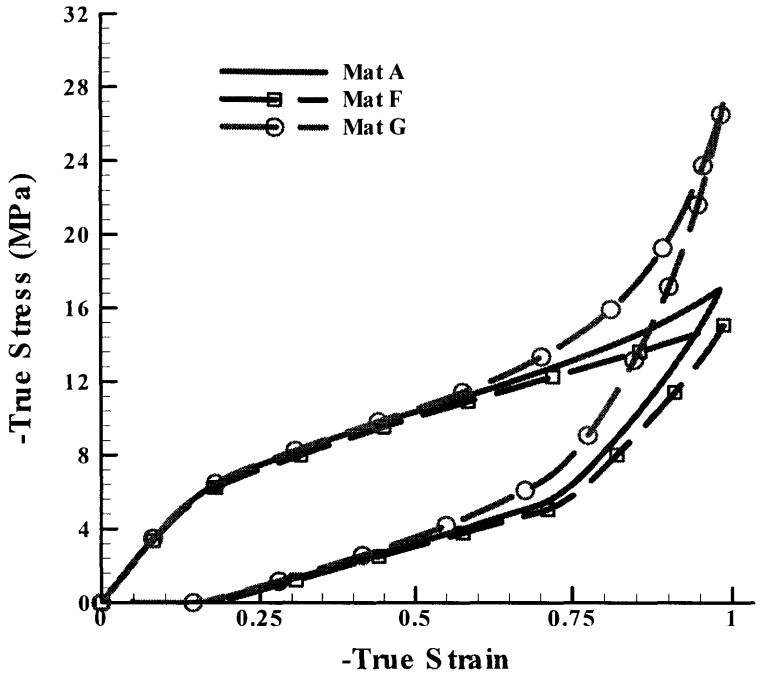

Figure 5-44: The true stress-true strain curves for Material A, Material F, and Material G.

Figure 5-45(a) shows the normal/tangential force vs. time curves from the simulations for the three materials. From Figure 5-45(a), it is clear that the smaller chain extensibility results in the smaller tangential forces as well as smaller normal forces. The normal force generally shows less sensitive to the change in chain extensibility than the tangential force. For instance, as the chain extensibility is reduced by half from Material A to Material G, the normal force decreases only by about 3% whereas the tangential force by about 20%. Figure 5-45(b) shows the effective friction coefficient from the simulations for the three materials. Therefore, decreasing the chain extensibility provides an effective way to reduce energy dissipation. It is also that found since the initial modulus of the hyperelastic rubbery spring is related with N through eqn.(4-13), which shows that decreasing N increases E_0^r. Therefore, the relationship of eqn.(5-5) obtained by varying μ and E^v cannot be generally held when N varies. However, eqn(5-5) can be still provide insight on the mechanics of scratching and be applied as long as N is constant.

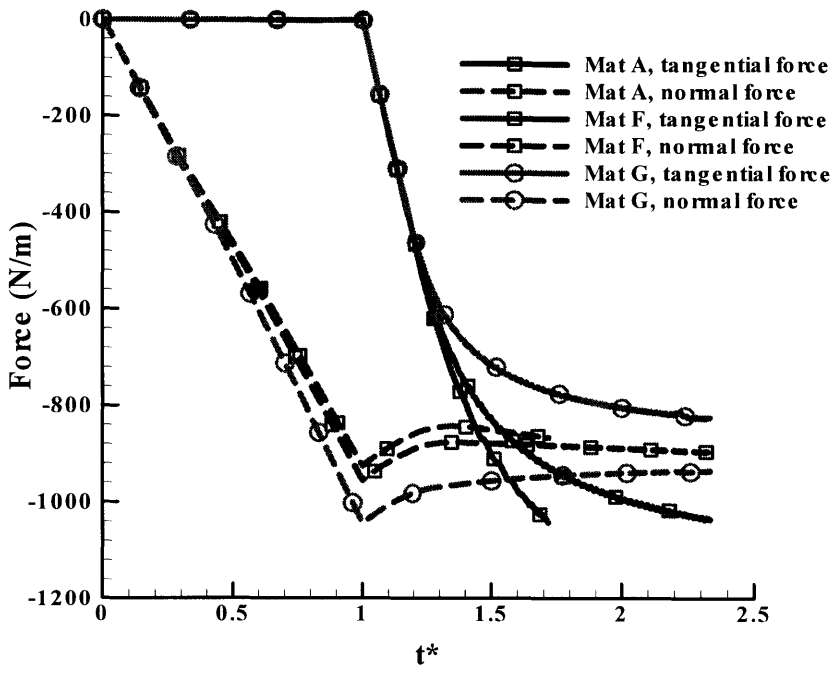

Figure 5-45(a)

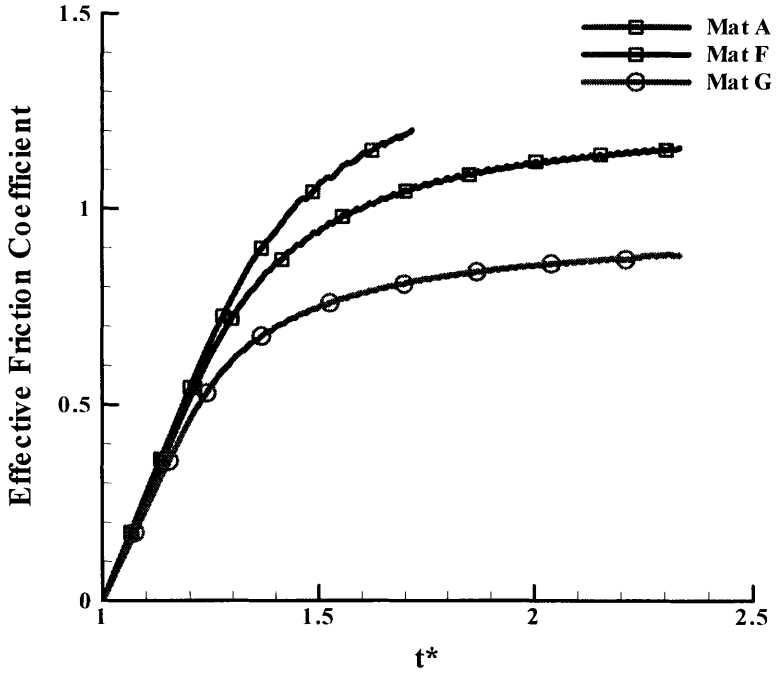

Figure 5-45(b)

Figure 5-45: Effects of chain extensibility on: (a) Normal/tangential force vs time curves; (b) Effective friction coefficient.

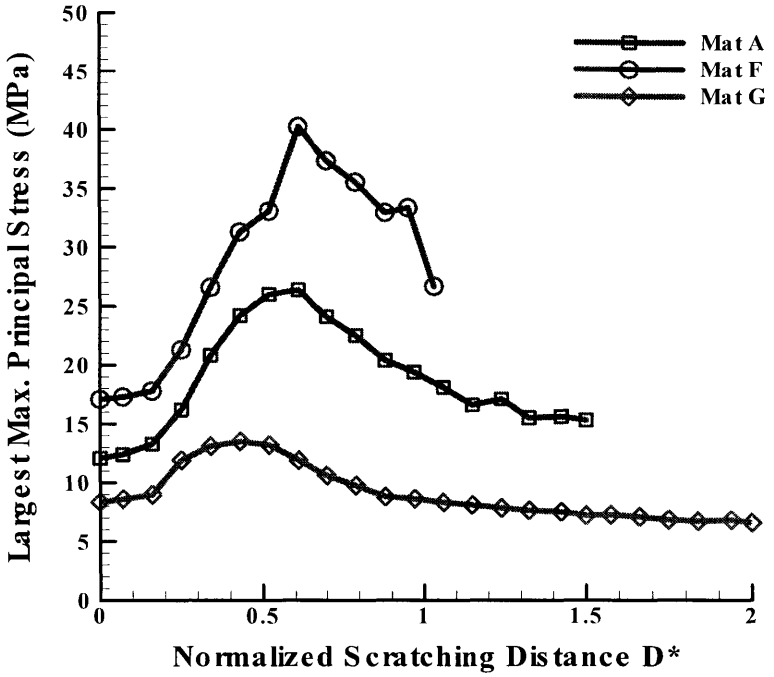

Figure 5-46(a)

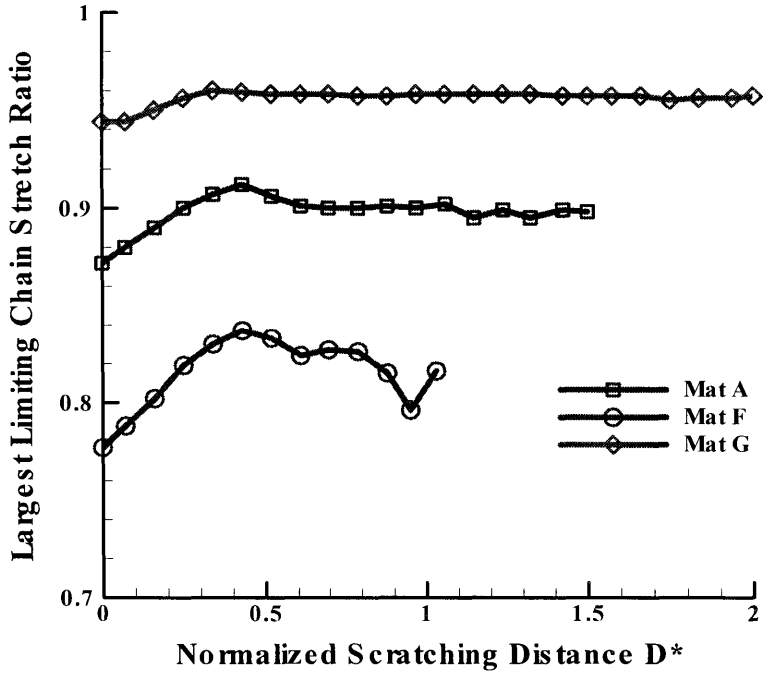

Figure 5-46(b)

Figure 5-46: Effects of chain extensibility on: The variations of (a) the largest maximum principal stress, and (b) the largest limiting chain stretch ratio with the normalized scratching distance.

Figure 5-46(a) shows the effects of chain extensibility on the variations of the largest

maximum principal stress with the normalized scratching distance. For the chain extensibility of $N = 2.63$, the peak value of the largest maximum principal stress is $S_3^{peak} = 13MPa$; For $N = 5.26$, $S_3^{peak} = 26MPa$; For $N = 10.63$, $S_3^{peak} = 41MPa$. Clearly, the peak value of the largest maximum principal stress is very sensitivity to the variation in chain extensibility. The smaller chain extensibility results in significant smaller peak value.

Figure 5-46(b) shows the effects of chain extensibility on the variations of the largest limiting chain stretch ratio with the normalized scratching distance. The material with smaller chain extensibility shows quite large limiting chain stretch ratio. Therefore, cautions should be applied when reducing chain extensibility if chain breakage is the dominant failure mode of the material.

5.5 Mechanics of the Scratching Tests for Glass Fiber Filled TPUs

In this section, effects of the interaction between a single fiber with different orientations and the wedge-type knife will be studied. Three representative fiber orientations, i.e., the horizontal, the vertical, and the lateral, are investigated. Figure 5-47 shows the FEM mesh and relative position of the fiber. Fiber dimensions of 16μm diameter and length to diameter ratio of 8 were used by Parsons[5-5]. Here, the diameter of 12μm and the same length to diameter ratio were used to accommodate the FEM mesh. In all the three cases, the lower edge of the fiber was 56μm above the surface of the material. Figure 5-47(a) shows a fiber in the horizontal configuration, where the left end of the fiber was about 50μm left to the centerline of the knife. Figure 5-47(b) shows a fiber in the vertical arrangement, where the left edge of the fiber is about 50μm away from the centerline of the knife. Figure 5-47(c) shows a fiber in the lateral arrangement, where the center of the fiber is about 50μm away from the centerline of the knife. The overall geometry of the model and boundary and loading conditions were the same as those in the study of wedge-type knife indentation/scratching study on unfilled TPUs. The indentation depth was δn=80μm. The indentation speed was 2μm/s and the scratching speed was 4μm/s. The Young's modulus of the glass fiber was 72GPa whereas the Poisson's ratio was

0.22[5-5].

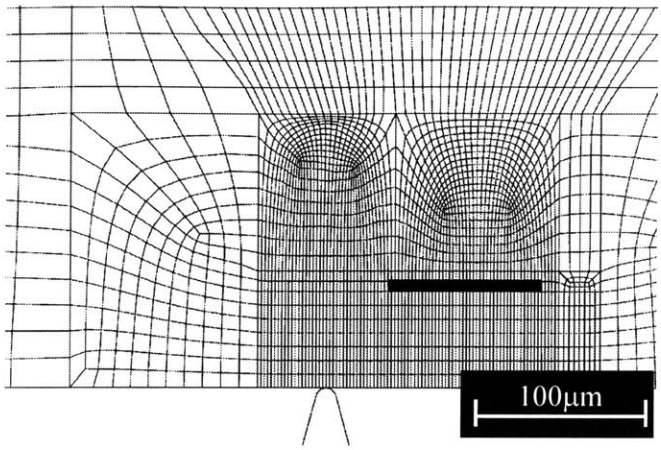

Figure 5-47(a)

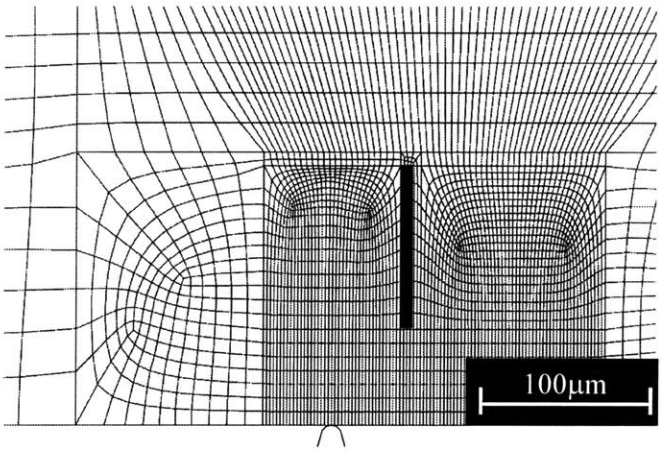

Figure 5-47(b)

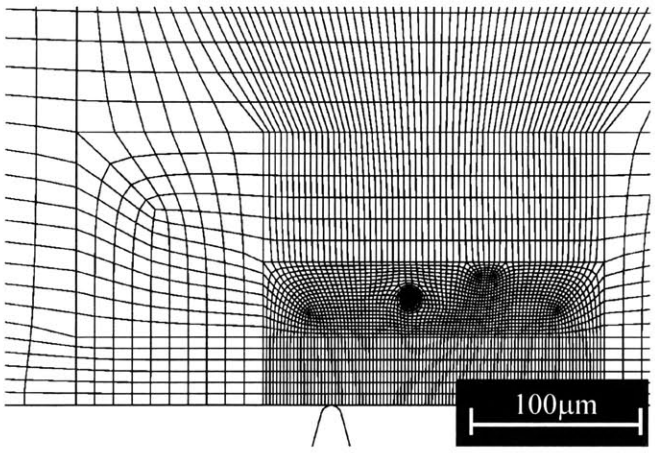

Figure 5-47(c)

Figure 5-47: FEM mesh and relative position of the fiber: (a) A horizontal fiber; (b) A vertical fiber; (c) A lateral fiber. The fibers are represented by the black blocks.

It should be noted that since the boundary value problems in above models are in plane strain state, the horizontal and vertical fibers are effectively "plates" with infinite width in z-direction whereas the lateral fiber is effectively a fiber with infinite length. The model with each representative fiber orientation thus reveals the overall interactions between the knife and the fibers that are predominately orientated in the same direction of the representative fiber.

5.5.1 The Horizontal Fiber

The scratching test on the glass fiber filled TPUs with a horizontal representative fiber was investigated. Figure 5-48 shows the normal/tangential force vs. normalized time t^* curves. The time is normalized according to eqn.(5-2). For the purpose of comparison, the results from indentation/scratching simulation on unfilled TPU are presented in Figure 5-48(b). From Figure 5-48, during indentation, the normal force demonstrates similar features as those observed in unfilled TPUs, since in the current case the knife is relatively far away from the fiber and thus cannot "feel" the existence of the fiber. Upon scratching, the knife cannot "feel" the fiber until it moves close enough to the fiber. From Figure 5-48(b), the normal and tangential forces for the filled TPU deviates from those for unfilled TPUs at about $t^* = 1.3$, corresponding to the scratching distance of 36μm, implying the knife starts to feel the fiber as it moves about 14μm away from the fiber. As the knife passes underneath the fiber, increases in both normal force and tangential force are observed, implying a larger resistance has to be overcome for an abrasive particle to move across a the horizontal fiber. In this study, the lower edge of the fiber is 56μm above the surface of the material. It is expected that an even larger resistance force should be overcome if the fiber were closer to the surface. In reality, abrasive particles may not be able to overcome such resistance and will be blocked[5-5].

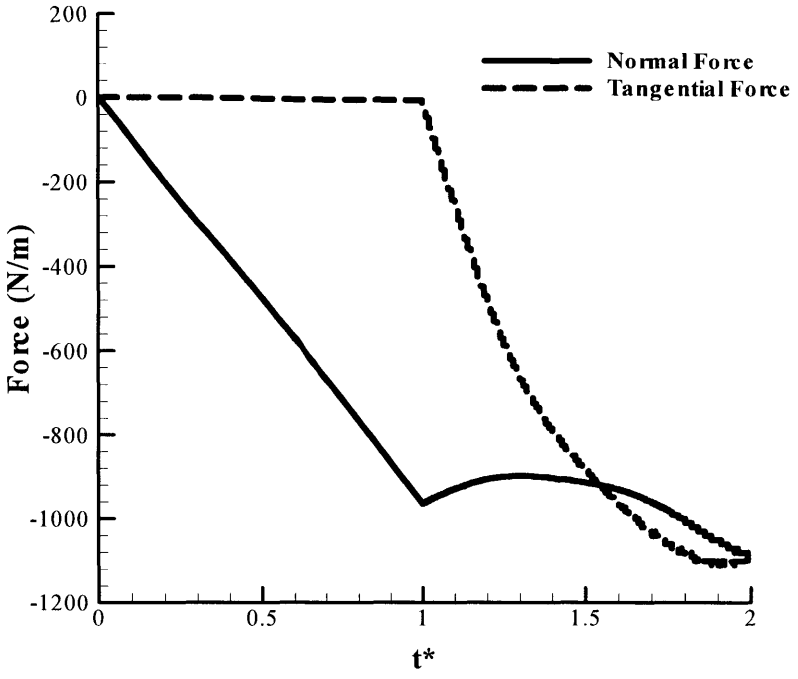

Figure 5-48(a)

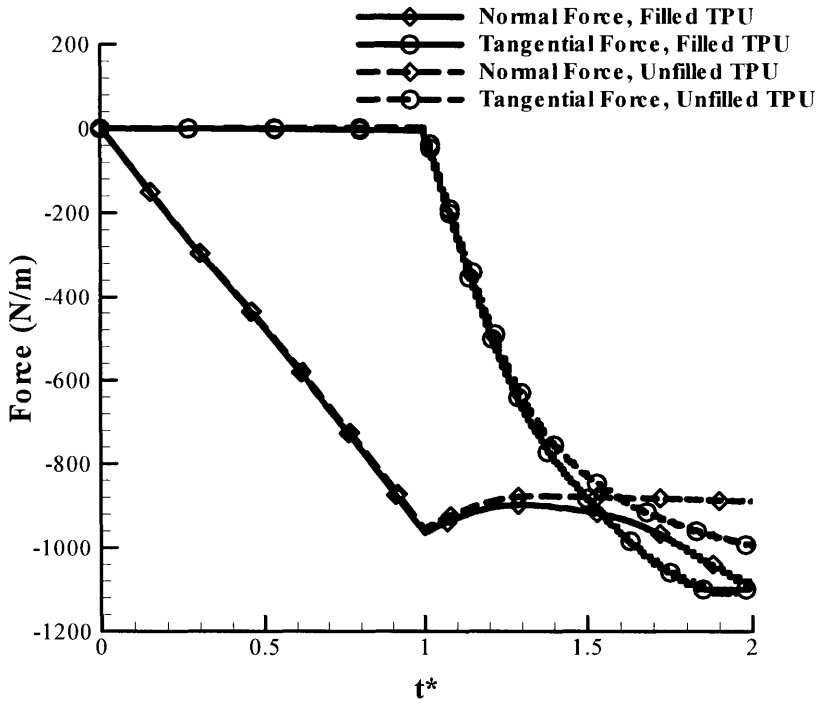

Figure 5-48(b)

Figure 5-48: Normal/tangential force vs. t^* curves from the numerical simulation for the case of the horizontal fiber.

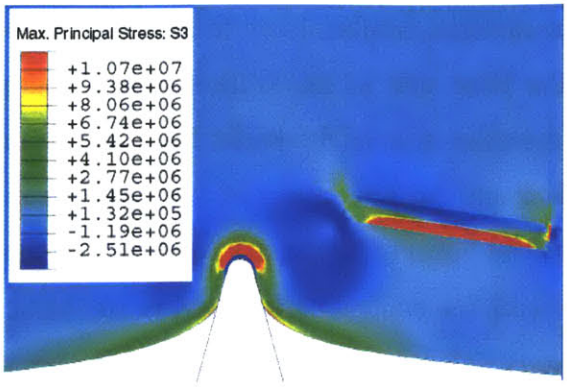

Figure 5-49(a)

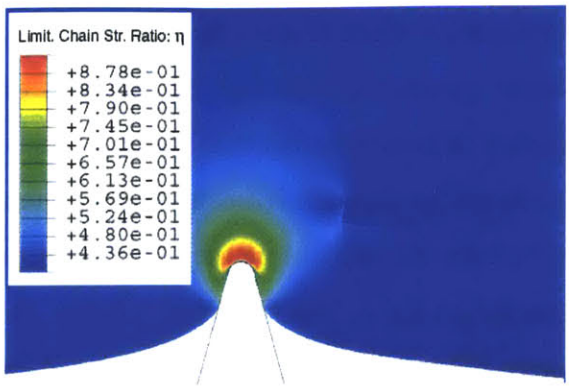

Figure 5-49(b)

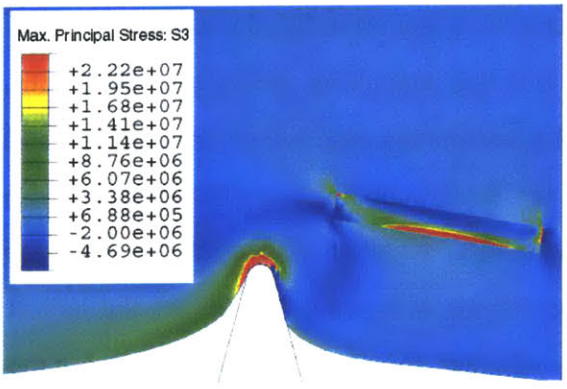

Figure 5-49(c)

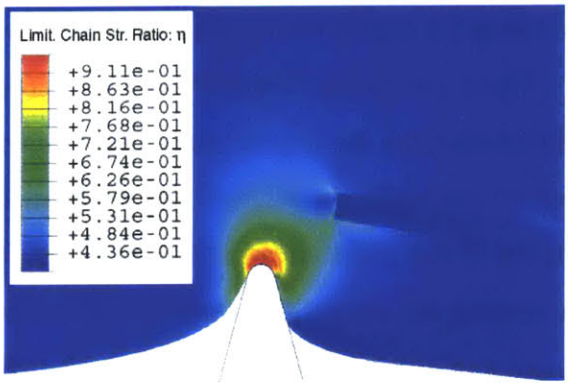

Figure 5-49(d)

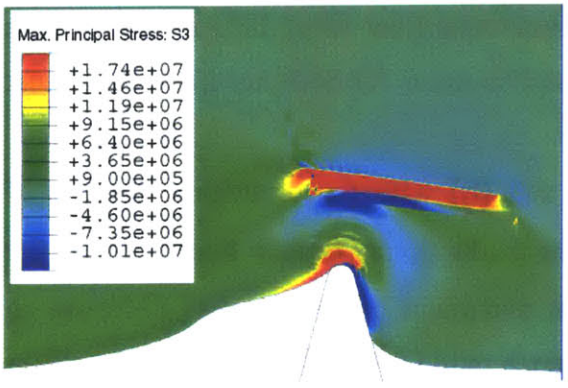

Figure 5-49(e)

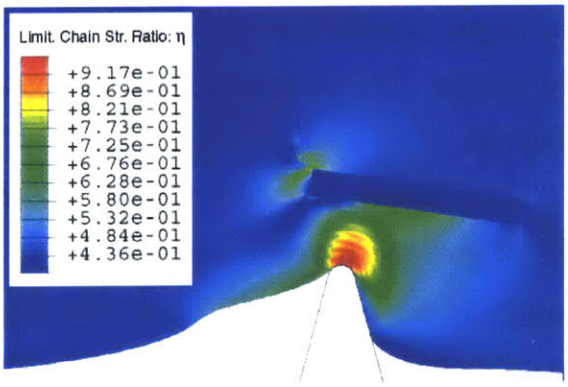

Figure 5-49(f)

Figure 5-49: Contour plots for (a) S_3 and (b) η at indentation; (c) S_3 and (d) η upon scratching δt=20μm; (e) S_3 and (f) η upon scratching δt=100μm for the scratching test with δn=80μm using the wedge-type knife.

Figure 5-49 shows the contour plots of the maximum principal stress S_3 and the limiting chain stretch ratio η during the scratching process. Upon indentation, i.e.,

δn=80μm, δt=0μm (Figure 5-49(a) and (b)), the material conformation to the knife tip is almost symmetric, although the material on the fiber side of the knife shows a larger amount of conformation than the material on the other side of the knife. Because of the incompatible deformation capabilities of the fiber and the TPU material, the fiber shows being bent upward during the indentation, which in turn provides extra resistance to the indentation force. The largest S_3 occurs underneath the contact surface and is 10.7MPa, which is smaller than that from the scratching test on unfilled TPU (12.1MPa). The largest limiting chain stretch ratio η occurs on the contact surface with $\eta^{max} = 0.88$, which is the almost identical as that from the scratching test on unfilled material.

Upon scratching (Figure 5-49(c) and (d)) with the scratching distance of δt=30μm, the location for the largest maximum principal stress moves onto the contact surface and behind the knife tip whereas the location for the maximum limiting chain stretch ratio moves to the place ahead of the knife tip. The similar features were observed from the scratching test on unfilled material. With the scratching distance of δt=30μm, the largest maximum principal stress is about 22.2MPa whereas the limiting chain stretch ratio increases moderately to 0.91. In comparison with the scratching test on unfilled material, the largest maximum principal stress for the horizontal fiber filled TPU is smaller than the unfilled TPU whereas the limiting chain stretch ratios for both materials are almost identical.

Upon further scratching (Figure 5-49(e) and (f)) with the scratching distance of δt=100μm, the material conformation to the knife tip is further biased. With the scratching distance of δt=100μm, the largest maximum principal stress decreases to 17.4MPa whereas the largest limiting chain stretch ratio is about 0.90, both of which are about the same as for the unfilled material.

Figure 5-50 shows the variations of the largest maximum principal stress and the largest limit chain stretch ratio vs. the scratching distance curves. The scratching distance is normalized according to eqn.(5-4), using the indentation depth of δn=80μm. The corresponding curves from the scratching test with δn=80μm on unfilled material are also shown in the figure. From Figure 5-50, the largest maximum principal stress for the horizontal fiber filled material is almost identical to that for unfilled material until

D*=0.3, corresponding to a scratching distance of about 24μm and about 26 μm away from the left end of the fiber. For D*>0.3, the horizontal fiber filled material shows relatively smaller amount of increase in the largest maximum principal stress and the peak value is about 24MPa, which is about 92% of the peak value for the unfilled material. The reason for the smaller peak value of the largest maximum principal stress in the horizontal fiber filled material is because the presence of the fiber provides the resistance to the material moving with the knife, hence facilitates the material to pass by the knife, and effectively reduces the stick phase, resulting in less stretch behind the knife and thus less maximum principal stress. As D*=1.0, which corresponds to the knife moves under the fiber, the largest maximum principal stress is almost the same as that for the unfilled material. It is also noticed that during the scratching process, very large S_3 exists in the material around the corner of the fiber, implying the possibility for the damage such as debonding occurring in these regions. From Figure 5-50(b), the variation of the largest limiting chain stretch ratio is almost identical to that from the unfilled material until the knife moves under the fiber, where the filled material shows larger limiting chain stretch ratio, but the amount of the difference between the filled and unfilled materials is small. The presence of a horizontal fiber, which is shown to reduce the peak value of the largest maximum principal stress, may benefit to the abrasive performance. However, the presence of a horizontal fiber also creates stress concentration around the corner of the fiber, which may cause debonding and fiber pullout. Indeed, this form of material damage, i.e. interface debonding and fiber pullout, was observed in Chapter 3. Therefore, from the point view of micro-mechanics, the presence of the horizontal fiber may benefit the performance, but such benefit may be overshadowed by the adversary effects due to interface debonding and fiber pullout.

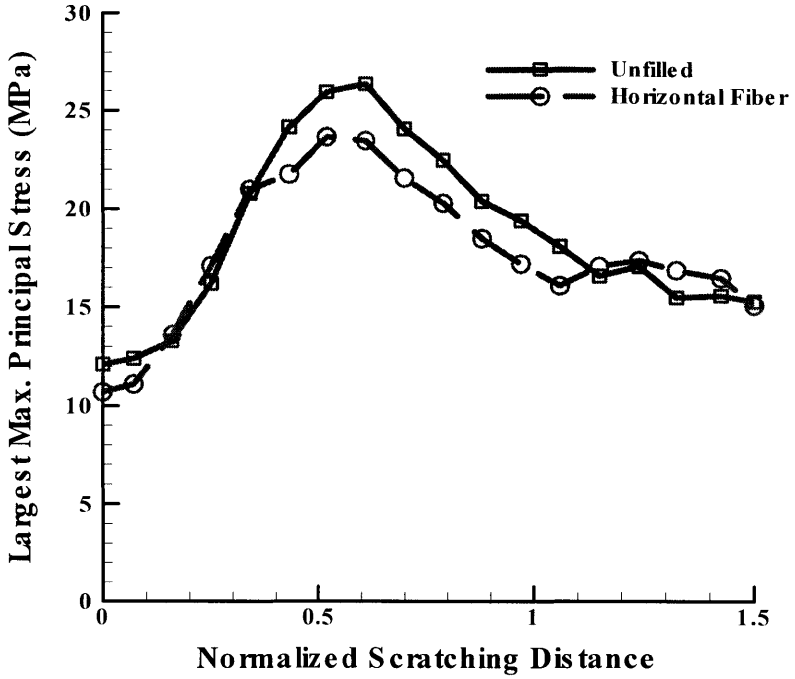

Figure 5-50(a)

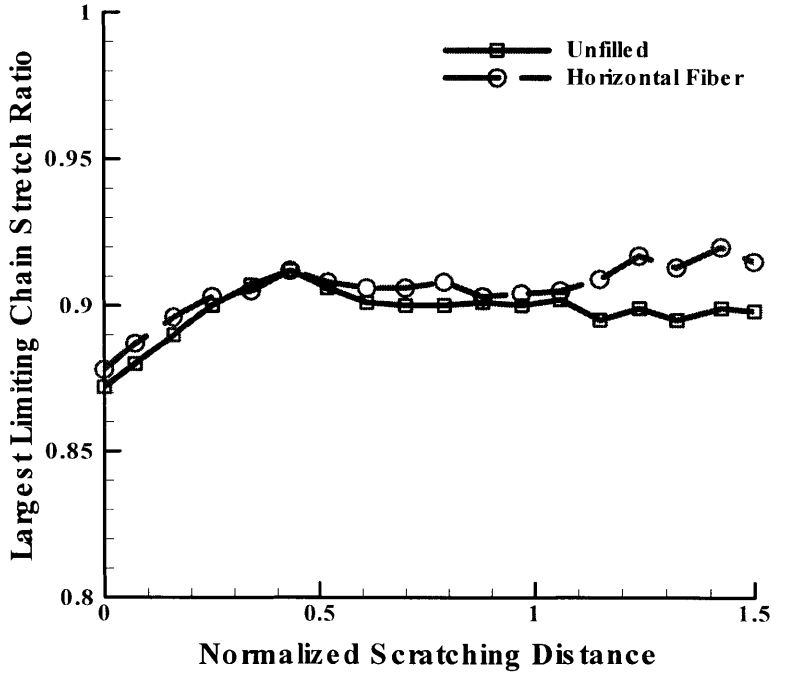

Figure 5-50(b)

Figure 5-50: Effects of a horizontal fiber on: The variations of (a) the largest maximum principal stress, and (b) the largest limiting chain stretch ratio.

5.5.2 The Vertical Fiber

The scratching simulation on the glass fiber filled TPUs with a vertical representative fiber was investigated. Figure 5-51 shows the normal/tangential force vs. normalized time t^* curves. The results from indentation/scratching test on unfilled TPU are presented in Figure 5-51(b). From Figure 5-51, during indentation, the normal force demonstrates similar features as those observed in unfilled TPUs. Upon scratching, the knife cannot "feel" the fiber until it moves closer to the fiber. In contrast to the observation from the case of a the horizontal fiber, the normal and tangential forces for the filled TPU deviates from those for unfilled TPUs at about $t^* = 1.1$, corresponding to the scratching distance of 12μm, implying the knife starts to feel the fiber as it moves about 40μm away from the fiber. From Figure 5-51, it is also noticed that the highest resistance due to the vertical fiber occurs at about $t^* = 1.6$, corresponding to the scratching distance of 72μm, in other words, the highest resistance due to the fiber is realized immediately after the knife passes the fiber due to drag from the fiber. After the knife passes the fiber, both normal force and tangential force decrease and follow the same course as determined from unfilled TPUs.

Figure 5-52 shows the contour plots of the maximum principal stress S_3 and the limiting chain stretch ratio η during the scratching process. Upon indentation, i.e., δn=80μm, δt=0μm (Figure 5-52(a) and (b)), the material conformation to the knife tip is almost symmetric and the distributions of the maximum principal stress and the limiting chain stretch ratio around the knife tip are almost symmetric. From Figure 5-52(a), the fiber shows the features of a cantilever subjected to bending and provides extra resistance to the indentation force. The largest S_3 occurs underneath the contact surface and is 11.0MPa, which is smaller than that from the scratching test on unfilled TPU (12.1MPa) but about the same as that for the horizontal fiber. The largest limiting chain stretch ratio η occurs on the contact surface with $\eta^{max} = 0.88$, which is almost identical as that from the scratching tests on unfilled material and filled material with a horizontal representative fiber.

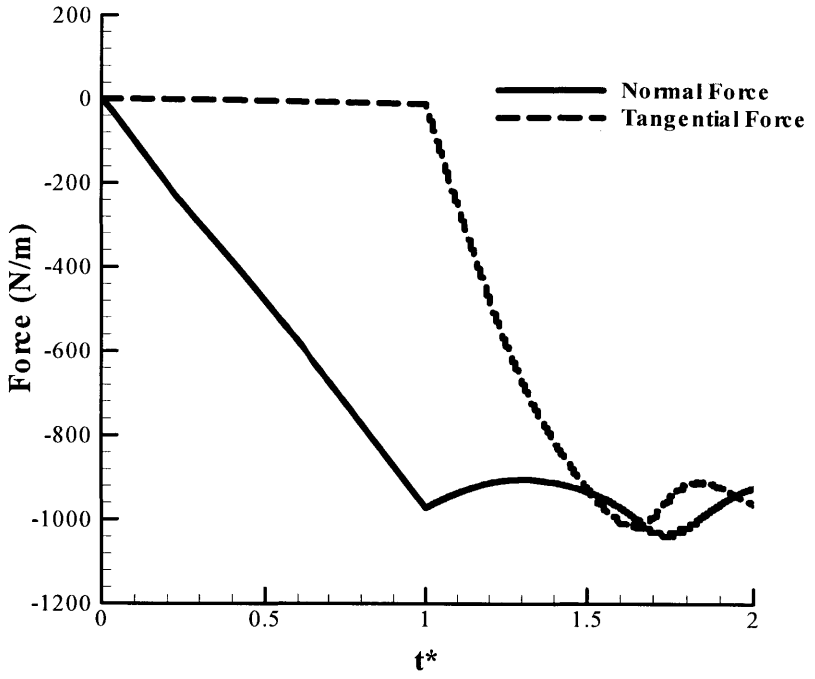

Figure 5-51(a)

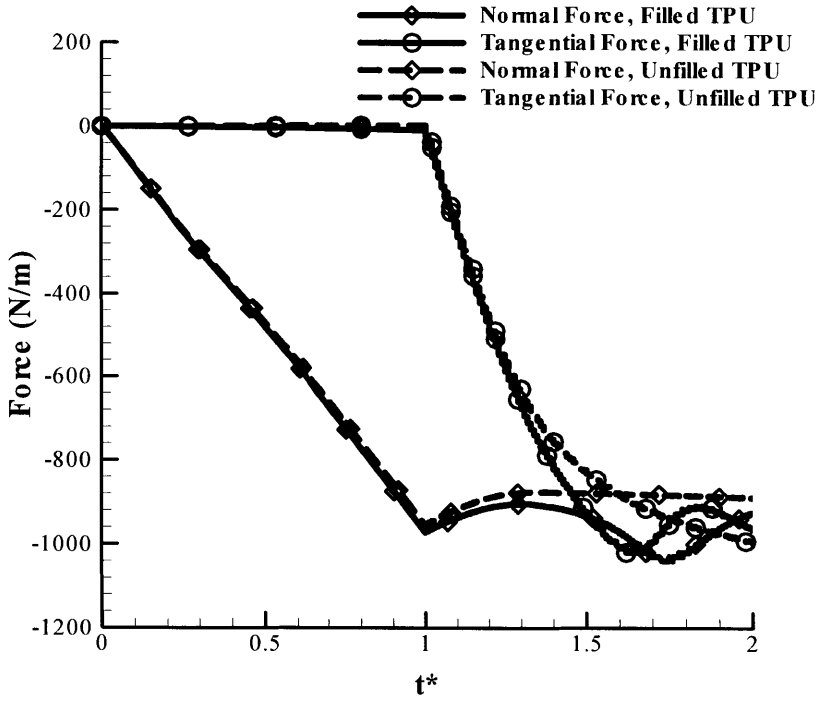

Figure 5-51(b)

Figure 5-51: Normal/tangential force vs. t^* curves from the numerical simulation for the case of the vertical fiber.

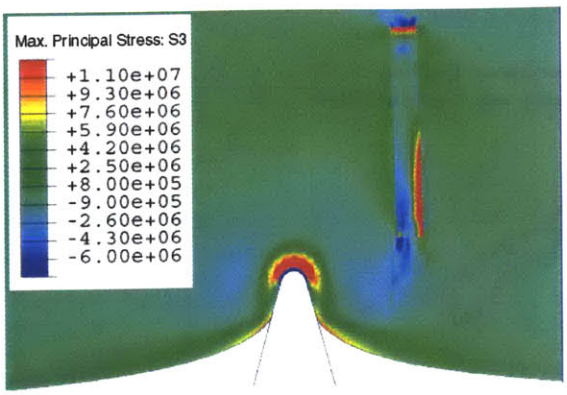

Figure 5-52(a)

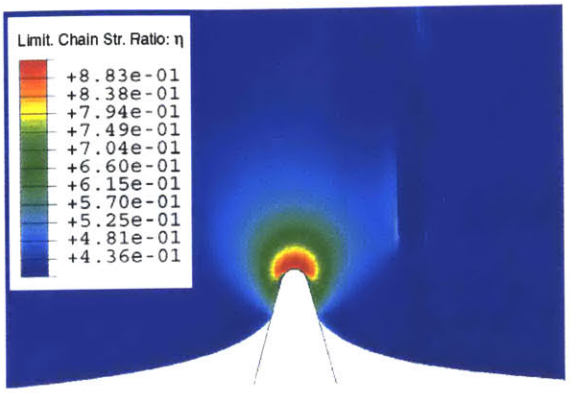

Figure 5-52(b)

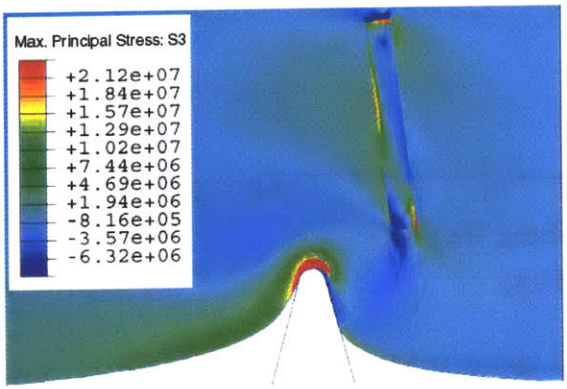

Figure 5-52(c)

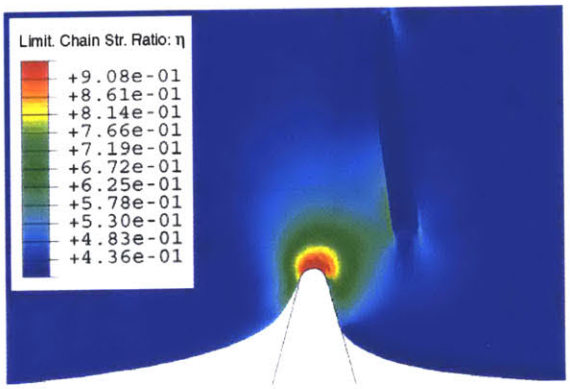

Figure 5-52(d)

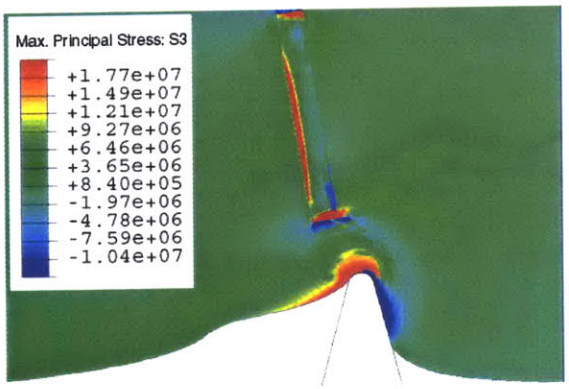

Figure 5-52(e)

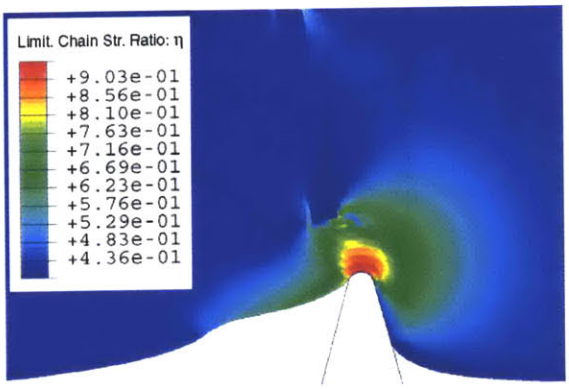

Figure 5-52(f)

Figure 5-52: Contour plots for (a) S_3 and (b) η at indentation; (c) S_3 and (d) η upon scratching δt=20μm; (e) S_3 and (f) η upon scratching δt=100μm for the scratching test with δn=80μm using the wedge-type knife.

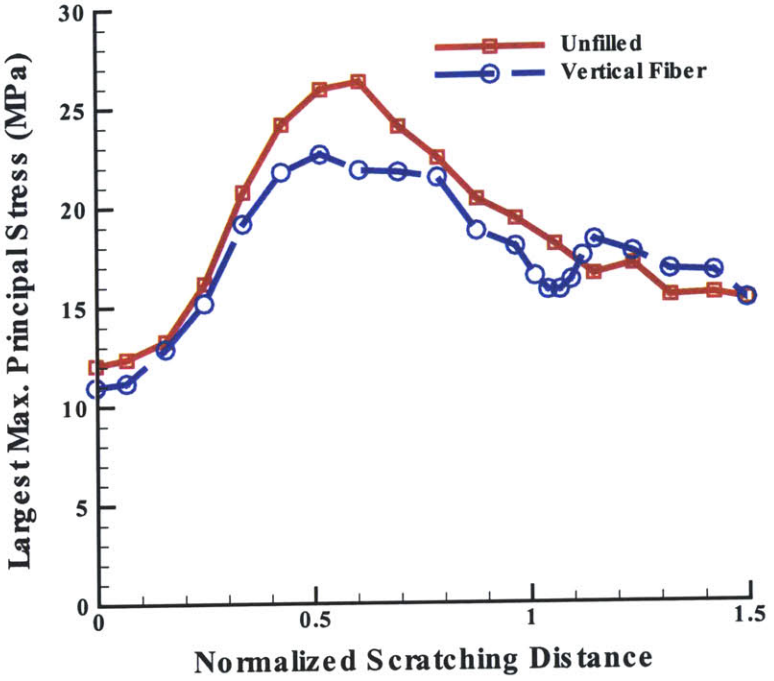

Figure 5-53(a)

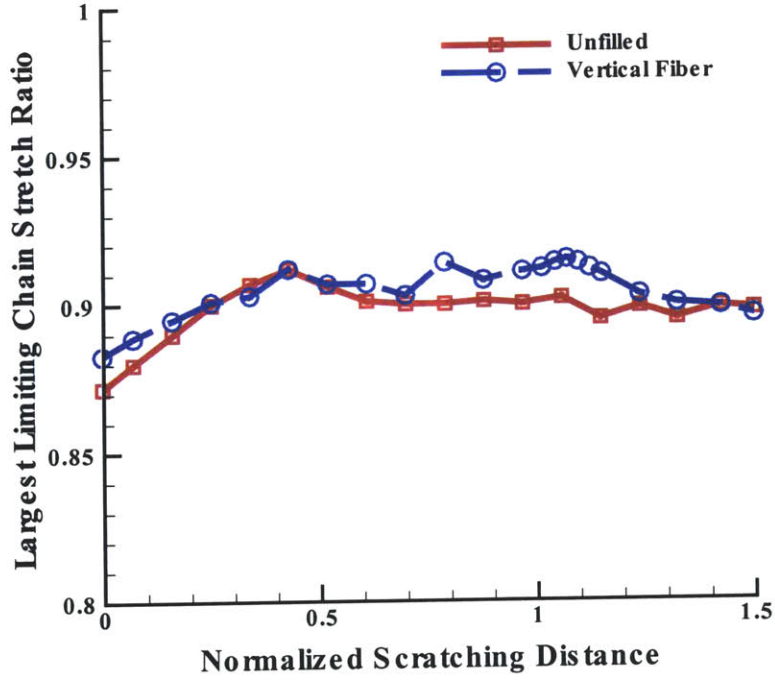

Figure 5-53(b)

Figure 5-53: Effects of a vertical fiber on: The variations of (a) the largest maximum principal stress; and (b) the largest limiting chain stretch ratio with the normalized scratching distance.

Upon scratching (Figure 5-52(c) and (d)) with the scratching distance of δt=30μm, the location for the largest maximum principal stress moves onto the contact surface and behind the knife tip whereas the location for the maximum limiting chain stretch ratio moves to the place ahead of the knife tip. The similar features were observed from the scratching test on the unfilled material. With the scratching distance of δt=30μm, the largest maximum principal stress is about 21.2MPa whereas the limiting chain stretch ratio increases moderately to 0.91. In comparison with the scratching test on unfilled material and fiber filled material with a horizontal fiber, the largest maximum principal stress for the vertical fiber filled TPU is smaller whereas the limiting chain stretch ratios are almost identical.

Upon further scratching (Figure 5-52(e) and (f)) with the scratching distance of δt=100μm, the material conformation to the knife tip is further biased. With the scratching distance of δt=100μm, the largest maximum principal stress decreases to 17.7MPa whereas the largest limiting chain stretch ratio is about 0.90, both of which are about the same as for the unfilled material and the filled materials with a horizontal fiber.

To further illustrate the variations of the largest maximum principal stress and the limiting chain stretch ratio, Figure 5-53 shows the variations of the largest maximum principal stress and the largest limit chain stretch ratio vs. the normalized scratching distance curves, defined by eqn.(5-4) and using the indentation depth of δn=80μm. The corresponding curves from the scratching simulation with δn=80μm on unfilled material are also shown in the figure. From Figure 5-53, the largest maximum principal stress for the horizontal fiber filled material is almost identical to that for unfilled material until D^*=0.3, corresponding to a scratching distance of about 24μm and about 30 μm away from the left end of the fiber. For D^*>0.3, the vertical fiber filled material shows relatively smaller amount of increase in the largest maximum principal stress and the peak value is about 22MPa, which is about 84% of the peak value for the unfilled material. As discussed in the case of the horizontal fiber, the presence of the fiber provides resistance to the material moving with the knife, hence effectively reduces the stick phase and results in less material stretch behind the knife and thus less maximum principal stress. Clearly, a vertical fiber provides a higher resistance than the horizontal

fiber does, thus reduces the maximum principal stress more effectively. It is also noticed from Figure 5-52 that during the scratching process, S_3 is essentially compression stress in the material around the corner of the fiber, implying vertical fiber might be not vulnerable to debonding. From Figure 5-53(b), the variation of the largest limiting chain stretch ratio is almost identical to that from the unfilled material until the knife moves under the fiber, where the filled material shows larger limiting chain stretch ratio, but the amount of the difference between the filled and unfilled materials is small. Clear due to the smaller peak value and less vulnerable to debonding, the presence of a vertical fiber is benefit to the abrasive performance.

5.5.3 The Lateral Fiber

The scratching simulation on the glass fiber filled TPUs with one lateral representative fiber was investigated. Figure 5-54 shows the normal/tangential force vs. normalized time t^* curves. The results from indentation/scratching test on unfilled TPU are presented in Figure 5-54(b). From Figure 5-54, due to the relatively small volume occupied by in the x-y plane, the fiber has no effects on the normal force and the tangential, i.e., the normal force and the tangential force follow the same courses as those from the test on unfilled TPUs. As one can expect, as the distance of between the fiber and the contact surface decreases, the knife will feel the fiber and both normal and tangential forces will increase. However, the increase will not be as significant as those with horizontal and vertical fibers because of the relatively small volume occupied by the fiber.

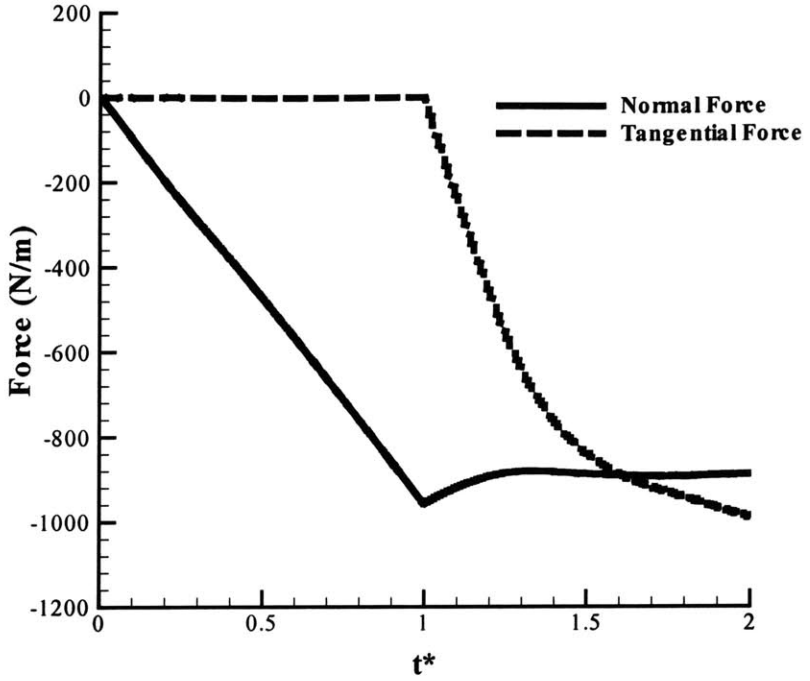

Figure 5-54(a)

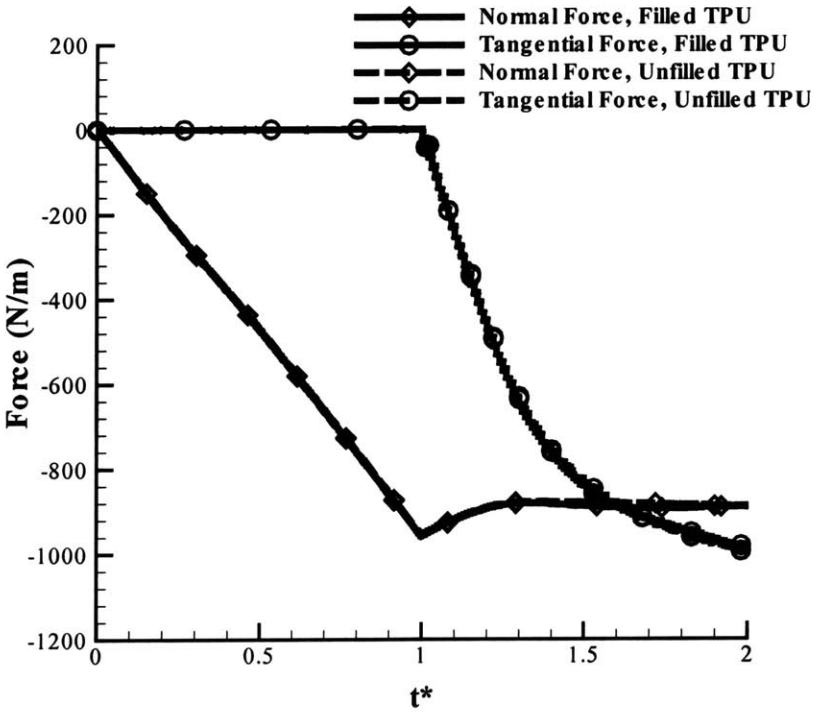

Figure 5-54(b)

Figure 5-54: Normal/tangential force vs. t^* curves from the numerical simulation for the case of the horizontal fiber.

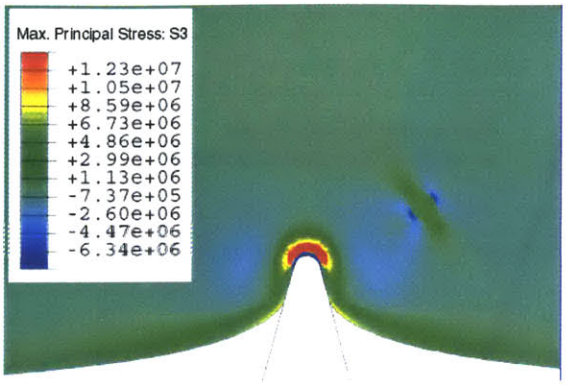

Figure 5-55(a)

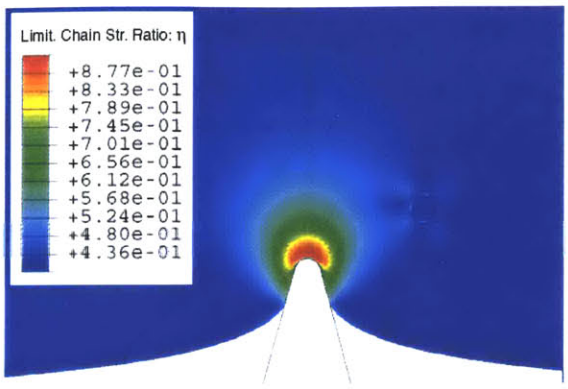

Figure 5-55(b)

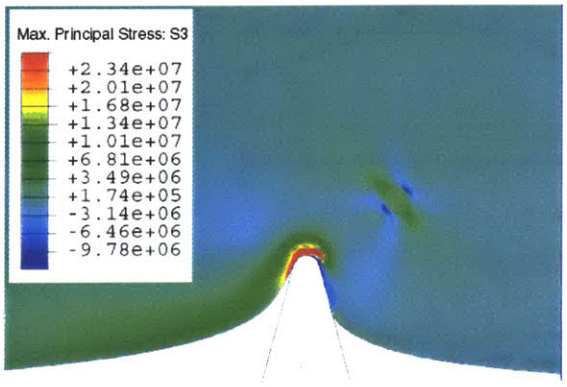

Figure 5-55(c)

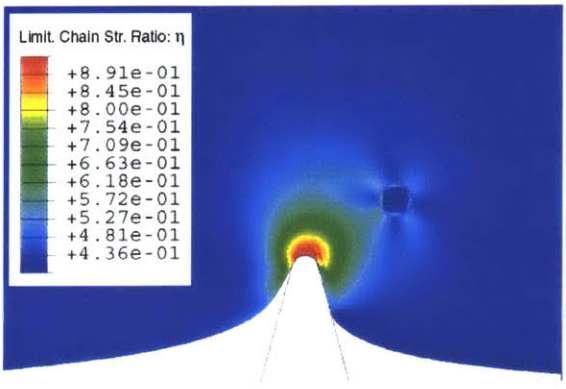

Figure 5-55(d)

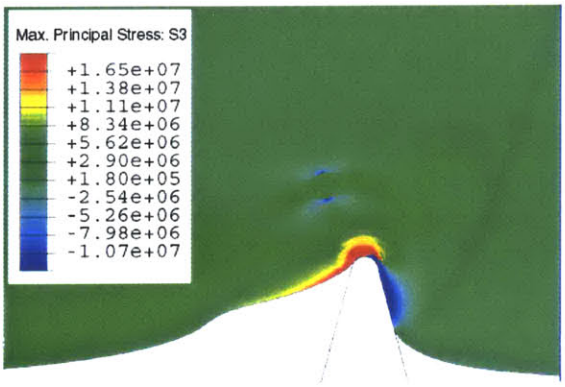

Figure 5-55(e)

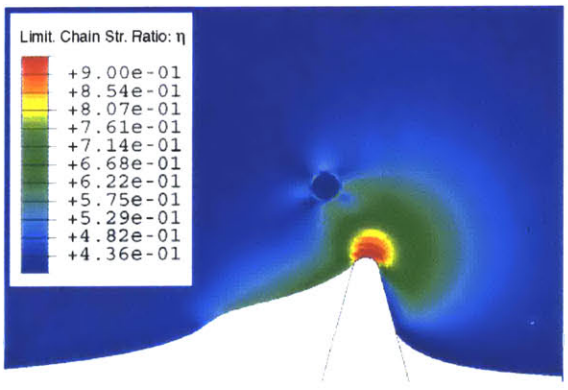

Figure 5-55(f)

Figure 5-55: Contour plots for (a) S_3 and (b) η at indentation; (c) S_3 and (d) η upon scratching δt=20μm; (e) S_3 and (f) η upon scratching δt=100μm for the scratching test with δn=80μm using the wedge-type knife.

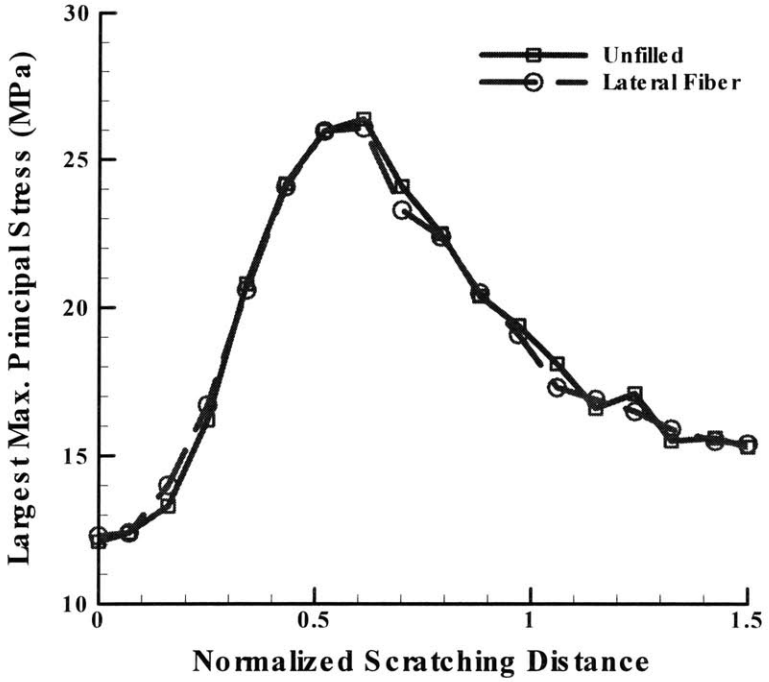

Figure 5-56(a)

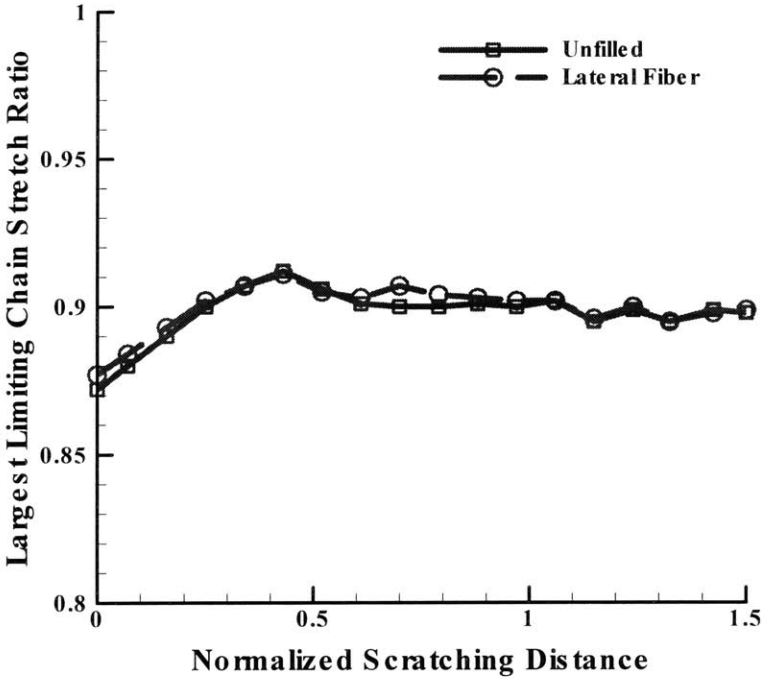

Figure 5-56(b)

Figure 5-56: Effects of a lateral fiber on: The variations of (a) the largest maximum principal stress; and (b) the largest limiting chain stretch ratio with the normalized scratching distance.

Figure 5-55 shows the contour plots of the maximum principal stress S_3 and the

limiting chain stretch ratio η during the scratching process. Upon indentation, i.e., δn=80μm, δt=0μm (Figure 5-55(a) and (b)), the material conformation to the knife tip is almost symmetric. The distributions of the maximum principal stress and the limiting chain stretch ratio are almost symmetric. The largest S_3 occurs underneath the contact surface and is 12.3MPa, which is about the same as that from the scratching test on unfilled TPU (12.1MPa). The largest limiting chain stretch ratio η occurs on the contact surface with $\eta^{\max} = 0.88$, which is also about the same as that from the scratching test on unfilled material.

Upon scratching with the scratching distances of δt=30μm (Figure 5-53(c) and (d)) and δt=100μm (Figure 5-55(e) and (f)), the presence of a lateral fiber does not change the distribution of the maximum principal stress and the limiting chain stretch ratio significantly, and the largest values for them are almost identical to those for unfilled materials.

To further illustrate the variations of the largest maximum principal stress and the limiting chain stretch ratio, Figure 5-56 shows the variations of the largest maximum principal stress and the largest limit chain stretch ratio vs. the scratching distance curves. Clearly, due to the relatively small volume occupied by the fiber in the x-y plane, the fiber has barely effects on the largest maximum principal stress and the largest limiting chain stretch ratio, i.e., the largest maximum principal stress and the largest limiting chain stretch ratio are almost identical to those for unfilled TPU during the entire scratching distance.

5.6 Summary

Extensive FEM simulations of indentation/scratching tests were conducted in this chapter to investigate the effects of indentation depth, contact conditions, cyclic scratching, contact friction, scratching speed, material properties, and fiber fillers. The FEM model was built based on the configuration of the tests with the consideration of the computational efficiency. The material stress-strain behavior was modeled by the constitutive model proposed in Chapter 4, which accounted for the various dependences of the stress-strain behavior of TPUs.

In order to judge the correctness of the proposed FEM model, the model was first used to simulate the indentation/scratching tests in Chapter 2. The FEM simulations showed excellent agreements in the normal and tangential forces with the test results and remark similarity in the displacement and strain fields obtained from image processing of micrographs in the SEM in situ indentation/scratching tests, verifying the capability of FEM model to predict the highly nonlinear deformation during indentation and scratching.

The FEM simulations with two different indentation depths were conducted to investigate the general mechanics. Upon indentation, the normal force increased linearly; upon scratching, the normal force experienced a decrease then became a constant, whereas the tangential force increased first linearly then gradually bent over toward a constant force, resulting in an overall nonlinear increase in tangential force. The contour plots at different stages of the indentation/scratching tests revealed the evolution of the maximum principal stress S_3 and limiting chain stretch ratio during the indentation/scratching process. During indentation, the largest maximum principal stress was tensile stress, and was a few microns under the contact surface due to the constraint applied by the frictional force on the contact surface; the largest limiting chain stretch ratio was on the contact surface. During scratching, the location of the largest maximum principal stress moved onto the material surface and fell behind the knife whereas the largest limiting chain stretch ratio moved in front of the knife tip where large compression stress prevailed. The largest maximum principal stress experienced a dramatic increase to a peak value as scratching started, then decreased to a constant value, whereas the largest limiting chain stress ratio increased moderately to a constant value. The peak values of S_3 and η were 17.5MPa and 0.87 for the test with indentation of 50μm whereas were 26MPa and 0.91 for the test with indentation of 80μm. The combination of high values in the test with indentation depth of 80μm may explain why the surface for the $\delta_n = 80\mu m$ test experienced large amount of damages whereas the surface for the $\delta_n = 50\mu m$ test essentially remained unchanged.

In seal applications, the surface of the sealant material is compressed onto the bushing surface, and the abrasive particles between these two surfaces abrade the sealant surface

and cause abrasive wear. FEM simulation using the bulk-type knife, a configuration consisting of a smooth surface with a small sharp protrusion, was conducted to investigate the effects of the superposition of the overall compression on the mechanics of the scratching test. It was found that the general mechanics showed the similar features as those observed in the wedge-type knife tests, except for the normal force during the indentation. Assuming that the height of the asperity is δ_1 and the overall compression is achieved by compressing the bushing onto the sealant material by δ_2, the indentation test using wedge-type knife with indentation depth of δ_1 provides smaller maximum principal stress and chain limiting stretch ratio response, whereas the indentation test using wedge-type knife with indentation depth of $\delta_1 + \delta_2$ provides higher maximum principal stress and chain limiting stretch ratio response.

During cyclic scratching, softening in normal and tangential forces were observed due to material softening after the first scratching. However, the variation of the normal and tangential force was similar as those in the first scratching. It was also found that even with softening, the peak value of the largest principal stress and the largest limiting chain stretch ratio remained very high values during the scratching process, implying that the material was subjected to repeated very high largest maximum principal stress and chain limiting stretch ratio during cyclic scratching.

TPU is well known as a material with low friction coefficient. However, very high friction coefficient (about 1.0) was observed in both tests and simulations. It was found that cyclic softening, rate dependence and hysteresis contributed to much of this large effective friction coefficient. Numerical simulations revealed that such high effective friction coefficient was a result of asymmetric conformation of the material to the knife tip due to the softening and hysteresis. During scratching process, the material behind the knife was in unloading state whereas the material in front of the knife underwent loading. Due to softening and hysteresis, for a given strain, the material under unloading had much lower stress response than that under loading state, such unbalanced stress response caused material asymmetric conformation, resulting high effective friction coefficients.

Scratching speed effects were also investigated by varying the speed used in the simulations from 4μm/s to 16μm/s. The largest limiting chain stretch ratio did not show

significant dependence on the scratching speed. However, the peak value of the largest maximum principal stress increased with increasing scratching speed. For scratching speed changing from 4μm/s to 16μm/s, the peak value increased by about 15%.

Parametric studies by varying contact friction force, scratching speed, and material properties of elastomers were conducted to identify and evaluate the influence of these factors on the abrasive wear performance of the material.

Effects of hysteresis were first investigated. It was found that the decrease in the hysteresis decreased both the normal force and the tangential force significantly. As hysteresis was totally removed, the normal force did not show the feature of decreasing to a stabilized value during scratching; instead, it maintained the force magnitude of immediately after the indentation; the tangential force showed a linear increase then became to a constant value. It was also found that reducing hysteresis decreased the largest maximum principal stress significantly, and decreased the largest limiting chain stretch moderately.

It was found that the small difference in the initial stress-strain response of material resulted in significant differences in the tangential forces. Generally, increasing the initial Young's modulus increased normal force and tangential force, as well as the largest maximum principal stress. However, increasing the initial modulus of the hyperelastic rubbery spring reduced the largest limiting chain stretch ratio and the effective friction coefficient whereas increase the modulus of the elastic spring of the viscoelastic-plastic component increased the largest limiting chain stretch ratio and the effective friction coefficient.

The extensibility of molecular chains in elastomers affects the stress-strain behavior of materials at moderate to large strain significantly. From our investigations, the material with less chain extensibility showed smaller effective friction coefficient and less tangential force. The smaller chain extensibility also resulted in significantly smaller peak value of the largest maximum principal stress, but significantly high chain limiting stretch ratio.

Addition of fibers into TPUs had been shown to improve the abrasive wear performance of the sealant material. Effects of fillers on the mechanics of scratching were studied by investigating three representative orientations of fibers in the material, i.e. a

horizontal fiber, a vertical fiber, and a lateral fiber. The presences of a horizontal fiber and a vertical fiber close the material surface were found to increase both the normal forces and tangential force as the knife approached to fiber. Clearly, the increase in normal force and tangential force would make asperities harder to move along the surface hence reduced the abrading distance and the possibility to agglomerate. A lateral fiber, however, did not provide such improvement. It was also found that during scratching, the horizontal fiber and vertical fiber could reduce stick phase during scratching, and hence could reduce the largest maximum principal stress and benefit the abrasive wear performance. However, large stress concentrations were also observed around the horizontal fiber, suggesting that interfacial damage and thus fiber pullout be occur. Therefore, the advantage of a horizontal fiber to decrease the largest maximum principal stress might be overshadowed by the damage created by fiber pullout.

References

[5-1] Kinloch, A.J., Young, R.J., Fracture Behavior of Polymers, Applied Science Publishers.

[5-2] Gent, A.N., Lindley, P.B., Proc. Roy. Soc., A249, 1957, pp195.

[5-3] Dencouer, R.L., Gent, A.N., J. Polym. Sci., A2, 6, 1958, pp1853.

[5-4] Gent, A.N., Tompkins, D.A., J. Appl. Phys., 40, 1969, pp2520.

[5-5] Parsons, E.M., Micromechanics of deformation and abrasive wear of fiber-filled elastomers, Master's thesis, Massachusetts Institute of Technology, 1999.

[5-6] Mechanics of Pneumatic Tires, Ed. S.K. Clark, U.S. Department of Transportation, 1981.

[5-7] Grosch, K.A., Rubber Chem. Technol., 69, 1996, pp495.

[5-8] Pan, X.D., Kelley, E.D., Hayes, M.W., Bulk viscoelastic contribution to the wet-sliding friction of rubber compounds, J. Polym. Sci., B: Polym. Phys., 41, 2003, pp757-771.

Chapter 6

Conclusions and Future Work

The goal of this thesis research is to provide fundamental understanding of abrasive wear of elastomeric materials due to the effect of abrasive particle indentation and scratching. To achieve this aim, both experimental and numerical studies were conducted. Fundamental considerations have been achieved in several area including experimental study of indentation and scratching of elastomers with direct observations of local deformation fields; characterizing and modeling the nonlinear rate-dependent, cyclic softening stress-strain behavior of elastomers; simulations of indentation and scratching of elastomeric materials. Details of each of these achievements are summarized below; this research has also triggered new directions for future work in this area as described below.

6.1 Summary of Conclusions

Abrasive wear occurs when an abrasive particle is compressed between two contact surfaces. The confined configuration makes it extremely difficult to establish direct observations of the deformation at the micron-scale during the wear process and prohibits numerical simulations that address the nonlinearities arising from large deformation, contact, and material stress-strain behavior. A two-dimensional simplification of the confined configuration was proposed, which simplified abrasive wear as a process where a knife indented and scratched the surface of an elastomer. Two types of knives were developed: The wedge-type knife and the bulk-type knife. The former simulated the interaction between a single abrasive particle and the elastomer whereas the latter studied the effect of an overall surface compression on the simultaneous knife indentation and scratching. With such a simplification, direct observations of abrasive wear process could be established and the cost for numerical simulations was reduced significantly, and allowed the dominant mechanics of abrasive wear of elastomeric materials being retained.

An in-situ micro indentation and scratching test system was first developed. The new

system conducted micro indentation/scratching test within an SEM and enabled simultaneous collection of video images of the indentation and scratching tests and the corresponding normal and tangential force data. For the indentation/scratching test using the wedge-type knife, it was observed that the variations of normal and tangential forces could be divided into three regions according to different dominant features of the test. The first region corresponded to the indentation, where the normal force increased initially nonlinearly then almost linearly and the material symmetrically conformed to the knife. The second region corresponded to the start of scratching where the tangential force increased almost linearly and the material around the contact surface moved with the knife, demonstrating features commonly known as stick phase. The material behind the knife gradually lost contact with the knife and the conformation of the material to the knife became biased. The third region corresponded to the scratching where the curve for tangential force gradually bent over to a constant value, and the knife slipped over the surface (known as slip phase). The material behind the knife lost contact with the knife whereas the material ahead of the knife was pushed by the knife, providing resistance to the knife movement. For the test using the bulk-type knife, the material deformation around the protrusion showed similar features as those observed in the tests using wedge-type knife.

Image processing, using digital image correlation technique, was successfully used to obtain displacement and strain fields during the indentation/scratching tests. For the test using the wedge-type knife, the displacement and strain fields showed symmetric features during indentation and biased features during scratching. For the test using the bulk-type knife, it was found that during indentation, due to the material being lifted by the protrusion (or asperity), the deformation of the material around the protrusion/asperity was essentially similar as that from the tests using the wedge-type knife. During scratching, however, due to the constraint applied by the contact between the smooth surface of the knife and the material, the deformation was generally less severe than that using wedge-type knife.

Topography changes during the cyclic scratching tests were studied using SEM and Zygo. For the test on unfilled TPU with a relatively smaller indentation depth, $\delta_n = 50\mu m$, no significant surface change was observed. Some small pits and plastic

deformations were observed during the cyclic scratching. The small pits were formed possibly due to small inclusion or inhomogeneity close to the surface and were about the same size as that of the initial damages in Gent and Pulford's bimodal model. However, instead of growing into larger damage, they were simply removed during the thereafter-scratching process. In contrast to the observations from the tests with $\delta_n = 50\mu m$, dramatic topography changes were observed from the tests with $\delta_n = 80\mu m$ on unfilled TPUs. The surface topography changes occurred in two forms: One was the surface peak-valley pattern due to plastic deformations, whereas the other one was material loss due to rupture of the material. As the number of scratching cycles increased, the dimensions of both plastic regions and surface damages increased, accompanied by new damages generated after each scratching.

For glass fiber filled TPUs, dramatic topography changes were also observed from the tests with $\delta_n = 80\mu m$. After the first scratching, the plastic deformation in the form of wrinkles dominated the surface topography. These plastic deformations resulted in surface damages after the 5^{th} scratching. These results implied that the fiber filled TPU would wear at a similar or even faster rate than the unfilled TPU, which consistent with Parsons' macroscopic testing of seals, where it was found that the role of the fibers in extending seal life was the prevention of particle ingestion as opposed to actual improvement/delay of wear rate.

The large strain nonlinear stress-strain behavior of thermoplastic polyurethanes (TPUs) exhibits strong hysteresis, rate dependence and cyclic softening. In this thesis work, a constitutive model capturing the major features of the stress-strain behavior of TPUs was developed. The proposed constitutive model decomposed material behavior into an equilibrium component and a rate dependent deviation from equilibrium. The cyclic softening behavior was attributed to be due to the softening of the equilibrium path as a result of the evolution of the effective volume fraction of the soft domain during the deformation process due to the relative motions among hard domains, upon which the occluded soft material was released to carry load. Numerical simulations of uniaxial compression tests verified the efficacy of the proposed new constitutive model.

Extensive FEM simulations of indentation/scratching tests were conducted to

investigate the effects of indentation depth, contact conditions, cyclic scratching, contact friction, scratching speed, material properties, and fiber fillers. The FEM model was first verified by comparing the variations of normal and tangential forces and the distributions of displacement fields from the tests and numerical simulations. The numerical simulations showed excellent agreements in the normal and tangential forces from the test results and remark similarity in the displacement and strain fields obtained from image processing of micrographs in the SEM in situ indentation/scratching tests, verifying the capability of FEM model to predict the highly nonlinear deformation during indentation and scratching.

The FEM simulations with two different indentation depths were conducted to investigate the general mechanics. Upon indentation, the normal force increased linearly; upon scratching, the normal force experienced a decrease then became a constant, whereas the tangential force increased first linearly then gradually bent over toward a constant force, resulting in an overall nonlinear increase in tangential force. During indentation, the largest maximum principal stress was tensile and occurred a few microns under the contact surface due to the constraint applied by the frictional force on the contact surface; the largest limiting chain stretch ratio was on the contact surface. During scratching, the location of the largest maximum principal stress moved onto the material surface and fell behind the knife whereas the largest limiting chain stretch ratio moved in front of the knife tip where large compression stress prevailed. The largest maximum principal stress experienced an initial dramatic increase to a peak value, then decreased to a constant value, whereas the largest limiting chain stretch ratio increased moderately to a constant value. The increases in the largest maximum principal stress and the largest chain limiting chain stretch ratio may account for the damage initiation. For instance, the peak value of the largest maximum principal stress and the largest chain limiting chain stretch ratio were 17.5MPa and 0.87 for the test with indentation of 50μm whereas were 26MPa and 0.91 for the test with indentation of 80μm. The latter were significantly higher than the former, which might account for why the surface for the $\delta_n = 80\mu m$ test experienced large amount of damages whereas the surface for the $\delta_n = 50\mu m$ test essentially remained unchanged.

FEM simulation using the bulk-type knife was conducted to investigate the effects of the superposition of an overall compression on the mechanics of the scratching test. It was found that the general mechanics showed similar features as those observed in the wedge-type knife tests. Assuming that the height of the asperity is δ_1 and the overall compression is achieved by compressing the bushing onto the sealant material by δ_2, the indentation test using wedge-type knife with indentation depth of δ_1 provides smaller maximum principal stress and limiting chain stretch ratio, whereas the indentation test using wedge-type knife with indentation depth of $\delta_1 + \delta_2$ provides larger maximum principal stress and limiting chain stretch ratio.

During cyclic scratching, softening in normal and tangential forces were observed due to material softening after the first scratching. However, the variations of the normal and tangential forces were similar to those in the first scratching. It was also found that even with softening, the peak value of the largest principal stress and the largest limiting chain stretch ratio remained very high value during the scratching process, implying that during cyclic softening the material was subjected to repeatedly very high maximum principal stress and chain stretching.

In both tests and simulations, a very high effective friction coefficient was observed. Numerical simulations revealed that such a high effective friction coefficient was a result of softening, hysteresis, and rate dependence of the stress-strain behavior of the material, which resulted in asymmetric conformation of the material to the knife tip during scratching. During scratching process, the material behind the knife was in unloading state whereas the material in front of the knife underwent loading. Due to softening and hysteresis, for a given strain, the material under unloading had much lower stress than that under loading, such unbalanced stress response caused greater material asymmetric conformation, resulting in high effective friction coefficients.

Scratching speed effects were also investigated by varying the speed used in the simulations from 4μm/s to 16μm/s. The largest limiting chain stretch ratio did not show significant dependence on the scratching speed. However, the peak value of the largest maximum principal stress increased with increasing scratching speed due to the rate dependency of the stress-strain behavior. For scratching speed changing from 4μm/s to

16μm/s, the peak value increased by about 15%.

Parametric studies of material properties by varying hysteresis, initial modulus, and chain extensibility were conducted to identify and evaluate the influence of these factors on the abrasive wear performance of the material. It was found that the decrease in the hysteresis decreased both the normal force and the tangential force significantly. It was also found that reducing hysteresis decreased the largest maximum principal stress significantly, and decreased the largest limiting chain stretch moderately.

The initial Young's modulus of TPUs consists of the contributions from equilibrium hyperelastic rubbery behavior and rate-dependent viscoplastic behavior. The effects of these two components on the mechanics of abrasive wear were investigated. Generally, increasing the initial Young's modulus increased normal force and tangential force, as well as the largest maximum principal stress. However, increasing the initial modulus of the hyperelastic rubbery spring or equilibrium behavior reduces the largest limiting chain stretch ratio and the effective friction coefficient whereas increasing the modulus of the elastic spring or rate dependent behavior of the viscoelastic-plastic component increases the largest limiting chain stretch ratio and the effective friction coefficient.

The extensibility of molecular chains in elastomers affects the stress-strain behavior of materials at moderate to large strain significantly. From our investigations, the material with less chain extensibility showed smaller effective friction coefficient and smaller tangential force. The smaller chain extensibility also resulted in significantly smaller peak value of the largest maximum principal stress but higher chain limiting stretch ratio.

Addition of fibers into TPUs had been shown to improve the abrasive wear performance of the sealant material. Effects of fillers on the mechanics of scratching were studied by investigating three representative orientations of fibers in the material, i.e. a horizontal fiber, a vertical fiber, and a lateral fiber. The presences of a horizontal fiber and a vertical fiber close to the material surface were found to increase both the normal forces and tangential force as the knife approached the fiber. Clearly, the increase in normal force and tangential force would make asperities harder to move along the surface hence reduced the abrading distance and the possibility to agglomerate. A lateral fiber, however, did not provide such improvement. It was also found that during scratching, the horizontal fiber and vertical fiber could reduce stick phase during scratching, and hence

could reduce the largest maximum principal stress and benefit the abrasive wear performance. However, large stress concentrations were also observed around the horizontal fiber, suggesting that interfacial damage and thus fiber pullout be occur. Therefore, the advantage of a horizontal fiber to decrease the largest maximum principal stress might be overshadowed by the damage created by fiber pullout. The vertical fiber, which did not show high stress concentration around it, may offer better wear performance than the horizontal fiber.

6.2 Future Works

In retrospect, we find that the current thesis work has approached such a stage that on the one hand, it extends our fundamental insight about the mechanics of abrasive wear of elastomeric materials; on the other hand, it also provides means to conduct more complicated analysis to account for the factors missed in current thesis research; moreover, it also raises some interesting questions that is worth for elaboration in the future. In the future, several directions are worth for future consideration:

1) Temperature effects. The energy dissipated during the relative motions of the two contact surfaces will raise the temperature of the material, which in turn changes its mechanical behavior. Thermoplastic polyurethanes are especially susceptible to temperature change because of its relative low transition temperature of the hard domain. The constitutive model developed in this work has been shown to be effective in the simulations of scratching tests using both wedge-type knife and bulk-type knife. Yet it is also open for accounting for the temperature in the model. Therefore, incorporating temperature into the constitutive model and study the temperature and mechanical property change will be an interesting yet important work for the future.
2) Multi-protrusion bulk-type knife tests. In seal applications, small asperities are ingested into the contact surface, then undergoes interactions with material surface as well as neighboring asperities. It will be very informative to study the mechanics of abrasive wear in the presence of multi-asperities. As a first step toward this end, multi-protrusion bulk-type knife will certainly be very informative in the study of the effects of these interactions on the mechanics of abrasive wear and on the

agglomerations of abrasive particles. The production of the bulk-type knife with one protrusion provides invaluable experience for the future work in this direction.

3) Simulations of damage initiation and progression. In the current thesis work, the maximum principal stress and the limiting chain stretch ratio have been used for the study of the mechanics of abrasive wear. However, the final goal of the study of abrasive wear is to predict the damage initiation and progression, and hence to improve material design. In this regard, it is importance to consider damage initiation and progression in the future. With the fundamental mechanics becomes clear in the current thesis work, one important thing left is to study the criterion for damage initiation and progression of elastomeric materials. As soon as such criterion is available, proper model will be generated and the scheme used in current study can be adapted to address this important problem.
4) Surface properties of TPU using nanoindentation and nanoscratching. Surface material, which consists of material between the surface and a few microns below the surface, has been found to have different properties from those of bulk materials in most materials. In the application of metallic and polymeric materials, surface modifications have been shown to be an effective way to improve wear performance of materials. However, it is unclear yet whether this surface property difference will change the abrasive wear performance of elastomers. Therefore, inspecting the evolution of surface properties using nanoindentation and nanoscratching during the scratching process and properly modeling such evolution will provide insight and direction to improve wear performance.
5) Surface stability and formation of Schallamach wave. It is well known that the formation of Schallamach due to the instability of the surface during scratching is responsible for the friction of elastomeric materials. In current research, the wrinkle-like surface profile resembles the small ridges formed due to Schallamach waves. However, it is unclear how Schallamach waves can be related to the mechanical properties of elastomers as well as abrasive wear. The numerical model proposed in the current work can be possibly applied to simulate this important phenomenon.
6) Multi-scale modeling. In the current thesis work, the dimension of the FEM model is a few millimeters in order to simulate real boundary conditions, whilst the area of

interests for mechanics of abrasive wear was only a few hundreds of microns where refined mesh was used to address the large deformation gradient. In such a model, tremendous number of nodes and elements had also been given to the transition region from the area of interest to the far field material, where the deformation was essentially small. As more complicated factors, such as multi-asperities, multi-fibers, and damages, have to be addressed in the future, the current FEM model would become less effective due to even more refined mesh has to be used in the area of the contact between the knife and the material. Multi-scale modeling is therefore highly desired in the future research. One idea for multi-scale modeling is to only model the small area of interest where the large deformation prevails and to apply proper boundary conditions to it. The boundary conditions for such an area can be obtained from a simulation using a full-size model but without the details around the area of interest, such as fibers, surface damages.

Appendix A

Durometer Hardness and the Stress-Strain Behavior of Elastomeric Materials[1]

Abstract

The Durometer hardness test is one of the most commonly used measurements to qualitatively assess and compare the mechanical behavior of elastomeric and elastomeric-like materials. This paper presents nonlinear finite element simulations of hardness tests which act to provide a mapping of measured Durometer Shore A and D values to the stress-strain behavior of elastomers. In the simulations, the nonlinear stress-strain behavior of the elastomers is first represented using the Gaussian (neo-Hookean) constitutive model. The predictive capability of the simulations is verified by comparison of calculated conversions of Shore A to Shore D values with the guideline conversion chart in ASTM D2240. The simulation results are then used to determine the relationship between the neo-Hookean elastic modulus and Shore A and Shore D values.

The simulation results show the elastomer to undergo locally large deformations during hardness testing. In order to assess the potential role of the limiting extensibility of the elastomer on the hardness measurement, simulations are conducted where the elastomer is represented by the non-Gaussian Arruda-Boyce constitutive model. The limiting extensibility is found to predict a higher hardness value for a material with a given initial modulus. This effect is pronounced as the limiting extensibility decreases to less than 5 and eliminates the one-to-one mapping of hardness to modulus. However, the durometer hardness test still can be used as a reasonable approximation of the initial neo-Hookean modulus unless the limiting extensibility is know to be small as is the case in many materials, such as some elastomers and most soft biological tissues.

Keyword: hardness, modulus, durometer, elastomer, soft tissue

---

[1] This work is published in *Rubber Chemistry and Technology*, Vol. 72, No. 2, May-June 2003, pp419-435.

A.1 Introduction

Durometer (Shore) hardness[A-1] is one of the most commonly used hardness tests for elastomeric materials. Durometer hardness measurements, which assess the material resistance to indentation, are widely used in the elastomer industry for quality control and for quick and simple mechanical property evaluation[A-1]. The hardness value is primarily a function of the elastic behavior of the material. The nondestructive and relatively portable nature of the test enables property evaluation directly on elastomeric products or components. This feature has also led to the use of hardness tests in mechanical property evaluation of soft tissues such as skin[A-3][A-4] and tumors surrounded by soft tissues[A-5].

Durometer hardness is related to the elastic modulus of elastomeric materials. Several theoretical efforts have been conducted in the past to establish the relationship between hardness and elastic modulus[A-6][A-7]. However, most of these efforts have been based on linear elasticity, even though the indentation in durometer hardness tests involves significant large-scale nonlinear deformation. Gent[A-6] obtained a simple relation between the elastic modulus and durometer Shore A hardness by approximating the truncated cone indentor geometry as a cylinder and using the classic linear elastic solution for the flat punch contact problem. Briscoe and Sebastian[A-7] considered the actual shape of the Shore A indentor and linear elasticity theory to obtain a prediction using an iterative solution. The difference between the Gent and the Briscoe and Sebastian results was as large as 15% to 25% for durometer hardness values larger than 50A. In this paper, the ability of durometer Shore hardness tests to provide properties for the stress-strain behavior of elastomers for small to large deformation is assessed. Fully nonlinear finite element analyses are conducted to simulate the durometer hardness tests. The nonlinear stress-strain behavior of the materials is modeled using the Gaussian (neo-Hookean) model and the Arruda-Boyce eight-chain non-Gaussian model. The latter constitutive model captures the limiting extensibility of elastomers (and also of soft tissues[A-8]) and thus permits evaluation of the relevance of correlating the durometer measurements to limiting aspects of material behavior. Durometer tests for Shore A and Shore D scales are simulated for the Gaussian (neo-Hookean) material. The ability of the

model to predict the corresponding Shore D hardness for a given Shore A hardness material acts as a verification. A mapping of Shore A and D values to the elastic modulus predictions is then provided. Comparisons of the new model with prior models are also given. The influence of the limiting extensibility of elastomeric materials on this mapping is assessed.

A.2 Models

A.2.1 The Model of Durometer Hardness Tests

The durometer hardness test is defined by ASTM D 2240[A-1], which covers seven types of durometer: A, B, C, D, DO, O, and OO. Table A-1 shows the comparison of different durometer scales.

Table A-1. Comparison of different scales of durometer tests.

Type A	10 20 30 40 50 60 70 80 90 100
Type B	10 20 30 40 50 60 70 80 90 100
Type C	10 20 30 40 50 60 70 80 90 100
Type D	10 20 30 40 50 60 70 80 90 100
Type DO	10 20 30 40 50 60 70 80 90 100
Type O	10 20 30 40 50 60 70 80 90 100
Type OO	10 20 30 40 50 60 70 80 90 100

Most commercially available products for durometer tests consist of, according to ASTM D 2240, four components: pressor foot, indentor, indentor extension indicating device, and calibrated spring, as shown in Figure A-1. The scale reading is proportional to the indentor movement (Figure A-2)

$$H = \frac{\Delta L}{0.025mm}, \quad \Delta L = L_0 - L \qquad \text{(A-1)}$$

where H is the hardness reading, ΔL is the movement of the indentor.

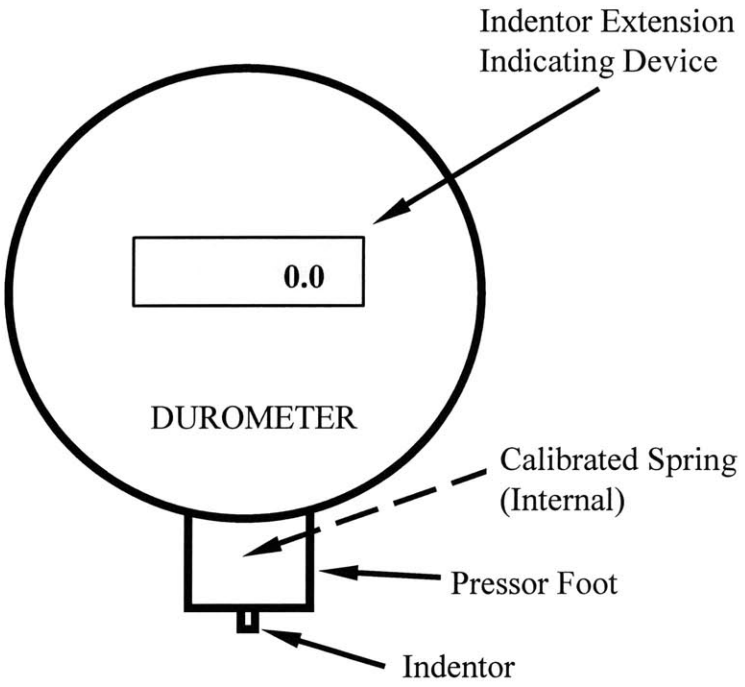

Figure A-1: A typical durometer

A durometer essentially measures the reaction force on the indentor through the calibrated spring when it is pressed into the material. The relation between the force measured and the movement of the indentor is

$$F = 0.55 + 3\Delta L \qquad \text{(A-2a)}$$

for type A, B and O durometers; and

$$F = 17.78\Delta L \qquad \text{(A-2b)}$$

for type C, D and DO durometers.

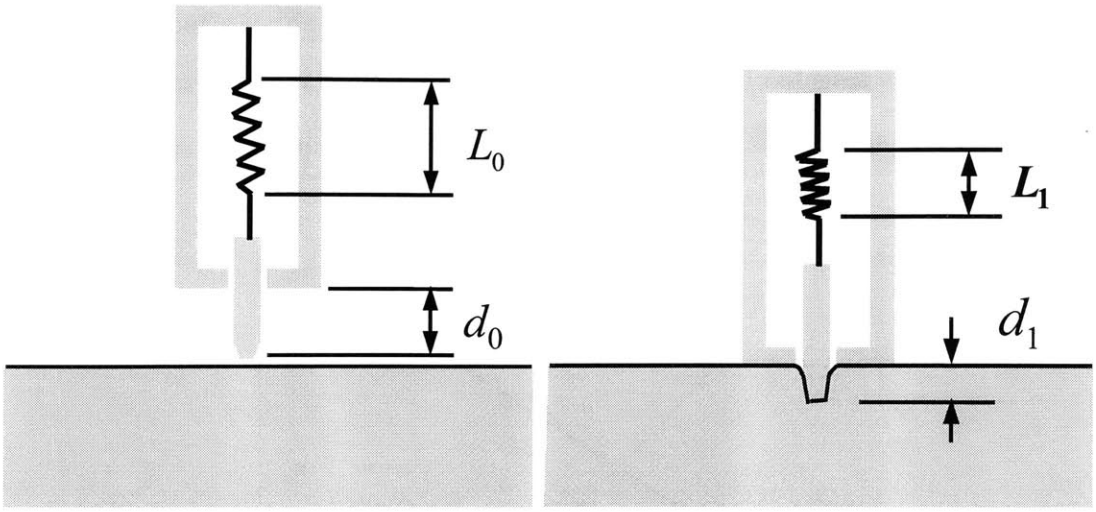

Figure A-2(a) Figure A-2(b)

Figure A-2: Schematics of the working mechanism of durometers. (a) Before the durometer is pressed down; (b) the durometer is pressed down.

In durometer tests, as the durometer is pressed onto the specimen surface, the indentor penetrates into the specimen, and is simultaneously pressed up into the device as well. This process is depicted in Figure A-2, where L_0 is the free length of the calibrated spring, d_0 is the distance between the indentor tip and the pressor foot lower surface and according to ASTM D 2240, $d_0 = 2.5mm$, d_1 is the corresponding distance in the fully loaded condition. Since the lower surface of the pressor foot is always in contact with the specimen surface when the reading is taken, it is straightforward to obtain (Figure A-2)

$$\Delta L + (d_1 - 0) = 2.5 \tag{A-3}$$

The indentor is in equilibrium, therefore

$$F_r(h)\big|_{h=d_1} = F \tag{A-4}$$

where F_r is the reacting force of the elastomeric specimen due to the indentor penetration denoted by h. Therefore, the objective equations relating the hardness measurement to the stress-strain behavior of the elastomers consist of eqn.(A-3) and eqn.(A-4). The exact form of $F_r(h)$ however is unknown. Gent[A-6] used the linear elastic Hertz contact solution for the case of a simplified indentor shape. Briscoe and Sebastian[A-7] considered the actual geometry of the indentor. This method however requires computationally cumbersome numerical methods for the solution. In this paper, we take

advantage of developments in nonlinear finite element method (FEM) and numerically simulate the hardness tests to obtain $F_r(h)$ in the form of a force vs indentation, F vs h, curve. The hardness scale reading is then obtained by finding the intercept point as shown in Figure A-3.

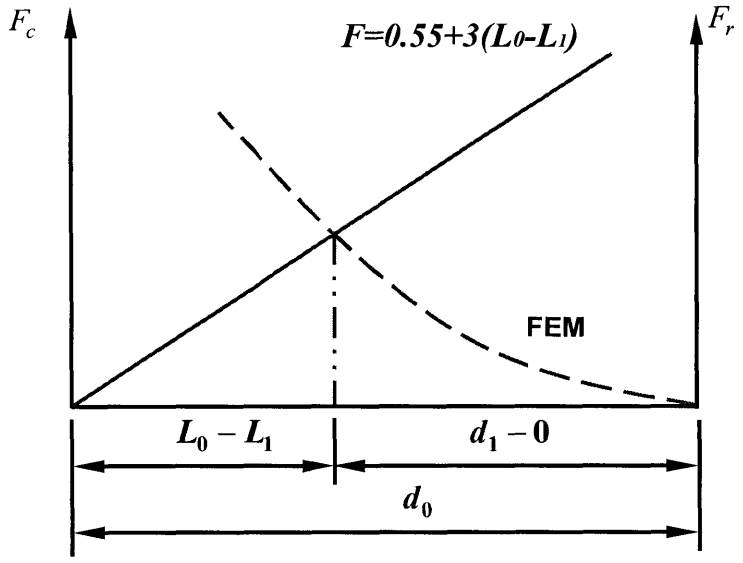

Figure A-3: Schematic of the method to obtain durometer readings.

A.2.2 FEM Models for Indentation Simulations

A.2.2.1 Geometry

The force vs indentation curve is obtained using a fully nonlinear finite element simulation of the indentation test. Since the indentors have axially symmetric cross sections, it is effective to model the problem as an axisymmetric one. As shown in Figure A-4, the vertical boundary AD is subjected to the axisymmetric boundary condition, $u_r\big|_{AD} = 0$. In order to reduce the influence from the specimen boundary, ASTM D 2240 requires that the test specimen should be at least 6mm in thickness and the locus of indentation should be at least 12mm away from any edges. Therefore, in Figure A-4, $AB = 15mm$, and $BC = 8mm$. Due to the existence of friction, the lower surface AB of the specimen cannot move freely along the horizontal direction, $u_r\big|_{AB} = u_z\big|_{AB} = 0$.

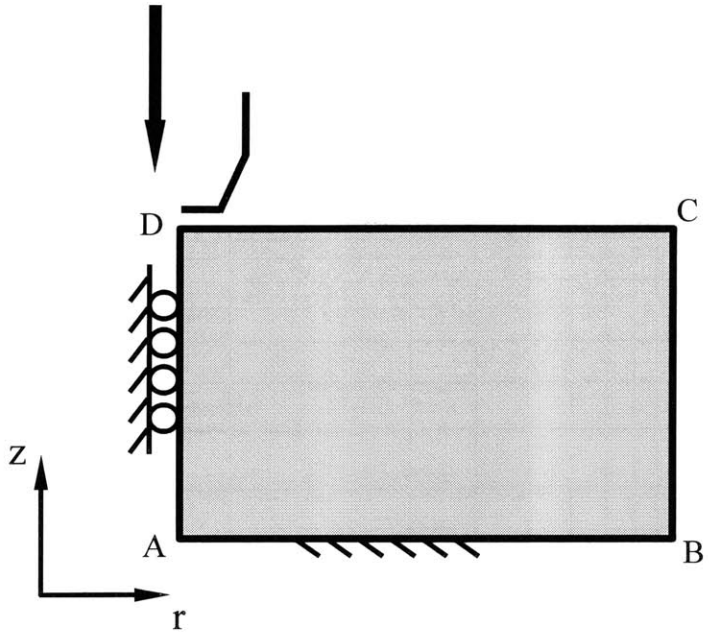

Figure A-4: The finite element method model for simulations of indentation.

The boundary value problem is solved using the finite element code ABAQUS. Axisymmetric 8-node, hybrid continuum elements with biquadratic interpolation of the displacement field and linear interpolation of pressure are used to model the elastomer. Figure A-5 shows the mesh used for the durometer A analyses. The indentor is modeled as a rigid surface since it is much stiffer than the elastomers being tested. The mesh is refined in the vicinity of the contact region where large gradients in stress and strain prevail. Several mesh densities were analyzed and an optimal mesh was finally chosen for use in all simulations. For durometer D analyses, a similar mesh has been used with the exception of the shape of the indentor.

The effect of friction on the simulation was studied by simulating selected cases of A-type and D-type tests using a friction coefficient of 0.3 between the indentor and the elastomer. Friction was found to increase the F vs h curve by no more than 4% in most cases. A similar result has been reported by Chang et al[A-9] for indentation with a rigid ball. Therefore, friction was neglected with exception that in D type analyses a friction coefficient of 0.1 was used to reduce the large deformation experienced by the elements on the contact surface.

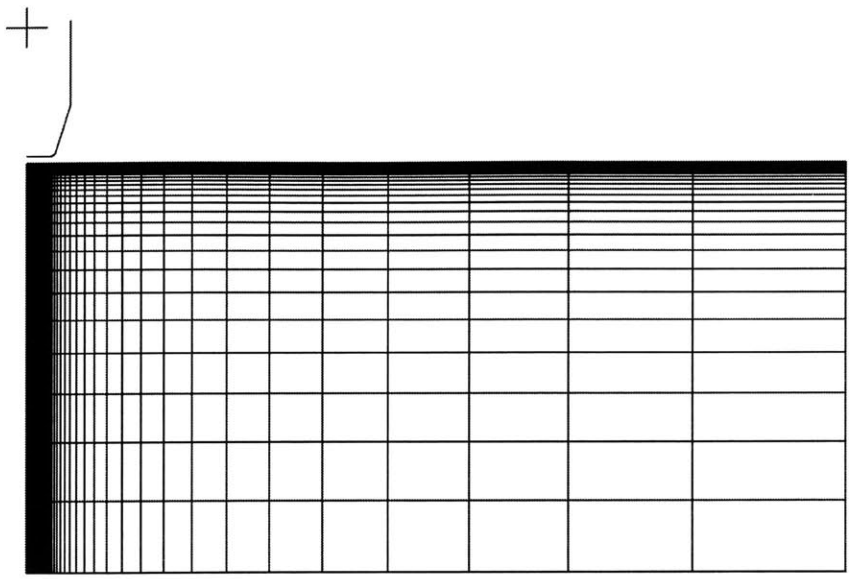

Figure A-5: The mesh used for the FEM simulations.

A.2.2.2 Material Model

The rubber elasticity constitutive laws in the simulations are the Gaussian (neo-Hookean) model[A-10] and the Arruda-Boyce eight-chain model[A-11]. Both models are based on the concept of an elastomer as a three-dimensional network of long chain molecules, linked together at points of cross-linkage. The Gaussian model assumes Gaussian chain statistics to apply and the strain energy density function is given by

$$W_G = \frac{1}{2}\mu\left(\lambda_1^2 + \lambda_2^2 + \lambda_3^2 - 3\right) = \frac{1}{2}\mu\left(I_1 - 3\right), \qquad \text{(A-5)}$$

where $\mu = nk\Theta$, n is the number of chains per unit volume, k is Boltzmann's constant, Θ is absolute temperature; λ_1, λ_2, and λ_3 are the three principal stretches and I_1 is the first invariant of the stretch $I_1 = \lambda_1^2 + \lambda_2^2 + \lambda_3^2$.

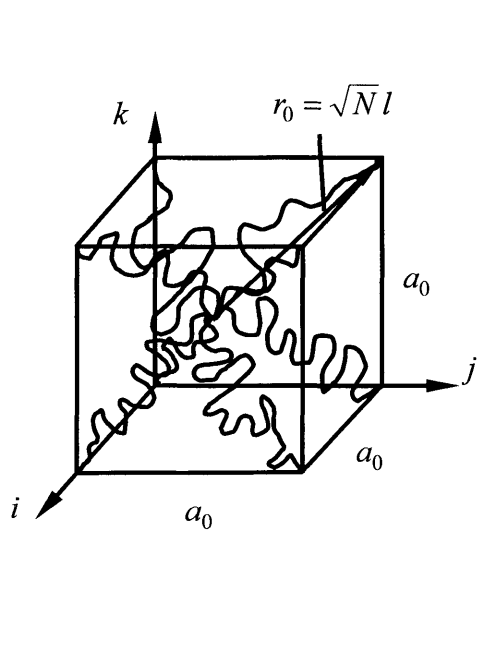

Figure A-6(a)

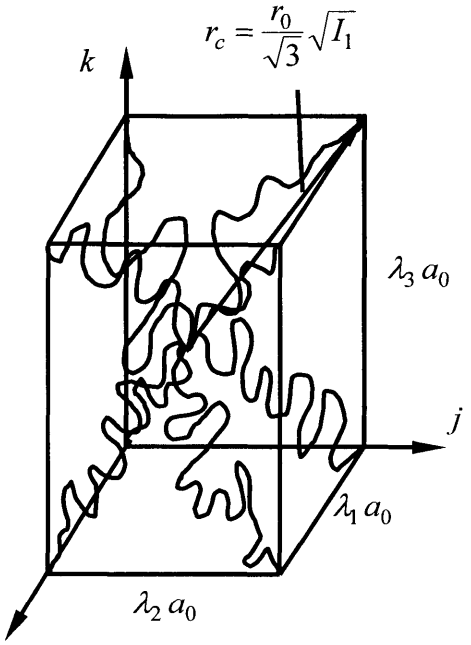

Figure A-6(b)

Figure A-6: The network for the eight chain model. (a) Unstretched state. (2) stretched state.

The limitation of the Gaussian theory is that as chains become highly stretched, the stress level is underpredicted, necessitating a non-Gaussian statistical theory to depict the behavior of the chain deformations approaching their limited extensibility. The Arruda-Boyce model employs a representative description of the network containing eight non-Gaussian chains extending from the center of a cube to each corner (see Figure A-6) to simulate the network structure of the polymer. The initial chain length is, from random walk statistics, given by $r_0 = \sqrt{N}l$, where N is the number of rigid links of length l between the points of cross linkage. The maximum length of the chain is Nl and the maximum chain stretch, which is called the locking stretch or limiting extensibility, is

$$\lambda_L = \frac{Nl}{r_0} = \sqrt{N} \tag{A-6}$$

The cube is deformed in the principal stretch space and the stretch of each chain in the network is

$$\lambda_{chain} = \frac{r_{chain}}{r_0} = \sqrt{\frac{I_1}{3}} \tag{A-7}$$

Note that the concept of the effective chain stretch λ_{chain} can also be applied to the Gaussian model. The strain energy density function for this 8-chain network is [A-11]

$$W_{AB} = \mu\left(\lambda_{chain}\sqrt{N}\beta + N\ln\frac{\beta}{\sinh\beta}\right) - \Theta c \qquad \text{(A-8)}$$

where β is the inverse Langevin function, $\beta = \mathcal{L}^{-1}[\lambda_{chain}/\sqrt{N}]$, and $\mathcal{L}[\beta] = \coth\beta - (1/\beta)$, c is a constant.

It can be shown that the initial elastic modulus of the material from a uniaxial tensile test is

$$E_0 = 3\mu \qquad \text{(A-9a)}$$

for the Gaussian model and

$$E_0 = 3\mu\left(1 + \frac{40425}{67375N} + \frac{39501}{67375N^3} + \frac{42039}{67375N^4} + \cdots\right) \qquad \text{(A-9b)}$$

for the Arruda-Boyce model using a power series expansion representative of the inverse Langevin function. Observe that the elastic modulus predicted by Gaussian model is independent of chain limiting extensibility. The difference between the initial moduli for the Arruda-Boyce model and the Gaussian model increases as N decreases or the crosslinking density increases; when N is 6, the difference is 10% and when N is 4, the difference is 16%.

A.3 Results and Discussions

A.3.1 Simulations on Durometer A and Durometer D

Finite element simulations of representative durometer hardness tests are conducted for Gaussian materials with $\mu = 1.6MPa$ for a Shore A test and $\mu = 30MPa$ for a Shore D test, respectively.

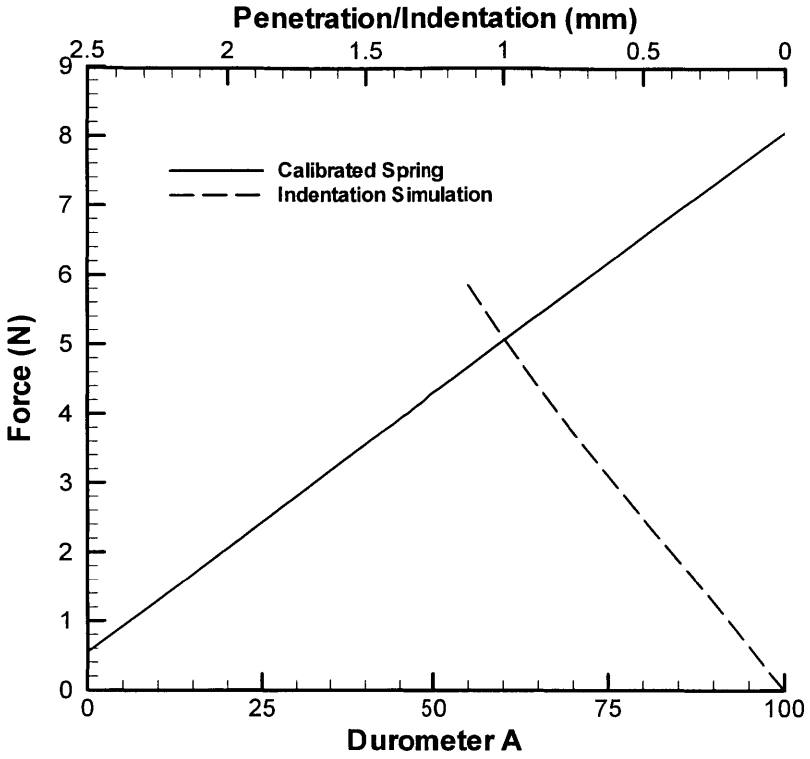

Figure A-7: The solid line is the force-penetration curve for the calibrated spring following eqn.(A-2(a)); The dashed line is the force-indentation curve from the Shore A test simulation for a Gaussian material with $\mu = 1.6MPa$.

In Figure A-7, the force-indentation curve from the simulation of the Shore A test is depicted together with the spring behavior described earlier in eqn.(A-2(a)). The Shore A hardness value is obtained by finding the intersection of these two curves, which occurs at an indentation depth of 1.00mm, giving a Shore A value of 60A. Figure A-8 (a) and (b) show the contours of principal strain and chain stretch ratio λ_{chain} at the indentation depth of 1.00mm, respectively. These contours reveal that the elastomer experiences modest to large strain for this representative case (the Shore A scale is commonly used to indicate the durometer of materials between 30A to 90A). The maximum chain stretch ratio is observed around the corner of the indentor tip and is 2.2. For elastomers with a low limiting extensibility, this result indicates that it may be necessary to consider this effect when relating durometer to nonlinear stress-strain behavior.

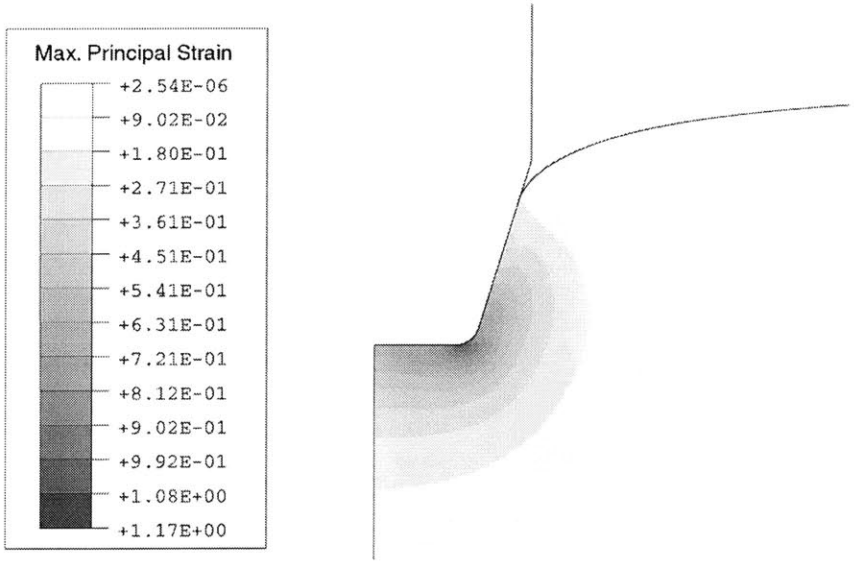

Figure A-8(a)

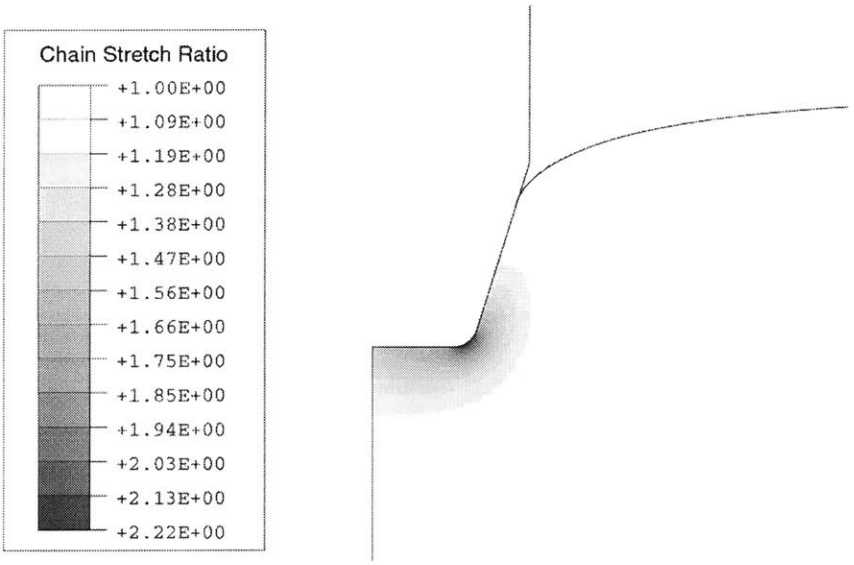

Figure A-8(b)

Figure A-8: Results for Shore A simulation for the Gaussian material with $\mu = 1.6MPa$. (a) contours of the maximum principal strain; (b) contours of the chain stretch ratio.

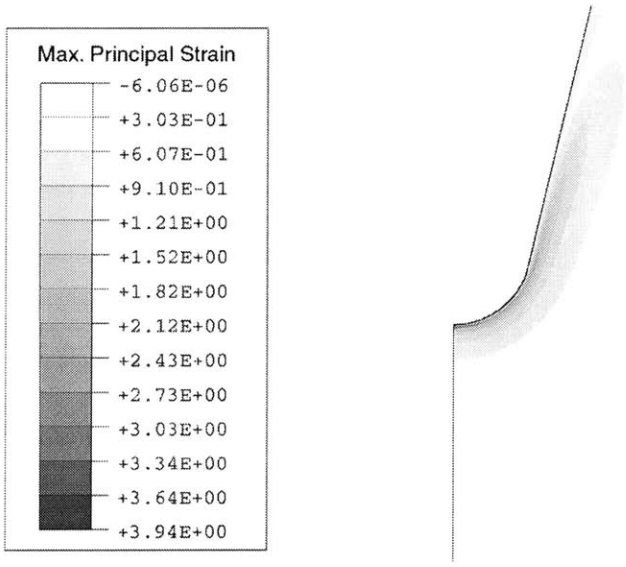

Figure A-9(a)

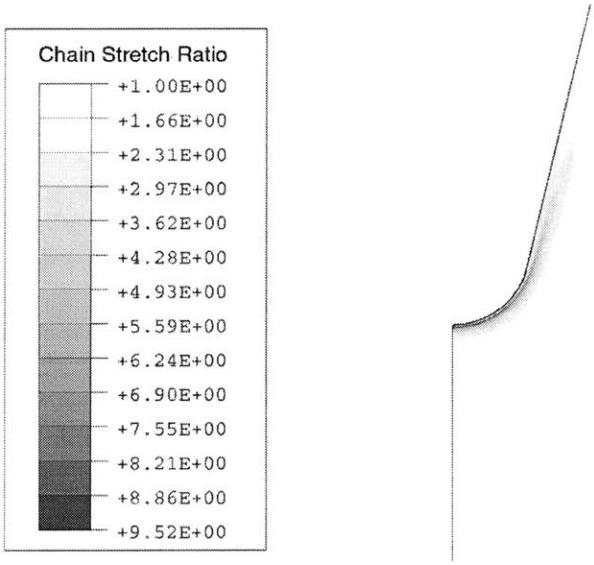

Figure A-9(b)

Figure A-9: Results for Shore D simulation for the Gaussian material with $\mu = 30MPa$ (a) Contours of the maximum principal strain; (b) Contours of the chain stretch ratio.

Similar to the Shore A case, the Shore D hardness value for the Gaussian material of $\mu = 30MPa$ is obtained by finding the intersection of the spring response of eqn.(A-2(b)) and the force-indentation curve for Shore D hardness indentation. The Shore hardness for this material is 62D and the penetration is 0.95mm. Figure A-9(a) and (b) show the maximum principal strain contour and the chain stretch ratio contour, respectively, at the

fully loaded indentation (0.95mm) for this representative Shore D test. The strains are highly localized for this cone shape indentor and are rather high. The maximum chain stretch ratio is 9.5, and maximum principal strain is 3.9, suggesting that the limiting extensibility of the material may play an important role in evaluating material Shore hardness.

A.3.2 Comparisons between Shore A and Shore D

To verify the proposed method, the finite element simulations of durometer hardness tests for scale A and scale D were conducted for three Gaussian materials with $\mu = 3.3MPa$, $\mu = 6.0MPa$, $\mu = 9.2MPa$, respectively. The materials were chosen to provide durometer readings where the A and D scales overlap.

Table A-2. Comparison of Shore A and Shore D hardness by simulations. Both Shore A and Shore D values are obtained for the same materials by finite element method so that a conversion between A scale and D scale is established. These conversions are compared with the comparison chart in Table A-1, given as errors in D values.

μ (MPa)	Duro A	Duro D (Simulated)	Duro D (from TableA-1)	Error
3.30	75	25	24	4%
6.0	85	32	29	10%
9.20	90	40	35	14%

For the material with $\mu = 3.3MPa$, the predicted durometer hardness is 75A and 25D. According to the guideline comparison chart in ASTM D 2240[A-1], the material with durometer hardness 75 in scale A should give a hardness of about 24 in scale D. Similar comparisons are made for materials with $\mu = 6.0MPa$, $\mu = 9.2MPa$ and are listed in Table A-2. It should be noted that the comparison chart in ASTM D 2240 is loosely defined and cannot be used for absolute comparison purposes. Indeed, conversions which differ slightly were found[A-12]. Therefore, although a relatively large error exists for 90A, Table A-2 shows generally good agreement between simulated values and values from the comparison chart. This verifies the capability of the current

finite element simulation to predict both A scale and D scale durometer hardness. The regions where direct conversions are not as reliable will be shown to occur at the tail end of the A scale where the relationship between the hardness and modulus becomes highly nonlinear.

A.3.3 Correlation between Gaussian Elastic Modulus and Hardness

Figure A-10 shows the relationship between the elastic modulus E_0 by eqn.(A-9(a)) for the Gaussian model vs shore hardness A obtained by finite element simulations. The Gent predictions, and the Briscoe/Sebastian predictions are also presented for comparison purposes. In Figure A-10, all predictions give the same trend for the relation between E_0 and shore A hardness. However, the fully nonlinear analysis generally gives a higher prediction of elastic modulus for a given hardness than the other three predictions. Figure A-11 shows the difference between the elastic modulus predicted by the fully nonlinear analyses and those predicted by the other two theories, given as deviations from the fully nonlinear analyses. The difference between the Briscoe/Sebastian theory and the fully nonlinear model ranges from 18% to 10% and shrinks as the hardness increases, since the deviation of their theory from the fully nonlinear analyses becomes smaller as the penetration of the indentor decreases due to the increasing stiffness of the elastomer. However, a different trend is observed in the difference between the Gent theory and the fully nonlinear analyses. The reason for this trend is because the Gent theory used the average diameter of the upper and lower surface of the truncated cone indentor as the diameter of the equivalent flat punch, whose deviation from the reality is pronounced as the penetration decreases.

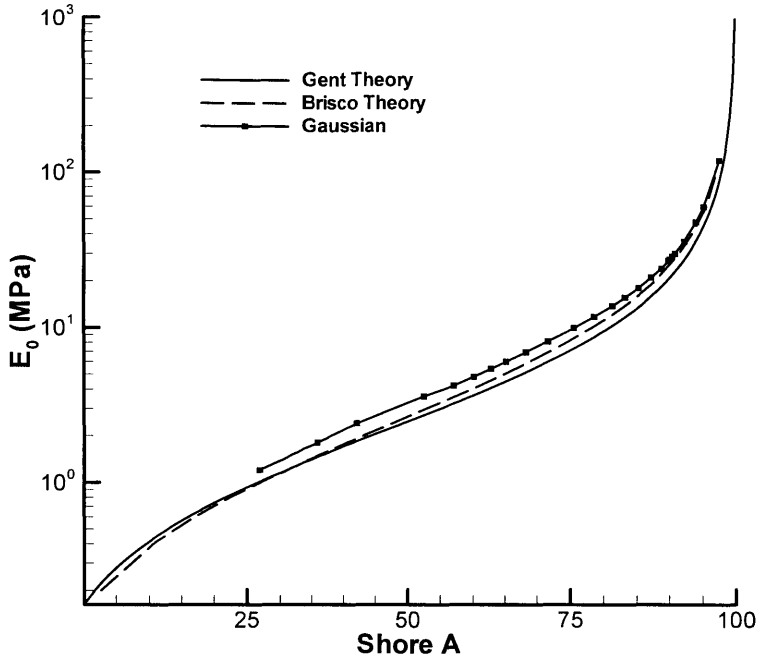

Fig. 10. Relations between Shore A hardness and initial elastic moduli of elastomeric materials.

A first order estimation for type D durometer hardness can be obtained using the linear elastic solution[A-13]. For the cone indentor, the normal force on the indentor is

$$F_r^D = \frac{2E}{\pi(1-\nu^2)} \tan\theta\, h^2 \tag{A-10}$$

Combining with eqn(A-5(b)), the relation between elastic modulus and durometer D hardness for $\theta = 15^\circ$, $\nu = 0.5$, is

$$H_D = 100 - \frac{20\left(-78.188 + \sqrt{6113.36 + 781.88E}\right)}{E} \tag{A-11}$$

Figure A-12 shows the comparison between simulated results and the first order approximations to D scale hardness. The two predictions give the same trend between the relation of elastic modulus and shore hardness D. However, the fully nonlinear analysis generally gives lower elastic modulus predictions than the linear elastic theory for a given hardness. The difference increases as the hardness increases.

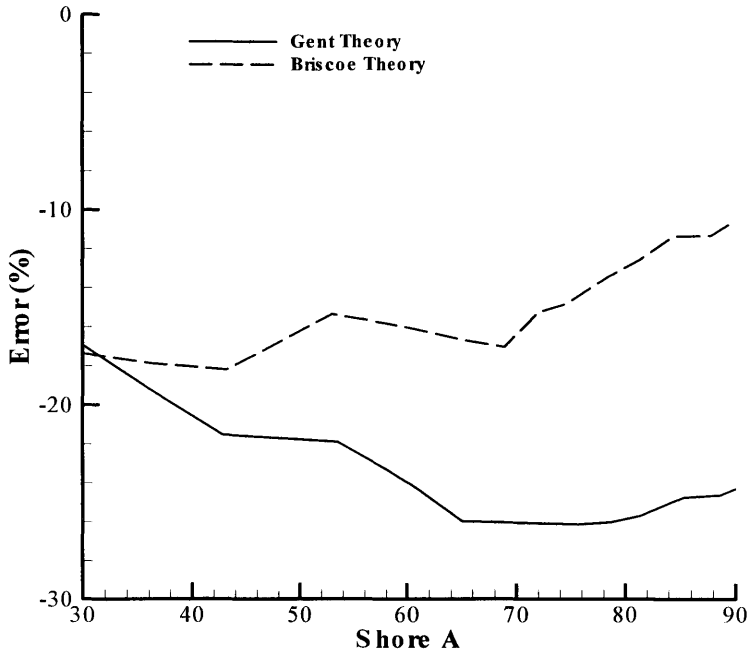

Figure A-11: The differences of the elastic modulus for the given hardness between the finite element analyses and the other theories, given as deviation from the finite element analyses.

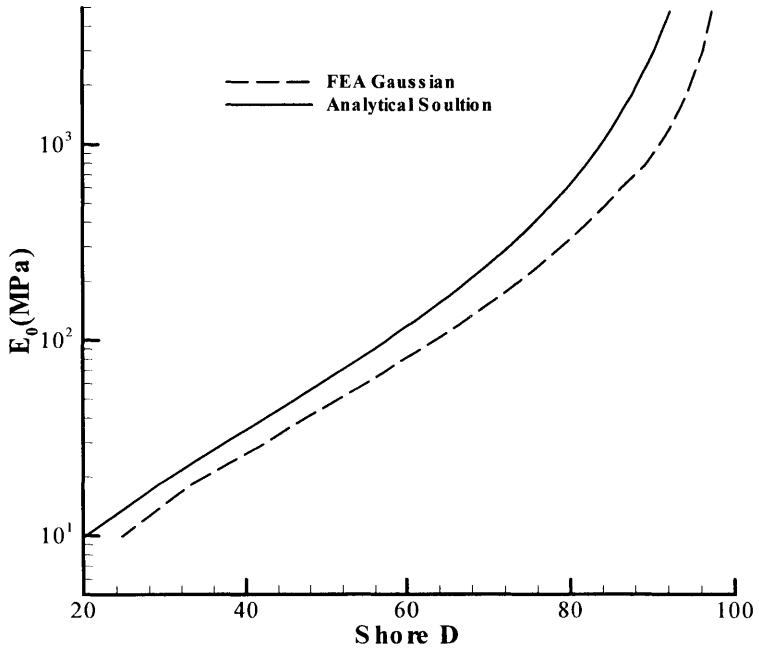

Fig. 12 The relation between Shore D hardness and initial elastic moduli of elastomeric and elastomeric-like materials.

Figure A-13 shows the relationship between elastic modulus and Shore A/Shore D hardness, given by finite element simulations. For both hardness scales, the logarithm of elastic modulus is proportional to the hardness values in the range of 20A(D) to 80A(D). The region where the two scales overlap corresponds to a linear region for Shore D, but mostly nonlinear region for Shore A. When the overlap is in the linear region for both scales, good conversions can be obtained, as for 75A to 25D; whereas when the overlap occurs in linear vs nonlinear regions, the conversions become worse, as for 90A to 40D, since the logarithm of the elastic modulus varies with Shore A values in a much faster rate than it does with Shore D values.

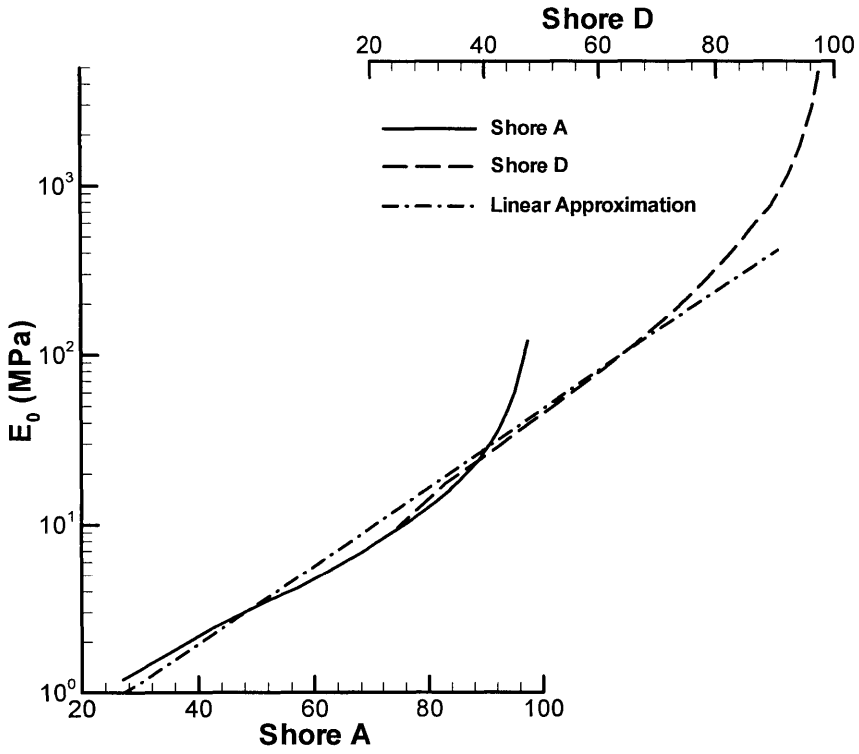

Figure A-13: The relations between elastic modulus and Shore A/Shore D hardness for elastomeric and elastomeric-like materials, given by finite element simulations. The linear approximation is given by eqn(20).

It is also noted that there exists an almost linear relation between the logarithm of elastic modulus and a hardness scale S

$$\log E_0 = 0.0235S - 0.6403 \qquad \text{(A-12a)}$$

$$S = \begin{cases} Shore\ A, & 20A < S < 80A \\ Shore\ D + 50, & 80A < S < 85D \end{cases} \qquad \text{(A-12b)}$$

A.3.4 Limiting Extensibility Effect

As seen from Figure A-8(b), large chain stretches can develop during the indentation process. For materials having small limiting extensibilities, this large chain stretch could be close to its locking stretch. Therefore, it is important to evaluate the effect of chain extensibility on the durometer hardness. Since the Arruda-Boyce material model captures the limiting extensibility of elastomeric materials, it is used in this section and then compared to the results that had been obtained using the Gaussian model.

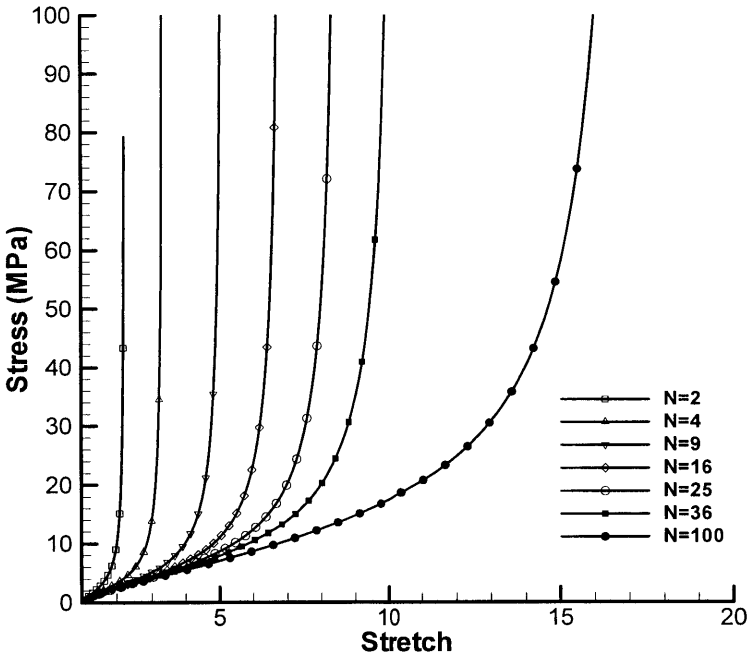

Fig. 14 The stress-stretch curves for $\mu = 1.35MPa$ and different Ns of the Arruda-Boyce model.

Figure A-14 depicts the tensile stress vs stretch curve for the Arruda-Boyce materials with $\mu = 1.35MPa$ and with various N values ranging from $N = 2$ to $N = 100$. At small stretches, the initial modulus for the material with smaller N is larger (eqn.(A-9(b))); At large stretches, the stiffness of the material with smaller N increases

dramatically. Note that $N = 100$ corresponds to a limiting chain extensibility of $\lambda_L = 10$ and the upturn of the stress stretch curve occurs at an axial stretch of about 17, and $N = 4$ corresponds to a limiting chain extensibility of $\lambda_L = 2$ and the upturn occurs at an axial stretch of about 3.4. Note that the chain limiting extensibility is significantly lower than the limiting extension of the sample observed in a uniaxial tensile test because the molecular chains in the underlying molecular network accommodate macroscopic deformation through both chain stretching and chain rotation.

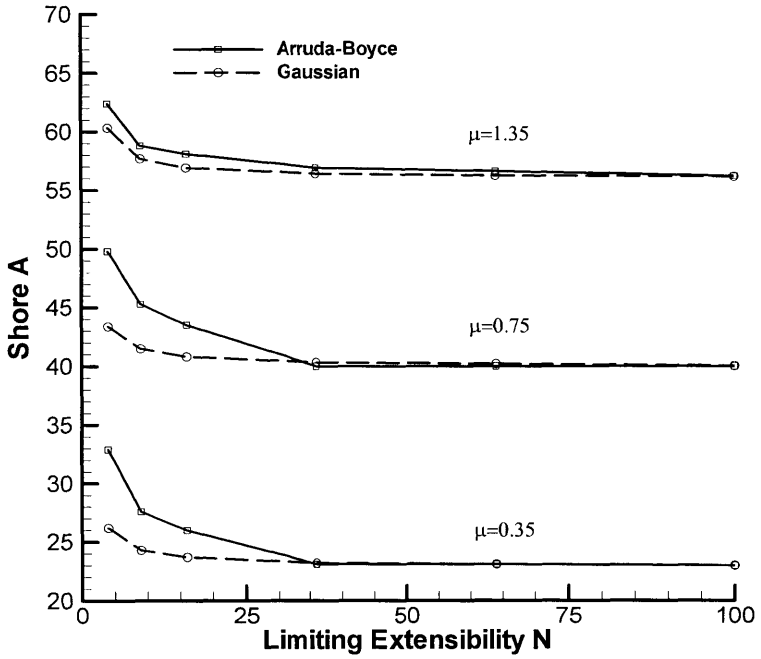

Figure A-15: The solid lines show the dependence of the durometer A hardness vs N for $\mu = 1.35MPa$, $\mu = 0.75MPa$ and $\mu = 0.35MPa$. The corresponding Gaussian results with the same E_0 are also presented as the dashed lines.

Figure A-15 shows the dependence of the durometer hardness vs limiting chain extensibility, N, for $\mu = 1.35MPa$, $\mu = 0.75MPa$ and $\mu = 0.35MPa$. The corresponding Gaussian result with the same E_0 is also presented. For N smaller than about 25 (corresponding to a limiting chain extensibility of $\lambda_L = 5$ and uniaxial tensile stretch of $\lambda = 8.5$), the predictions which account for the non-Gaussian behavior of the elastomer begin to deviate from those using the Gaussian material model and are substantially

higher than those of the Gaussian material as N decreases. These higher hardness predictions are not purely a result of the effect of N on the initial modulus since the simulations using the Gaussian model with the same initial E_0 give lower predictions of hardness. The higher hardness prediction also result from the durometer test applying stretches that approach the limiting chain extensibility for cases when N is less than 25.

The effect of the limiting extensibility is also influenced by μ. As shown in Figure A-15, when μ is small, large chain stretch can develop during indentation, the effect of the limiting extensibility is pronounced. When μ increases, the penetration of the indentor becomes small. Hence, the molecular chains are unlikely to be stretched close to their locking stretch, and the effect of the limiting extensibility is reduced. As shown in Table A-3, when $\mu = 2.15MPa$, the difference in Shore A hardness is less than 4% when N varies from 4 to 100. Therefore, it is more likely that when λ_L is less than 5 and μ is less than $2MPa$ the effect of the chain limiting extensibility is important. Note that limiting extensibilities significantly less than 5 are quite common in soft biological tissues[A-8][A-14] as well as in elastomers.

Table A-3 gives predictions of Shore hardness A for different combinations of μ and N in the Arruda-Boyce model. In Table A-3, different combinations of N and μ may lead to the same predicted durometer hardness. Table A-4 gives two examples of N and μ pairs which lead to Shore 73.6A. The corresponding initial elastic moduli are also listed in Table A-4. Although the materials have the same durometer hardness, their elastic moduli are different by about 5%. It is therefore important to notice that predicting elastic moduli from durometer tests sometimes gives ambiguous results due to the limiting extensibility of the chain. There does not exist a one-to-one mapping between the initial elastic modulus and durometer hardness.

Table A-3. Predictions of durometer A hardness for different combinations of μ and N in the Arruda-Boyce model.

		N				
		4	9	16	36	64
μ (MPa)	0.35	32.9	27.6	26.0	23.1	23.1
	0.55	42.9	37.9	35.8	31.6	31.6
	0.75	49.8	45.3	43.5	40.0	40.0
	0.95	54.9	50.9	49.9	48.5	48.5
	1.35	62.4	58.8	58.1	56.9	56.6
	1.75	67.7	64.6	63.6	63.1	62.5
	2.15	71.8	68.9	68.2	67.3	67.1
	2.55	74.9	72.4	71.8	70.9	70.7
	2.95	77.5	75.2	74.5	73.7	73.6
	3.35	79.6	77.5	77.0	76.3	76.1
	3.75	81.4	79.4	78.9	78.2	78.2
	4.15	82.9	81.1	80.4	80.0	79.9
	4.45	83.8	82.1	81.6	81.2	81.0
	5.0	85.4	83.8	83.3	83.0	82.8
	5.0	86.6	85.1	84.7	84.3	84.2
	6.0	87.6	86.2	85.8	85.5	85.4
	9.0	91.4	90.5	90.2	90.0	89.9
	12.0	93.4	92.7	92.4	92.3	92.2

Table A-4. Materials with different material parameters have same durometer hardness.

N	μ (MPa)	Duro (A)	E_0 (MPa)
5.76	2.55	73.6	8.59
36	2.95	73.6	9.01

Table A-5. Material with higher durometer hardness and higher elastic modulus can have higher extensibility.

N	μ (MPa)	E_0 (MPa)	Duro (A)	Maximum extension
9	0.95	3.06	50.9	480%
16	2.55	7.95	71.8	690%

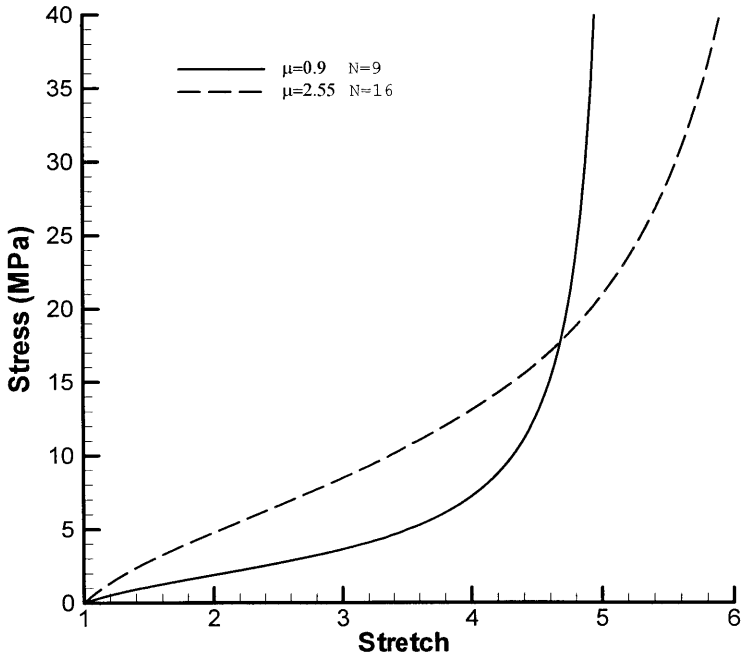

Figure A-16: The stress-stretch curves for two different Arruda-Boyce materials. The material with $\mu = 2.55MPa$ and $N = 16$ has larger initial elastic modulus and larger extensibility.

In the applications of durometer hardness, many researchers assume that larger durometer hardness corresponds to larger elastic modulus but less extensibility. However, one should be precautious when making this inference. For instance, considering two combinations of μ and N in the Arruda-Boyce model in Table A-5, the second combination gives larger durometer hardness, but has higher extensibility as well, as it can be seen from the stress-stretch curves (Figure A-16).

A.4 Conclusions

Durometer hardness tests were analyzed using fully nonlinear finite element simulations accounting for both material and geometrical nonlinearities. The simulation results are verified by matching the predicted durometer hardness in scale D with ASTM D 2240 for the Gaussian material with the given durometer hardness in scale A. The relations between elastic modulus and the durometer hardness A scale and D scale are provided. The fully nonlinear finite element analyses predict higher values of the elastic modulus than those given by the Gent theory and the Briscoe/Sebastian theory. The influence of the limiting extensibility of the elastomer is evaluated using the non-Gaussian Arruda-Boyce eight-chain model. The chain extensibility eliminates the one-to-one mapping between the elastic modulus and the durometer hardness. The limiting extensibility also increases the reaction force to the indentation and thus increases the hardness of the material. This effect is pronounced as the chain extensibility decreases to values of λ_L less than 5, particularly when μ is less than $2MPa$. These results indicate that the durometer hardness test can be used to provide a reasonable approximation (the error is generally less than 4% for large λ_L and μ) to the initial neo-Hookean modulus using the plot of Figure A-13 or eqn.(A-12), however care must be used if the limiting extensibility is known to be small. The mapping does not address the time dependence of the material behavior, the initial yield-like phenomenon present in thermoplastic elastomers, or the initial anisotropy existing in many soft tissues. However, it does provide the framework for exploring such complexities in future work.

References

[A-1] ASTM Designation, D 2240-97.

[A-2] ASTM Designation, D1415-88.

[A-3] Falanga, V., Bucalo, B., Use of a durometer to assess skin hardness, J. American Acad. Dermatology, vol.29, pp47-51, 1993.

[A-4] Reisfeld, P.L., A hard subject-use of a durometer to assess skin hardness, J. American Acad. Dermatology, vol.31, pp515-515, 1994.

[A-5] Ladeji-Osias, J.O., Langrana, N.A., Analytical evaluation of tumors surrounded by soft tissue, Proceedings of the 22nd Annual EMBS International Conference, July 23-28, 2000, Chicago, IL, pp2114-2117.

[A-6] Gent, A.N., On the relation between indentation hardness and Young's modulus, Trans. Inst. Rubber Ind, vol.34, pp46~57, 1958.

[A-7] Brsicoe, B., Sebastian, K.S., An analysis of the durometer indentation, Rubber Chem. Tech., Vol. 66, pp837~836, 1993.

[A-8] Bischoff, J.E., Arruda, E.M., Grosh, K., Finite element modeling of human skin using an isotropic, nonlinear elastic model constitutive model, J. Biomech, 33, pp645~652, 2000.

[A-9] Chang, W.V, and Sun S.C., Nonlinear elastic analysis of the hardness test on rubber-like materials, Rubber Chem. Tech., Vol.64, pp202~210, 1991.

[A-10] Treloar, L.R.G., The physics of Rubber Elasticity, Oxford University Press, Oxford, 1975.

[A-11] Arruda, E.M., Boyce, M.C., A three-dimensional constitutive model for the large stretch behavior of rubber elastic materials, J. Mech. Phys. Solids, Vol. 41, No.2, pp389, 412, 1993.

[A-12] Hill, D.J.T., Killen, M.I., et al., Laboratory wear testing of polyurethane elastomers, Wear, 208, pp155-160, 1997.

[A-13] Sneddon, I.N., The relation between load and penetration in the axisymmetric Boussinesq problem for a punch of arbitrary profile, Int. J. Eng. Sci., vol.3, pp47, 1965.

[A-14] Fung, Y.C., Biomechanics: mechanical properties of living tissues, Springer-

Verlag, New York, 1993.

Appendix B

Determination of Mechanical Properties of Carbon Nanotubes and Vertically Aligned Carbon Nanotube Forests Using Nanoindentation[1]

Abstract

Vertically aligned carbon nanotubes (VACNT) have been a recent subject of intense investigation due to the numerous potential applications of VACNTs ranging from field emission and vacuum microelectronic devices to the creation of super-hydrophobic surfaces and as a source of well defined CNTs. In this paper, a new method to determine the mechanical properties of VACNT and constituent nanotubes using nanoindentation tests is proposed. The study of nanoindentation on a VACNT forest reveals a process whereby nanotubes are consecutively bent during the penetration of the indentor. Therefore, the resistance of a VACNT forest to penetration is due to successive bending of nanotubes as the indentor encounters nanotubes. Using a micro-mechanical model of the indentation process, the effective bending stiffness $(EI)_{eff}$ of constituent nanotubes in the VACNT array is then deduced from nanoindentation force-penetration depth curves. A simple method accounting for the multiwalled structure of multiwall nanotubes is used to interpret the obtained $(EI)_{eff}$ in terms of an effective bending modulus E_t^b, an effective axial modulus E_t^a, and a wall modulus E_t^w of a nanotube. Nanoindentation tests on three VACNT forest samples reveal the effective bending modulus of multiwall carbon nanotubes to be $E_t^b = 0.91 \sim 1.24 TPa$, and effective axial modulus to be

[1] This work has been accepted by Journal of Mechanics and Physics of Solids, and will be published soon.

$E_t^a = 0.90TPa \sim 1.23TPa$. These values are in good agreement with tests conducted on isolated MWCNTs. Taking the mechanical wall thickness to be $0.075nm$, the nanotube wall modulus is found to be $E_t^w = 4.14TPa \sim 5.61TPa$, which is in good agreement with predictions from atomic simulations. The use of nanoindentation together with the proposed micromechanical model of the successive bending of nanotubes as the indentor penetrates into the forest is hereby shown to result in a novel approach for determining not only the dependence of the indentation resistance on the key structural features of the forest (CNT diameter, length and areal density), but also provides a measure of the stiffness of the constituent carbon nanotubes. This new technique requires no special treatment of the samples, making it promising to apply this method to a large number of tests to determine the statistical properties of CNTs, and implying the potential use of this method as a quality control measurement in mass production.

Keyword: A. Nanoindentation; Mechanical Properties; B. Multiwalled Carbon Nanotubes; Vertically Aligned Carbon Nanotubes; Nanofibers.

B.1. Introduction

Carbon nanotubes (CNTs) are a subject of intensive investigations due to their remarkable electrical and mechanical properties (Baughman et al., 2002). CNTs exist in one of two forms: Single-walled carbon nanotubes (SWCNTs) or multi-walled carbon nanotubes (MWCNTs), and can be further classified by their chirality (the wrapping angle of the hexagonal atomic thin layer). The primary methods used to produce CNTs are carbon-arc discharge, laser ablation of graphite, and chemical vapor deposition (CVD). In many applications, it is desirable that CNTs have well defined diameters and lengths so that the properties of CNTs can be readily tailored for their applications. Recently, plasma enhanced chemical vapor deposition (PECVD) has been used to grow forest-like vertically aligned carbon nanotubes (VACNTs) onto substrates coated with a suitable metal catalyst (Huang et al., 1998; Chhowalla et al., 2001; Huang et al., 2002; Han et al., 2002). There is presently great interest in VACNTs for field emission and vacuum microelectronic devices, as well as for the creation of super-hydrophobic surfaces and as a technique for producing well defined CNTs. Compared with the efforts focused on optimizing the PECVD growth conditions, however, little attention has been given to the mechanical properties of these forests even though the stiffness and mechanical integrity will be important issues in their ultimate success.

Due to the nanometer scale of dimensions, it is a challenge to experimentally measure mechanical properties of CNTs. The first measurement of the elastic modulus of CNTs was conducted by Treacy et al. (1996) whereby the amplitude of thermally-induced vibrations of isolated nanotubes was measured within a TEM; classical beam theory, where the nanotubes were idealized as solid rods, was then used to calculate the modulus. The effective bending modulus derived from this method ranged from $0.4TPa$ to $4.15TPa$ with $1.8TPa$ as an average value over 11 CNTs. In addition to the large range in the value of the elastic modulus, this method is also limited by the requirement that the vibration of nanotubes must be neither too high nor too small for TEM detection. Wong et al. (1997) dispersed MWCNTs on a smooth flat surface and pinned the nanotubes by the deposition of an array of square pads on this substrate. An AFM was then used to

scratch the surface at the "free" end of the nanotube and the lateral force and displacement were measured. Beam theory, assuming a solid cross section, was then used to reduce the data, yielding a modulus of MWCNTs $1.28 \pm 0.59 TPa$. It should be noted that although adhesive and frictional forces might increase scratching resistance, they were neglected in their method. Salvetat et al (1999) deposited CNTs on a well polished alumina ultra-filtration membrane, on which a CNT occasionally laid over a pore. The tube was then subjected to bending using nanoindentation. The effective bending modulus from this method was found to be $0.81 \pm 0.41 TPa$. These three techniques, each providing bending modulus measurements on individual nanotubes, require complicated preparations before the measurements can be conducted. In these methods, the effective bending modulus E_f^b is determined using beam theory whereby an effective bending stiffness $(EI)_{eff}$ is measured and the modulus is then determined assuming an effective moment of inertia $I_{eff} = \pi\left(D_o^4 - D_i^4\right)/64$, where D_o is the outer diameter and D_i is the inner diameter. Furthermore, this is approximated as $I_{eff} \approx \pi D_0^4/64$, since D_i is typically much smaller than D_o. The modulus is then computed to be

$$E_f^b \approx \frac{(EI)_{eff}}{I_{eff}} \tag{B-1}$$

In this paper, nanoindentations on VACNT forests will be shown to provide a measure of the indentation resistance of a nanotube forest coating as well as a statistical measure of the effective bending stiffness $(EI)_{eff}$ and effective bending modulus E_f^b of MWCNTs when combined with a simple analytical model of nanoindentation tests. Further reduction of the results, which account for the nested tube structure of a MWCNT, enables the calculations of a wall modulus and a tube axial modulus. Below, descriptions of the materials and the experimental procedure are first presented. A model of the behavior of VACNT forests during nanoindentation is then presented and is used together with tests to determine the average bending stiffness, bending modulus, wall modulus, and axial modulus of the constituent nanotubes in the VACNT forest studied. Nanoindentation is thus shown to be an excellent new technique to measure both the

indentation resistance of VACNT forests and the elastic modulus of individual constituent CNTs.

B.2. Experimental Procedure

B.2.1 Materials

Three vertically aligned carbon nanotube forest samples were prepared at University of Cambridge using PECVD (Plasma Enhanced Chemical Vapor Deposition) method (Chhowalla et al., 2001) with different nickel catalyst thickness (ranging from 3.5nm to 7nm) and growth time. The samples were then studied at MIT under a JOEL SEM, with the samples tilted by 0° (observed from top), 15°, and 25°. Figure B-1 shows images where samples were tilted by 25° so that the forest-like landscapes of the VACNTs were clearly depicted. The areal density measurement for each sample was conducted by counting the number of nanotubes in the image, then dividing the total number of nanotubes by the total area of the image; measurements were made on images with the sample tilted by 0°, 15° and 25°, then averaged over these three measurements. The diameter and length were measured from images with the samples tilted by 0° (for diameter only), 15°, and 25°, respectively. For each image, at least 30 nanotubes were randomly selected for measurements. The length and diameter measurements were further verified by measuring nanotubes that had been laid flat on the substrate with a pair of tweezers. The average and deviation of diameter and length, and the areal density (number of tubes per μm^2 of substrate) for each of the three samples are listed in Table 1.

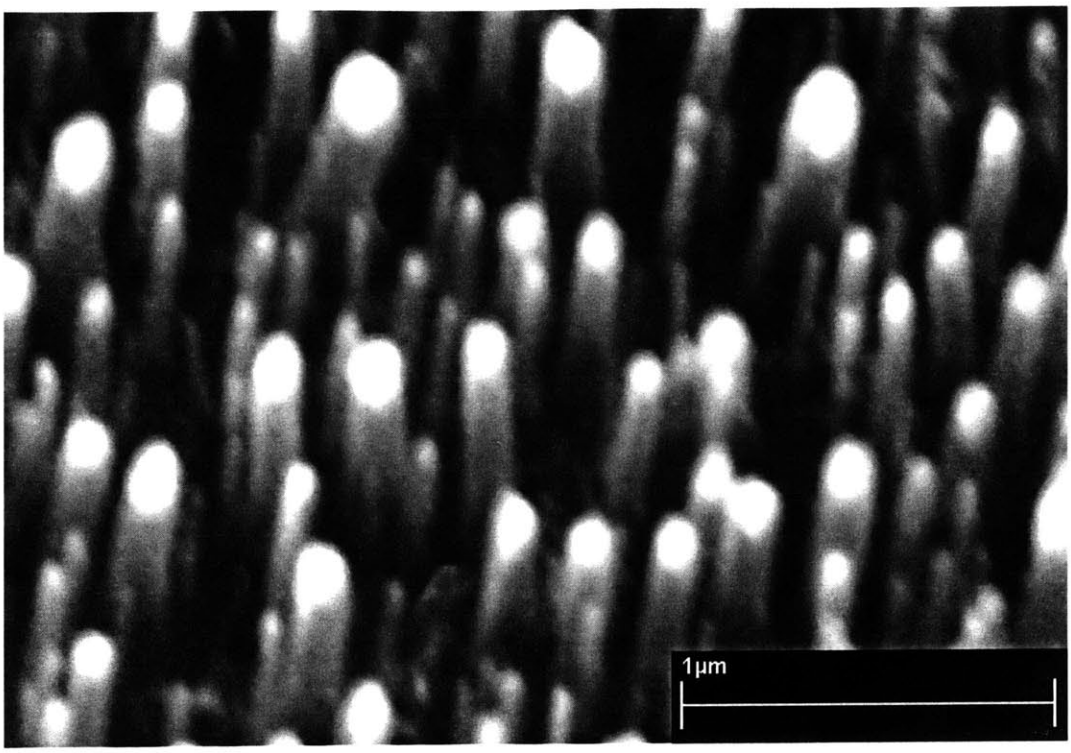

Figure B-1(a)

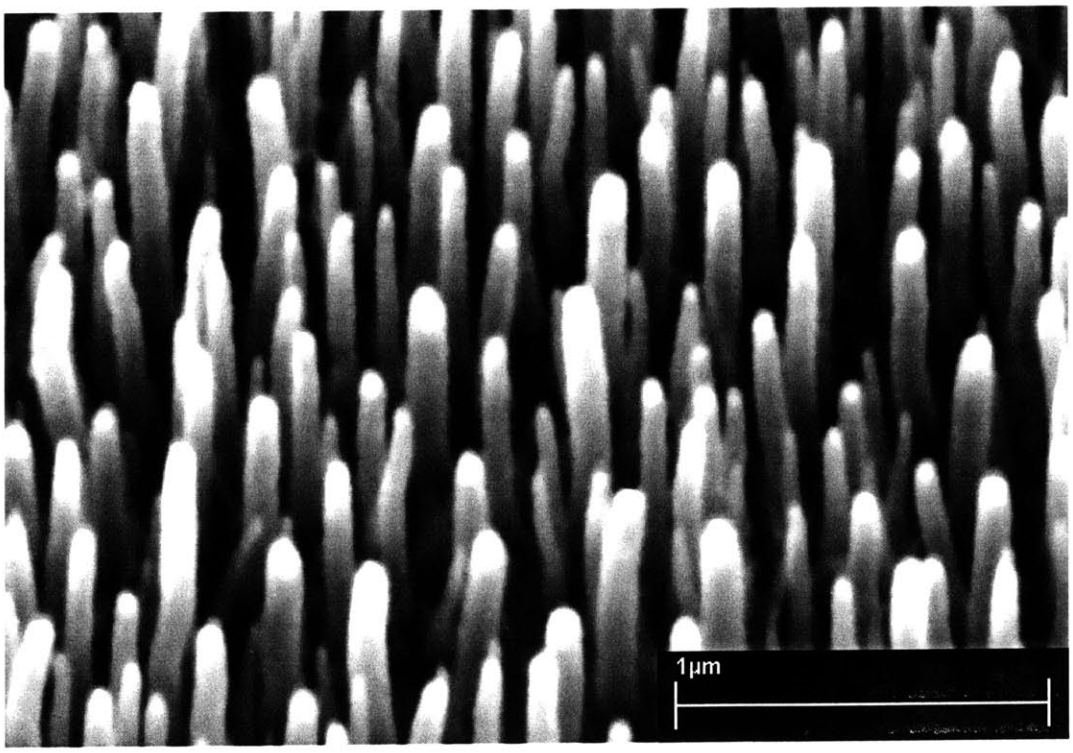

Figure B-1(b)

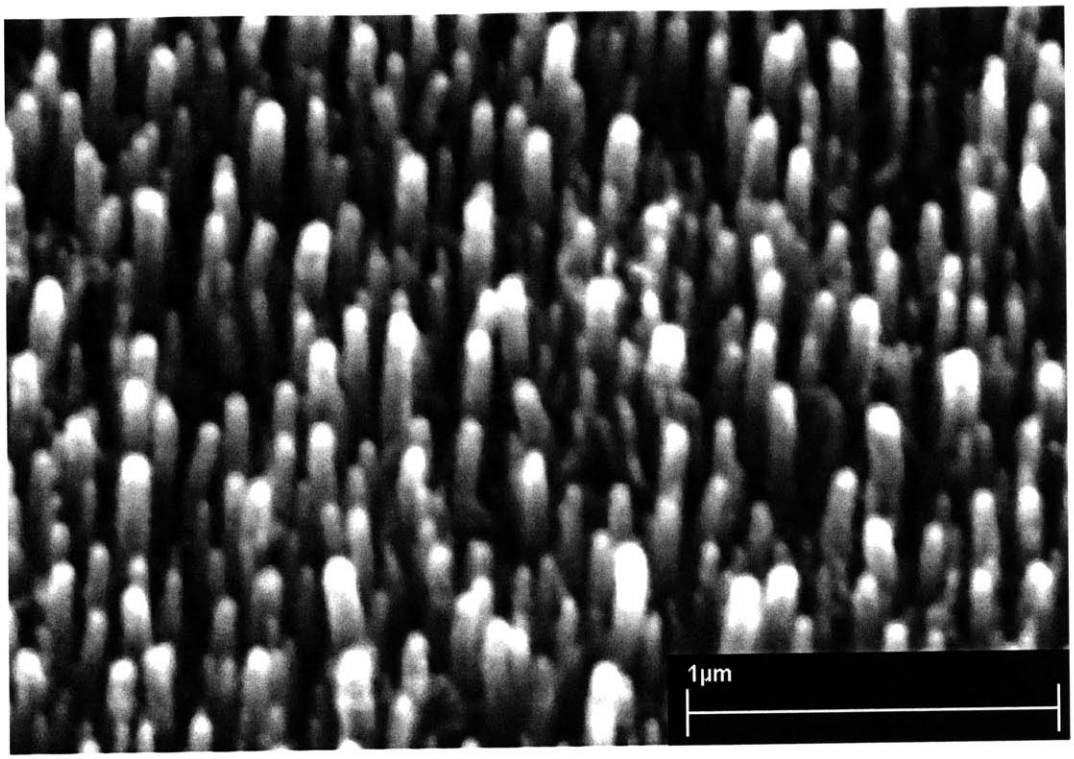

Figure B-1(c)

Figure B-1. Vertically aligned carbon nanotubes: (a) Sample A; (b) Sample B; (c) Sample C. The samples are tilted by 25° to reveal the forest-like landscapes.

Table. 1 Dimensions of the three VACNT samples.

Sample	Outer diameter		Length		Areal Density	
	Average $\overline{D}_o(nm)$	Deviation $\sigma_{D_o}(nm)$	Average $L(nm)$	Deviation $\sigma_L(nm)$	$m(\mu m^{-2})$	Percentage of Area Covered by CNTs (%)
A	104	36	930	123	27	23
B	90	17	1150	160	26	17
C	55	13	570	107	40	10

B.2.2 Nanoindentation

Nanoindentation tests on VACNT forests were conducted at MIT using a Digital Instrument Dimension 3100 SPM (Scanning Probe Microscopy). The nanoindentation cantilever is made of stainless steel and has a diamond tip. The working resonant

frequency is about 55kHz to 60 kHz in tapping mode. Figure B-2 shows a schematic of the geometry of the diamond tip and the cantilever (Digital Instrument, 1998). The diamond tip is a three-sided pyramid, with an apex angle $\phi = 60°$, measured from a face to an edge of the pyramid. According to the specification from the tip supplier, the radius of the diamond tip is less than 25nm.

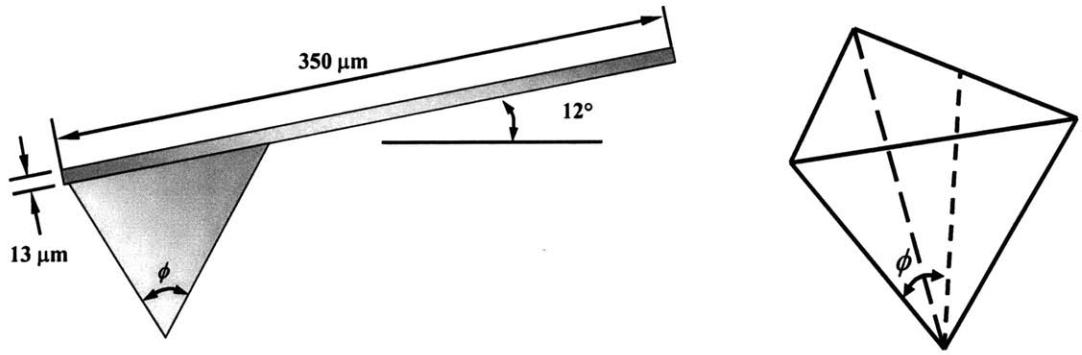

Figure B-2. Schematics of the geometry of the diamond tip of the nanoindentor.

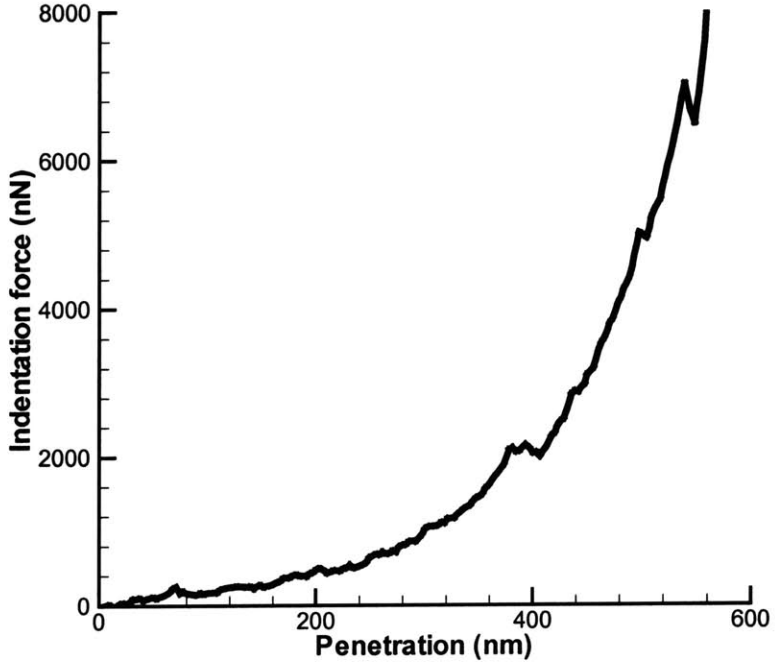

Figure B-3. Typical indentation force-penetration curve (f-p curve) during nanoindentation of VACNT forest.

The standard procedure for nanoindentation tests within an AFM was followed. The tapping mode is first engaged to scan the surface and the area of interest is located. When nanoindentation is initiated, the tip is lifted slightly (typically about 100nm~300nm) above the surface. As the nanoindentation is executed, the tip is driven by the piezo-scanner toward the surface until a pre-set reaction force is reached. The tip is then retracted back to its initial position.

Figure B-3 shows a typical indentation force-penetration curve (f-p curve) for a nanoindentation test on a VACNT forest sample. The indentation force starts from zero until a certain penetration depth is reached, then grows in a nonlinear manner where the slope of the curve increases as the penetration depth increases.

B.3. A Model Based on Beam Theory and Statistics

B.3.1 Physical Process of Nanoindentation on VACNT Forest

When the pyramidal diamond tip indents into the VACNT forest, individual nanotubes are subjected to bending deformation. Figure B-4 illustrates this process with a 2D schematic, where the tip is depicted as a wedge with a semi-apex angle of θ. Only two nanotubes are shown in the Figure B-sequences for the sake of brevity. The lengths of the nanotubes are L. The tip is initially located a distance h_0 above the top surface of the nanotubes (Figure B-4(a)). In Figure B-4, the penetration h is measured from the top level of VACNT forest, and $h+h_0$ gives the total travel distance of the indentor. The value of h_0 will vary from test to test and is determined using the method outlined in Appendix A. As the tip is driven towards the substrate surface, at a certain penetration depth of h_1, a surface of the indentor encounters a nanotube (Figure B-4(b)). This first nanotube then bends as the indentor penetration depth increases; at a certain penetration depth of h_2, the indentor surface encounters a second nanotube (Figure B-4(c)). This process continues until a pre-set maximum force is reached. The tip then retracts back to its original position. The indentation force vs. penetration depth curve (f-p curve) can be predicted using the model presented below.

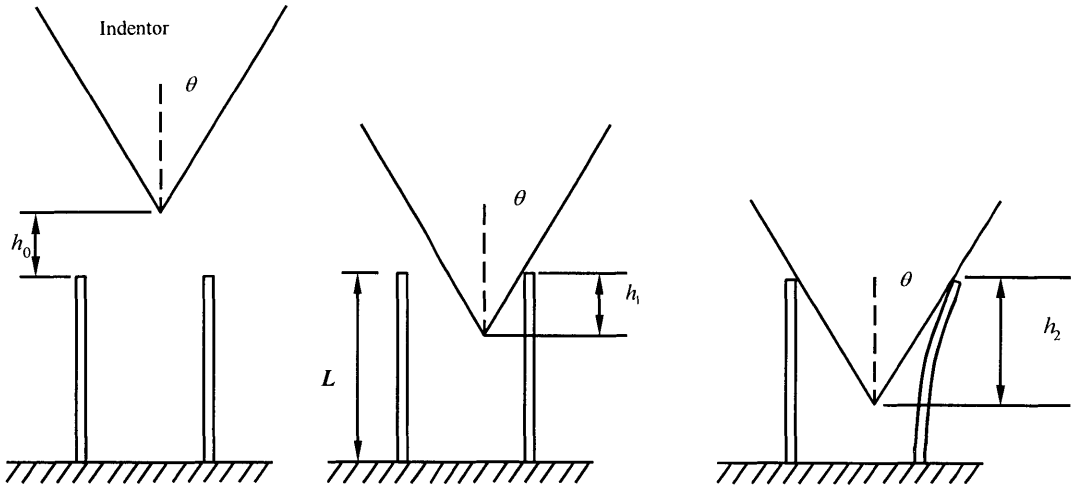

Figure B-4(a) Figure B-4(b) Figure B-4(c)

Figure B-4. Schematics of consecutive contacts of the indentor and nanotubes in a nanoindentation test (a) Before the nanoindentation; (b) The tip encounters one nanotube; (c) The tip encounters two nanotubes.

B.3.2 The Consecutive Contact Model

When a nanotube is in contact with the indentor, (see the free body diagram of Figure B-5), the bending deflection at the tip of the nanotube can be estimated using beam theory and is related to the indentation force P_i and lateral force T_i by (see Appendix B for the formulation):

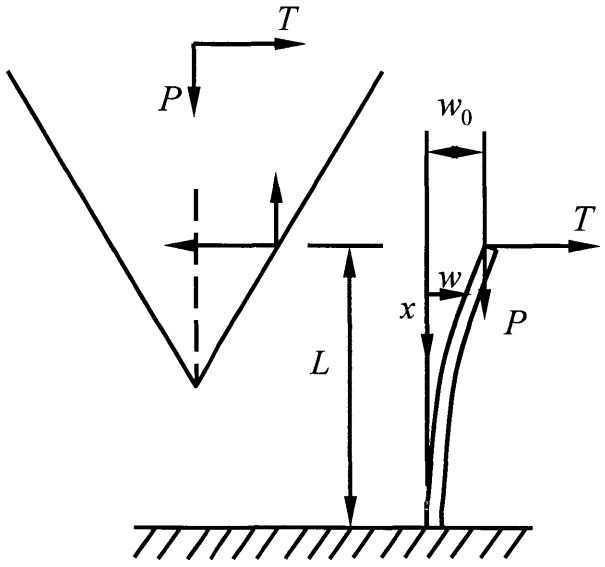

Figure B-5. Free body diagram of a nanotube touched by the indentor.

$$w_0 = \frac{T_i}{P_i}\left(\frac{\tan k_i L}{k_i} - L\right), \tag{B-2}$$

where $k_i = \sqrt{P_i/(EI)_{eff}}$. $(EI)_{eff}$ is the effective bending stiffness of a nanotube in the VACNT forest and is the variable to be determined. The deflection w_0 of the nanotube is related to the geometry of the indentor and the depth of penetration; it is given by:

$$w_0 = (h - h_i)\tan\theta, \tag{B-3}$$

where h is the penetration depth of the indentor, h_i is the penetration at which the ith nanotube is touched by the tip. Assuming any frictional force at the contact surface can be neglected gives

$$\frac{P_i}{T_i} = \tan\theta. \tag{B-4}$$

Then, combining eqn.(B-2), (B-3), and (B-4), a nonlinear relationship between penetration depth h and indentation force P_i for a single nanotube is obtained

$$h = h_i + \frac{1}{(\tan\theta)^2}\left(\frac{\tan k_i L}{k_i} - L\right), \quad k_i = \sqrt{P_i/(EI)_{eff}}\ . \tag{B-5}$$

For the case where n nanotubes are in contact with the tip, the total indentation force P is given by

$$P = \sum_{i=1}^{n} \alpha_i P_i\ , \tag{B-6}$$

where $\alpha_i = 0$ when $h \le h_i$, and $\alpha_i = 1$, when $h > h_i$. The parameters α_i and h_i can be determined through geometrical calculations.

As illustrated in Figure B-4, the value of h_i for an individual nanotube depends on the position of the indentor relative to the nanotube. Nevertheless, for a large number of indentation tests, the average value $\bar{h}_i$ for the ith contact can be calculated using statistical information about the VACNT. The diamond tip is a three-sided pyramid with an apex angle of 60° measured from a face to an edge of the pyramid. At a depth h, the area enclosing the cross-section of the indentor and a nanotube with diameter D_o (Figure B-6) is given by

$$A = 0.813h^2 + 4.110D_o h + 3.141D_o^2 \quad (\mu m^2) \tag{B-7}$$

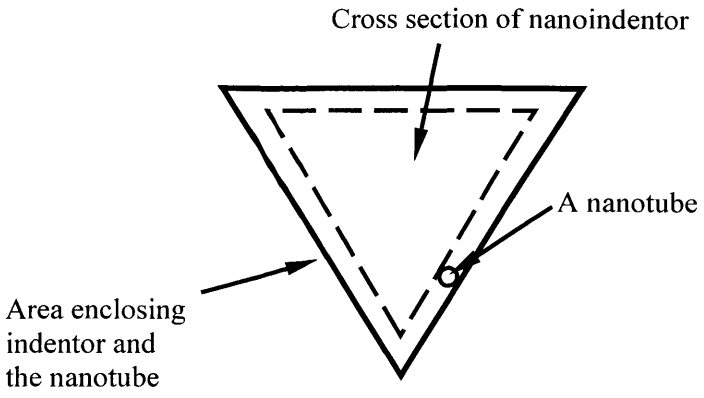

Figure B-6. Area enclosing the cross-sectional area of the indentor and a nanotube with diameter D_o.

The nanotube areal density is denoted by m nanotubes per μm^2. Therefore, the average number i of nanotubes in contact with the indentor at a given depth $\bar{h}_i$ is given by

$$i = Am. \tag{B-8}$$

The effective bending stiffness $(EI)_{eff}$ is determined by best fitting the average of the f-p curves from tests with theoretical predictions using eqn.(B-5)~(B-7), where $(EI)_{eff}$ and h_0 are variables. The elastic modulus of the walls of a CNT and the effective bending modulus of the MWCNT can then be determined from $(EI)_{eff}$ and the geometry of the MWCNTs, as will be described later.

B.3.3 Example

We now consider the indentation of an example VACNT forest with nanotube diameter of $80nm$, length of $1100nm$, areal density $m = 5\ tubes/\mu m^2$, and effective bending stiffness $(EI)_{eff} = 2.1N(nm)^2$. Nanotubes are randomly distributed over the substrate. Figure B-7 presents the average indentation force vs penetration curve that would be measured for the nanoindentation tests and shows the force contributions from the successive interactions between the indentor and individual nanotubes.

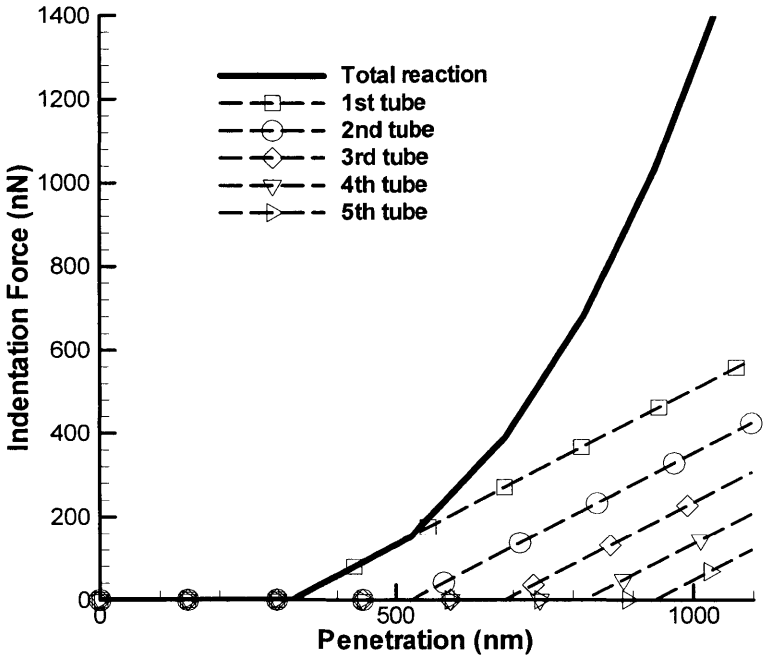

Figure B-7. Superposition of interactions between the indentor and nanotubes encountered by the indentor during nanoindentation gives the total penetration resistance. The thick line is the total resistance. The thin lines are the resistance forces from individual nanotubes.

The f-p curve in Figure B-7 is also a representative curve and would vary depending upon the particular location of the indentation. In addition, there is typically a range in geometric features (diameter and length) of nanotubes in a VACNT forest. A statistically representative model can be achieved by generating a VACNT array, where positions, diameters, and lengths of nanotubes are varied in a statistical manner. Then, several indentations on such a VACNT are simulated and averaged to determine the indentation vs penetration curve (Note that several curves are also experimentally measured and averaged). For the purpose of comparison and discussion, the prediction using average geometrical parameters will be denoted as the representative average simulation (RAS), while the simulations using random distributions of geometrical parameters will be referred to as statistical simulations.

B.3.4 Parametric Studies: Sensitivities of Penetration Resistance to Geometrical

Parameters of VACNTs.

Using the model of nanoindentation proposed above, the sensitivity of the indentation resistance curve to various geometrical parameters is examined, including the effects of indentation locations, spatial distribution of the CNTs, distribution in the diameter and length of the CNTs.

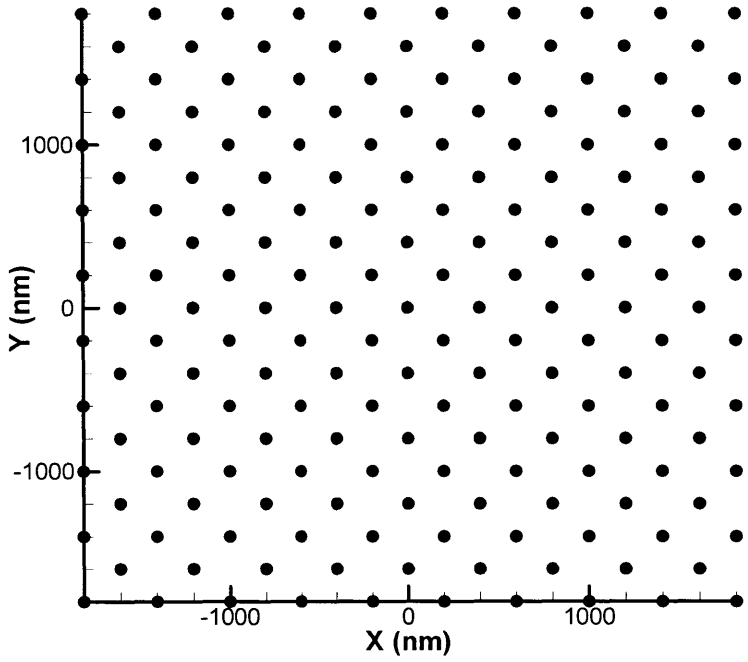

Figure B-8. A two dimensional F.C.C. pattern of nanotubes.

As discussed above, an individual f-p curve depends on the location where the indentor penetrates into the VACNT forest. To further illustrate this effect, a two dimensional FCC (Face Centered Cube) spatial distribution of nanotube positions is created with an areal density of $m = 12\ tubes/\mu m^2$ (Figure B-8). The diameter and length of nanotubes are $80nm$ and $1100nm$, respectively, and are taken to be identical for all nanotubes. $(EI)_{eff}$ is taken to be $2.1N(nm)^2$. Six nanoindentation tests are conducted numerically (Case1), with indentation positions chosen deliberately (Figure B-9(a)).

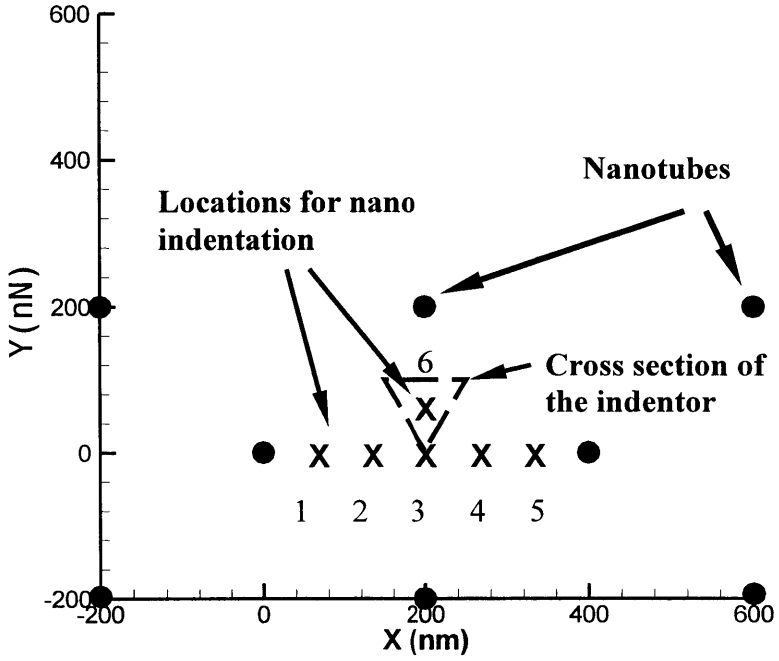

Figure B-9(a)

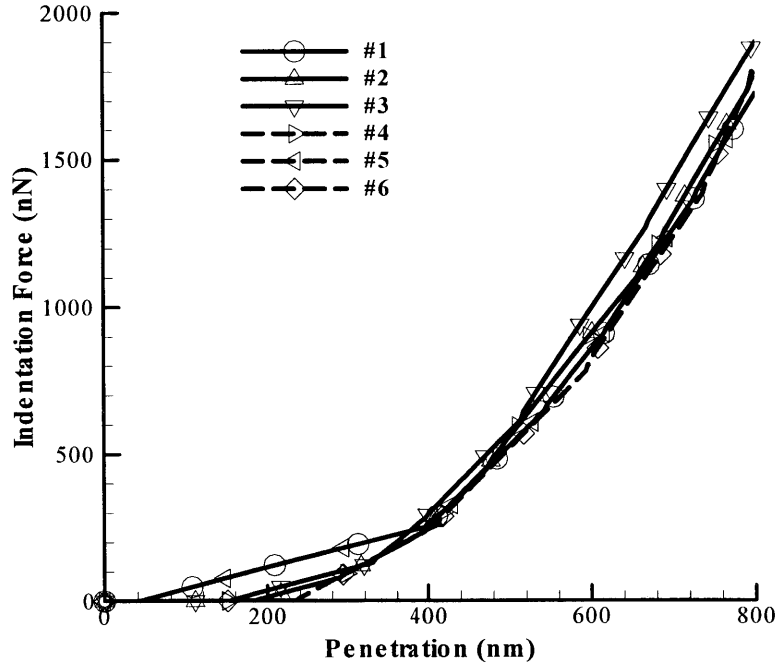

Figure B-9(b)

Figure B-9. Case 1: nanoindentations on a two dimensional F.C.C. patterned VACNT forest, (a) locations of nanoindentations; (b) f-p curves.

The f-p curves (Figure B-9(b)) for the indentations at positions 1 and 5, and 2 and 4, are identical, respectively, due to symmetry. The interaction between nanotubes and the indentor occurs first for the indentations at positions 1 and 5. Position 6 is deliberately chosen so that the indentation at this point encounters two nanotubes simultaneously at the first touch. Therefore, the initial slope of the indentation force-penetration curve for position 6 is twice that of other curves. It is also noted that the chosen indentation positions capture the overall variations in f-p curves. Indeed, f-p curves from numerical nanoindentation simulations with randomly chosen indentation positions showed no significant variation from those of Figure B-9(b).

To study the dependence of the indentation resistance of a VACNT forest on the distribution of nanotubes, the positions of nanotubes are allowed to vary randomly (Figure B-10(a)) on the substrate (Case 2), while areal density is retained to be about $12\ tubes/\mu m^2$. The length and diameter are taken to be the same values as those in the above study. 20 nanoindentations at randomly chosen positions are conducted, and Figure B-10(b) shows the f-p curves from the first 6 nanoindentations for the sake of brevity. As expected, given the random distribution of nanotubes on the substrate, the indentation force-penetration curves show greater variation compared to the curves from nanoindentation on a regular FCC patterned nanotube forest. When nanotubes form a regular pattern, there is a limited variation in indentation locations relative to neighboring nanotubes and thus a limited variation in the number of CNTs that will be encountered as a function of penetration depth. In contrast, if nanotubes are randomly distributed, the occurrence of consecutive contacts is unpredictable and highly varied, especially for VACNT forests of low areal density. As the areal density increases, such variation is reduced.

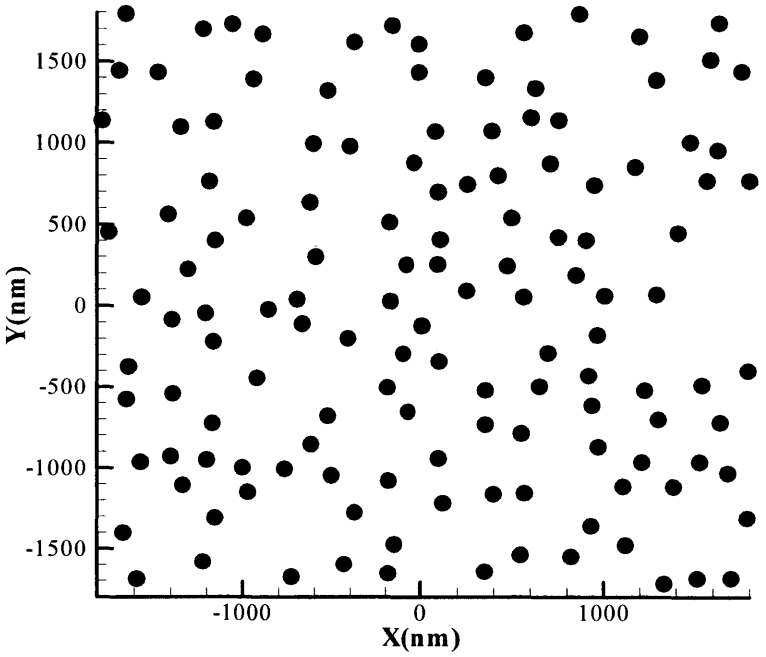

Figure B-10(a)

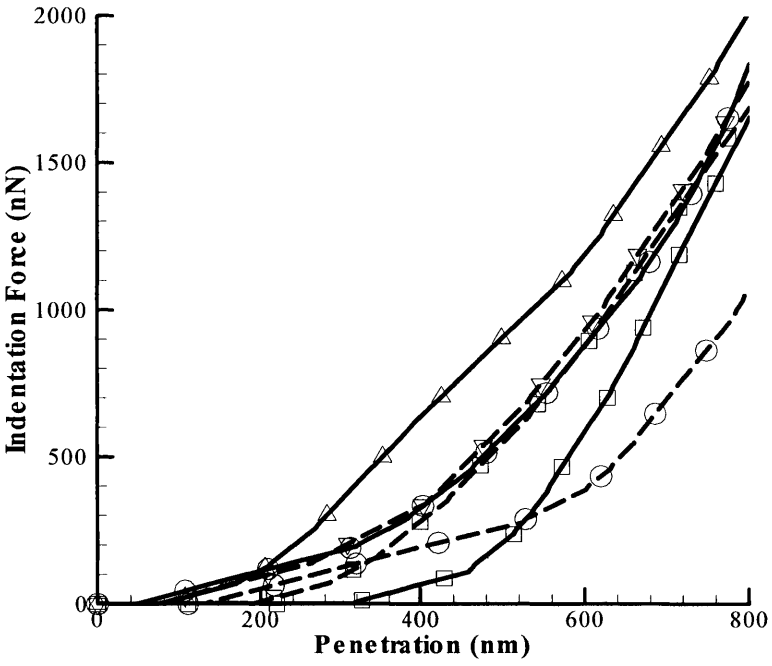

Figure B-10(b)

Figure B-10. Case 2: random nanoindentations on a VACNT forest where nanotubes are randomly distributed, (a) positions of nanotubes; (b) f-p curves.

Figure B-11 shows the effect of a distribution in lengths on the f-p curves of a VACNT forest (Case 3). The nanotubes are spatially arranged in a two dimensional FCC pattern (Figure B-8). All nanotubes have identical diameter of 80nm, but a Gaussian distribution in lengths with an average length of 1100nm and standard deviation of 20%. Compared with Figure B-9(b), where the lengths of nanotubes are fixed, the variation in length results in a significant scattering in the f-p curves.

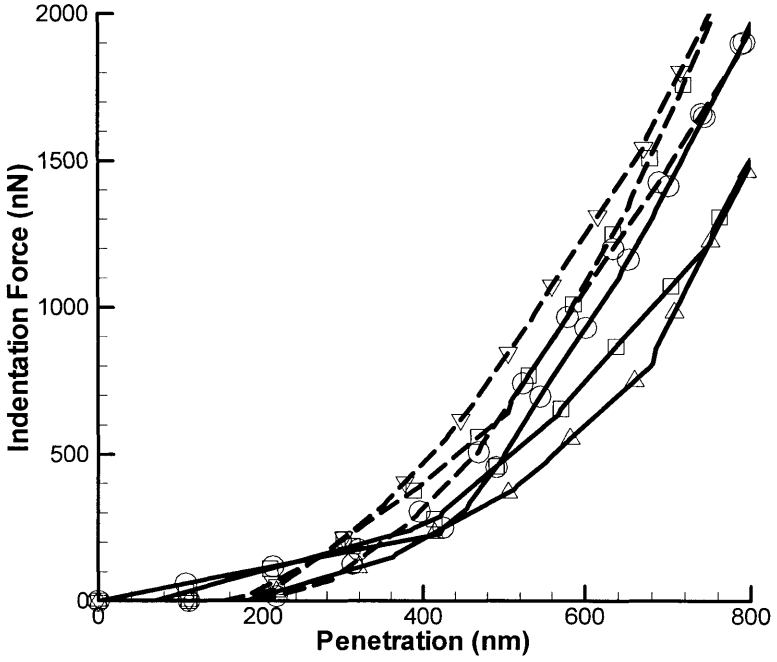

Figure B-11. Case 3: random nanoindentations on a VACNT forest where the nanotubes are distributed following a two dimensional F.C.C. pattern, and all the nanotubes have identical diameter of 80nm, but average length of 1100nm with deviation of 20%.

Figure B-12 shows the effect of a distribution in nanotube diameter on the nanoindentation of a VACNT forest (Case 4). The nanotubes are spatially arranged in a two dimensional FCC pattern (Figure B-8). All nanotubes have identical length of 1100nm, but a Gaussian distribution in diameter with an average diameter of 80nm and standard deviation of 20%. The effective bending stiffness for each nanotube is scaled through

$$(EI)_{eff,j} = (EI)_{eff}\left(\frac{(D_o)_j}{\overline{D}_o}\right)^4, \qquad \text{(B-9)}$$

where $(EI)_{eff} = 2.1N(nm)^2$. The variation in diameter is seen to give a wider range in f-p curves because of the fact that the standard deviation of 20% in D_o generates a higher deviation in $(EI)_{eff}$ according to eqn. (B-9).

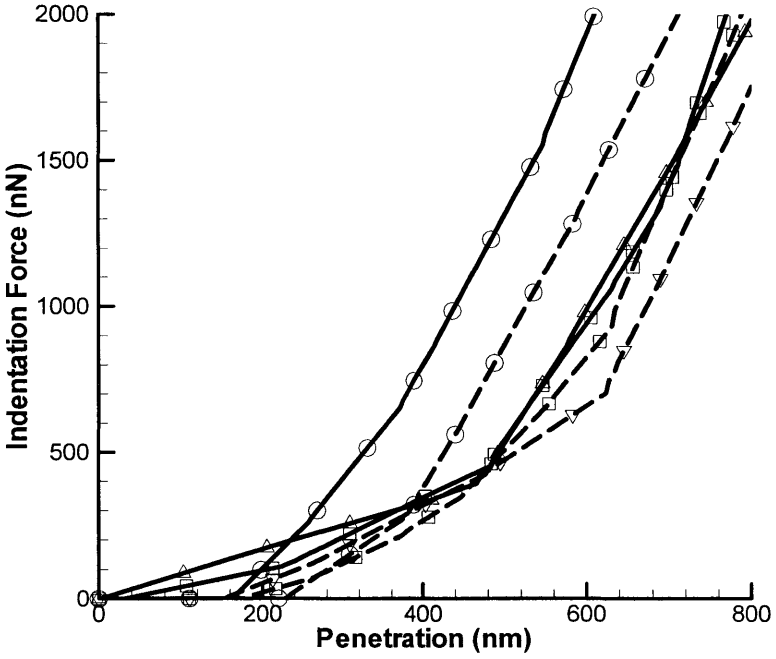

Figure B-12. Case 4: nanoindentations on a VACNT forest where the nanotubes are distributed following a two dimensional F.C.C. pattern, and all the nanotubes have identical length of 1100nm, but average diameter of 80nm with deviation of 20%.

Figure B-13 shows the effect of a distribution in spatial positions, lengths and diameters on the nanoindentation of a VACNT forest (Case 5). The nanotubes are randomly distributed, and have a Gaussian distribution in length and diameter with average length of 1100nm and average diameter of 80nm, and standard deviation of 20% for both. As expected, the indentation force-penetration curves are significantly scattered.

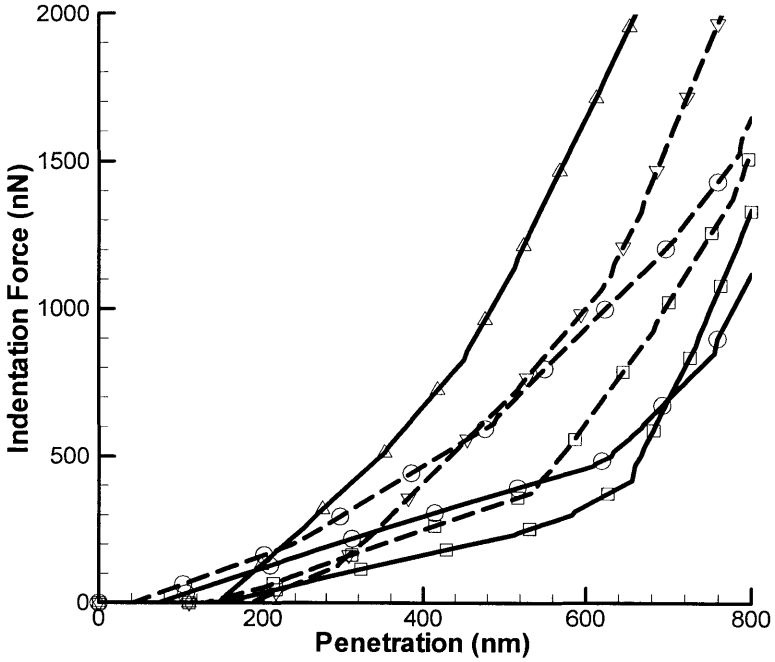

Figure B-13. Case 5: random nanoindentations on a VACNT forest where the nanotubes are randomly distributed, and have average length of 1100nm with deviation of 20%, average diameter of 80nm with deviation of 20%.

Figure B-14(a) shows the average f-p curves over 6 simulations for Case 1, and over 20 simulations for Case 2 to Case 5. Although large scatters in f-p curves for Case 2, 3 and 5 are observed, the average curves over 20 simulations converge to the representative average simulation (RAS). The only exception is Case 4, where the average f-p curve shows a stiffer response than those predicted in other cases.

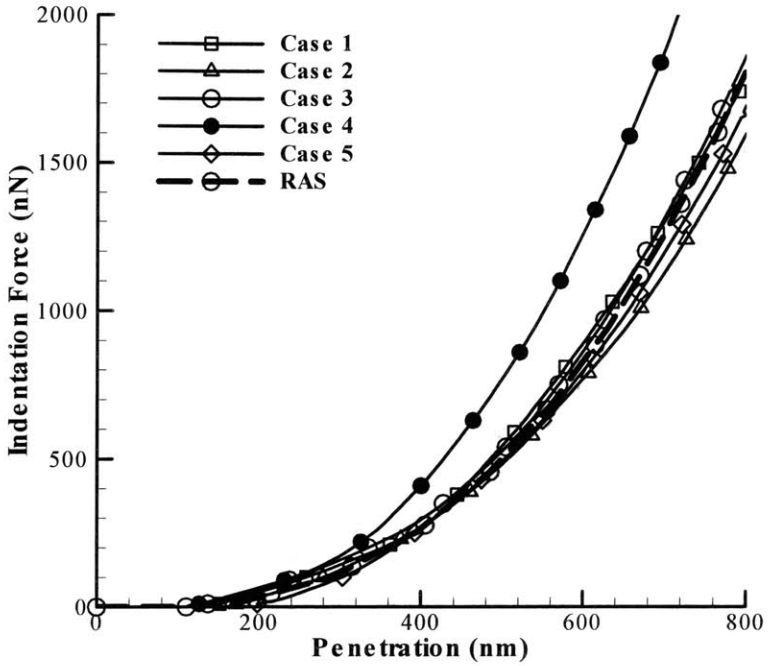

Figure B-14(a)

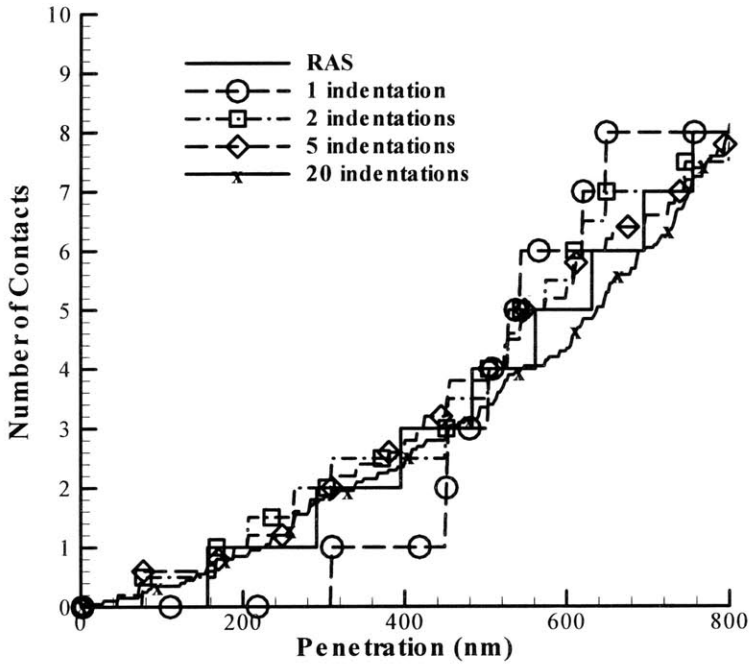

Figure B-14(b)

Figure B-14. (a) Average f-p curves for Case 1-5; (b) Number of contacts vs. penetration depth curves from Case 2.

It is also noticed that the average f-p curves are smooth whereas the RAS curve has distinct changes in the slope. Figure B-14(b), depicting the average number of contacts vs. penetration depth curve for Case 2 and for the RAS, clearly demonstrates how the number of the contacts changes from a jump function of penetration depth for an individual indentation to a continuous function over the average of 20 indentations.

The parametric study has demonstrated that a statistically representative f-p indentation resistance curve can be obtained. Averaging the f-p curves obtained from indentation at several locations provides a representation of the behavior of the VACNT even for a relatively sparse array with a 20% variation in CNT geometry. Therefore, experiments should be conducted at several locations and averaged in order to best represent the VACNT behavior; comparison with simulations can then be used to identify CNT properties.

B.4. Results and Discussions

B.4.1 VACNT Indentation

Nanoindentation tests were conducted on three VACNT forest samples, whose dimensions are listed in Table 1. In the experiment on each sample, more than 60 nanoindentations were executed at different locations, each of which was at least 800nm away from another. The first 20 f-p curves for each sample are shown in Figure B-15 (a), (b) and (c), while the average curve for each VACNT is calculated over all experiments. Also note that repeated indentations at some random locations showed good repeatability when the indentation force is less than about 8000nN, demonstrating both the elastic nature of the indentation and the repeatability of this measurement.

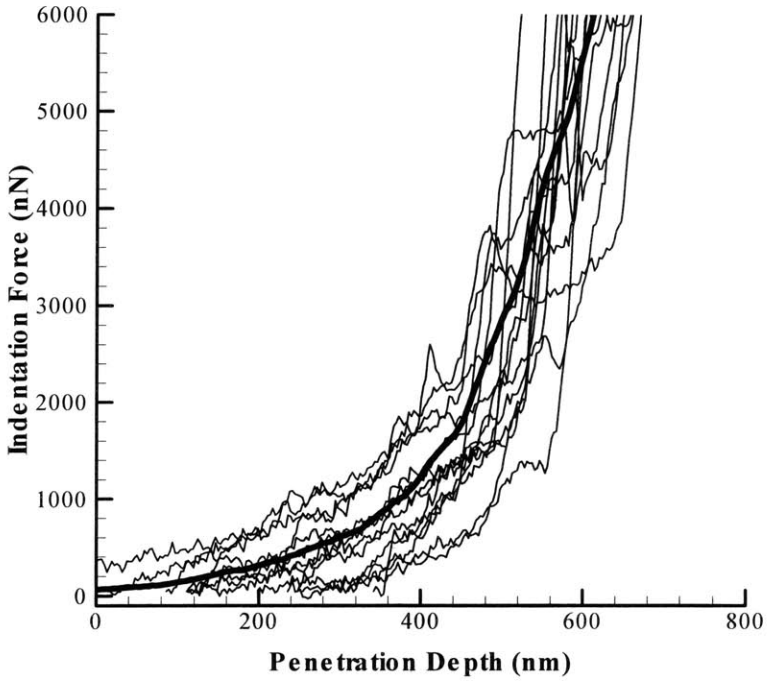

Figure B-15(a)

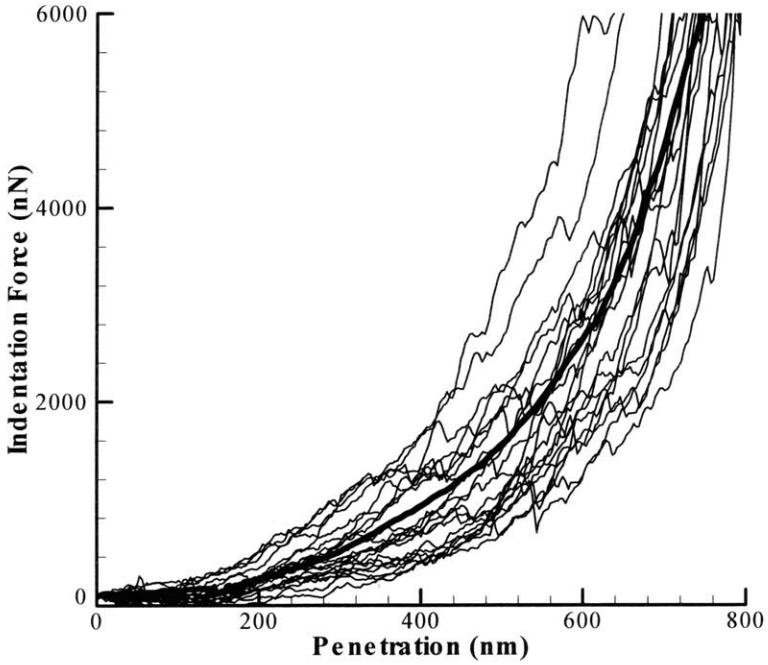

Figure B-15(b)

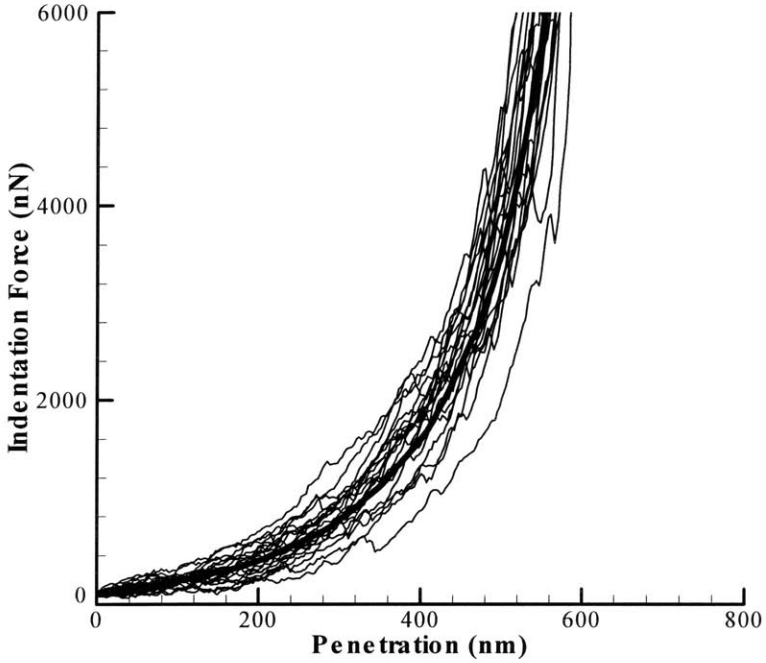

Figure B-15(c)

Figure B-15. Indentation force-penetration curves for (a) Sample A; (b) Sample B; and (c) Sample C; The thin solid lines are experimental curves; the thick solid lines are averaged curves.

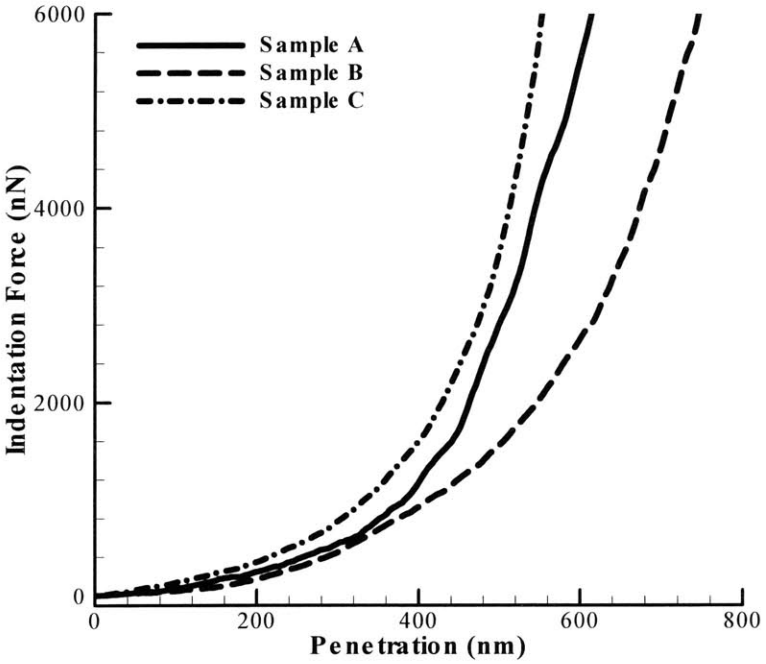

Figure B-16. Average f-p curves for the three samples from experiments.

Figure B-15 shows the f-p curves for 20 nanoindentation tests on each of the three samples, where the thick solid lines give the average experimental f-p curves and the thin lines give the f-p curves from the first 20 tests. Figure B-16 compares the average f-p curves from the three samples. As discussed before, since Sample C has the highest nanotube areal density, the f-p curves from Sample C show less scatter than those from Sample A and Sample B. Since Sample C has the largest areal density and smallest length, it has the highest indentation resistance. Although Sample A and Sample B have nearly the same areal density, Sample A has a larger average diameter and a smaller average length, resulting in a stiffer penetration resistance than that from sample B.

The theoretical models, together with numerical simulations, are now used to determine the effective bending stiffness $(EI)_{eff}$ of the nanotubes in each sample. In the model, both h_0 and $(EI)_{eff}$ are variables for optimization to minimize the deviation of the average of statistical simulations from the average of experimental results. Appendix A discusses the details on how to obtain the parameters $(EI)_{eff}$ and h_0.

Figure B-17 compares the average curves from statistical simulations and from experiments. Figure B-18 shows the f-p curves from 20 simulated nanoindentations on the three samples, where the areal density, length, and diameters of nanotubes are generated statistically, following the data in Table 1. Table 2 lists the predicted effective bending stiffness for the three samples.

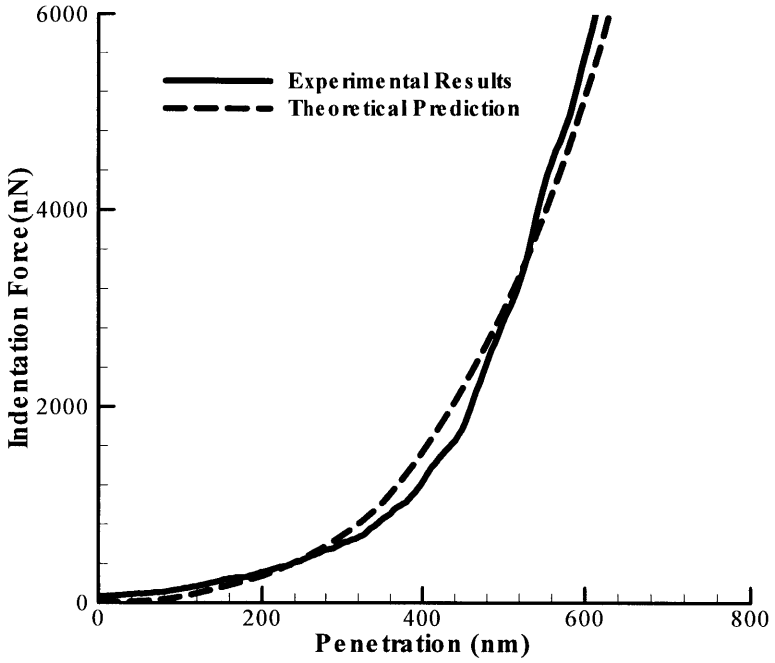

Figure B-17(a)

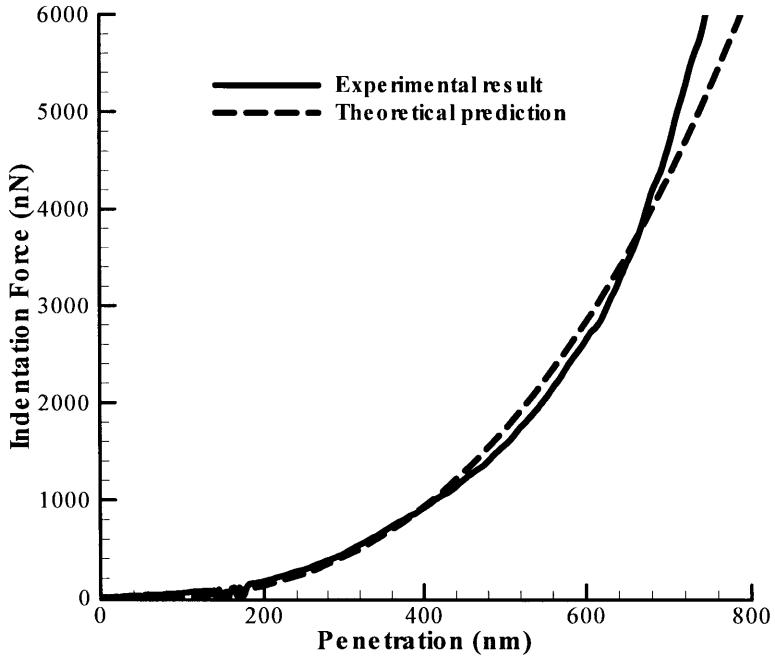

Figure B-17(b)

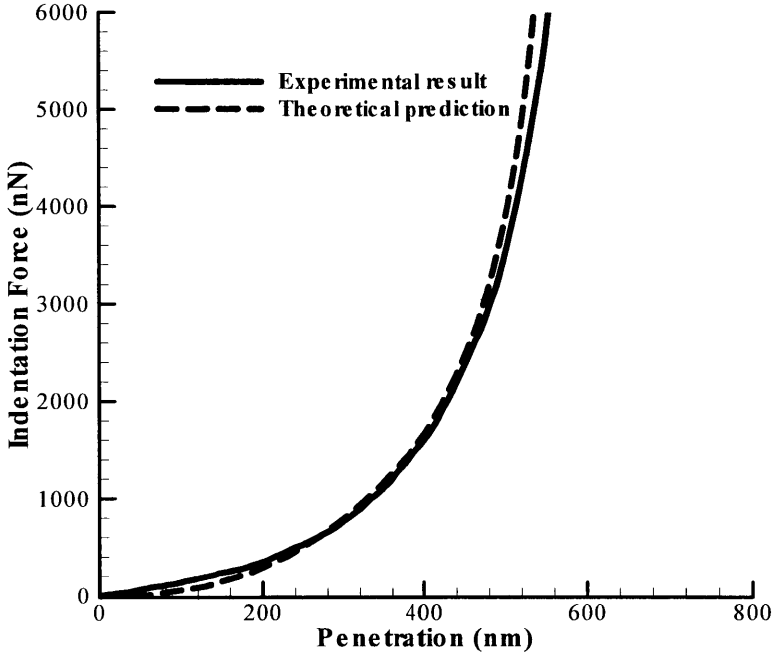

Figure B-17(c)

Figure B-17. The average curves from theoretical predictions and from experiments for (a) Sample A; (b) Sample B; (c) Sample C.

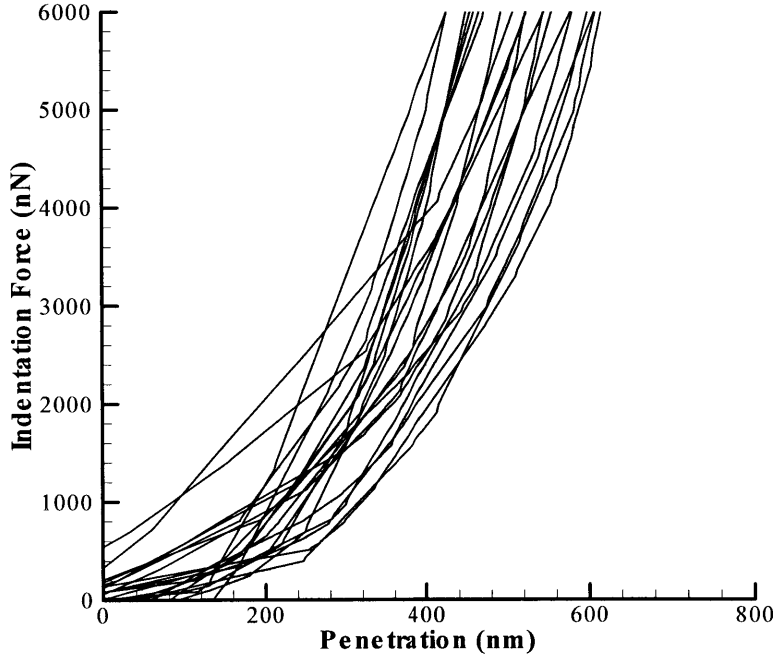

Figure B-18(a)

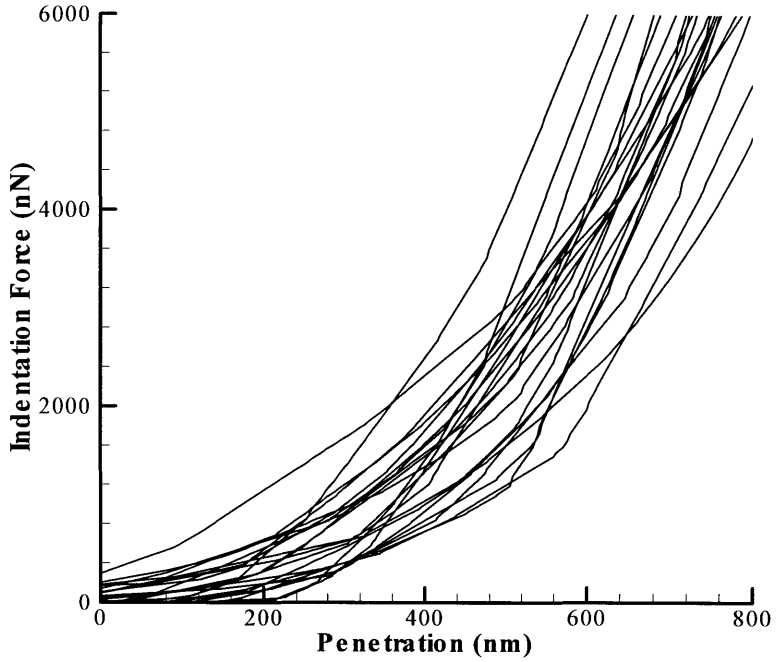

Figure B-18(b)

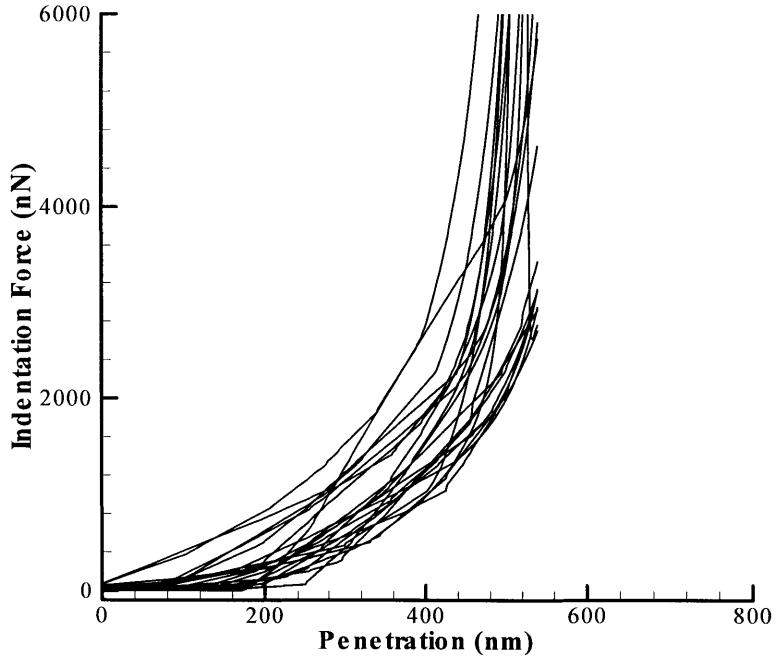

Figure B-18(c)

Figure B-18. Indentation force-penetration curves from 20 simulated nanoindentations on the three samples, where the areal density, length, and diameters of nanotubes follow the statistical data in Table 1. (a) Sample A; (b) Sample B; (c) Sample C.

Table 2. Predictions of effective bending moduli for the three VACNT samples.

VACNT sample	$(EI)_{eff}\ (N(nm)^2)$
A	5.2
B	4.0
C	0.51

B.4.2 Determination of Bending and Axial Modulus of Constituent MWCNTs

The elastic modulus of the constituent nanotubes is now reduced from the measured $(EI)_{eff}$ using various approaches.

An effective bending modulus E_t^b is estimated following the technique used by other investigators in experimental studies on isolated nanotubes. The effective bending modulus of the MWCNT, E_t^b, is calculated by dividing the measured effective bending stiffness, $(EI)_{eff}$, by an effective moment of inertia, I_{eff}, which is assumed to be given by the outer diameter of the MWCNT D_o,

$$E_t^b = \frac{(EI)_{eff}}{I_{eff}} = \frac{64(EI)_{eff}}{\pi D_o^4}. \qquad \text{(B-10)}$$

The effective bending modulus for samples A, B, and C are calculated to be $0.91TPa$, $1.24TPa$, and $1.14TPa$, respectively. These values are in good agreement with the values obtained by Wong et al. (1997) and by Salvetat et al. (1999). However, note that by using $(EI)_{eff} = E_t^b \times \pi D_o^4 / 64$, important details of the nanotube structure are neglected.

To further verify the new method and investigate mechanical properties of nanotube structure, the multi-walled nature of the structure is considered in interpreting $(EI)_{eff}$. A MWCNT consists of concentric walls of effective wall thickness t and inter-wall spacing s, as shown in Figure B-19. The walls maintain an inter-wall spacing of s due to normal van der Waals interaction. This separation is sustained during bending as observed in TEM (e.g., Poncharal et al., 1999). The shear interaction/stiffness between walls is

observed to be very low (Cumings and Zettl, 2000; Yu et al., 2000). Indeed, this has led to proposals that CNTs be used as slider bearings (Cumings and Zettl, 2000; Kolmogorov and Crespi, 2000). These wall to wall interactions suggest that the effective bending stiffness $(EI)_{eff}$ of the MWCNT can be well approximated through the sum of the bending stiffness of each tube. This summation approach has also been proposed by Govindjee and Sackman (1999).

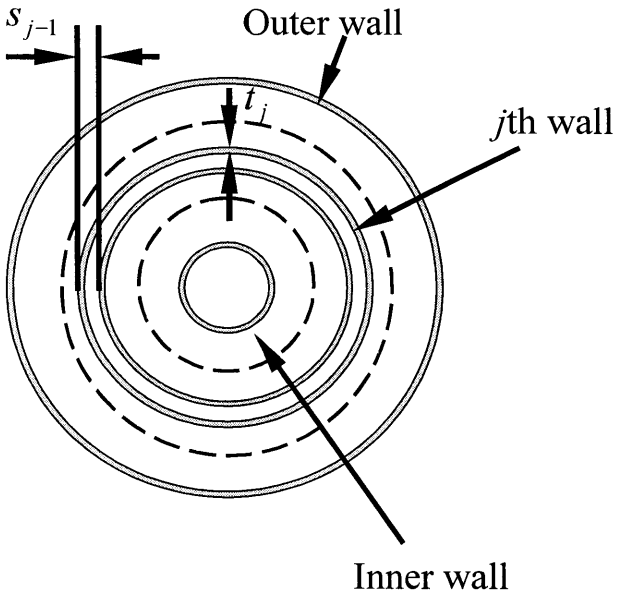

Figure B-19. Schematic of the cross section of the multiwalled structure of MWCNTs.

For the jth wall, the moment of inertia I_j and cross sectional area A_j are given by

$$I_j = \frac{\pi}{64}\left[D_j^4 - \left(D_j^4 - 2t\right)^4\right], \tag{B-11a}$$

$$A_j = \frac{\pi}{4}\left[D_j^2 - \left(D_j - 2t\right)^2\right], \tag{B-11b}$$

where D_j is the outer diameter for the jth tube. The outer diameter of the (j-1)th wall is

$$D_{j-1} = D_j - 2s. \tag{B-12}$$

The total bending stiffness $(EI)_{eff}$ and axial modulus $(EA)_{eff}$ of a MWCNT are then given by

$$(EI)_{eff} = \sum_{j=1}^{N} E_t^w I_j = E_t^w \sum_{j=1}^{N} I_j \ , \tag{B-13a}$$

$$(EA)_{eff} = \sum_{j=1}^{N} E_t^w A_j = E_t^w \sum_{j=1}^{N} A_j \ , \qquad \text{(B-13b)}$$

where N is the number of walls, and E_t^w is the modulus of a tube wall and is taken to be identical for all walls in a CNT. Since $(EI)_{eff}$ is the bending stiffness measured in the test, the tube wall modulus E_t^w is obtained as:

$$E_t^w = \frac{(EI)_{eff}}{\sum_{j=1}^{N} I_j}. \qquad \text{(B-14a)}$$

If the effective axial stiffness $(EA)_{eff}$ of a nanotube is the summation of the axial stiffness of the N walls in the nanotube, then the effective axial Young's modulus E_t^a of a nanotube can be obtained as

$$E_t^a = \frac{E_t^w \sum_{j}^{N} A_j}{A_t}, \qquad \text{(B-14b)}$$

where A_t is the total cross sectional area, $A_t = \pi D_o^2 / 4$.

The inter-wall spacing, s, is set by the equilibrium spacing of the walls as determined by the van der Waals interactions, and values have been reported ranging from $0.34nm$ to $0.39nm$ (Saito et al., 1993; Sun et al., 1996; Kiang et al., 1998); here we take $s = 0.344nm$. The effective mechanical wall thickness has been determined by investigators by comparing atomistic level simulations and shell theory, e.g. Yakobson et al. (1996). Investigators suggest that the effective mechanical thickness of a nanotube wall range from $t \approx 0.066nm$ to $0.075nm$ (see Pantano et al., 2003). The inner diameter of various VACNT structures is typically less than $10nm$, while the exact value of inner diameter should be determined from HRTEM. Nevertheless, from eqn.(B-11(a)), the inner tubes of diameter less than $10nm$ contribute minutely to the total moment of inertia. Therefore, $D_i \approx 6nm$ is used in current analysis. Using $D_i = 6nm$, $t = 0.075nm$, and $s = 0.344nm$, we obtain the wall modulus, E_t^w, the tube axial modulus, E_t^a, and the average number of walls, N for each sample. Results are given in Table 3. These predictions are in good agreement with other theoretical and experimental reports, and

verifies the efficacy of the new method. For example, when using a mechanical thickness of $0.075nm$, atomistic simulations give a wall modulus of $4.8TPa$ (see Pantano et al., 2003), which agrees well with predicted values of $4.14TP$ to $5.61TPa$ in Table 3.

Table 3. E_t^b, E_t^w, E_t^a, and N for the three samples.

Sample	$(EI)_{eff}\left(N(nm)^2\right)$	$E_t^b(TPa)$	$E_t^w(TPa)$	$E_t^a(TPa)$	N
A	5.2	0.91	4.14	0.90	143
B	4.0	1.24	5.61	1.23	123
C	0.51	1.14	5.11	1.11	72

B5. Conclusions

Nanoindentation tests have been used to determine the mechanical properties of vertically aligned carbon nanotube (VACNT) forests and constituent carbon nanotubes. A study of the physical process of nanoindentation on VACNT forests reveals a process where nanotubes are consecutively bent during the penetration of the indentor. Unlike nanoindentation on homogenous materials, such as thin film coatings, where the elastic modulus and yield stress of coating materials are typically obtained, the resistance of VACNT forests to penetration is a result of superposition of the bending responses of nanotubes as the indentor successively encounters tubes in the forest. Nanoindentation tests, together with a micro-mechanical model using beam theory, were used to determine the effective bending stiffness $(EI)_{eff}$ of the MWCNT of the VACNTs studied. A simple method which accounts for the multiwalled structure of multiwall nanotubes was used to interpret the obtained $(EI)_{eff}$ in terms of the modulus of a nanotube wall E_t^w, and the effective axial modulus of a nanotube E_t^a.

Nanoindentation tests on three VACNT forest samples revealed the effective bending modulus of the MWCNTs to be $E_t^b = 0.91TPa \sim 1.24TPa$, effective axial modulus to be

$E_t^a = 0.9TPa \sim 1.23TPa$, and the wall modulus to be $E_t^w = 4.14TPa \sim 5.61TPa$, using a mechanical wall thickness of $0.075nm$. The good agreement of these predictions with other theoretical and experimental results supports the effectiveness of the new method.

The use of nanoindentation together with the proposed micromechanical model of the successive bending of nanotubes as the indentor penetrates into the forest is shown to provide a relatively easy measure of the bending stiffness, wall modulus and axial modulus of the constituent nanotubes. This new technique requires no special treatment of the samples, making it promising to apply this method to a large number of tests to determine the properties of CNTs in a statistical manner, which sometimes is more important than knowing properties for a few isolated nanotubes. The simplicity of the measurement suggests the potential use of this method as a quality control measurement in mass production. This proposed technique has been shown to be effective on VACNTs with random distributions of CNTs and would be even more effective on regularly patterned and more uniform VACNTs, where processes for producing such VACNTs are under investigations by several groups. For highly dense arrays, the model can be extended to account for the van der Waals interactions by monitoring the proximity of neighboring tubes during tube bending in much the same way as the interactions between nanoindentor and nanotubes were determined. The proposed nanoindentation and corresponding reduction of data are also applicable to vertically aligned nanofibers. Indentation of vertically aligned nanofibers is currently being investigated.

Acknowledgement

This research was funded in part by the CMI (Cambridge-MIT Institute) Project of Carbon Nanotube Enabled Materials, and in part by the AFOSR DURINT on Microstructure, Processing and Mechanical Performance of Polymer Nanocomposites (Air Force Contract No. F49620-01-1-0447).

Appendix A: Reducing $(EI)_{eff}$ and h_0

The parameter h_0 can be eliminated by scrutiny of the nanoindentation process using DI Dimension 3100 SPM. In such a nanoindentation, the output from the test is indentation

force vs. piezo-scanner indentation movement (z movement) curve (f-z curve, which can be directly obtained from the raw output, photo detector voltage vs. z movement curve), which is constructed such that the indentation movement is measured backward starting from the point where the maximum indentation force is reached. It is therefore recognized that depending on where the maximum force is reached, the output f-z curve floats along the indentation direction. A force-penetration curve (Figure B-20) can be deduced from the f-z curve. In Figure B-20, we define the interaction distance as measuring the distance between the point where the indentor encounters the first nanotube and the point where the maximum indentation force is reached. Clearly, the penetration depth is distinct from the interaction distance by the amount of $h_0 + h_1$. As the number of tests increases, the difference between the average of interaction distance and the average penetration depths approaches $h_0 + \overline{h_1}$. The benefit of interaction distance is that h_0 falls at the end of interaction distance, making h_0 a trivial parameter.

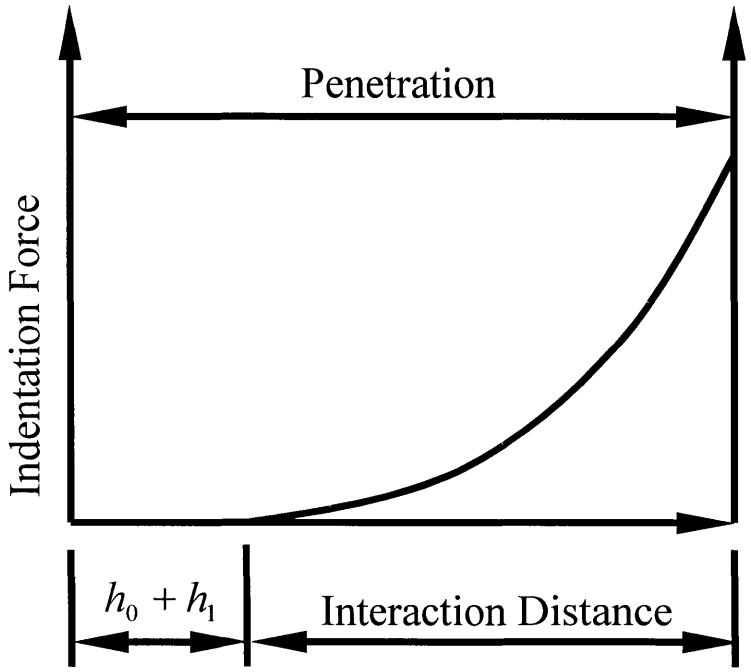

Figure B-20. Penetration and interaction distance.

Taking advantage of this feature, we proposed a method to determine $(EI)_{eff}$. The method requires to reconstruct all f-p curves from experiments and simulations, and starts with choosing a suitable reference indentation force f_0 and a reference position q^0. As

discussed in Appendix B, a small value of f_0 should be used (in this paper, $f_0 = 4000nN$ is used for the three samples). We denote the ith f-p curve as $f_i = f_i(p_i)$, and $f_i(p_i^0) = f_0$. We then shift the ith curve so that $f_i(q^0) = f_0$, which can be obtained simply by a coordinate translation where $q_i = p_i + (q^0 - p_i^0)$. Such a process makes all the curves converge to a point where $f = f_0$ and $q = q^0$. The shifted curves are then averaged. The same process should also apply to curves from statistical simulations. The two averaged curves are compared and the final $(EI)_{eff}$ is determined such that the best agreement between the two averaged curves can be reached.

Appendix B: Bending deformation of a tube

From the free body diagram (Figure B-5), the moment at any point x along the tube is

$$M = -T_i x - P_i(w_0 - w) \tag{B-15}$$

Classical beam theory gives the relationship between moment and curvature (taking deflection and curvature to be related by $\kappa = \frac{d^2w}{dx^2}$) to be

$$(EI)_{eff}\frac{d^2w}{dx^2} = T_i x + P_i(w_0 - w). \tag{B-16}$$

Although the nature of the bonding between nanotubes and substrate is not clear, SEM micrographs taken at the locations where tweezers swept over the surface show crater shape debris on the substrate, implying a strong connection between nanotubes and substrate. Therefore, it is reasonable to assume a clamped boundary condition at the end of the tube, e.g.

$$w\big|_{x=L} = 0 \text{ and } \left.\frac{dw}{dx}\right|_{x=L} = 0. \tag{B-17}$$

Taking $k_i^2 = P_i / (EI)_{eff}$, and $y = w_0 - w$, eqn.(B-16) and eqn.(B-17) can be written as

$$\frac{d^2y}{dx^2} + k_i^2 y = -\frac{T_i x}{(EI)_{eff}}, \tag{B-18}$$

with boundary conditions

$$y\big|_{x=0} = 0 \text{ and } \left.\frac{dy}{dx}\right|_{x=L} = 0. \tag{B-19}$$

The general solution to eqn. (B-18) is

$$y = A\cos k_i x + B\sin k_i x - \frac{T_i}{P_i}x, \tag{B-20}$$

where A and B are constants determined from eqn.(B-19),

$$A = 0, \text{ and } B = \frac{T_i}{P_i k_i \cos k_i L}. \tag{B-21}$$

Therefore,

$$w = w_0 - \frac{T_i}{P_i k \cos k_i L}\sin k_i x + \frac{T_i}{P_i}x. \tag{B-22}$$

Since $w\big|_{x=L} = 0$,

$$w_0 = \frac{T_i}{P_i}\left(\frac{\tan k_i L}{k_i} - L\right), \tag{B-23}$$

and

$$w = \frac{T_i}{P_i k_i \cos k_i L}(\sin k_i L - \sin k_i x) - \frac{T_i}{P_i}(L - x). \tag{B-24}$$

The slope of the nanotube deformation of the tube is $-w'$, and

$$w' = \frac{T_i}{P_i}\left(1 - \frac{\cos k_i x}{\cos k_i L}\right). \tag{B-25}$$

Since the nanotubes are bent by the side surface of the indentor, the slope cannot exceed the slope of the side surface, or

$$-w' < \tan\theta. \tag{B-26}$$

If the inequality (B-26) is violated, the solution to this problem becomes complicated due to the change of the contact condition between the tube and the indentor from a point contact to a line contact. Nevertheless, a simple approximation to the solution can be realized using iterative method. Starting with eqn.(B-25), an effective length L' can be obtained with $-w'\big|_{x=L'} = \tan\theta$. This new L' and previous P_i are then used to calculate new k_i, P_i. This process will continue until inequality (B-26) is satisfied.

The occurrence of violation of inequality (B-26) depends on the nanoindentation location relative to the nanotube and usually is at large penetration depth. It should be noted that as penetration depth increases, the deflection of a tube could be so large that classical beam theory, which is based on small deformation assumption, will deviate from the true solution. The deformation at large penetration will be even more complicated by the increased possibilities of the interactions between nanotubes. Therefore, it is authors' suggestion that using above theory only for penetration depth less than about 70% of the average length of constituent CNTs.

References

Baughman, R.H., Zakhidov, A.A., de Heer, W.A., 2002. Carbon nanotubes – the route toward applications. Science, 297, August, pp787-792.

Chhowalla, M., Teo, K.B.K., Ducati, C., Rupesinghe, N.L., Amaratunga, G.A.J., Ferrari, A.C., Roy, D., Roberston, J., Milne, W.I., 2001. Growth process conditions of vertically aligned carbon nanotubes using plasma enhanced chemical vapor deposition. J. Appl. Phys., 90, pp5308-5317.

Cumings, J., Zettl, A., 2000. Low friction nanoscale linear bearing realized from multiwall carbon nanotubes, Science, 289, pp602-604.

Digital Instrument, 1998. Nanoindentation and nanoscratching with SPMs, for NanoScope version 4.32 software. Support Note No. 225, Rev. F.

Govindjee, S., Sackman, J.L., 1999. On the use of continuum mechanics to estimate the properties of nanotubes. Solid State Comm., 110, pp227-230.

Huang, Z. P., Xu, J.W. , Ren, Z. F., Wang, J. H., Siegal, M. P., Provencio, P. N., 1998. Growth of large-scale well-aligned carbon nanotubes by plasma enhanced hot filament chemical vapor deposition. Appl. Phys. Lett., 73, pp3845-3847.

Huang, Z.P., Wang, D.Z., Wen, J.G., Sennett, M., Gibson, H., Ren, Z.F., 2002. Effect of nickel, iron and cobalt on growth of aligned carbon nanotubes. Appl. Phys. A, 74, pp387-391.

Han, J.H., Lee, C.H., Jung, D.Y., Yang, C.W., Yoo, J.B., Park, C.Y., Kim, H.J., Yu, S., Yi, W., Park, G.S., Han, I.T., Lee, N.S., Kim, J.M., 2002, NH3 effect on the growth of carbon nanotubes on glass substrate in plasma enhanced chemical vapor deposition.

Thin Solid Films, 409, pp120-125.

Kiang, C.H., Endo, M., Ajayan, P.M., Dresselhaus, G., Dresselhaus, M.S., 1998. Size effects in Carbon Nanotubes. Phys. Rev. Lett. 81(9), pp1869-1872.

Kolmogorov, A.N., Crespi, V.H., 2000. Smoothest bearings: interlayer sliding in multiwalled carbon nanotubes. Phy. Rev. Lett., 85(22), 4727-4730.

Pantano, A., Boyce, M.C., Parks, D.M., 2003. Mechanics of deformation of single and multiwalled carbon nanotubes. Accepted for publication, J. Mech. Phys. Solids.

Poncharal, P., Wang, Z.L., Ugarte, D., de Heer, W.A., 1999. Electrostatic deflections and electromechanical resonances of carbon nanotubes, Science, 283, pp1513-1516.

Salvetat, J.P., Bonard, J.M., Thomson, N.H., Kulik, A.J., Forro, L., Benoit, W., Zuppiroli, L., 1999. Mechanical properties of carbon nanotubes. Appl. Phys. A, 69, pp255-260.

Saito, Y., Yoshikawa, T., Bandow, S., Tomita, M., Hayashi, T., 1993. Interplayer spacing in carbon nanotubes. Phys. Rev. B, 48 (3), pp1907-1909.

Schmitt, C.C., Elings, J.R., Serry, M. Nanoindenting, scratching and wear testing using scanning probe microscopy. Digital Instruments, Internet materials.

Sun X., Kiang C.H., Endo M., Takeuchi K., Furuta T., Dresselhaus M.S., 1996. Stacking characteristics of graphene shells in carbon nanotubes Phys. Rev. B. vol54, n18, 1996, pp12629-12632.

Treacy, M.M.J., Ebbesen, T.W., Gibson, J.M., 1996. Exceptionally high Young's modulus observed for individual carbon nanotubes, Nature, 381, pp678.

Wong, E.W., Sheehan, P.E., Lieber, C.M., 1997. Nanobeam mechanics: elasticity, strength, and toughness of nanorods and nanotubes. Science, vol.277, Sep., pp1971-1975.

Yu, M.F., Yakobson, B.I., Ruoff, R.S., 2000. Controlled sliding and pullout of nested shells in individual multiwalled carbon nanotubes. J. Phy. Chem. B, 104, pp8764-8767.

Yakobson, B.I., Brabec, C.J., Bernholc, J., 1996. Nanomechanics of carbon tubes: instabilities beyond linear response. Phy. Rev. Lett., 76 (14), pp2511-2514.